

**Gravitational Wave Background from Compact Objects
and a New Search for Supermassive Black Hole Binaries**

Von der Fakultät für Mathematik und Physik
der Gottfried Wilhelm Leibniz Universität Hannover
zur Erlangung des Grades

**Doktor der Naturwissenschaften
Dr. rer. nat.**

genehmigte Dissertation
von

M.Sc. Pablo Antonio Rosado González

geboren am 28. November 1986, in Sevilla (Spanien)

2013

Referent: Herr Prof. Dr. Bruce Allen.

Korreferenten: Herr Prof. Dr. Joseph Romano und Herr Prof. Dr. Bernard Schutz.

Tag der Promotion: 6. Dezember 2013.

Abstract

The theory of General Relativity predicts the emission of gravitational waves (GWs), although so far we have only indirect proof of their existence. The first detection of GWs will not only be another positive test of Einstein's theory, but will also start the era of GW astronomy. In particular, the detection of the GW background (GWB) can unveil information about the early stages of the universe, that cannot be reached with any other type of observations.

The GW background is spread over the entire spectrum of GW frequencies. In some frequency intervals, the GWB is dominated by the incoherent superposition of waves from astrophysical systems, like compact binaries and rotating neutron stars. Such a background can hinder the detection of other sources of GWs; this GWB is called unresolvable. The GWB is one of the four main types of signals that are currently searched for with ground-based GW detectors. Moreover, it is the main search goal of an alternative method of GW detection: the Pulsar Timing Array (PTA).

This thesis studies the GWB produced by binary systems containing a black hole, a neutron star, or a white dwarf, and that produced by rotating neutron stars, such as pulsars, magnetars and gravitars. This study, that covers the frequency ranges of all current and planned GW detectors, is performed in a clear and self consistent way, and improves upon previous investigations, that have been carried out in a confusing or even incorrect manner. The detectability of the GWB, and whether or not it is unresolvable, are two of the main topics of this work.

The PTA aims to detect GWs produced by supermassive black hole binaries (MBHBs). There exist very efficient pipelines that search for individual sources and for an unresolvable background of GWs from MBHBs. However, it is so far unclear if the PTA signal is an unresolvable GWB or rather the superposition of the GWs emitted by only a few single systems. This work, besides presenting the GWB produced by MBHBs, attempts to clarify the expected PTA signal.

The peculiar properties of galaxies that can host MBHBs are studied in a simulated universe (produced in the Millennium Simulation). These galaxies present a characteristic distribution of redshifts and stellar masses, and the traces of a recent merger (necessary for the formation of a MBHB) can be identified by looking at the number of neighbouring galaxies. These particular features allow a search to be performed for MBHB hosts in a real galaxy catalog (the Sloan Digital Sky Survey); the efficiency of the search is tested on the simulated universe. We also address the question of whether or not PTA sources are more likely to be found in galaxy clusters. Finally, one of the main outcomes of this work is a list of real MBHB candidates.

Keywords: gravitational wave background, binary systems, rotating neutron stars, supermassive black hole binaries, pulsar timing array, data analysis.

Kurzfassung

Die Allgemeine Relativitätstheorie sagt die Existenz von Gravitationswellen (GW) voraus, die bislang nur indirekt bewiesen wurde. Die erste Detektion von Gravitationswellen wird nicht nur ein weiterer Beweis für Einsteins Theorie sein, sie wird gleichzeitig der Beginn der GW-Astronomie sein. Insbesondere die Detektion der GW-Hintergrundstrahlung (GWH) kann Informationen über das frühere Universum enthüllen, die anderen Beobachtungsarten nicht zugänglich sind.

Die GWH erstreckt sich über das gesamte GW-Frequenzspektrum. In manchen Frequenzintervallen ist die GWH von inkohärenter Überlappung dominiert, die von astrophysikalischen Systemen erzeugt wird, wie kompakten Doppelsternen oder rotierenden Neutronensternen. Eine solche GWH kann die Detektion anderer GW-Quellen stören und wird als ‘unauflösbar’ bezeichnet. Die GWH ist eine von vier Arten möglicher Signale, die derzeit mit terrestrischen GW-Detektoren gesucht werden. Außerdem ist die GWH das wichtigste Ziel einer alternativen Methode zur GW-Detektion, das sogenannte Pulsar Timing Array (PTA).

Diese Dissertation erforscht die von Binärsystemen erzeugte GWH, die ein Schwarzes Loch, einen Neutronenstern, oder einen Weißen Zwerg beinhalten, sowie die GWH von rotierenden Neutronensternen, wie Pulsaren, Magnetaren oder Gravitaren. Diese Arbeit, die Frequenzintervalle aller gegenwärtigen und geplanten GW-Detektoren betrachtet, verbessert vorherige Studien, die widersprüchliche oder sogar inkorrekte Herleitungen enthalten. Die Detektierbarkeit der GWH und ihre Auflösbarkeit sind zwei der Hauptthemen dieser Arbeit.

Das PTA versucht GW zu detektieren, die von Binärsystemen supermassereicher Schwarzer Löcher (BSSL) emittiert werden. Derzeit existieren sehr effektive Verfahren, um sowohl individuelle Quellen als auch eine unauflösbare GWH zu detektieren. Nichtsdestotrotz ist bisher unklar, ob das PTA-Signal eine unauflösbare GWH ist, oder eher eine Überlappung von GW von wenigen Systemen. Diese Arbeit stellt einer Berechnung der GWH von BSSL dar, und versucht das erwartete PTA-Signal aufzuklären.

Weiterhin werden die besonderen Eigenschaften von Galaxien mit BSSL untersucht. Dazu wird ein simuliertes Universum (von der Millennium Simulation) herangezogen. Galaxien mit BSSL zeigen eine besondere Verteilung der Rotverschiebungen und der stellaren Massen. Die Spuren einer kürzlich erfolgten Kollision mit einer anderen Galaxie (erforderlich, um BSSL zu produzieren) können durch die Messung der Anzahl von Nachbargalaxien identifiziert werden. Mit dieser Information kann eine Suche nach BSSL mithilfe eines echten Kataloges für Galaxien (Sloan Digital Sky Survey) durchgeführt werden. Die Effizienz einer solchen Suche wird im simulierten Universum getestet. Diese Doktorarbeit untersucht auch, ob PTA-Quellen sich häufiger in Galaxienhaufen befinden, und beinhaltet auch eine Liste echter BSSL Kandidaten.

Schlagnworte: Gravitationswellenhintergrund, Binärsysteme, rotierende Neutronensterne, supermassereiche Schwarze Löcher, Pulsar Timing Arrays, Datenanalyse.

Contents

Abstract	i
Kurzfassung	iii
Contents	iii
1 Introduction	1
1.1 Main achievements and caveats of Chapter 2	1
1.2 Main achievements and caveats of Chapter 3	2
1.3 Main achievements and caveats of Chapter 4	3
2 Gravitational wave background from binary systems	5
2.1 Introduction	5
2.2 Characterization of the background	7
2.2.1 Notation	7
2.2.2 Terminology	7
2.2.3 Heuristic proof of the lack of confusion noise	10
2.2.4 Cosmological model	10
2.2.5 Spectral function	14
2.2.6 Resolvability of the background	18
2.2.7 Continuity of the background	21
2.3 Models for the ensembles	23
2.3.1 Energy spectrum	23
2.3.2 Interval of time per frequency bin	25
2.3.3 Maximum frequencies	25
2.3.4 Minimum frequencies	26
2.3.5 Calculations for stellar binaries	29
2.3.6 Calculations for massive black hole binaries	33
2.4 Results	35
2.5 Discussion	41
2.5.1 On the coalescence rate of stellar binaries	41
2.5.2 On the minimum frequency of stellar binaries	42
2.5.3 On the minimum frequency of massive black hole binaries	43
2.5.4 On the condition of resolvability	43
2.5.5 On the definition of the overlap function	44
2.5.6 Comparison with previous work	46
2.6 Summary and conclusions	49

3	Gravitational wave background from rotating neutron stars	51
3.1	Introduction	51
3.2	Characterization of the background: an overview	53
3.2.1	Quantification of the background	54
3.2.2	Resolvability of the background	56
3.2.3	Detectability of the background	57
3.3	Characterization of the background: a detailed derivation	59
3.3.1	Formation rate of systems	59
3.3.2	Time evolution of the ensemble	59
3.3.3	Spectral function and overlap function	61
3.4	Model for the ensemble of rotating neutron stars	63
3.4.1	Neutron star model	63
3.4.2	Formation rate of neutron stars	65
3.4.3	Energy evolution	65
3.4.4	Frequency evolution	68
3.4.5	Initial frequency distribution	69
3.4.6	Magnetic field and ellipticity distributions	69
3.4.7	Minimum and maximum frequencies	70
3.5	Results	72
3.5.1	Gravitars	72
3.5.2	A more realistic expectation	76
3.5.3	Upper limit for magnetars	76
3.5.4	Detection prospects	78
3.6	Discussion	87
3.6.1	Comparison with previous work	87
3.6.2	On the formation rate	87
3.7	Summary and conclusions	89
3.7.1	Regarding the calculation of the spectral function	89
3.7.2	Regarding the detection of the background of rotating neutron stars	89
3.8	Appendix I: Simple formulas for the background of rotating neutron stars	91
3.9	Appendix II: Simple formulas for the background of binary systems	93
3.10	Appendix III: On Blandford’s argument	94
4	A new method to search for supermassive black hole binaries	95
4.1	Introduction	95
4.2	Description of the catalogs	98
4.2.1	Real catalog	98
4.2.2	Fake catalog	99
4.2.3	Adapted catalog	100
4.3	Description of the searches	105
4.3.1	Probabilities of B-galaxies	105
4.3.2	Probabilities of PTA-galaxies	108
4.3.3	Including clustering in the search	111
4.3.4	Extending the search to larger redshifts	114

4.4	Results	117
4.4.1	Clustering of B-galaxies	117
4.4.2	Efficiency of the search for B-galaxies	121
4.4.3	Efficiency of the search for PTA-galaxies	124
4.4.4	Efficiency of the search when including clustering information	126
4.4.5	Efficiency of the search at larger redshifts	126
4.4.6	Assigning probabilities to real galaxies	128
4.5	Discussion	136
4.6	Summary and conclusions	141
4.7	Appendix: queries for the data	144
	Bibliography	146
	Acknowledgements	163
	Curriculum Vitae	165
	List of publications	167

1 Introduction

Gravitational waves (GWs) [33] are oscillations of the space-time that propagate at the speed of light, emitted by accelerated objects. Their generation is predicted by Einstein's theory of General Relativity [250]. There are plenty of experiments that confirm the predictions of this theory; an extraordinary example is the study of the properties of the double pulsar PSR J0737-3039 [143]. The direct detection of gravitational waves has not been achieved yet, despite the tremendous effort of a large community of scientist around the globe [130, 92]. There is, however, a crucial proof of the generation of GWs by binary systems [177, 176], provided by the observations of the Hulse-Taylor binary system PSR B1913+16 [94, 252]. In this thesis we assume the emission of GWs as predicted by Linearized Gravity [161, 147].

This thesis comprises three main parts that correspond to three different articles; two of them are already published in a refereed journal [207, 208], and the third one is awaiting publication. Each part contains its own introduction and conclusions, and is self consistent. There is only a small overlap between the first and second part, since they both introduce the basic concepts of the gravitational wave background (GWB) and its quantification.

Chapters 2 and 3 are almost identical to the corresponding published papers. Some minor typos have been corrected, figures have been adapted to the format of the thesis, and some fragments of the text have been slightly modified to make the reading consistent with the style of this document. These two papers have been written by P. A. R., with the help and supervision of Bruce Allen (who also suggested the initial idea of the articles).

Chapter 4 may differ from the published article (that will soon be submitted), depending on the suggestions and criteria of the referees and journal editors. The text of the paper has been written by P. A. R., with some contributions by Alberto Sesana (second author of the article); all the calculations have been carried out by P. A. R., with the suggestions and guidance of Alberto Sesana, who also first proposed the main idea of the work.

A summary of the main achievements and caveats of the three parts of the thesis is now depicted.

1.1 Main achievements and caveats of Chapter 2

This chapter introduces some of the fundamentals of the GWB, and describes how it is usually quantified in a detailed and consistent way. The notation and terminology introduced here are the same used in Chapter 3, and are also consistent with Chapter 4.

The resolvability of the GWB (which roughly tells if the signals that form the GWB can be individually distinguished) is investigated; definitions and mathematical tools to quantify it are provided. Experts working on the field of GWB data analysis have commented on these definitions, both in private communications and in other refereed publications. For example in Appendix A of [241], these definitions have been revised to account for the effect of the GW detector noise on our ability to resolve individual signals. The suggested definitions may be

1 Introduction

more convenient from the perspective of the GWB data analysis; however, when adopting them, the resolvability is not anymore an intrinsic property of the GWB, but strongly depends on the properties of the specific detector.

To quantify the resolvability, we introduce the *overlap function*, as a generalization for the *duty cycle*, commonly used in the literature. The importance of this generalization has been well accepted and taken into account in subsequent papers, although the terminology *duty cycle* has been kept (for example in [260]). In fact, *overlap function* may be a rather unfortunate name, since it can be confused with the *overlap reduction function*, which is a key tool when cross-correlating data from different detectors [11, 69].

Predictions for the resolvable and unresolvable GWB produced by compact binary systems (containing a black hole, a white dwarf, or a neutron star) are presented over the entire GW frequency spectrum. The large uncertainties involved in the calculations are taken into account to produce upper and lower limits on the expected levels of GWB. The detectability of the resulting backgrounds, however, is not thoroughly addressed. To properly claim whether or not a GWB is detectable by an instrument, the signal-to-noise ratio should be calculated (as performed in Chapter 3 for rotating neutron stars). An even more realistic approach is to analyze the data of a detector in which simulated signals have been artificially introduced, mimicking the predicted GWB (this has been accomplished for the Einstein Telescope, ET, in [202]).

The GWB produced within the frequency band of current and planned GW detectors turns out to be resolvable (adopting our criterion on the resolvability, that does not take into account the detector noise), i.e. signals produced by individual systems do not overlap within any bin of the observed frequency interval.

1.2 Main achievements and caveats of Chapter 3

The introduction of this chapter is similar to the previous, although the sources of GWB mentioned and their corresponding references have a small overlap. Moreover, the quantification of the GWB is carried out in a slightly different manner (while the result, of course, is equivalent to that of the previous chapter), so that the evolution of systems that contribute to the GWB can be more easily taken into account.

We predict the levels of GWB produced by rotating neutron stars, such as pulsars, magnetars and gravitars. To do so, we take into account that each rotating stars may evolve over long periods of time. The evolution of the individual signals with time is especially relevant when considering gravitars (that spin down more slowly than highly magnetized neutron stars).

Different predictions are presented, for different assumptions on the intrinsic properties of neutron stars and the statistical properties of their ensemble. The biggest source of discrepancy among the predictions comes from the models for the spin period distribution. For one of the models, the GWB from rotating neutron stars is not expected to be detectable by any current or planned GW observatory; however, another model may even lead to the presence of an unresolvable background in the frequency band of ET.

The perspectives for current and planned GW observatories to detect this GWB are studied. We calculate a robust upper limit for its amplitude; it does not produce a signal-to-noise ratio large enough to be detected by Advanced LIGO. An upper limit is also obtained for the GWB produced by magnetars; it could be detectable by ET. Under the most conservative assumptions (based on observational information of active pulsars), the GWB is too faint to be detected by

any instrument. However, if there exists a sufficient number of rotating neutron stars with a low magnetic field, they could produce an unresolvable GWB detectable by ET.

1.3 Main achievements and caveats of Chapter 4

For years the GW community has been wondering whether the Pulsar Timing Array (PTA) will most likely detect an unresolvable GWB produced by massive black hole binaries (MBHBs), or whether MBHBs will rather be observed as single resolvable sources of GWs. The main goal of this chapter is to better understand the type of signal that the PTA will detect. It was Bruce Allen who first suggested P. A. R. to address this issue; then, Alberto Sesana proposed the use of a galaxy catalog to cope with the topic.

The results combine a simulated universe (derived from the Millennium Simulation, MS) with real observations (of the spectroscopic Sloan Digital Sky Survey, SDSS), to assign to each real galaxy the probability of hosting a MBHB observable by the PTA. We thus find the most likely candidates to be first detected as single sources of GWs; these candidates could be used in forthcoming targeted searches.

The efficiency of the methods used to identify MBHBs are tested thoroughly on the simulated local universe. We also find that these methods could perform better when getting deeper in redshift or using more complete catalogs.

The main caveat of this work is the procedure used to account for the observational limitations of the SDSS. In order to assign galaxies more accurate probabilities of hosting MBHBs, a more sophisticated method should be used.

We also investigate the clustering of galaxies that may host a MBHB. Although this bit of information cannot be efficiently applied to refine the search for MBHBs, it allows us to support the idea that the first individually observable PTA sources are more likely to be found in dense galaxy groups.

The techniques developed here, that are alternative to those applied in previous searches for MBHBs, constitute a step forward towards the understanding of the expected PTA signal. Our results would support the detection of a low-frequency stochastic background rather than loud individual sources; however, a more detailed study of the candidates, and more complete catalogs (covering a larger area of the sky) would be necessary to confirm this claim.

2 Gravitational wave background from binary systems

Originally published as:
P. A. Rosado, *Phys. Rev. D* 84:084004, 2011.
Copyright 2011 by the American Physical Society.

Basic aspects of the background of gravitational waves and its mathematical characterization are reviewed. The spectral energy density parameter $\Omega(f)$, commonly used as a quantifier of the background, is derived for an ensemble of many identical sources emitting at different times and locations. For such an ensemble, $\Omega(f)$ is generalized to account for the duration of the signals and of the observation, so that one can distinguish the resolvable and unresolvable parts of the background. The unresolvable part, often called confusion noise or stochastic background, is made by signals that cannot be either individually identified or subtracted out of the data. To account for the resolvability of the background, the overlap function is introduced. This function is a generalization of the duty cycle, which has been commonly used in the literature, in some cases leading to incorrect results. The spectra produced by binary systems (stellar binaries and massive black hole binaries) are presented over the frequencies of all existing and planned detectors. A semi-analytical formula for $\Omega(f)$ is derived in the case of stellar binaries (containing white dwarfs, neutron stars or stellar-mass black holes). Besides a realistic expectation of the level of background, upper and lower limits are given, to account for the uncertainties in some astrophysical parameters such as binary coalescence rates. One interesting result concerns all current and planned ground-based detectors (including ET). In their frequency range, the background of binaries is resolvable and only sporadically present. In other words, there is no stochastic background of binaries for ground-based detectors.

2.1 Introduction

The gravitational wave background [11, 145] is formed by a large number of independent gravitational wave sources. This chapter focuses on the background produced by coalescing binary systems. These are isolated pairs of massive objects that inspiral towards each other by emitting gravitational radiation until they coalesce.

We review the characterization of the background, for which the spectral energy density parameter, or simply *spectral function*, $\Omega(f)$, is often used. This function gives the present fractional energy density (per logarithmic frequency interval) of gravitational radiation at an observed frequency f . A formula for $\Omega(f)$ is obtained in a clear, self-consistent way, for an ensemble of many identical sources emitting at different times and locations. This formula is generalized to distinguish whether the signals are resolvable or not, or whether they are observed continuously or sporadically.

The *resolvability* of the signals is an important topic of this chapter. Roughly speaking, signals are unresolvable if their waveforms are observed simultaneously at similar frequencies (differing less than the frequency resolution). Many unresolvable signals form an unresolvable background. If such a background dominates in a certain frequency interval, one cannot see the

2 Gravitational wave background from binary systems

waveforms of its components, but a pattern that rather looks like instrumental noise. For that reason it is often called *confusion noise*. The other part of the background is *resolvable*. The waveforms of the resolvable part can be distinguished and in some circumstances subtracted out of the data of a detector [20, 46].

There are many studies in the literature about astrophysical sources that contribute to the background at present. A few examples of these sources are: core-collapse supernovae [67], rotating neutron stars [68, 197], formation of neutron stars [44, 45], inspiralling or coalescing stellar binaries [215, 63, 199, 201, 200], inspiralling or coalescing massive black hole binaries [222, 223] and magnetars [198]. But there are inconsistencies in the literature; for example, according to [51], the results of some of the previous papers [44, 45] (and also [52, 201], as pointed out in [261]) are incorrect, due to a wrong $[1 + z]$ factor in the calculations. Besides, according to [79], the definition of the spectral function used in many papers is misleading or misinterpreted. Finally, as we discuss further on, in some of the mentioned papers, the continuous and unresolvable backgrounds are not properly defined. To avoid possible misunderstandings or mistakes we tend to present all calculations and definitions as clearly as possible.

We calculate the contributions to the background of the strongest emitting binary systems. These are the ones composed of white dwarfs, neutron stars, stellar-mass black holes or massive black holes. The resulting energy spectra are given as maximum, most likely, and minimum expectations, taking into account the present uncertainties in the quantities involved.

We show that ground-based detectors do not encounter any unresolvable background in their *frequency window* (the frequency range in which they reach their optimal sensitivity). This applies to present detectors, such as TAMA300 [14], GEO600 [141], Virgo [37], and LIGO [130], but also to planned detectors, such as the advanced versions of LIGO and Virgo [130, 70], LCGT¹ [120], and ET [190]. At these frequencies, there is not even a resolvable continuous background, i.e., signals are not always present. Whether or not these signals can be subtracted out of the data is an issue we do not deal with in this work.

This chapter considers a frequency range wider than the frequency windows of ground-based detectors. It includes the windows of all existing and future detectors, such as LISA² [49] or BBO [181], and also reaches the frequency range of interest for the PTA [92].

The obtained unresolvable background turns out to be dominated by white dwarf binaries (at frequencies below ~ 0.1 Hz) and by massive black hole binaries (below $\sim 10^{-4}$ Hz). This confusion noise could enter the band of LISA and would certainly enter the band of BBO and the complete Parkes PTA [149].

The outline of this chapter is as follows:

In Section 2.2 we first explain our notation and give some relevant terminology. We then give a simple heuristic proof of the fact that there is neither an unresolvable nor a continuous background in the frequency window of ground-based detectors. The formula of the spectral function is derived for an ensemble of many identical sources emitting at different times and locations. The obtained formula agrees with that of [180]. The concept of resolvability is studied, and the spectral function is generalized to account for it. To get to that point, we introduce the *overlap function* $\mathcal{N}(f, \Delta f, z)$. This function gives the average number of signals observed with redshifts smaller than z and frequencies between f and $f + \Delta f$, where Δf is the frequency resolution.

¹Now called KAGRA [230].

²In this chapter we consider the configuration of the old LISA mission (that was proposed by the time when this work was written).

We then use the overlap function to distinguish the continuous and discontinuous parts of the background.

In Section 2.3 we present the models used to quantify the background of stellar binaries and massive black hole binaries. The main physical quantities involved in the calculations (such as mass ranges and coalescence rates) are presented in this section. A semi-analytical formula for the spectral function is derived in the case of stellar binaries.

Section 2.4 contains the main results of the chapter. The spectral function is shown in the different regimes of resolvability and continuity. The curves in the plots are given as maximum, most likely, and minimum expected.

In Section 4.5 we justify some of the approximations and assumptions of the previous sections. We compare our results with others from the literature. Our notions of continuous background and unresolvable background are compared with the ones of previous work. We also show that the overlap function, which turns out to be a generalization of the duty cycle, is a proper quantifier of the resolvability and continuity of the background.

The main conclusions and results are summarized in Section 2.6.

2.2 Characterization of the background

2.2.1 Notation

All magnitudes are measured in the frame of the cosmological fluid, since massive objects that are not subject to external forces come quickly to rest with respect to this frame.

We use the index “*e*” (for *emission*) for quantities measured close to the system at the time of the emission of the radiation. For example, f_e (emitted frequency) is the frequency of a wave, measured soon after its emission, before the expansion of the universe stretches its wavelength. Quantities measured here and now (which are called *observed* quantities) have no index. The frequency of the wave of the previous example, measured today, is thus denoted by f .

We use the indices “low”, “upp”, “min” and “max” to refer to *lower*, *upper*, *minimum* and *maximum*, respectively.

2.2.2 Terminology

We now introduce some terminology to avoid confusion or ambiguity throughout this chapter.

By *system* we mean a certain configuration of physical objects that is a source of gravitational waves. An example of system is a pair of neutron stars inspiralling towards each other.

We use the term *ensemble* for the collection of systems, all having similar properties and behaviour, formed from the Big Bang until now. An example is the population of coalescing neutron star binaries in the universe.

By *signal* we refer to the total gravitational radiation emitted by a system. One system emits only one signal, that can range over a large frequency interval and exist over a long interval of time. Despite the interval of time it lasts, a signal is assumed to be characterized by a certain redshift, which remains the same from the beginning until the end of the signal³ (in Section 2.5.2 we discuss the validity of this assumption). A signal is composed of *signal elements*, each characterized by a certain infinitesimal frequency interval.

³This assumption is not adopted for the calculations of Chapter 3.

2 Gravitational wave background from binary systems

The *total (gravitational wave) background* is the collection of all gravitational waves in the present universe. It can be divided into different parts, according to different criteria. For example, *primordial* and *contemporary* parts, *resolvable* and *unresolvable* parts or *continuous* and *discontinuous* parts. One can also divide the total background into many different parts, each conformed by the contribution of a certain ensemble. By extension, we use the word *background* when referring to both the total background and to its different parts. Hence, we can talk about the background of neutron star binaries, which is the collection of signals of the ensemble of neutron star binaries. The part of this background that fulfills the condition of unresolvability would be the unresolvable background of neutron star binaries.

Primordial versus contemporary background

The *primordial background* [10, 145] is composed of gravitational radiation emitted in the early universe, at very large redshifts. It is analogous to the background formed by the cosmic electromagnetic radiation [174, 26, 23]. In the case of the latter, the radiation was released (when photons decoupled from matter) roughly a hundred thousand years after the Big Bang. On the other hand, the primordial gravitational radiation was produced in a tiny fraction of the first second of the universe (see Section 9.4.3 (d) of [90] by K. S. Thorne and references therein). In this background might be hidden waves from inflation and cosmic strings [9, 248].

The other part of the total background is still being produced at present and thus we refer to it as the *contemporary background*. It is made by many different systems that formed in the past (at redshifts less than ~ 20 , which is the largest redshift assumed for the systems we study) and can also form today. Examples of such systems are coalescing binaries, rapidly-rotating compact objects or core-collapse supernovae (some references were given in Section 2.1).

In certain frequency ranges one can get a clear view of primordial signals, whereas in others the contemporary signals dominate. The detection of the primordial background would be the most direct way to observe processes of the very early universe. But valuable information would also be gained from the detection of the contemporary background, for example about binary formation and coalescence rates. Furthermore, predictions of the contemporary background can set constraints on the frequency ranges where the primordial one could be detected. The contemporary background is the main topic of this chapter.

In the literature, primordial and contemporary backgrounds are often called *cosmological* and *astrophysical*, respectively. We do not use these words to avoid ambiguity, since sometimes both terminologies are used together, for example when talking about *cosmological populations of astrophysical sources* [216], which might be confusing for non-specialized readers.

Unresolvable versus resolvable background

It is useful to classify the components of the background depending on their resolvability. We now briefly comment on this concept; precise definitions of what we mean by resolvable and unresolvable backgrounds can be found in Section 2.2.6.

Signals spend different intervals of time at different ranges of frequencies. In the case of binaries, they evolve much more rapidly at higher than at lower frequencies. At lower frequencies they will thus overlap (i.e., they will be observed at the same time) more frequently than at higher ones. A frequency bin of width Δf , which is the frequency resolution allowed by the detector and by the data analysis method, will often be filled by one or more signals at low frequencies.

On the other hand, a frequency bin at high frequencies will be filled by one or more signals only sporadically, since signals are very short.

An unresolvable part of the background exists as soon as a frequency bin is constantly occupied by an average of one or more signals. At frequencies where such a background dominates, the waveforms of the signals cannot be distinguished from each other. When a waveform is not resolvable, one cannot obtain information from it, such as the characteristics of the system that emitted that radiation. Moreover, such waveforms cannot be subtracted out from the data.

The rest of the background is the resolvable part. The waveforms of this part can be distinguished from each other. One can thus obtain information about the system by studying the waveform of the emitted radiation.

For some authors, what we call the unresolvable background is defined as the *stochastic background*, and the remaining gravitational radiation is called the *total gravitational wave signal* [223]. This is a reasonable definition, but conflicts with what is often called *stochastic background* by many other authors (for example in [217] and other papers cited in Section 2.1). A more precise definition for *stochastic background* can be found in [11].

Continuous versus discontinuous background

We now briefly comment on the concept of continuity of the background. In Section 2.2.7 we give precise definitions of what we mean by continuous and discontinuous backgrounds.

A continuous background exists in a frequency interval $[f_{\text{low}}, f_{\text{upp}}]$ (that can be, for example, the frequency window of a detector) as soon as this interval is constantly occupied by one or more signals. If in that interval there are gaps between signals, or the signals occur sporadically, the background is discontinuous.

The condition of continuity tends to that of unresolvability when $f_{\text{upp}} - f_{\text{low}}$ tends to Δf . If a background is not continuous in an interval of frequencies, it is not continuous either in a smaller interval. Therefore, only a continuous background can be unresolvable.

We point out that the continuity of the background is not as relevant as the resolvability. However, we include it in this chapter for two reasons:

First, the continuity has been often used in the literature (for example in the already mentioned papers [201, 200]) to define the different regimes of the background. Once we know how to account for the continuity, we will realize that it is not the right tool to be used. Instead, the resolvability is the fundamental property of the background.

Second, the continuity can be used to determine how often the background is observed. Suppose we want to detect a signal of some kind, but there is a background covering the signal. If the background is discontinuous in a frequency band, sometimes that signal can be clearly seen, without any background. On the other hand, if the background is continuous, we need to subtract it from the data in order to see that other signal. As we show in Figure 2.6, ET has no continuous background from binaries in its frequency window; BBO, on the contrary, has a continuous background of binaries crossing its frequency window, so the subtraction of background signals is necessary in order to detect other kinds of signals (this problem has been treated in [46]).

2.2.3 Heuristic proof of the lack of confusion noise for ground-based detectors

We now justify, in a simple heuristic way, that there is no continuous background (and therefore no unresolvable background either) from binary systems at frequencies larger than 10 Hz.

A neutron star binary takes $\sim 10^3$ s to evolve from 10 Hz to the coalescence (which can be proved by using Equation (2.62)). The most realistic coalescence rate for these binaries (see Table 2.1) is of $\sim 10^5 \text{ yr}^{-1}$, in the whole observable universe. This implies ~ 0.003 coalescences per second. One could naively say that, on average, one would see $\sim 10^3 \times 0.003 = 3$ signals. But that would only be true if all binaries were close to us, at redshift ~ 0 . The farthest binaries (close to redshift ~ 5) that we observe today at frequency ~ 10 Hz, emitted at $\sim 10 \times [1 + z] = 60$ Hz (using Equation (2.3)) and needed just ~ 8 s to coalesce. An interval of time of ~ 8 s at redshift ~ 5 is now observed as an interval of $\sim 8 \times [1 + z] = 48$ s (using Equation (2.5)). This implies that an average of $\sim 48 \times 0.003 \approx 0.14$ signals are observed. The number of signals expected to be observed is thus a number between 3 and 0.14, which, after doing the proper calculation, turns out to be smaller than 1. Hence, neutron star binaries do not produce a continuous background at frequencies higher than 10 Hz.

Other binaries whose signals could produce a continuous background in the frequency window of ground-based detectors are those containing a stellar-mass black hole. But these binaries have a smaller coalescence rate and need less time to coalesce, from an initial frequency of 10 Hz. The product *coalescence rate* \times *duration of signal* would thus be even smaller. Therefore they do not produce a continuous background either.

At frequencies larger than 10 Hz, hence, there is no continuous background from binary systems. Between 1 and 10 Hz one could have a continuous background, but it turns out to be well below the realistic sensitivity of a ground-based detector (see Figure 2.6).

2.2.4 Cosmological model

Metric

We assume a spatially flat, homogeneous and isotropic universe, described by a Friedmann-Robertson-Walker metric,

$$ds^2 = -c^2 dt_e^2 + a^2(t_e) [dr^2 + r^2(d\theta^2 + \sin^2(\theta) d\phi^2)], \quad (2.1)$$

where c is the speed of light. The time coordinate t_e is chosen to be, for convenience, the look-back time: it is 0 at present and $t_0 \approx 13.7$ Gyr at the Big Bang. The usual *look-forward* time would be just $t' = t_0 - t_e$, with which the form of the metric would not change. The dimensionless cosmological scale factor, $a(t_e)$, is chosen to be $a(0) = 1$ at present. The coordinates r , θ and ϕ are called comoving coordinates, because they *move* with the cosmological fluid. For example, two objects at rest with respect to the fluid, at positions r_1 and r_2 (and equal values of θ and ϕ), have a *comoving distance* $r = r_2 - r_1$. This comoving distance remains the same at every future time. However, the physical (proper) distance between them is $r_{\text{phys}}(t_e) = a(t_e)r$, and changes with time as the universe expands. Setting $r = 0$ at the Earth, the coordinate r of a distant object is its comoving distance from us.

Redshifting

The definition of the cosmological redshift z is given by

$$1 + z = \frac{a(0)}{a(t_e)}, \quad (2.2)$$

where, as already said, $a(0) = 1$. This equation gives the value of the scale factor at the time of emission of a graviton (or a photon) that is today observed with a redshift z .

We now see how the expansion of the universe affects frequencies and energies of gravitational waves, as well as infinitesimal intervals of time (a derivation can be found in Section 4.1.4 of [147]). A frequency f_e of a wave emitted by a system at a redshift z corresponds to

$$f = \frac{f_e}{1 + z} \quad (2.3)$$

at the present time. Since the energy of a graviton is proportional to its frequency, a graviton emitted with an energy E_e is today observed with

$$E = \frac{E_e}{1 + z}. \quad (2.4)$$

An infinitesimal lapse of time dt_e (emitted interval of time) measured at redshift z is today observed as

$$dt = dt_e[1 + z]. \quad (2.5)$$

From (2.3), it follows that an infinitesimal frequency interval df_e emitted at redshift z is today observed as

$$df = \frac{df_e}{1 + z}. \quad (2.6)$$

Similarly, from (2.4), an infinitesimal energy interval dE_e corresponds to

$$dE = \frac{dE_e}{1 + z} \quad (2.7)$$

today.

Volumes

Some important quantities in this chapter are defined as densities, i.e. per unit volume (by which we mean the spatial volume). Because of the expansion, it is convenient to speak of two different volumes: *physical* and *comoving* volume.

The element of physical volume $d\mathcal{V}$ at fixed time t_e in the metric (2.1) is given by $a^3(t_e) r^2 \sin(\theta) dr d\theta d\phi$. We consider only sources uniformly distributed in the sky, so we can integrate for all angles θ and ϕ , obtaining

$$d\mathcal{V} = 4\pi a^3(t_e) r^2 dr. \quad (2.8)$$

The factor $a^3(t_e)$ accounts for the expansion in the three space dimensions.

The element of comoving volume $d\mathcal{V}_c$ is defined by $d\mathcal{V}_c = a^{-3}(t_e) d\mathcal{V}$, which, using (2.8), gives

$$d\mathcal{V}_c = 4\pi r^2 dr. \quad (2.9)$$

2 Gravitational wave background from binary systems

Suppose eight galaxies (that, at large scales, can be thought as point-like) are placed at the vertices of a cube. With the expansion, the galaxies separate from each other and the physical volume of the cube increases, but its comoving volume remains always the same. Since we are assuming that all massive objects are at rest with respect to the fluid, no system enters or leaves a certain comoving volume. For this reason it is straightforward to measure densities (for example, the number density of systems) per unit comoving volume.

It is useful to write the element of comoving volume in terms of redshifts, instead of distances. For that, we have to find a way to transform infinitesimal intervals of comoving distance dr into infinitesimal intervals of redshift dz . Suppose we observe today two gravitons, one emitted at redshift z and the other at $z + dz$. Since both reach us at the same time, and both travel at the same velocity c with respect to the cosmological fluid, the one with larger redshift was emitted at a time dt_e before the other, and thus at a comoving distance dr further away from us than the other. The path of the gravitons, moving in a radial direction ($d\theta = d\phi = 0$), is obtained by setting $ds^2 = 0$ in (2.1), which gives

$$dr = \frac{c}{a(t_e)} dt_e. \quad (2.10)$$

To write dt_e in terms of redshifts, we use the definition of the redshift. One can differentiate Equation (2.2) with respect to t_e , obtaining $dz/dt_e = -\dot{a}(t_e)/a^2(t_e)$. Using (2.2) again and the definition of the Hubble expansion rate⁴, $H(t_e) = -\dot{a}(t_e)/a(t_e)$ (where the minus sign appears because of the use of a look-back time), one obtains

$$dt_e = \frac{1}{[1+z]H(z)} dz. \quad (2.11)$$

Here, the Hubble expansion rate has been written as a function of the redshift, instead of the time. The form of $H(z)$ is derived further on in this section. Introducing (2.11) in (2.10), we obtain a relationship between dr and dz ,

$$dr = \frac{c}{a(t_e)} \frac{1}{[1+z]H(z)} dz = \frac{c}{H(z)} dz, \quad (2.12)$$

where the terms $a(t_e)$ and $[1+z]$ have canceled out, using (2.2). Finally, inserting (2.12) in (2.9), the element of comoving volume becomes

$$d\mathcal{V}_c = 4\pi r^2(z) \frac{c}{H(z)} dz. \quad (2.13)$$

Here, $r(z)$ is obtained by integrating (2.12),

$$r(z) = \int_0^z \frac{c}{H(z')} dz'. \quad (2.14)$$

Gravitons emitted between redshift z and $z + dz$ define a shell of comoving volume given by $d\mathcal{V}_c$.

The Hubble expansion rate can be written as a function of the redshift. For that, we use the Friedmann equation (see Chapter 27 of [161]),

$$H^2(t_e) = \frac{8\pi G}{3} \rho(t_e) - \frac{kc^2}{a^2(t_e)} + \frac{\Lambda}{3}, \quad (2.15)$$

⁴The cosmological parameters assumed in this chapter were the most recent by the time when this work was written.

where G and Λ are the gravitational and cosmological constants, respectively. This equation is obtained from the Einstein equation, imposing the metric (2.1) and the stress-energy tensor of a perfect fluid (see Chapter 5 of [161]). We assume a spatially flat universe, which means with zero curvature, $k = 0$. The term $\rho(t_e)$ is obtained from the equation of a perfect fluid of density ρ and pressure p (which is also obtained from the Einstein equation),

$$\dot{\rho} - 3H(t_e) \left[\rho(t_e) + \frac{p(t_e)}{c^2} \right] = 0. \quad (2.16)$$

We can solve this equation considering a universe dominated by non-relativistic matter (also called dust), $\rho(t_e) = \rho_m(t_e)$, with the equation of state $p_m = 0$. One obtains $\rho_m(t_e) \propto a^{-3}(t_e)$, which, using (2.2), becomes

$$\rho_m(z) = \rho_m^0 [1 + z]^3, \quad (2.17)$$

where ρ_m^0 is the current value of the density of matter. One can also solve (2.16) using the equation of state of relativistic matter (radiation), $p_r = \rho c^2/3$. But one can prove that the resulting density, $\rho_r(z) = \rho_r^0 [1 + z]^4$, dominates in the Friedmann equation only at very large redshifts. The redshift at which both densities, $\rho_m(z)$ and $\rho_r(z)$ equate is $z_{eq} \approx 3 \times 10^3$ (from [96]). Considering the redshifts involved in this chapter ($z < 20$) we neglect $\rho_r(z)$ compared to $\rho_m(z)$. Inserting (2.17) in (2.15) and rewriting the latter in terms of the present value of the Hubble expansion rate, $H_0 = [74.2 \pm 3.6] \text{ km s}^{-1} \text{ Mpc}^{-1}$ (from [205]),

$$H(z) = H_0 \mathcal{E}(z), \quad (2.18)$$

where

$$\mathcal{E}(z) = \sqrt{\Omega_m [1 + z]^3 + \Omega_\Lambda}. \quad (2.19)$$

Here,

$$\Omega_m = \frac{8\pi G \rho_m^0}{3H_0^2} \quad \text{and} \quad \Omega_\Lambda = \frac{\Lambda}{3H_0^2} \quad (2.20)$$

are two dimensionless quantities called the density parameters of matter and dark energy, respectively. The most recent values for the cosmological parameters obtained by the Wilkinson Microwave Anisotropy Probe after seven years of measurements are given in [96]. We adopt a density parameter of matter $\Omega_m = 0.27$ and of dark energy $\Omega_\Lambda = 0.73$. For simplicity we do not consider any uncertainty in these values.

For a better understanding of the relationship between volumes and redshifts, we can see Figure 2.1, where a Penrose diagram [89] for the metric (2.1) is shown. Each point of the diagram represents a two-sphere at a certain *conformal time*. The (look-forward) conformal time is defined by

$$d\eta = -[1 + z] dt_e. \quad (2.21)$$

The coordinates of Figure 2.1 are defined by

$$\begin{cases} r' = \arctan(\eta + r) - \arctan(\eta - r) \\ \eta' = \arctan(\eta + r) + \arctan(\eta - r) \end{cases}. \quad (2.22)$$

Introducing (2.21) in (2.1), the path of a graviton fulfills $dr = c d\eta$. In the diagram we use $c = 1$, so that $r = \eta$ and thus $r' = \eta'$ for all null paths. All gravitons that reach us today have traveled along the null path shown (the straight solid line connecting $z = 0$ and z_{\max}). This path cuts the

2 Gravitational wave background from binary systems

horizontal axis at the moment of the Big Bang, fixing the horizon of our observable universe. For each infinitesimal interval of time $d\eta$ (that describes the difference between the emission of two gravitons that reach us today) there is a corresponding interval dz , along the null path, which represents a shell of infinitesimal comoving volume $d\mathcal{V}_c$.

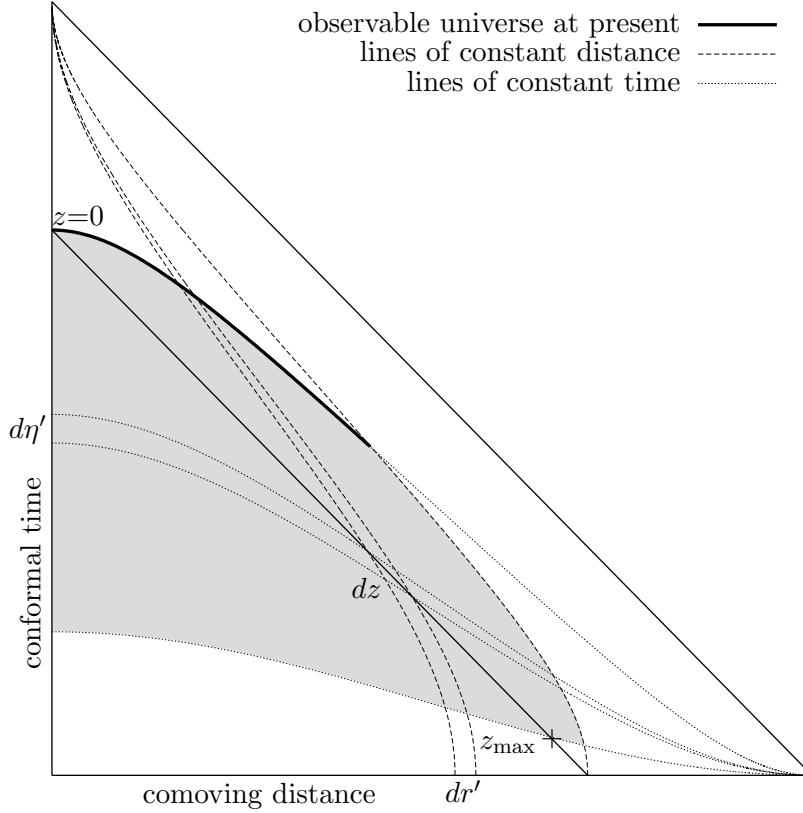


Figure 2.1: Penrose diagram of a universe described by the metric (2.1). The straight black line crossing $z = 0$ and $z = z_{\max}$ contains all the gravitons that we observe today.

2.2.5 Spectral function

Under the assumptions (discussed in [11]) that the background is Gaussian, stationary, isotropic and unpolarized, all the information about it is contained in a dimensionless function called the spectral function, defined by

$$\Omega(f) = \frac{\rho_{\text{ln}}(f)}{\rho_c} = \frac{\varepsilon_{\text{ln}}(f)}{c^2 \rho_c}, \quad (2.23)$$

where f is the observed gravitational wave frequency. The present critical density of the universe is

$$\rho_c = \frac{3H_0^2}{8\pi G}. \quad (2.24)$$

This is the density that closes a universe with zero cosmological constant. This means that ρ_c is the density that, inserted in Equation (2.15) (using $\Omega_\Lambda = 0$), gives a zero curvature ($k = 0$) at

present ($t_e = 0$). The function $\varepsilon_{\ln}(f)$ is defined in such a way that the total energy density of gravitational waves in the present universe is

$$\varepsilon_T = \int \varepsilon_{\ln}(f) d \ln f. \quad (2.25)$$

In the literature, $\varepsilon_{\ln}(f)$ is often written as

$$\varepsilon_{\ln}(f) = \frac{d\varepsilon}{d \ln f}. \quad (2.26)$$

Some other authors (see [79], and Section by L. P. Grishchuk in Part III of [121]) prefer not to use this notation, arguing that it may lead to misunderstandings (one could mistakenly think that the energy density is differentiated). Regardless of the notation, Equation (2.25) must be fulfilled, so that $\varepsilon_{\ln}(f) d \ln f$ is the energy per unit physical volume of gravitational waves between $\ln f$ and $\ln f + d \ln f$. Thus, $\Omega(f)$ is the fractional energy density of gravitational radiation, per logarithmic frequency interval, in the present universe.

We first describe a system as seen by an observer close to it at the time of emission. The energy released in gravitational radiation between logarithmic frequencies $\ln f_e$ and $\ln f_e + d \ln f_e$ is

$$dE_e = P_e(f_e) d \ln f_e. \quad (2.27)$$

This defines $P_e(f_e)$: the energy spectrum of a system at the time of emission. From (2.27) it follows that $P_e(f_e) = dE_e/d \ln f_e$.

The energy spectrum of a system at the time of emission can be related to the energy spectrum today. The present energy dE radiated by that system, with a logarithmic observed frequency between $\ln f$ and $\ln f + d \ln f$, is

$$dE = P(f) d \ln f, \quad (2.28)$$

which defines $P(f) = dE/d \ln f$. Applying (2.6) and (2.7) to Equation (2.28), one obtains

$$\frac{dE_e}{1+z} = P(f) d \ln f_e. \quad (2.29)$$

Comparing it to Equation (2.27),

$$P(f) = [1+z]^{-1} P_e(f_e) = [1+z]^{-1} P_e(f[1+z]). \quad (2.30)$$

The function $P_e(f[1+z])$ is explicitly given for the case of a binary system in Equation (2.59).

We now calculate the energy spectrum per unit comoving volume of an ensemble. The number of systems per unit comoving volume during a time dt_e is

$$dn = \dot{n}(z) dt_e. \quad (2.31)$$

Here, $\dot{n}(z) = dn/dt_e$ is the signal comoving density rate (number of signals per unit emitted interval of time per unit comoving volume). The comoving energy density spectrum of an ensemble is

$$p(f) = \int P(f) dn = \int P(f) \dot{n}(z) dt_e. \quad (2.32)$$

Recall that $P(f)$ in general depends on z , according to (2.30). The integrals in (2.32) contain all systems formed from the Big Bang until today. Thus the limits of the time integral are 0 (today)

2 Gravitational wave background from binary systems

and t_0 (the beginning of the universe). We can now change variables to write the previous integral in terms of redshifts, using the paths of gravitons as explained in Section 2.2.4,

$$p(f) = \int_0^\infty P(f)\dot{n}(z)\frac{dt_e}{dz}dz. \quad (2.33)$$

Since we have chosen $a(0) = 1$, the comoving volume and the physical volume are identical at present. Therefore,

$$p(f) = \varepsilon_{\ln}(f). \quad (2.34)$$

This means, the comoving energy density spectrum $p(f)$ measured today is what in Equation (2.23) was called ε_{\ln} : the present energy density of gravitational radiation per logarithmic frequency interval (of a certain ensemble). Using (2.23), (2.33), and (2.34),

$$\Omega(f) = \frac{\varepsilon_{\ln}(f)}{\rho_c c^2} = \frac{1}{\rho_c c^2} \int_0^\infty P(f)\dot{n}(z)\frac{dt_e}{dz}dz. \quad (2.35)$$

In this formula, only the term dt_e/dz depends on the choice of cosmological model.

A similar derivation of (2.35) (using different notation) can be found in [180]. In that paper, the formula for the spectral function, called $\Omega_{\text{gw}}(f)$, is given in Equation (5). The terms $N(z)$ and $[1+z]^{-1}[f_r dE_{\text{gw}}/df_r]|_{f_r=f[1+z]}$ corresponds, with our notation, to $\dot{n}(z)dt_e/dz$ and $P(f)$, respectively.

In Equation (2.33) one can clearly see the assumption of a homogeneous universe, which is implicitly imposed by the metric (2.1). At any position within a shell of width dz there is the same number of systems. In other words, $\dot{n}(z)$ is the same at every point on a line of constant time, in Figure 2.1.

The spectral function of an ensemble can be expressed more conveniently. We write it in terms of the energy spectrum at the time of emission, $P_e(f[1+z])$, for our particular cosmological model. Using (2.11) and (2.30),

$$\Omega(f) = \frac{1}{\rho_c c^2 H_0} \int_0^\infty \frac{P_e(f[1+z])\dot{n}(z)}{[1+z]^2 \mathcal{E}(z)} dz. \quad (2.36)$$

The spectral function of the total contemporary background would be the sum of the spectral functions of all different types of ensembles.

But $\Omega(f)$ does not include all redshifts and frequencies, since $\dot{n}(z)$ and $P_e(f_e)$ have support only for $z \in [z_{\min}, z_{\max}]$ and $f_e \in [f_{\min}, f_{\max}]$, respectively. The maximum frequency f_{\max} is the one above which no more gravitational waves are emitted. The minimum frequency f_{\min} is the one below which the contribution in gravitational waves is dismissed. For example, neutron star binaries started to form at a redshift $z_{\max} \sim 5$ (~ 12 Gyr ago), are still forming at present, so $z_{\min} \sim 0$, and emit in a range of frequencies from ~ 0.01 mHz to ~ 1 kHz (these ranges are justified in Section 2.3). These limits in redshift and frequency must be taken into account in the integral of (2.36).

To understand how (2.36) changes with the introduction of these limits, it is helpful to make a plot of redshifts versus frequencies. Each horizontal line of such a plot gives the range of possible frequencies of a signal at a certain redshift. If we plotted on the horizontal axis the emitted frequencies f_e , the limits f_{\min} , f_{\max} , z_{\min} , and z_{\max} would define a rectangle, containing all the points (f_e, z) where both $\dot{n}(z)$ and $P_e(f_e)$ have support. But representing redshifts versus

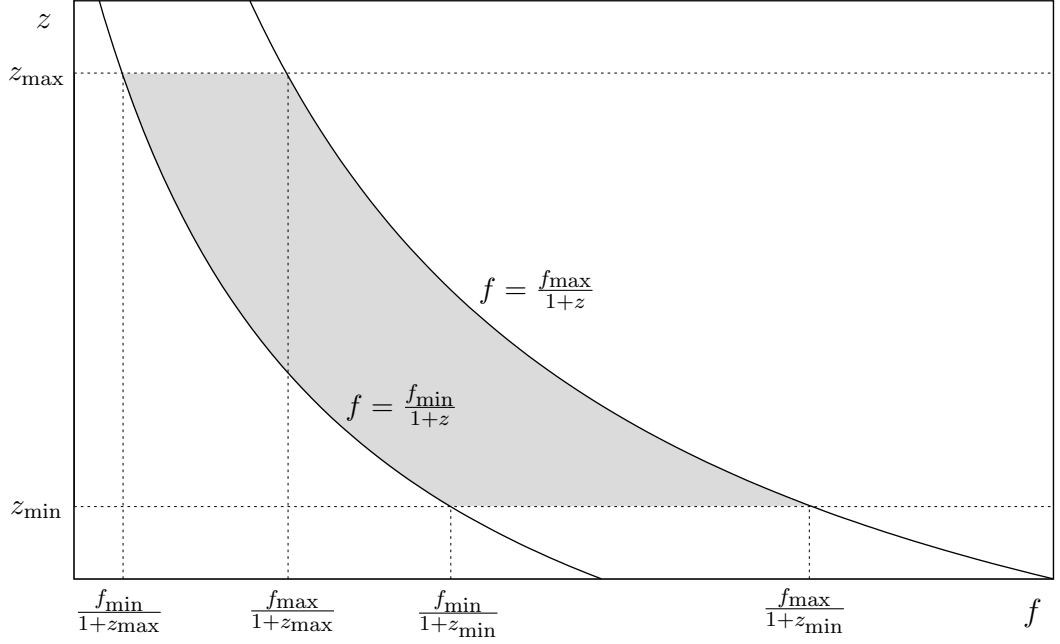


Figure 2.2: Redshift versus observed frequency. The spectral function of the total background of a certain ensemble has support only within the shaded area.

observed frequencies f , one obtains the plot of Figure 2.2 (which is no longer a rectangle). The shaded area represents the support of $\Omega(f)$.

We insert two redshift functions $z_{\text{low}}(f)$ and $z_{\text{upp}}(f)$ in the integration limits of (2.36), in such a way that the integral is non-zero only in the shaded area of Figure 2.2. This is achieved with

$$z_{\text{low}}(f) = \begin{cases} z_{\text{max}}, & f \leq \frac{f_{\text{min}}}{1+z_{\text{max}}} \\ \frac{f_{\text{min}}}{f} - 1, & \frac{f_{\text{min}}}{1+z_{\text{max}}} < f < \frac{f_{\text{min}}}{1+z_{\text{min}}} \\ z_{\text{min}}, & \frac{f_{\text{min}}}{1+z_{\text{min}}} \leq f \end{cases}, \quad (2.37)$$

and

$$z_{\text{upp}}(f) = \begin{cases} z_{\text{max}}, & f \leq \frac{f_{\text{max}}}{1+z_{\text{max}}} \\ \frac{f_{\text{max}}}{f} - 1, & \frac{f_{\text{max}}}{1+z_{\text{max}}} < f < \frac{f_{\text{max}}}{1+z_{\text{min}}} \\ z_{\text{min}}, & \frac{f_{\text{max}}}{1+z_{\text{min}}} \leq f \end{cases}. \quad (2.38)$$

With these limits, only signals emitted with frequencies between f_{min} and f_{max} , at redshifts between z_{min} and z_{max} , contribute to $\Omega(f)$.

Changing the integration limits in (2.36), the spectral function becomes

$$\Omega(f) = \frac{1}{\rho_c c^2 H_0} \int_{z_{\text{low}}(f)}^{z_{\text{upp}}(f)} \frac{P_e(f[1+z]) \dot{n}(z)}{[1+z]^2 \mathcal{E}(z)} dz. \quad (2.39)$$

This formula gives the spectral function of the total background produced by an ensemble, measured at the present time. In the next section we generalize this formula to account for the resolvability of the signals.

2 Gravitational wave background from binary systems

In several papers, the integral in Equation (2.39) contains an extra $[1+z]^{-1}$ factor (see [51], where the origin of this misleading factor is explained). Recall the definition of $P_e(f[1+z])$ in Equation (2.27), and notice that the integral in (2.39) is not equivalent to, for example, that in Equation (9) of [201], where the extra $[1+z]^{-1}$ factor is introduced.

Notice that the energy spectrum $P_e(f_e)$ does not depend on time. We are thus adding the contribution of each system as if it were instantaneous (this means, as if it were a point in the Penrose diagram of Figure 2.1). This is justified if the inspiral times are much smaller than the cosmic timescales, so the time a system needs to evolve from emitting at f_{\min} to f_{\max} is much less than the Hubble time, $H_0^{-1} \approx 13$ Gyr. In Section 2.5.2 we point out that this assumption is not always fulfilled, but it turns out to be irrelevant in practice.

2.2.6 Resolvability of the background

In this section we introduce the *overlap function*, $\mathcal{N}(f, \Delta f, z)$, that allows us to define and quantify the resolvability of the background.

We first define some quantities that are necessary for the definitions of the different parts of the background. Let $\mathcal{B}(f, z_1, z_2)$ be the collection of signal elements with observed frequencies between f and $f + df$ and with redshifts between z_1 and z_2 . Let $\tau_e(f_e, \Delta f_e)$ be the interval of time (measured close to the system at the moment of emission) that a system at z spends emitting between f_e and $f_e + \Delta f_e$. Written in terms of observed frequencies, this interval of time is $\tau_e(f, \Delta f, z)$. We define $\dot{N}(z)$ in such a way that $\dot{N}(z)dz$ is the number of signals produced per unit emitted interval of time between z and $z + dz$. Since $\dot{n}(z)$ is the number of signals per unit emitted interval of time per unit comoving volume at redshift z , $\dot{N}(z)$ is given by

$$\dot{N}(z) = \dot{n}(z) \frac{d\mathcal{V}_c}{dz}. \quad (2.40)$$

The value of $\dot{N}(z)$ at a certain redshift z can be considered an average over an interval of time that is much longer than a typical observation time, but much shorter than the Hubble time. For the sake of simplicity let us assume that we know precisely this function, and that it gives the exact number of signals produced per unit emitted interval of time. For instance, if we have $\int_0^z \dot{N}(z)dz = 1 \text{ hour}^{-1}$, one signal is assumed to be produced between redshift 0 and z exactly every hour.

Let us illustrate the resolvability with the following example: One signal is produced every hour between z and $z + dz$, i.e. $\dot{N}(z)dz = 1 \text{ hour}^{-1}$. Each signal spends one hour between f and $f + \Delta f$, i.e. $\tau_e(f, \Delta f, z) = 1 \text{ hour}$. Thus, whenever we see that frequency bin, it will be occupied by $\tau_e(f, \Delta f, z) \times \dot{N}(z)dz = 1$ signal produced between z and $z + dz$. If, for the same $\dot{N}(z)dz$, we consider a different range of frequencies, where $\tau_e(f, \Delta f, z) = 2 \text{ hours}$, we will always see in that frequency bin 2 overlapping signals, which will not be distinguishable. We can perform a similar calculation, considering all redshifts between z_1 and z_2 : $\int_{z_1}^{z_2} \tau_e(f, \Delta f, z) \times \dot{N}(z)dz$ gives the number of signals between redshift z_1 and z_2 that overlap in a frequency bin. If that number is larger than 1, those signals cannot be resolved. This leads us to the definition of the overlap function.

The overlap function is defined by

$$\mathcal{N}(f, \Delta f, z) = \int_{z_{\text{low}}(f)}^z \tau_e(f, \Delta f, z') \dot{N}(z') dz'. \quad (2.41)$$

It thus gives the expected number of signals with redshifts smaller than z and frequencies between f and $f + \Delta f$. For example, $\mathcal{N}(f, \Delta f, z) = 1$ implies that, as soon as one signal leaves a frequency bin, another signal enters it, so the bin is constantly occupied by one signal. Hence, $\mathcal{N}(f, \Delta f, z) > 1$ implies that signals overlap in a frequency bin. We can impose $\mathcal{N}(f, \Delta f, z) = \mathcal{N}_0$ and invert this equation with respect to the redshift z . The obtained function,

$$\mathcal{N}^{-1} = \mathcal{N}^{-1}(f, \Delta f, \mathcal{N}_0) \quad (2.42)$$

is the redshift such that all signals between f and $f + \Delta f$ with redshifts smaller than $\mathcal{N}^{-1}(f, \Delta f, \mathcal{N}_0)$ sum \mathcal{N}_0 . To obtain an overlap larger than \mathcal{N}_0 at a certain frequency f , one has to consider only signals from redshifts larger than $\mathcal{N}^{-1}(f, \Delta f, \mathcal{N}_0)$. In Section 2.3.5 we give a formula for $\mathcal{N}^{-1}(f, \Delta f, \mathcal{N}_0)$ for an ensemble of binary systems.

We now give some relevant definitions:

The *total background* of an ensemble between frequency f and $f + df$ is $\mathcal{B}(f, z_{\text{low}}(f), z_{\text{upp}}(f))$. One can assign a spectral function to it, $\Omega_{\text{total}}(f)$.

The total background can be divided into two parts: *resolvable* and *unresolvable*. If there exists a certain z_* such that $z_{\text{low}}(f) < z_* < z_{\text{upp}}(f)$ and $\mathcal{N}(f, \Delta f, z_*) = 1$, the *unresolvable part* is $\mathcal{B}(f, z_*, z_{\text{upp}}(f))$, and the *resolvable part* is $\mathcal{B}(f, z_{\text{low}}(f), z_*)$. If there is no z_* such that $z_{\text{low}}(f) < z_* < z_{\text{upp}}(f)$ and $\mathcal{N}(f, \Delta f, z_*) = 1$, the resolvable part coincides with the total background and the unresolvable part is the empty set. One can assign a spectral function to the resolvable part of the background, $\Omega_{\text{resolvable}}(f)$, and to the unresolvable part, $\Omega_{\text{unresolvable}}(f)$.

The resolvable part *dominates* at a frequency f when $\Omega_{\text{resolvable}}(f) > \Omega_{\text{unresolvable}}(f)$. When this happens, even if there is an unresolvable background present, it is weak compared to the background of the closer (stronger) signals, and thus the latter can still be resolved. On the other hand, the unresolvable part *dominates* at a frequency f when $\Omega_{\text{unresolvable}}(f) > \Omega_{\text{resolvable}}(f)$. In this case, even if there are some close resolvable signals, they cannot be resolved in practice, since they are obscured by the superposition of many weak distant signals.

In Section 2.5.4 other possible criteria for the resolvability of the background are commented on.

In Figure 2.3 we give an illustrative example to understand the definitions of the different parts of the background. There we plot the evolution in time of the observed frequency of many similar signals, like the ones produced by an ensemble of binaries. The horizontal axis range is an interval of time of the order of a typical observation time. This axis is divided in small intervals Δt , which is the time resolution. The vertical axis can be considered the frequency window of a hypothetical detector, with such a low instrumental noise that allows us to observe signals emitted at very large redshifts. This axis is divided into small intervals Δf , the frequency resolution. Darker *pixels* in the plot represent stronger backgrounds, i.e. with larger spectral function. The bin $(\Delta f)_1$ is in a range of frequencies where the total background is completely resolvable: all signals can be clearly distinguished from each other. In $(\Delta f)_2$, an unresolvable part starts to contribute, but close binaries can still be clearly distinguished from each other, since the resolvable part dominates. Finally, in $(\Delta f)_3$ the unresolvable part of the background dominates over the resolvable one. One should keep in mind that this example does not accurately follow the definition of unresolvability, since the spectral function does not account for individual signals.

We now generalize the formula of the spectral function to account for the resolvability of the background. We solve the integral in (2.39) for the signals that fulfill the condition

2 Gravitational wave background from binary systems

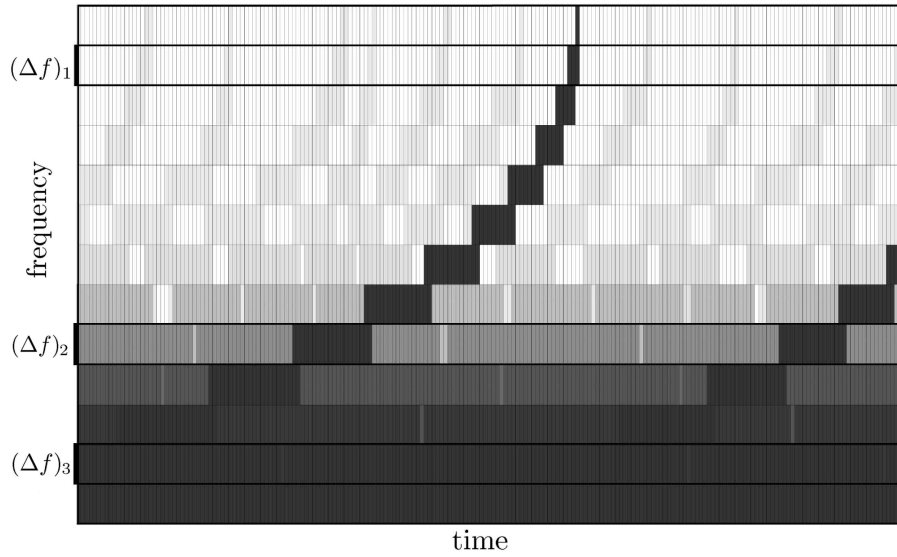


Figure 2.3: Observed frequency versus time. Each line represents the evolution of one signal (like the one produced by a binary). Closer signals, as well as the superposition of many signals, are plotted darker than distant individual signals. Three frequency bins are distinguished: in $(\Delta f)_1$ the total background is completely resolvable, in $(\Delta f)_2$ there is an unresolvable part and a dominating resolvable part, and in $(\Delta f)_3$ there is a dominating unresolvable part and a resolvable part.

$\mathcal{N}(f, \Delta f, z) \geq \mathcal{N}_0$. For that, we can retain the same upper limit of the integral, $z_{\text{upp}}(f)$, and change the lower one, replacing $z_{\text{low}}(f)$ by

$$\bar{z}(f, \Delta f, \mathcal{N}_0) = \begin{cases} z_{\text{upp}}(f), & f < f_{\text{p,min}} \\ \mathcal{N}^{-1}(f, \Delta f, \mathcal{N}_0), & f_{\text{p,min}} \leq f \leq f_{\text{p,max}} \\ z_{\text{upp}}(f), & f_{\text{p,max}} < f \end{cases} . \quad (2.43)$$

We have introduced four *limiting frequencies*: $f_{\text{p,max}}$ ($f_{\text{p,min}}$) represents the maximum (minimum) frequency at which the unresolvable part of the background is present, and $f_{\text{d,max}}$ ($f_{\text{d,min}}$) represents the maximum (minimum) frequency at which the unresolvable part dominates over the resolvable. Using (2.43) we obtain the spectral function of an ensemble with more than \mathcal{N}_0 signals per frequency bin Δf ,

$$\Omega(f, \Delta f, \mathcal{N}_0) = \frac{1}{\rho_c c^2 H_0} \int_{\bar{z}(f, \Delta f, \mathcal{N}_0)}^{z_{\text{upp}}(f)} P_e(f[1+z]) \frac{\dot{n}(z)}{[1+z]^2 \mathcal{E}(z)} dz. \quad (2.44)$$

This is the main equation of this chapter and a generalization of Equation (2.39) with which we can distinguish the different regimes of the background.

The unresolvable background is fully characterized by the spectral function $\Omega(f, \Delta f, \mathcal{N}_0)$. It is not easy to determine whether the assumptions mentioned at the beginning of Section 2.2.5 are always fulfilled for such a background. But it is clear that valuable information is lost when using the spectral function to characterize a resolvable background, where signals can be individually distinguished.

The spectral function of the unresolvable part of the background is, according to the definitions given at the beginning of this section,

$$\Omega_{\text{unresolvable}}(f) = \Omega(f, \Delta f, 1), \quad (2.45)$$

where Δf can be chosen as the inverse of the observation time. On the other hand, the spectral function of the resolvable part is

$$\Omega_{\text{resolvable}}(f) = \Omega_{\text{total}}(f) - \Omega_{\text{unresolvable}}(f), \quad (2.46)$$

where

$$\Omega_{\text{total}}(f) = \Omega(f, \Delta f, 0). \quad (2.47)$$

Here, $\Omega(f, \Delta f, 0)$ coincides with the $\Omega(f)$ given in Equation (2.39), and the value of Δf becomes irrelevant.

Another picture that illustrates the distinct parts of the background is in Figure 2.4. This graph is the same as that in Figure 2.2, but also represents the redshift function $\bar{z}(f, \Delta f, \mathcal{N}_0)$ that defines the frontier between the resolvable (light-shaded area) and unresolvable (dark-shaded) parts of the background.

The mathematical definitions of the limiting frequencies can be understood by looking at the graph in Figure 2.4. The frequencies $f_{d,\text{min}}$ and $f_{d,\text{max}}$ are the ones at which the resolvable and the unresolvable parts have equal spectral function, so

$$\Omega_{\text{unresolvable}}(f_{d,\text{min/max}}) = \Omega_{\text{resolvable}}(f_{d,\text{min/max}}), \quad (2.48)$$

The frequencies $f_{p,\text{min}}$ and $f_{p,\text{max}}$ are the ones at which the function $\mathcal{N}^{-1}(f, \Delta f, \mathcal{N}_0)$ intersects $z_{\text{upp}}(f)$, so

$$\mathcal{N}^{-1}(f_{p,\text{min/max}}, \Delta f, \mathcal{N}_0) = z_{\text{upp}}(f_{p,\text{min/max}}). \quad (2.49)$$

In Section 2.3.5 we calculate these limiting frequencies for an ensemble of binary systems.

So far we have distinguished the regimes of resolvability by using the frequency resolution Δf , but not the time resolution Δt . In Section 2.5.5 we show how to redefine the overlap function to account for the time resolution. In practice, the effect of introducing a realistic Δt in the calculations turns out to be irrelevant for our work.

In Section 2.5.6 we show that the overlap function is a generalization of what in the literature is often called the *duty cycle*, $D(z)$. The latter is proven to be a good quantifier of the unresolvability of the background only for very short signals (*bursts*). Furthermore, we use the name *overlap function* and not *duty cycle*, because the latter may be confusing: $D(z)$ can be greater than unity, unlike the typical duty cycles used in electronics or in gravitational wave detectors.

2.2.7 Continuity of the background

The overlap function can be used to characterize not only the resolvability but also the continuity of the background. We now give some definitions, similar to the ones given in the previous section:

Given a frequency interval $[f_{\text{low}}, f_{\text{upp}}]$ (that can be the frequency window of a detector), the total background $\mathcal{B}(f, z_{\text{low}}(f), z_{\text{upp}}(f))$ of an ensemble between frequency f and $f + df$ (where $f_{\text{low}} \leq f \leq f_{\text{upp}}$) can be divided into two parts: *discontinuous* and *continuous*. If there exists

2 Gravitational wave background from binary systems

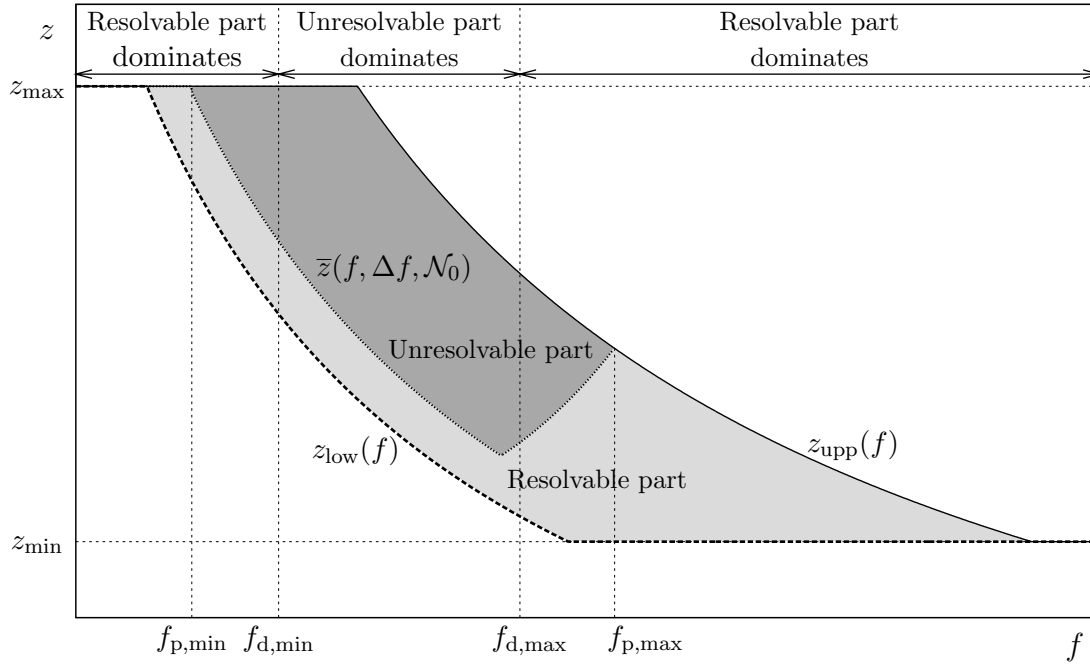


Figure 2.4: Redshift versus observed frequency. Each horizontal line contains the possible observed frequencies of a signal. The light-shaded (dark-shaded) area represents the resolvable (unresolvable) part of the background. The redshift functions $z_{\text{low}}(f)$, $\bar{z}(f, \Delta f, \mathcal{N}_0)$, and $z_{\text{upp}}(f)$ are shown with dashed, dotted, and solid lines, respectively. The frequencies $f_{p,\text{min}}$ and $f_{p,\text{max}}$ delimit the interval where the unresolvable part is present. The frequencies $f_{d,\text{min}}$ and $f_{d,\text{max}}$ delimit the interval where the unresolvable part dominates.

a certain z_* such that $z_{\text{low}}(f) < z_* < z_{\text{upp}}(f)$ and $\mathcal{N}(f, \min(f_{\text{max}}, f_{\text{upp}}) - f, z_*) = 1$, the *continuous part* is $\mathcal{B}(f, z_*, z_{\text{upp}}(f))$, and the *discontinuous part* is $\mathcal{B}(f, z_{\text{low}}(f), z_*)$. If there is no z_* such that $z_{\text{low}}(f) < z_* < z_{\text{upp}}(f)$ and $\mathcal{N}(f, \Delta f, z_*) = 1$, the discontinuous part coincides with the total background and the continuous part is the empty set. One can assign a spectral function to the discontinuous part of the background, $\Omega_{\text{discontinuous}}(f)$, and to the continuous part, $\Omega_{\text{continuous}}(f)$.

The definitions of resolvable and unresolvable backgrounds are valid both for signals which frequency increases in time, such as binaries, and for signals which frequency decreases (for which one could change Δf by $-\Delta f$ in the definitions). On the other hand, the given definitions of discontinuous/continuous backgrounds assume that the frequency increases in time. For signals with decreasing frequency, the condition of continuity would be $\mathcal{N}(f, f - \max(f_{\text{low}}, f_{\text{min}}), z_*) \geq 1$.

In the following, when talking about the continuous background, we will assume $f_{\text{low}} = 0$ and $f_{\text{upp}} = \infty$. This implies that any part of the background that is not continuous in this circumstance is definitely discontinuous, for any other choice of f_{low} and f_{upp} . Besides, the unresolvable background is necessarily continuous.

So, the spectral function of the continuous background is

$$\Omega_{\text{continuous}}(f) = \Omega(f, f_{\text{max}} - f, 1). \quad (2.50)$$

The spectral function of the discontinuous background is

$$\Omega_{\text{discontinuous}}(f) = \Omega_{\text{total}}(f) - \Omega_{\text{continuous}}(f), \quad (2.51)$$

where $\Omega_{\text{total}}(f)$ is the same of Equations (2.47) and (2.39).

2.3 Models for the ensembles

This chapter is focused on the contemporary background produced by coalescing binary systems. These are systems composed of two objects that inspiral towards each other, producing gravitational waves with an increasing frequency until they coalesce. In order to emit gravitational waves significantly, they must be sufficiently massive and/or compact. Each binary is assumed to be isolated and describing an orbit of zero eccentricity. Its components are assumed to be non-spinning.

We sort the binary systems into two classes: stellar binaries and massive black hole binaries.

By *stellar binary* we mean a system whose components have masses of the order of a solar mass (or tens of it). We consider those stellar binaries formed by two stellar-mass black holes (from now on we call this type of binary BH-BH), a stellar-mass black hole and a neutron star (BH-NS), two neutron stars (NS-NS), a neutron star and a white dwarf (NS-WD) or two white dwarfs (WD-WD). The majority of the star formation rates in the literature vanish at redshifts larger than 5 or 6 (see for example [41, 186, 1, 93, 162, 62, 254]). If we expect no star formation at higher redshifts, no coalescence from stellar binaries is expected either. We choose then a maximum redshift for binary coalescences of $z_{\text{max}} = 5$. The minimum redshift is chosen $z_{\text{min}} = 0$, since these binaries can also form at present.

Massive black hole binaries (from now on in this chapter, MBH-MBH) are systems believed to exist in the center of many galaxies [115, 148]. Their components have masses that range from $\sim 10^2 M_{\odot}$ to $\sim 10^{10} M_{\odot}$. We consider four different models for massive black hole formation, presented in [15]: two of them (called SE/SC, for *small seeds* and *efficient/chaotic accretion*) with light-seed black holes produced as remnants of Population III stars, and two with heavy-seed black holes formed from dynamical instabilities in the nuclei of protogalaxies (called LE/LC, for *large seeds* and *efficient/chaotic accretion*). These formation models allow coalescences at redshifts reaching $z \approx 20$.

2.3.1 Energy spectrum

We assume that the energy lost by a system when emitting gravitational radiation between f_e and $f_e + df_e$ is of the form

$$dE_{e,\text{sys}} = -\kappa [f_e]^b df_e, \quad (2.52)$$

for real constants κ and b . This formula is valid for all systems considered in this chapter (binaries) and also other systems (see for example the emission model of magnetars in [198]). In particular, for a binary system,

$$\kappa = \frac{1}{3} [G^2 \pi^2 \mathcal{M}^5]^{1/3} \quad \text{and} \quad b = -\frac{1}{3}. \quad (2.53)$$

2 Gravitational wave background from binary systems

Here we have introduced the chirp mass \mathcal{M} of the binary, defined by

$$\mathcal{M} = \frac{[m_1 m_2]^{3/5}}{[m_1 + m_2]^{1/5}}, \quad (2.54)$$

where m_1 and m_2 are the masses of the two components of the binary.

This energy spectrum is obtained by assuming that the energy of the system, as well as the separation of the bodies, varies slowly with time. This is valid as long as the orbit is far wider than the last stable one (see Equation (2.67)). In these circumstances, the system is well described by the Newtonian equations of motion of two point masses in a circular orbit.

We thus derive Equation (2.52) for binary systems using Newtonian mechanics. The energy of the system, in terms of the separation s between the stars of masses m_1 and m_2 is

$$E_{e,\text{sys}} = -\frac{1}{2} \frac{G m_1 m_2}{s}. \quad (2.55)$$

We reduce the two-body problem to one fictitious body, of mass equal to the reduced mass of the system, $m_1 m_2 / [m_1 + m_2]$, suffering the same force as each of the real bodies. Applying Newton's second law,

$$\frac{G m_1 m_2}{s^2} = \frac{m_1 m_2}{m_1 + m_2} [2\pi f_{e,\text{orbit}}]^2 s, \quad (2.56)$$

where $f_{e,\text{orbit}}$ is the orbital frequency, that is related to the frequency of the gravitational waves in the quadrupolar approximation by

$$f_e = 2f_{e,\text{orbit}}. \quad (2.57)$$

Introducing it in Equation (2.56) one obtains a formula that relates the separation of the masses with the frequency of the gravitational waves,

$$s = \left[\frac{G[m_1 + m_2]}{\pi^2 f_e^2} \right]^{1/3}. \quad (2.58)$$

Replacing (2.58) in (2.55) and differentiating, one finally obtains the energy spectrum (2.52) with the values of κ and b given in (2.53). A more detailed derivation of Equation (2.52) can be found in Chapter 4 of [147].

What we need is the energy spectrum of the gravitational radiation at the time of emission, in terms of observed frequencies, $P_e(f[1+z])$ (recall the formula of $\Omega(f, \Delta f, \mathcal{N}_0)$ in Equation (2.44)). Using (2.3), (2.27), and (2.52),

$$P_e(f[1+z]) = \frac{dE_e}{d \ln f_e} = \left| \frac{dE_{e,\text{sys}}}{d \ln f_e} \right| = f_e \kappa [f_e]^{-1/3} = \kappa f^{2/3} [1+z]^{2/3}. \quad (2.59)$$

The absolute value has been introduced because $P_e(f[1+z])$ is a positive quantity; dE_e is the amount of gravitational wave energy within a frequency interval, regardless of whether the energy of the system increases or decreases with the frequency. Equation (2.59) must be inserted in (2.44),

$$\Omega(f, \Delta f, \mathcal{N}_0) = \frac{\kappa f^{2/3}}{\rho_c c^2 H_0} \int_{\bar{z}(f, \Delta f, \mathcal{N}_0)}^{z_{\text{upp}}(f)} \frac{\dot{n}(z)}{[1+z]^{4/3} \mathcal{E}(z)} dz, \quad (2.60)$$

to obtain the spectral function of an ensemble of binary systems.

2.3.2 Interval of time per frequency bin

To calculate the overlap function we need the interval of time that a system spends emitting in a frequency bin. The frequency of the radiation emitted by a binary evolves in (look-forward) time following the relation

$$\frac{df_e}{dt_e} = \frac{96}{5}\pi^{8/3} \left[\frac{GM}{c^3} \right]^{5/3} f_e^{11/3}, \quad (2.61)$$

the derivation of which can be found in Chapter 4 of [147]. Integrating (2.61) between f_e and $f_e + \Delta f_e$ one obtains the interval of time that the signal spends in that frequency interval,

$$\tau_e(f_e, \Delta f_e) = \delta_2 \left[f_e^{-8/3} - [f_e + \Delta f_e]^{-8/3} \right], \quad (2.62)$$

where

$$\delta_2 = \frac{5c^5}{256\pi^{8/3}[GM]^{5/3}}. \quad (2.63)$$

The interval of time $\tau_e(f_e, \Delta f_e)$ can be written in terms of observed frequencies,

$$\tau_e(f, \Delta f, z) = \delta_2 Q(f, \Delta f) [1 + z]^{-8/3}, \quad (2.64)$$

where we have defined

$$Q(f, \Delta f) = f^{-8/3} - [f + \Delta f]^{-8/3}. \quad (2.65)$$

The function $\tau_e(f, \Delta f, z)$ gives the interval of time that a signal, produced at a redshift z , needs to change from an observed frequency f to $f + \Delta f$. We remark that this is an absolute (positive) interval of time, and not a look-back time.

In certain conditions $Q(f, \Delta f)$ can be simplified, by performing a Taylor expansion around $\Delta f = 0$,

$$Q(f, \Delta f) \approx \frac{8}{3} \Delta f f^{-11/3}, \quad (2.66)$$

for $\Delta f \ll f$.

2.3.3 Maximum frequencies

The energy spectrum of binary systems (Equation (2.52)) is assumed to be zero outside a certain frequency range $[f_{\min}, f_{\max}]$. We now present our choices of f_{\max} for each type of system. We omit the index e to simplify the notation, but one should keep in mind that f_{\max} is an emitted frequency.

For all binaries that do not contain a white dwarf, f_{\max} is reached when both stars are as close to each other as s_{iso} . This is the separation at the last stable orbit (see for example Box 25.6 in [161]),

$$s_{\text{iso}} = \frac{6G[m_1 + m_2]}{c^2}, \quad (2.67)$$

which is 3 times the sum of the Schwarzschild radii of both stars. Using Equation (2.58), the frequency of the last stable orbit is

$$f_{\max}^{\text{iso}} = \frac{1}{6\sqrt{6}\pi} \frac{c^3}{G[m_1 + m_2]}, \quad (2.68)$$

2 Gravitational wave background from binary systems

where we have used the index “Iso” to distinguish this maximum frequency from the following ones.

For WD-WD, since the radius of a white dwarf is much bigger than its Schwarzschild radius, we assume that the maximum frequency is reached when both stars *touch* each other. This happens when the separation between them is $r_1 + r_2$, the sum of their radii. This separation corresponds to a frequency (using again Equation (2.58))

$$f_{\max}^{\text{WD-WD}} = \frac{1}{\pi} \sqrt{\frac{G[m_1 + m_2]}{[r_1 + r_2]^3}}. \quad (2.69)$$

For r_1 and r_2 one can use

$$r_i = 0.0112 R_{\odot} \sqrt{\left[\frac{m_i}{m_{\text{Cha}}} \right]^{-2/3} - \left[\frac{m_i}{m_{\text{Cha}}} \right]^{2/3}}, \quad (2.70)$$

where $m_{\text{Cha}} \approx 1.44 M_{\odot}$ is Chandrasekhar’s mass. This formula gives the approximate radius r_i of a white dwarf as a function of its mass m_i . It is obtained from Equations (27) and (28) (where there is an extra factor M_{\odot} on the right side) in [163].

For NS-WD, we use the same criterion as for WD-WD, but considering that the radius of the neutron star is negligible with respect to the radius of the white dwarf. Hence, the maximum frequency is

$$f_{\max}^{\text{NS-WD}} = \frac{1}{\pi} \sqrt{\frac{G[m_1 + m_2]}{r_1^3}}, \quad (2.71)$$

where r_1 is the radius of the white dwarf, that can be calculated with (2.70).

2.3.4 Minimum frequencies

There is a certain minimum frequency, f_{\min} , such that the gravitational radiation emitted by a system below this frequency is disregarded, because other mechanisms of energy loss are more effective. It is difficult to find a precise description of these mechanisms for each type of system. We adopt a simple criterion, for all stellar binaries, that fixes the value of f_{\min} : the interval of time between the beginning of the inspiral phase (when the binary emits at frequency f_{\min}) and the coalescence (when it emits at f_{\max}) cannot be larger than a certain interval of time T_{\max} . This condition is equivalent to $\tau_e(f_{\min}, f_{\max} - f_{\min}) = T_{\max}$. Using Equation (2.62), one obtains

$$f_{\min} = \left[\frac{T_{\max}}{\delta_2} + f_{\max}^{-8/3} \right]^{-3/8}. \quad (2.72)$$

For all systems considered in this chapter we can reasonably perform the approximation

$$f_{\min} \approx \left[\frac{T_{\max}}{\delta_2} \right]^{-3/8}. \quad (2.73)$$

As we did with the maximum frequencies, we omit the index e to simplify the notation, but f_{\min} is always an emitted frequency. The assumption of a maximum inspiral time is justified in Section 2.5.2. The maximum inspiral times chosen are $T_{\max} = 12$ Gyr for stellar binaries and 75 Myr for massive black hole binaries. These choices are now explained.

Maximum inspiral time for stellar binaries

For stellar binaries, T_{\max} is the look-back time at which the first stellar binaries coalesced (at $z \approx 5$). Integrating (2.11),

$$T_{\max} = \int_0^5 \frac{1}{[1+z]H(z)} dz \approx 12 \text{ Gyr}. \quad (2.74)$$

This choice of T_{\max} is somewhat arbitrary and even leads to an inconsistency: only binaries that coalesced at small redshifts could have that much time to evolve from an initial frequency f_{\min} until the coalescence. Moreover, at frequencies close to the minimum one, the approximation of short inspiral times compared to the Hubble time, commented at the end of Section 2.2.5, is not valid anymore. In Section 2.5.2 we justify our choice of T_{\max} , the exact value of which turns out to be unimportant in practice.

Maximum inspiral time for massive black hole binaries

The process that leads to two massive black holes coalescing can be briefly summarized in three main phases [225]: *dynamical friction*, *gravitational slingshot* and *gravitational radiation*. When two dark matter halos containing black holes merge, the black holes suffer dynamical friction [191] with the environment and sink to the center, forming a wide binary (with large orbital period). At a certain distance the dynamical friction phase ceases to be effective. Then the binary can continue to shrink because of three-body interactions with surrounding stars [158]. These stars are ejected from the center and subtract some energy from the binary in the process. This phase is called *gravitational slingshot* because of the ejection of stars. Eventually the dynamical friction plus the slingshot phases shrink the orbit enough, so that the binary can continue inspiralling until a coalescence in a finite interval of time by only emitting *gravitational radiation*, which constitutes the third phase. Other possible evolutions involving interaction with surrounding gas have been investigated in the literature [55, 61, 112].

We impose that the minimum frequency is the one at which the gravitational slingshot phase ends and the gravitational radiation starts to dominate (see the discussion in Section 2.5.3). As we now show, this condition is reasonably well fulfilled by imposing the same maximum inspiral time $T_{\max} = 75 \text{ Myr}$ for all masses.

The frequency at which the slingshot and radiation phases overlap is the one at which the energy spectra of the two phases are equal,

$$\left. \frac{dE_e}{df_e} \right|_S = \left. \frac{dE_e}{df_e} \right|_R. \quad (2.75)$$

The variation of the energy of the gravitational waves with their frequency, in any of the two phases, can be written as

$$\frac{dE_e}{df_e} = \frac{dE_e}{dt_e} \frac{dt_e}{ds} \frac{ds}{df_e} = \frac{dE_e}{dt_e} \left[\frac{ds}{dt_e} \right]^{-1} \frac{ds}{df_e}. \quad (2.76)$$

Here, dt_e is an interval of time and s is the separation of the two black holes, which is the semi-major axis of the ellipse described. Since the orbit is assumed circular, s corresponds to the radius of the orbit. The term dE_e/dt_e is the same in both phases. Also ds/df_e has the same form

2 Gravitational wave background from binary systems

in the two phases. Only the evolution of the semi-major axis in time, ds/dt_e , is different. Thus, instead of finding the frequency that fulfills Equation (2.75), we can obtain the separation s at which

$$\left. \frac{ds}{dt_e} \right|_S = \left. \frac{ds}{dt_e} \right|_R, \quad (2.77)$$

and then calculate the corresponding frequency using (2.58).

Following [225] (or similarly [191]), we write the evolution in time of the semi-major axis of a binary in the two phases. In the gravitational radiation phase, this evolution fulfills

$$\left. \frac{ds}{dt_e} \right|_R = -\frac{64G^3 m_1 m_2 [m_1 + m_2]}{5c^5 s^3}, \quad (2.78)$$

whereas in the gravitational slingshot phase,

$$\left. \frac{ds}{dt_e} \right|_S = -\frac{\mathcal{H}\sigma_* s^2}{2\pi r_c^2}. \quad (2.79)$$

In the latter, \mathcal{H} is the hardening rate, σ_* is the velocity dispersion of the stars in the bulge of the galaxy, and r_c is the core radius (see [191] for more details). We use the value of \mathcal{H} reached in the limit of a very hard binary, $\mathcal{H} \approx 15$. It is known that there is a correlation between σ_* and the mass of the massive black hole m_{BH} hidden in the bulge (see [66] and [73]). This relation (from the most recent fits, by [81]) is

$$\log_{10} \left(\frac{m_{\text{BH}}}{M_\odot} \right) = c_1 + c_2 \log_{10} \left(\frac{\sigma_*}{200 \text{ km s}^{-1}} \right), \quad (2.80)$$

with $(c_1, c_2) = (8.12 \pm 0.08, 4.24 \pm 0.41)$. From this equation we obtain $\sigma_*(m_{\text{BH}})$ and use $m_{\text{BH}} = m_1 + m_2$ to account for the two components of the binary. The core radius r_c , in the limit of a very hard binary, grows during the gravitational slingshot phase until it reaches

$$r_c \approx \frac{3G[m_1 + m_2]}{4\sigma_*^2} \ln \left(\frac{Gm_2}{4\sigma_*^2 s} \right), \quad (2.81)$$

where m_2 is the mass of the lighter black hole.

We now calculate the separation s at which both phases overlap. Replacing (2.78) and (2.79) in (2.77),

$$s^5 \ln^{-2} \left(\frac{Gm_2}{4\sigma_*^2 s} \right) = \frac{72\pi G^5 m_1 m_2 [m_1 + m_2]^3}{5\mathcal{H}c^5 \sigma_*^5}. \quad (2.82)$$

This equation can be numerically solved for each pair of equal masses $m_1 = m_2 = m$, obtaining the separation (let us call it s_R) at which the gravitational radiation phase starts to dominate. Using (2.58) one can calculate the frequency f_R that corresponds to s_R . It turns out that the obtained dependence of f_R with m is very accurately fitted by $f_{\text{min}}(m)$, defined in Equation (2.73), using $T_{\text{max}} \approx 75 \text{ Myr}$. This is a numerical coincidence that eases further calculations. The origin of this coincidence is the following: omitting the logarithm on the left side of Equation (2.82), $s_R \propto m/\sigma_*$ while $\sigma_* \propto m^{1/4.24}$. This leads to $s_R \propto m^{0.764}$. According to Equation (2.58), $f \propto m^{1/2} s^{-3/2}$ and therefore $f_R \propto m^{-0.646}$. On the other hand, according to Equation (2.73), $f_{\text{min}} \propto m^{-5/8} = m^{-0.64}$. Therefore, the dependences of f_R and f_{min} with m are almost the same. As a conclusion, setting a maximum inspiral time of 75 Myr is (almost) equivalent to considering only waves emitted during the gravitational radiation phase.

2.3.5 Calculations for stellar binaries

Coalescence rate

The signal comoving density rate $\dot{n}(z)$, that was defined in Equation (2.31), represents, in the case we study now, the number of binaries per unit emitted interval of time per unit comoving volume that coalesce at a redshift z . We can thus call it the *coalescence rate* or simply *rate*.

To obtain $\dot{n}(z)$, one could choose a star formation rate from the literature (which is usually a function of the redshift) and transform it into a coalescence rate, for which a coalescence probability distribution is necessary. This procedure is followed for example in [53]. In Section 2.5.1 we show that the use of a constant coalescence rate is well justified, given the large uncertainties in the local coalescence rate. Therefore, to simplify calculations, we assume a rate of the form

$$\dot{n}(z) = \begin{cases} 0, & 0 < z < z_{\min} \\ R, & z_{\min} \leq z \leq z_{\max} \\ 0, & z_{\max} < z \end{cases}, \quad (2.83)$$

for a real constant R . The values of R for each ensemble are given in Table 2.1.

Some of the coalescence rates in the literature are estimated only within our galaxy. We need to extrapolate those coalescence rates, given per Milky Way equivalent galaxy, MWEG^{-1} , to the rest of the universe. One simple way to translate galactic rates into rates per cubic megaparsec, Mpc^{-3} , is explained in Section 3 of [179]. We use the same conversion factor of [132], which is referred to [114],

$$1 \text{ MWEG}^{-1} = 0.0116 \text{ Mpc}^{-3}. \quad (2.84)$$

A similar factor is given in Equation (4) of [187]. The conversion (2.84) assumes that the blue-light luminosity of the Milky Way is $1.7 \times 10^{10} L_{B,\odot}$, where $L_{B,\odot}$ is the blue luminosity of the Sun, while that of the close universe is $0.0198 \times 10^{10} L_{B,\odot}$ per cubic megaparsec. All these factors are very uncertain, as discussed, for example, in [101]. We assume no uncertainty in (2.84) but then round the coalescence rates to one significant figure.

Spectral function

We now rewrite $\Omega(f, \Delta f, \mathcal{N}_0)$ in a simple way. Introducing the constant rate R in (2.60),

$$\Omega(f, \Delta f, \mathcal{N}_0) = \delta_1 f^{2/3} [g(z_{\text{upp}}(f)) - g(\bar{z}(f, \Delta f, \mathcal{N}_0))]. \quad (2.85)$$

Here,

$$\delta_1 = \frac{R\kappa}{\rho_c c^2 H_0} \quad (2.86)$$

and $g(z)$ is the solution of the integral

$$g(z) = \int [1+z]^{-4/3} \mathcal{E}^{-1}(z) dz. \quad (2.87)$$

We solve this integral semi-analytically in Section 2.3.5.

2 Gravitational wave background from binary systems

	BH-BH	BH-NS	NS-NS	NS-WD	WD-WD
Minimum $R/[\text{Myr}^{-1} \text{Mpc}^{-3}]$	1×10^{-4}	6×10^{-4}	1×10^{-2}	2×10^{-2}	2×10^1
Most likely $R/[\text{Myr}^{-1} \text{Mpc}^{-3}]$	5×10^{-3}	3×10^{-2}	1	4×10^{-1}	1×10^2
Maximum $R/[\text{Myr}^{-1} \text{Mpc}^{-3}]$	3×10^{-1}	1	9	9	5×10^2

Table 2.1: Minimum, most likely and maximum coalescence rates assumed for each type of ensemble. The coalescence rates of BH-BH and BH-NS are taken from [152], where they refer to [103] and [228], respectively. For NS-NS, the values are taken from [102] (our minimum and maximum values are the minimum and maximum ones allowed by the uncertainties). The rates of NS-WD and WD-WD are taken from Table 1 in [164]. In Section 2.4 we consider also the recent coalescence rates of BH-BH predicted in [31], of $R = 0.36_{-0.26}^{+0.50} \text{Mpc}^{-3} \text{Myr}^{-1}$. The values given in the literature per Milky Way equivalent galaxy are converted using (2.84). All coalescence rates are rounded to one significant figure.

Overlap function

We obtain an explicit formula for the overlap function of binary systems with a constant coalescence rate. Introducing (2.13) and (2.64) in (2.41),

$$\begin{aligned} \mathcal{N}(f, \Delta f, z) &= \int_{z_{\text{low}}(f)}^z \left[\delta_2 Q(f, \Delta f) [1 + z']^{-8/3} \right] R \\ &\times \left[4\pi \left[\frac{c}{H_0} \int_0^{z'} \mathcal{E}^{-1}(z'') dz'' \right]^2 \frac{c}{H_0} \mathcal{E}^{-1}(z') \right] dz'. \end{aligned} \quad (2.88)$$

This intricate equation can be rewritten to obtain a simple expression for the overlap function,

$$\mathcal{N}(f, \Delta f, z) = \delta_2 \delta_3 Q(f, \Delta f) [\bar{g}(z) - \bar{g}(z_{\text{low}}(f))]. \quad (2.89)$$

Here we have defined

$$\delta_3 = 4\pi R \frac{c^3}{H_0^3} \quad (2.90)$$

and

$$\bar{g}(z) = \int [1 + z]^{-8/3} \left[\int_0^z \mathcal{E}^{-1}(z') dz' \right]^2 \mathcal{E}^{-1}(z) dz. \quad (2.91)$$

This integral cannot be analytically solved. One can invert (2.89) with respect to the redshift, obtaining

$$\mathcal{N}^{-1}(f, \Delta f, \mathcal{N}_0) = \bar{g}^{-1} \left(\frac{\mathcal{N}_0}{\delta_2 \delta_3 Q(f, \Delta f)} + \bar{g}(z_{\text{low}}(f)) \right). \quad (2.92)$$

In Section 2.3.5 we give a semi-analytical solution for $\mathcal{N}(f, \Delta f, z)$ and $\mathcal{N}^{-1}(f, \Delta f, \mathcal{N}_0)$.

Limiting frequencies

The limiting frequencies $f_{p,\min}$, $f_{d,\min}$, $f_{d,\max}$ and $f_{p,\max}$ are defined in Section 2.2.6. For the systems we study, $f_{p,\min}$ and $f_{d,\min}$ turn out to be close to $f_{\min}/[1+z_{\max}]$, which is the minimum frequency at which the spectral function has support. For simplicity, we assume

$$f_{p,\min} = f_{d,\min} = \frac{f_{\min}}{[1+z_{\max}]}. \quad (2.93)$$

On the other hand, the frequencies $f_{d,\max}$ and $f_{p,\max}$ must be calculated using Equations (2.48) and (2.49), respectively.

We now show how to calculate $f_{p,\max}$. Inserting Equation (2.92) in (2.49),

$$Q(f_{p,\max}, \Delta f) = \frac{\mathcal{N}_0}{\delta_2 \delta_3 [\bar{g}(z_{\text{upp}}(f_{p,\max})) - \bar{g}(z_{\text{low}}(f_{p,\max}))]}. \quad (2.94)$$

One can obtain $f_{p,\max}$ by solving this equation. However, one can use a more convenient formula for $f_{p,\max}$, that we present now. All stellar binaries satisfy $f_{\min}/[1+z_{\min}] < f_{p,\max}$, so $z_{\text{low}}(f_{p,\max}) = z_{\min}$. Adopting a frequency resolution $\Delta f = 1 \text{ yr}^{-1}$, the condition $\Delta f \ll f_{p,\max}$ is fulfilled by all stellar binaries. We can thus use the approximation of Equation (2.66) in (2.94), obtaining

$$f_{p,\max} \approx \begin{cases} \left[\frac{8\Delta f \delta_2 \delta_3 [\bar{g}(z_{\max}) - \bar{g}(z_{\min})]}{3\mathcal{N}_0} \right]^{3/11}, & \Xi \leq 1 \\ \left[\frac{8\Delta f \delta_2 \delta_3 \left[\bar{g}\left(\frac{f_{\max}}{f_{p,\max}} - 1\right) - \bar{g}(z_{\min}) \right]}{3\mathcal{N}_0} \right]^{3/11}, & \Xi > 1 \end{cases}, \quad (2.95)$$

where the dimensionless parameter Ξ is defined by

$$\Xi = \frac{Q\left(\frac{f_{\max}}{1+z_{\max}}, \Delta f\right) \delta_2 \delta_3 [\bar{g}(z_{\max}) - \bar{g}(z_{\min})]}{\mathcal{N}_0}. \quad (2.96)$$

If $\Xi \leq 1$, we have a simple formula for $f_{p,\max}$. The condition $\Xi \leq 1$ is fulfilled by all stellar binaries that do not contain a white dwarf. For NS-WD and WD-WD, $\Xi > 1$, and one has to solve Equation (2.95) numerically.

Similarly, one can obtain a formula for the limiting frequency $f_{d,\max}$, using Equations (2.48), (2.85) and (2.66). We point out that $f_{d,\max}$ is by definition smaller than $f_{p,\max}$. In addition, one can show that $f_{d,\max}/f_{p,\max}$ cannot be smaller than a certain factor F , so

$$F \leq \frac{f_{d,\max}}{f_{p,\max}} < 1. \quad (2.97)$$

The value of this factor is

$$F = \left(\frac{\bar{g}\left(g^{-1}\left(\frac{1}{2}[g(z_{\max}) + g(z_{\min})]\right)\right) - \bar{g}(z_{\min})}{\bar{g}(z_{\max}) - \bar{g}(z_{\min})} \right)^{3/11}. \quad (2.98)$$

For $z_{\max} = 5$ and $z_{\min} = 0$, one obtains $F \approx 0.6$. All stellar binaries except WD-WD fulfill that $f_{d,\max} \approx 0.6 \times f_{p,\max}$. For WD-WD, $f_{d,\max}$ and $f_{p,\max}$ are almost equal; moreover, they

2 Gravitational wave background from binary systems

are almost as large as f_{\max} . This means that the total background of WD-WD is almost entirely dominated by its unresolvable part.

One should notice that $\Omega(f, \Delta f, 0)$ is equivalent to the old definition of the spectral function, $\Omega(f)$, in Equation (2.39). Setting $\mathcal{N}_0 = 0$, the function $\mathcal{N}^{-1}(f, \Delta f, 0)$ becomes $z_{\text{low}}(f)$ (using Equation (2.92)). Then, the limiting frequencies $f_{p,\min}$ and $f_{p,\max}$ become $f_{\min}/[1 + z_{\max}]$ and $f_{\max}/[1 + z_{\min}]$, respectively (see Figures 2.2 and 2.4). Using Equation (2.43), $\bar{z}(f, \Delta f, 0)$ becomes identically $z_{\text{low}}(f)$, and thus Equations (2.39) and (2.44) become equivalent.

Semi-analytical solutions

In order to obtain a semi-analytical solution for $\Omega(f, \Delta f, \mathcal{N}_0)$, we need two functions, $g(z)$ and $\bar{g}(z)$, that fit accurately the numerical solutions of the integrals in Equations (2.87) and (2.91).

A possible choice of the functions $g(z)$ and $\bar{g}(z)$ is

$$g(z) = a_1 \arctan^{a_4} (a_2 z^{a_3}) \quad (2.99)$$

and

$$\bar{g}(z) = \bar{a}_1 \arctan^{\bar{a}_4} (\bar{a}_2 z^{\bar{a}_3}), \quad (2.100)$$

for certain parameters (a_1, a_2, a_3, a_4) and $(\bar{a}_1, \bar{a}_2, \bar{a}_3, \bar{a}_4)$ that must be numerically calculated. The optimal parameters between $z_{\min} = 0$ and $z_{\max} = 5$ are

$$(a_1, a_2, a_3, a_4) = (0.5604, 1.235, 1.0047, 0.8364) \quad (2.101)$$

and

$$(\bar{a}_1, \bar{a}_2, \bar{a}_3, \bar{a}_4) = (0.07024, 0.8658, 1.3236, 1.511). \quad (2.102)$$

These values can be used for all ensembles of stellar binaries, since the integrals in Equations (2.87) and (2.91) depend only on cosmological parameters.

The semi-analytical formula for the overlap function, using (2.100), becomes

$$\mathcal{N}(f, \Delta f, z) = \delta_2 \delta_3 Q(f, \Delta f) \bar{a}_1 \arctan^{\bar{a}_4} (\bar{a}_2 z^{\bar{a}_3}). \quad (2.103)$$

We invert it with respect to the redshift, obtaining

$$\mathcal{N}^{-1}(f, \Delta f, \mathcal{N}_0) = \left[\frac{1}{\bar{a}_2} \tan \left(\left[\frac{\mathcal{N}_0}{\bar{a}_1 \delta_2 \delta_3 Q(f, \Delta f)} \right]^{1/\bar{a}_4} \right) \right]^{1/\bar{a}_3}. \quad (2.104)$$

Introducing it in (2.43) we obtain a formula for $\bar{z}(f, \Delta f, \mathcal{N}_0)$.

Finally, using (2.99), the semi-analytical formula for the spectral function of binary systems is

$$\Omega(f, \Delta f, \mathcal{N}_0) = \delta_1 a_1 f^{2/3} \left[\arctan^{a_4} (a_2 z_{\text{upp}}^{a_3}(f)) - \arctan^{a_4} (a_2 \bar{z}^{a_3}(f, \Delta f, \mathcal{N}_0)) \right]. \quad (2.105)$$

The redshift function $z_{\text{upp}}(f)$ is given in (2.38). The limiting frequency $f_{p,\max}$ can be calculated as explained in Section 2.3.5, using the semi-analytical formula (2.100) for $\bar{g}(z)$.

Mass ranges

We calculate the spectral function of an ensemble assuming that all similar objects have equal mass. For example, in the ensemble of NS-WD, all neutron stars have equal mass m_{NS} and all white dwarfs have equal mass m_{WD} . For this reason, given a range of possible masses for an object, we should not consider values of masses too different from the mean one.

For a neutron star, we assume a mass in the range $1.3 \leq m_{\text{NS}}/M_{\odot} \leq 1.7$. This interval is taken from [235], where the lower limit predicted is $(0.878 - 1.284) M_{\odot}$, and the upper limit, $(1.699 - 2.663) M_{\odot}$. We use the largest mass of the lower limit and the smallest mass of the upper limit and round all values to two significant figures. The most likely value is the average of both limits of the interval. So, our choice for the masses of neutron stars is

$$(m_{\text{NS}}^{\min}, m_{\text{NS}}^{\text{med}}, m_{\text{NS}}^{\max}) = (1.3, 1.5, 1.7) M_{\odot}. \quad (2.106)$$

The mass distribution of white dwarfs of spectral type DA, according to [134], is described by a Gaussian distribution with mean $\mu = 0.606 M_{\odot}$ and standard deviation $\sigma = 0.135 M_{\odot}$. The distribution of white dwarfs of spectral type DB has $\mu = 0.758 M_{\odot}$ and $\sigma = 0.192 M_{\odot}$. Since we do not make a distinction between DA and DB white dwarfs, we calculate the Gaussian distribution that best fits the average of both distributions, obtaining $\mu = 0.663 M_{\odot}$ and $\sigma = 0.177 M_{\odot}$. Similar results can be obtained using, for example, the distributions given in [107]. We assume a minimum mass of $\mu - \sigma = 0.49 M_{\odot}$ and a maximum one of $\mu + \sigma = 0.84 M_{\odot}$. Thus,

$$(m_{\text{WD}}^{\min}, m_{\text{WD}}^{\text{med}}, m_{\text{WD}}^{\max}) = (0.49, 0.66, 0.84) M_{\odot}. \quad (2.107)$$

For stellar-mass black holes, we calculate the mean μ and standard deviation σ of the list of masses given in Table 1 of [262], obtaining $\mu = 7.8 M_{\odot}$ and $\sigma = 3.7 M_{\odot}$. We assume for the minimum mass $\mu - \sigma = 4.1 M_{\odot}$ and for the maximum one $\mu + \sigma = 12 M_{\odot}$. Again, the most likely value is the average of both. Similar results can be achieved with the masses of Table 1 of [38]. The masses we use are, therefore,

$$(m_{\text{BH}}^{\min}, m_{\text{BH}}^{\text{med}}, m_{\text{BH}}^{\max}) = (4.1, 7.8, 12) M_{\odot}. \quad (2.108)$$

2.3.6 Calculations for massive black hole binaries

The masses of MBH-MBH range several orders of magnitude. It is reasonable to expect a very different number of signals produced by binaries of chirp mass $10^2 M_{\odot}$ than by binaries of $10^{10} M_{\odot}$. To be consistent with the given definition of ensemble (a population of many systems with similar properties and behaviour), MBH-MBH form a *superensemble* composed of many ensembles, each one characterized by an infinitesimal range of chirp masses.

The coalescence rate now depends on the chirp mass and the redshift. Instead of $\dot{n}(z)$ one now has a signal comoving density rate of the form $\dot{\tilde{n}}(\mathcal{M}, z)$. This gives the number of signals per unit emitted interval of time per unit comoving volume per unit chirp mass. We do not have an analytical formula for $\dot{\tilde{n}}(\mathcal{M}, z)$ ⁵.

The spectral function of the total background of the superensemble is

$$\Omega_{\text{total}}(f) = f^{2/3} \int_{z_{\min}}^{z_{\max}} \int_{\mathcal{M}_{\text{low}}(z', f)}^{\mathcal{M}_{\text{upp}}(z', f)} I_1(\mathcal{M}', z') d\mathcal{M}' dz', \quad (2.109)$$

⁵The numerical values of the functions $\dot{\tilde{n}}(\mathcal{M}, z)$ (for each of the four models mentioned at the beginning of Section 2.3) were kindly provided by A. Sesana and M. Volonteri in a private communication

2 Gravitational wave background from binary systems

where

$$I_1(\mathcal{M}, z) = \frac{8[G\pi\mathcal{M}]^{5/3}}{9c^2H_0^3} \dot{\bar{n}}(\mathcal{M}, z)[1+z]^{-4/3}\mathcal{E}^{-1}(z). \quad (2.110)$$

One can notice that (2.109) is the same as (2.60), just changing $\dot{n}(z)$ by $\dot{\bar{n}}(\mathcal{M}, z)d\mathcal{M}$ and integrating over chirp mass. The functions $\mathcal{M}_{\text{low}}(z, f)$ and $\mathcal{M}_{\text{upp}}(z, f)$ give, at every frequency and redshift, the minimum and maximum chirp masses that can contribute, respectively. In other words, the interval $[\mathcal{M}_{\text{low}}(z, f), \mathcal{M}_{\text{upp}}(z, f)]$ contains the chirp masses of those binaries which, at redshift z , have minimum frequency $f_{\text{min}} \leq f$ and maximum frequency $f_{\text{max}} \geq f$. They are obtained by inverting f_{min} (Equation (2.73)) and f_{max} (Equation (2.68)), respectively, with respect to \mathcal{M} . Hence,

$$\mathcal{M}_{\text{low}}(z, f) = \left[\frac{5c^5}{256\pi^{8/3}G^{5/3}T_{\text{max}}} \right]^{3/5} [f[1+z]]^{-8/5}, \quad (2.111)$$

and

$$\mathcal{M}_{\text{upp}}(z, f) = \frac{c^3}{6\sqrt{6}2^{6/5}\pi G} [f[1+z]]^{-1}. \quad (2.112)$$

In the last equation we have used that, if the two masses of the binary are equal, then $m_1 = m_2 = m = 2^{1/5}\mathcal{M}$.

The overlap function of the total background of the superensemble is

$$\mathcal{N}(f, \Delta f, z) = \int_{z_{\text{min}}}^z \int_{\mathcal{M}_{\text{low}}(z', f)}^{\mathcal{M}_{\text{upp}}(z', f)} Q(f, \Delta f) I_2(\mathcal{M}', z') d\mathcal{M}' dz', \quad (2.113)$$

where

$$I_2(\mathcal{M}, z) = \left[\frac{5c^5}{256\pi^{8/3}[G\mathcal{M}]^{5/3}} [1+z]^{-8/3} \right] \dot{\bar{n}}(\mathcal{M}, z) \\ \times \left[4\pi \left[\frac{c}{H_0} \int_0^z \mathcal{E}^{-1}(z') dz' \right]^2 \frac{c}{H_0} \mathcal{E}^{-1}(z) \right]. \quad (2.114)$$

Equation (2.113) is the same as (2.88), just changing $\dot{n}(z)$ by $\dot{\bar{n}}(\mathcal{M}, z)d\mathcal{M}$ and integrating over chirp mass.

Section 4 of [223] describes a discrepancy between a semi-analytical calculation of the unresolvable background of MBH-MBH and a Monte Carlo simulation. The discrepancy occurs because the semi-analytical approach does not take into account the discrete nature of the systems. To account for it, they change the range of masses considered in the semi-analytical calculation. We now proceed in a similar way, to calculate the unresolvable part of the background.

The average number of signals with frequency equal or larger than f and chirp mass equal or larger than \mathcal{M} is

$$\bar{\mathcal{N}}(f, \mathcal{M}) = \int_{\mathcal{M}}^{\mathcal{M}_{\text{max}}} \int_{z_{\text{low}}(\mathcal{M}', f)}^{z_{\text{upp}}(\mathcal{M}', f)} Q(f, f_{\text{max}}(\mathcal{M}') - f) I_2(\mathcal{M}', z') dz' d\mathcal{M}'. \quad (2.115)$$

We impose that a signal, emitted at frequency f by a binary with chirp mass \mathcal{M} , can contribute to the continuous or the unresolvable background only if $\bar{\mathcal{N}}(f, \mathcal{M}) \geq 1$. The largest chirp mass

$\overline{\mathcal{M}}(f)$ that contributes at frequency f is obtained by solving $\overline{\mathcal{N}}(f, \overline{\mathcal{M}}(f)) = 1$. We calculate $\overline{\mathcal{M}}(f)$ numerically, use it as the upper limit of the integral over chirp mass in Equation (2.113), and equate $\mathcal{N}(f, \Delta f, z)$ to 1:

$$\mathcal{N}(f, \Delta f, z) = \int_{z_{\min}}^z \int_{\mathcal{M}_{\text{low}}(z', f)}^{\overline{\mathcal{M}}(f)} Q(f, \Delta f) I_2(\mathcal{M}', z') d\mathcal{M}' dz' = 1. \quad (2.116)$$

Inverting the result of this equation with respect to the redshift, one obtains $\mathcal{N}^{-1}(f, \Delta f, 1)$. Signals with frequency f emitted by binaries with chirp masses in the range $[\mathcal{M}_{\text{low}}(z, f), \overline{\mathcal{M}}]$ form an unresolvable background if their redshifts are larger than $\mathcal{N}^{-1}(f, \Delta f, 1)$.

The spectral function of the unresolvable background is, therefore,

$$\Omega_{\text{unresolvable}} = f^{2/3} \int_{\mathcal{N}^{-1}(f, \Delta f, 1)}^{z_{\max}} \int_{\mathcal{M}_{\text{low}}(z', f)}^{\overline{\mathcal{M}}(f)} I_1(\mathcal{M}', z') d\mathcal{M}' dz'. \quad (2.117)$$

Similarly, one can solve

$$\mathcal{N}(f, f_{\max} - f, z) = \int_{z_{\min}}^z \int_{\mathcal{M}_{\text{low}}(z', f)}^{\overline{\mathcal{M}}(f)} Q(f, f_{\max} - f) I_2(\mathcal{M}', z') d\mathcal{M}' dz' = 1 \quad (2.118)$$

and invert it with respect to the redshift, obtaining a function $\mathcal{N}^{-1}(f, f_{\max} - f, 1)$. Replacing $\mathcal{N}^{-1}(f, \Delta f, 1)$ by $\mathcal{N}^{-1}(f, f_{\max} - f, 1)$ in Equation (2.117), one gets

$$\Omega_{\text{continuous}} = f^{2/3} \int_{\mathcal{N}^{-1}(f, f_{\max} - f, 1)}^{z_{\max}} \int_{\mathcal{M}_{\text{low}}(z', f)}^{\overline{\mathcal{M}}(f)} I_1(\mathcal{M}', z') d\mathcal{M}' dz', \quad (2.119)$$

which is the spectral function of the continuous background.

2.4 Results

The main results of this chapter are presented in Figures 2.5, 2.6, 2.7, and 2.8. In Figure 2.5 we show the spectral function of the total background of each ensemble. In Figure 2.6, the spectral function is plotted only in those regions where the background is continuous. Finally, Figure 2.7, which is the most relevant plot of the three, shows the unresolvable background produced by the different ensembles, assuming $\mathcal{N}_0 = 1$ and $\Delta f = 1 \text{ yr}^{-1}$. In these three figures, the values of masses and coalescence rates are the most likely ones.

One can clearly conclude, from Figure 2.7, that ground-based detectors operate (and will operate) in a frequency range clean of confusion noise from binary systems. Without taking into account other possible sources of unresolvable background, this frequency range could be a good scenario for the detection of primordial backgrounds.

In Figure 2.8 we have plotted the contribution of each ensemble separately. For each ensemble, there are three different curves of $\Omega(f, \Delta f, \mathcal{N}_0)$: one *maximum*, one *minimum* and one *most likely*, depending on the values of masses and rates.

For stellar binaries, the most likely expectation of $\Omega(f, \Delta f, \mathcal{N}_0)$ is obtained by using the most likely chirp mass and coalescence rate. The upper curve of $\Omega(f, \Delta f, \mathcal{N}_0)$ is the upper envelope of all curves that are obtained using the maximum rate and sweeping over all possible values

2 Gravitational wave background from binary systems

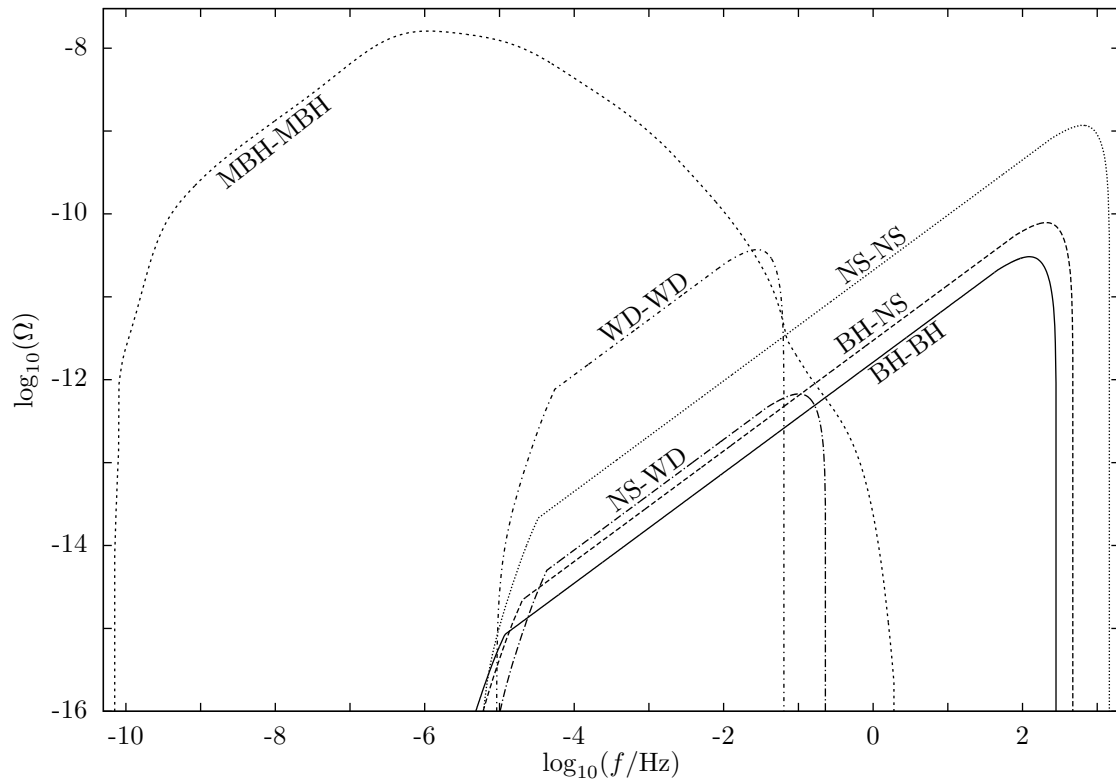


Figure 2.5: Spectral function of the total background versus observed frequency. The contributions of the different ensembles are calculated with the most likely values of masses and coalescence rates. No restrictions in the duration of the signals are assumed in this plot, which means that also very short and sporadic signals are taken into account. As discussed in the text, the spectral function in such circumstances should not be compared to the sensitivity curves of a detector.

of chirp mass. Similarly, the lower curve is the lower envelope of all curves obtained with the minimum rate and sweeping over all chirp masses.

For massive black hole binaries, the most likely curve is the average of the spectral functions calculated, as explained in Section 2.3.6, for each of the four models considered. The upper and lower curves are 10 and 1/10 times the most likely, respectively. These uncertainties have not been precisely calculated. Given the lack of observational information about many of the parameters involved, any accurate calculation of the uncertainties would be arbitrary. More precise errors are calculated in [223], based on the results of different theoretical models. The ranges of uncertainty given in [223] are similar to the ones we propose.

One sees in Figure 2.7 that the unresolvable background is clearly dominated by the contribution of WD-WD, below $\sim 10^{-1}$ Hz, and of MBH-MBH, below $\sim 10^{-4}$ Hz.

The contribution of galactic binaries, which is believed to produce confusion noise in the frequency window of LISA, has not been included in the plots, since it cannot be calculated using $\Omega(f)$. The spectral function is calculated assuming signals that are distributed homogeneously

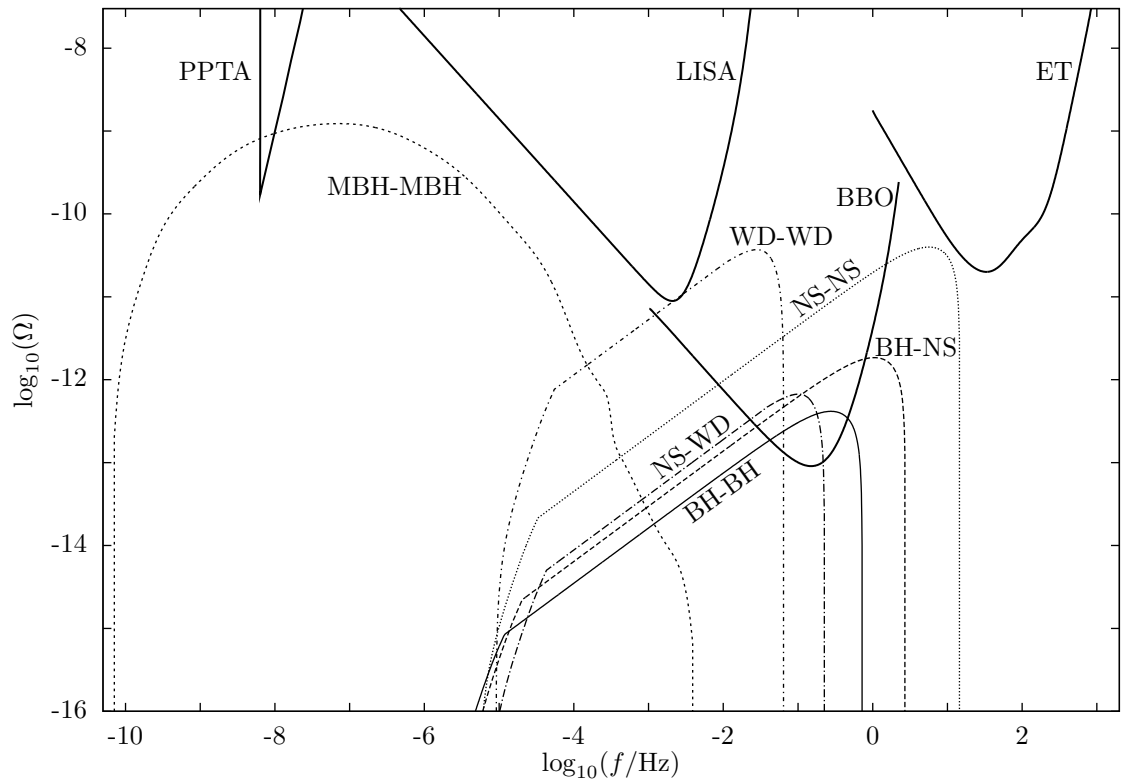


Figure 2.6: Spectral function of the continuous background versus observed frequency. ET (from [194]), BBO (from [46]) and the complete Parkes PTA (from [223]) are plotted for comparison.

and isotropically in the universe. This means, $\Omega(f)$ is related to the average density of gravitational waves in the universe. But within the galaxy the density is larger than the average. Moreover, galactic binaries are distributed anisotropically along the galactic disc. If one uses the spectral function to plot the contribution of galactic binaries, one is claiming that the density of gravitational waves in the universe is as large as the one inside the galaxy. Some papers in the literature which deal with the confusion noise produced by galactic binaries are [165, 209]. The most important contribution to this background is the one by WD-WD. According to [116], galactic WD-WD produce a background about an order of magnitude larger than that of extragalactic ones.

One has to be careful when interpreting Figure 2.5. That plot gives us information about the averaged total energy density of gravitational waves produced by each ensemble. The curve of the total background of NS-NS, for instance, enters the window of ET, but that does not mean that ET will see a constant noise curve like that. The signals of NS-NS are, in that frequency range, short signals, that will often (but not constantly) be detected with ET. The effective sensitivity curve of ET is thus not affected by NS-NS. On the other hand, an unresolvable background of WD-WD with a rate larger than the most likely one would certainly affect the sensitivity of LISA. To avoid misunderstandings we have not plotted the sensitivity curves of any detectors

2 Gravitational wave background from binary systems

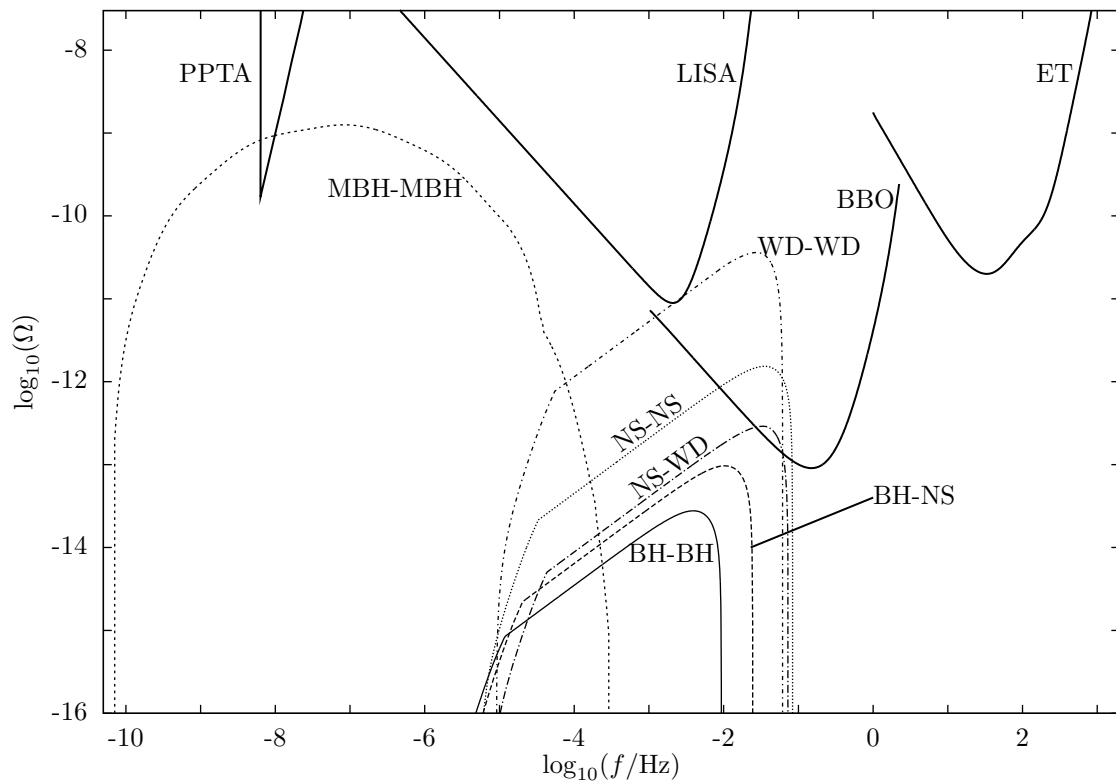


Figure 2.7: Spectral function of the unresolvable background versus observed frequency, using $\mathcal{N}_0 = 1$ and $\Delta f = 1 \text{ yr}^{-1}$. The contributions of the different ensembles are calculated with the most likely values of masses and coalescence rates.

together with the total background. In Figure 2.6 we have plotted sensitivity curves just to show that the background is discontinuous in the frequency band of ground-based detectors.

At frequencies close to the last stable orbit, the Newtonian spectrum that we have calculated may differ considerably from the real one, since the assumption of slow orbits made in Section 2.3.1 is no longer fulfilled. Thus, the exact shape of the spectral function at such frequencies is not accurate. However, the continuous and unresolvable parts of the background lie safely at lower frequencies.

A new prediction on the coalescence rate of BH-BH was published [31] during the writing of the work described in this chapter. The rate given in that paper, of $R = 0.36_{-0.26}^{+0.50} \text{ Mpc}^{-3} \text{ Myr}^{-1}$, is much larger than the one in Table 2.1. This high estimate is based on the observation of two binaries, both containing a stellar-mass black hole and a Wolf-Rayet star. Such rates have also been predicted by simulations [22], considering low-metallicity galaxies. We show in Figure 2.9 the total, continuous and unresolvable backgrounds, respectively, that such a rate would produce, assuming the same mass ranges for black holes given in Section 2.3.5. In Figure 2.9 we also show the upper and lower limits allowed by the new rate.

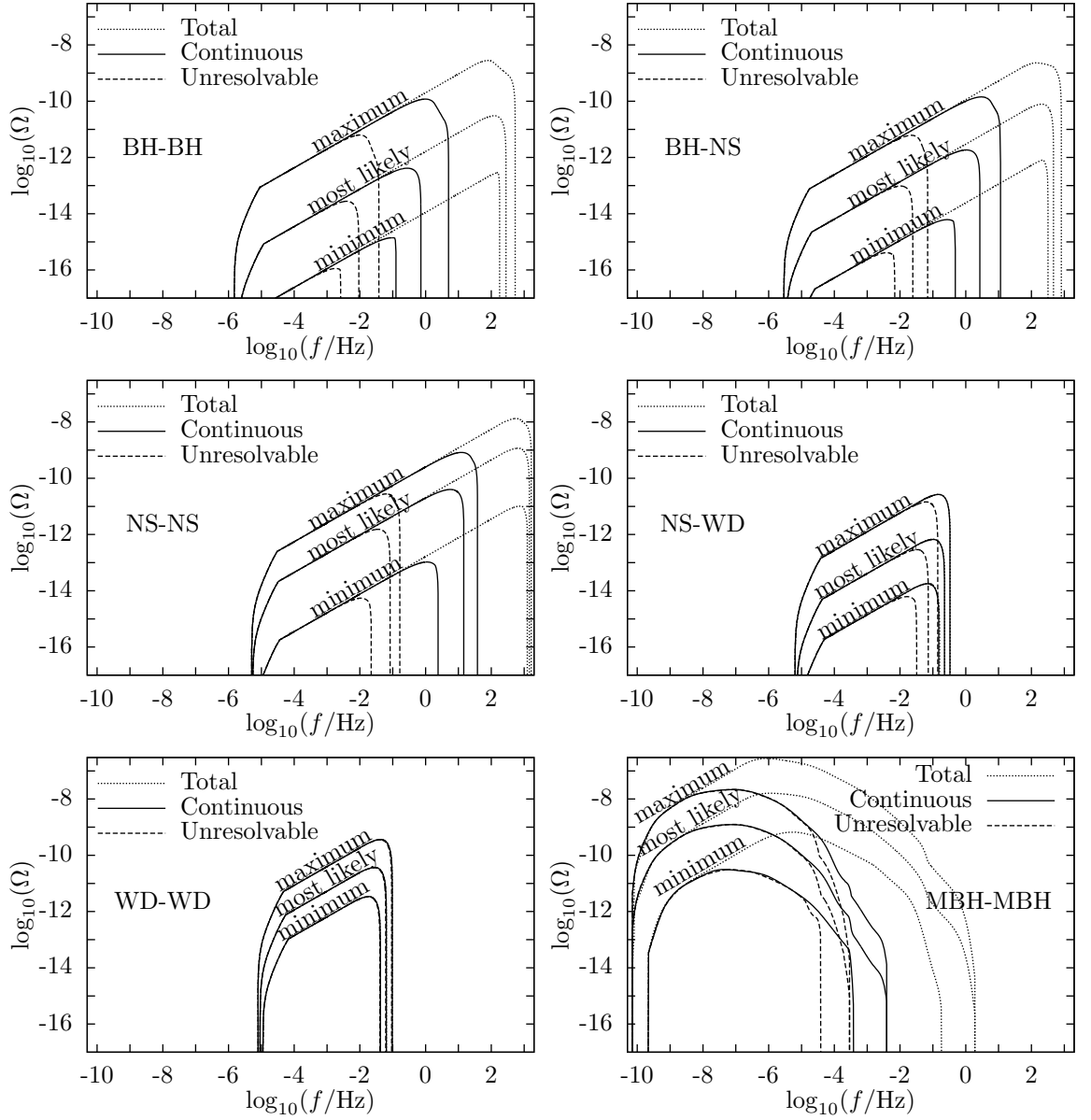


Figure 2.8: Spectral function of the total, continuous and unresolvable backgrounds of the different ensembles, versus observed frequency. In each plot there are nine curves: three of them are calculated with the highest values of coalescence rates, three with the most likely, and three with the lowest values possible. Three of the curves represent the total background, three the continuous part, and three the unresolvable part. In the case of NS-WD, the total and continuous curves are almost indistinguishable. The same occurs for WD-WD with the total, continuous and unresolvable curves.

2 Gravitational wave background from binary systems

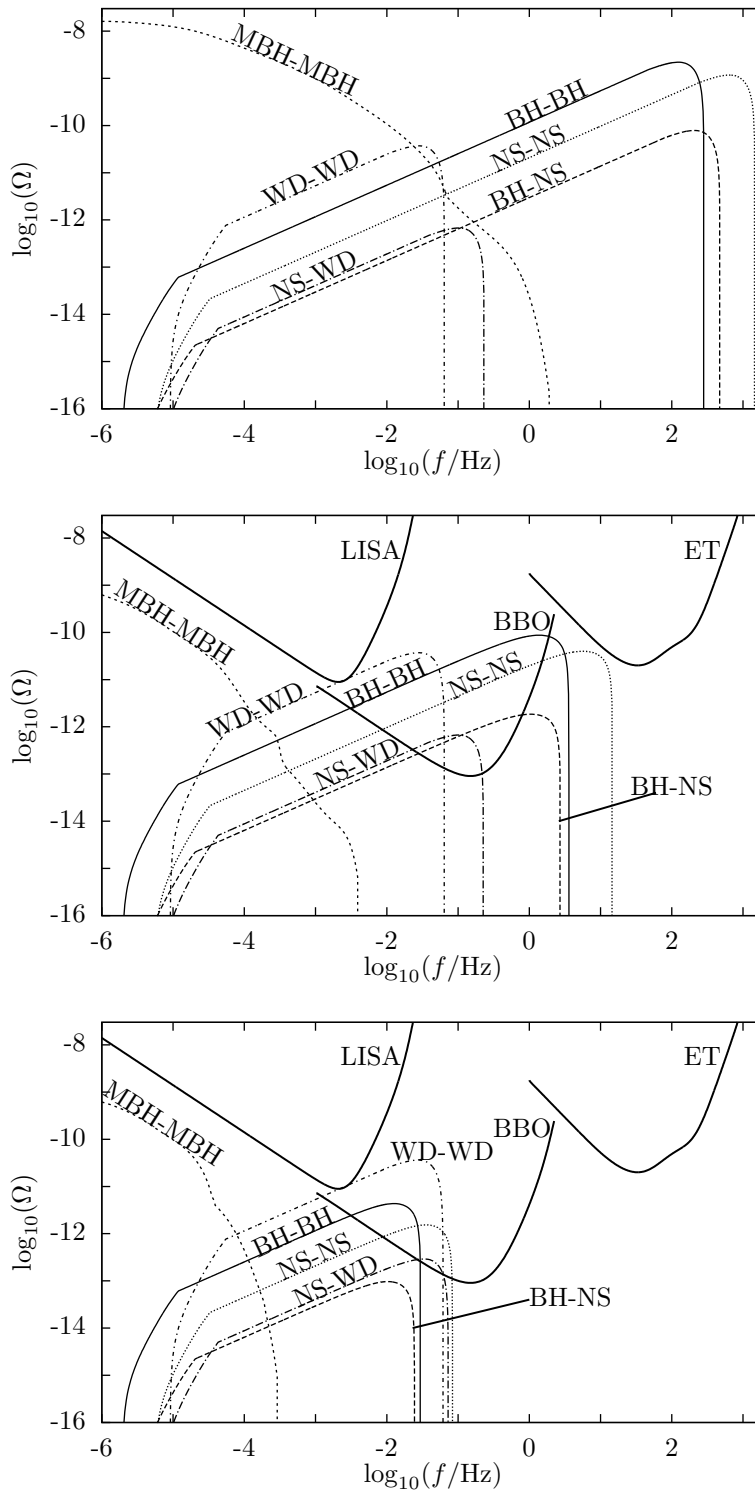


Figure 2.9: Spectral function of the total (top), continuous (middle) and unresolvable (bottom) background versus observed frequency. The contributions of the different ensembles are calculated with the most likely values of masses and coalescence rates of Table 2.1, except for the case of BH-BH. The high rate of BH-BH, taken from the recent paper [31], is $R = 0.36^{+0.50}_{-0.26} \text{ Mpc}^{-3} \text{ Myr}^{-1}$.

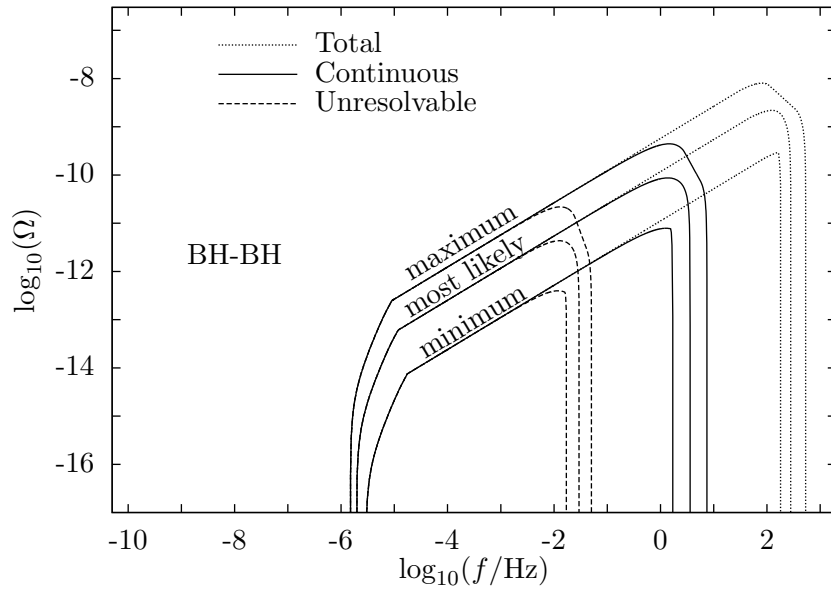


Figure 2.10: Spectral function of the total, continuous, and unresolvable backgrounds of the ensemble of BH-BH, versus observed frequency. This plot is analogous to that in Figure 2.8, but using the rate from [31] of $R = 0.36^{+0.50}_{-0.26} \text{ Mpc}^{-3} \text{ Myr}^{-1}$, instead of the one in Table 2.1.

2.5 Discussion

2.5.1 On the coalescence rate of stellar binaries

In Section 2.3.5 we have assumed a coalescence rate that has the same value during all cosmological epochs (see Equation (2.83)). We now justify that this assumption is reasonable, considering the uncertainties in the local coalescence rate.

In [200] the coalescence rates of BH-NS and NS-NS are calculated as a function of the redshift (see Figure 2 of that paper). The rates peak at around $z \approx 1$ and then decrease, becoming zero between redshift 5 and 6. The difference between the rate at the peak and the local rate (at $z = 0$) is a factor of ≈ 2.1 , for NS-NS, and ≈ 1.7 , for BH-NS. One can calculate $g(z)$ (using our Equation (2.87)) and $\bar{g}(z)$ (Equation (2.91)) introducing in the integrals a normalized non-constant rate like the ones of Figure 2 of [200]. The obtained functions $g(z)$ and $\bar{g}(z)$ differ from the ones calculated with a constant rate by less than a factor of ~ 2 . The value of this factor would not change significantly if one used other rate functions (as pointed out in [180] regarding the value of $\langle(1+z)^{-1/3}\rangle$). Since the spectral function and the overlap function are proportional to $g(z)$ and $\bar{g}(z)$, respectively, the overall difference between using a constant and a non-constant rate would also be less than a factor of 2. On the other hand, the value of the local rate has an uncertainty of several orders of magnitude (see Table 2.1). We thus consider that a factor of 2 is negligible compared to a factor of (at least) 100. In addition, we can see in Figure 2.16 that our estimate of the total background agrees with that of [201], which was calculated using a non-constant coalescence rate.

Assuming that the rates of other type of stellar binaries have a similar behaviour than those

shown in [200], we can conclude that the use of a constant rate is a good approximation for stellar binaries.

2.5.2 On the minimum frequency of stellar binaries

In Section 2.3.4 we have defined f_{\min} as the gravitational wave frequency such that a binary, emitting at this frequency, needs an interval of time equal to T_{\max} , the maximum inspiral time, to reach coalescence. But one could in principle find, for each type of binary, a more precise criterion to define f_{\min} .

One could define f_{\min} , for example, as a function of the velocity kick that the components of the binary experience at formation. This velocity kick, which can be provoked by a non-symmetrical supernova explosion, can push one component of the binary with enough energy in a direction opposite to that of the other component and disrupt the binary. So f_{\min} could be the frequency at which the orbital velocity equals the velocity kick. With such a criterion, using realistic values of these kicks [255, 256, 72], one obtains too long inspiral times, in some cases orders of magnitude longer than the age of the universe.

Our choice of T_{\max} is in fact almost as long as the age of the universe. Therefore, only binaries that coalesced recently could have had that much time to evolve from their formation, as commented on in Section 2.3.4. However, when considering long inspiral periods, one takes into account part of the contribution from binaries that have not yet coalesced.

In Section 2.2.5 we point out that the formula of the spectral function assumes short inspiral times, so that each signal starts and finishes at approximately the same redshift. But each system needs ≈ 12 Gyr to complete the process, and the expansion of the universe is indeed relevant during that interval of time. We now investigate the effect of this apparent inconsistency.

Our rate R accounts for coalescences (and not for births) of binary systems. This means that we are counting systems that are emitting at frequencies close to f_{\max} , the frequency of the coalescence. What we may be counting wrong are systems emitting at low frequencies.

Suppose a binary, very close to us, that started inspiralling ≈ 12 Gyr ago and coalesces right now. We only see the high frequency part of the spectrum, which is not redshifted. The waves emitted at the beginning of the inspiral (at low frequencies, ≈ 12 Gyr ago) are now far from us. But an observer located that far away would observe those waves today highly redshifted. Our mistake, assuming short inspiral times, is to claim that the distant observer measures that low frequency radiation without any redshift. So the spectral function should be more redshifted (and thus have lower amplitude) at low frequencies.

We now estimate below which frequency this effects starts to be important. For that, we assume the following: we assign wrong redshifts as soon as the difference in redshift between birth and coalescence of a signal is larger than 1. In units of time (using Equation (2.11)), a difference in redshift of 1 implies timescales larger than ≈ 7 Gyr at redshifts close to zero and larger than ≈ 0.4 Gyr at redshifts close to 5. To be conservative, we assume that these effects are important when inspiral times are larger than 0.4 Gyr. The lifetime of a binary is larger than 0.4 Gyr if its minimum frequency is lower than $\approx 4 \times 10^{-5}$ Hz for BH-BH, $\approx 7 \times 10^{-5}$ Hz for BH-NS, $\approx 1 \times 10^{-4}$ Hz for NS-NS, and $\approx 2 \times 10^{-4}$ Hz for NS-WD or WD-WD. These frequencies are in a range where the spectra of all stellar binaries are covered under an unresolvable background of MBH-MBH.

We thus conclude that the exact values of the minimum frequencies are not relevant in practice. Furthermore, the assumption of short inspiral times is not fulfilled for stellar binaries at

frequencies close to the minimum, but this does not affect the results.

2.5.3 On the minimum frequency of massive black hole binaries

The minimum frequency of each massive black hole binary, as explained in Section 2.3.6, is assumed to be the frequency f_R at which the slingshot and radiation phases overlap. This means that we dismiss the gravitational waves radiated during the slingshot phase.

It turns out that the introduction of the slingshot phase in the calculations has a very small effect (well within the uncertainty ranges) in the spectral function of the superensemble, at frequencies below $\sim 10^{-9}$ Hz. The reason is the following: for each ensemble of masses between \mathcal{M} and $\mathcal{M} + d\mathcal{M}$, the effect of introducing the slingshot phase is noticeable only at frequencies below $f_{\min}(\mathcal{M})$ (the one calculated using Equation (2.73) with $T_{\max} = 75$ Myr). But the main contribution of each ensemble to the superensemble is at high frequencies, where they have larger spectral functions (because of the $f^{2/3}$ factor). In the superensemble, the only appreciable low-frequency contributions are those from ensembles with the largest masses and with non-zero coalescence rates. Therefore, the effect of introducing the slingshot phase in the superensemble is noticeable only at frequencies close to $f_{\min}(\mathcal{M})$, when \mathcal{M} is in the range of large masses (of $\sim 10^8 - 10^9 M_{\odot}$). These frequencies are smaller than $\sim 10^{-9}$ Hz.

2.5.4 On the condition of resolvability

In Section 2.2.6 we state that signals between f and $f + df$ with redshifts larger than z_* such that $z_{\text{low}}(f) < z_* < z_{\text{upp}}(f)$ and $\mathcal{N}(f, \Delta f, z_*) = 1$ are unresolvable. We are hence imposing a one-bin-rule: we are not able to distinguish signals if there are more than one per frequency bin. Other authors suggest other possible criteria, such as the three-bin-rule or the eight-bin-rule [42]. According to these criteria, the condition of unresolvability is reached when each three (or eight) frequency bins are occupied by at least one signal. We now comment on how using one of these criteria would change our results.

Imposing an eight-bin-rule makes the condition of unresolvability less restrictive: signals become unresolvable at higher frequencies than for the one-bin-rule. The results would be almost unaffected in the case of WD-WD, since the curve of the unresolvable background is almost as large as that of the total background. The spectral function of the unresolvable background for the remaining stellar binaries would be slightly extended to higher frequencies. We can calculate the spectral function with the eight-bin rule, just by changing Δf by $8 \times \Delta f$, so $\Omega_{\text{unresolvable}}(f) = \Omega(f, 8\Delta f, \mathcal{N}_0)$. In Figure 2.11 we compare the spectral functions of the unresolvable background calculated with the one- and the eight-bin-rule, for the case of NS-NS with the most likely values of masses and coalescence rates.

One can note that imposing an eight-bin-rule, instead of a one-bin-rule, has the same effect of assuming an observation time of eight years, instead of one. The expected observation time of LISA is indeed three years; for the PTA, longer observation times are feasible. So, for MBH-MBH, redoing the calculations with the eight-bin-rule is compensated with the use of longer observation times. As pointed out in [223], the unresolvable background changes by less than a factor of 2 for observation times between one and ten years.

We now discuss another possible definition of unresolvable background. In Section 2.2.6 we say that, when the unresolvable part of the background dominates, there still exists a resolvable part. We could consider this resolvable part as also unresolvable. For that, we could just change

2 Gravitational wave background from binary systems

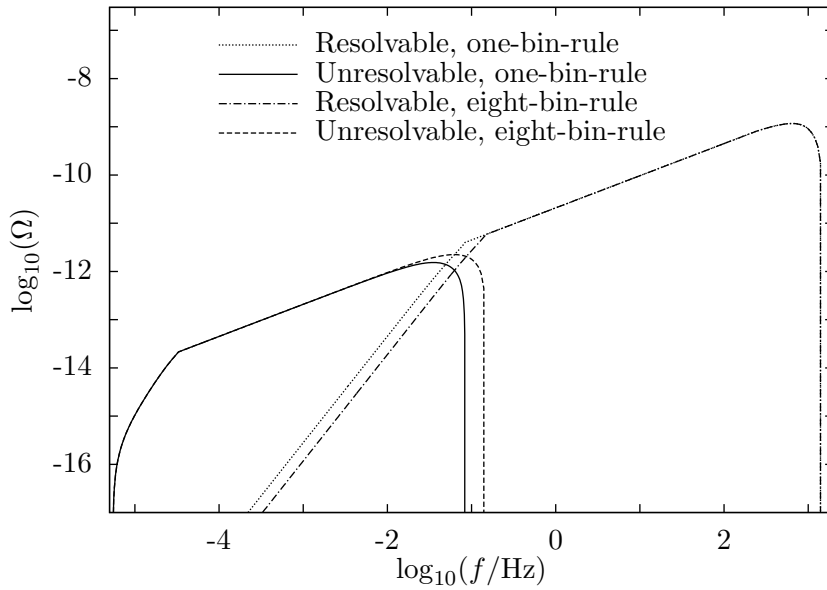


Figure 2.11: Spectral function of the resolvable and unresolvable parts of the background of NS-NS, versus observed frequency. The values of masses and coalescence rates adopted are the most likely ones. The resolvable and unresolvable parts calculated with the one- and with the eight-bin rule are compared.

the definition of $\bar{z}(f, \Delta f, \mathcal{N}_0)$ in Equation (2.43) to

$$\bar{z}(f, \Delta f, \mathcal{N}_0) = \begin{cases} z_{\text{upp}}(f), & f < f_{\text{p,min}} \\ \mathcal{N}^{-1}(f, \Delta f, \mathcal{N}_0), & f_{\text{p,min}} \leq f \leq f_{\text{d,min}} \\ z_{\text{low}}(f), & f_{\text{d,min}} < f < f_{\text{d,max}} \\ \mathcal{N}^{-1}(f, \Delta f, \mathcal{N}_0), & f_{\text{d,max}} \leq f \leq f_{\text{p,max}} \\ z_{\text{upp}}(f), & f_{\text{p,max}} < f \end{cases} \quad (2.120)$$

On the left side of Figure 2.12, a plot of redshifts versus observed frequencies (analogous to that in Figure 2.4) is shown, using the new definition of $\bar{z}(f, \Delta f, \mathcal{N}_0)$. There we see that, between $f_{\text{d,min}}$ and $f_{\text{d,max}}$, there is no resolvable background. On the right side of Figure 2.12 we show the spectral function obtained by inserting (2.120) in (2.44), for the case of NS-NS with the most likely values of masses and coalescence rates. The difference between the spectral functions with the old and the new definitions of $\bar{z}(f, \Delta f, \mathcal{N}_0)$ is just a small peak at frequency $f_{\text{d,max}}$.

Since the results are almost unchanged, we prefer the definition of unresolvable background given in Section 2.2.6, because the definition of $\bar{z}(f, \Delta f, \mathcal{N}_0)$ given in Equation (2.43) is simpler than that in (2.120).

2.5.5 On the definition of the overlap function

In Section 2.2.6 we mention that the time resolution, Δt , should be taken into account to define the resolvability, but in practice it is not important. We now explain how Δt could be introduced in the overlap function and why it is not necessary, in the circumstances considered in this chapter.

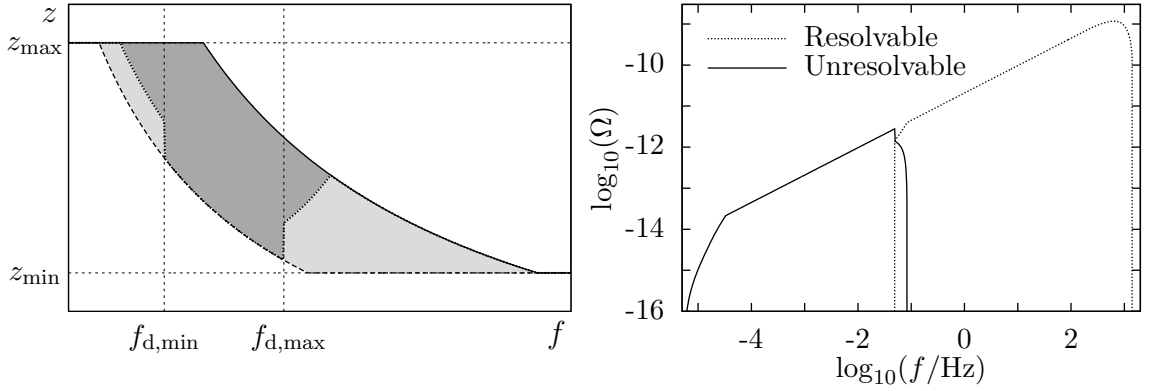


Figure 2.12: Redshift versus observed frequency (left plot, analogous to that in Figure 2.4) and spectral function versus observed frequency (right plot, analogous to that in Figure 2.8, corresponding to NS-NS with the most likely values of masses and coalescence rates). The difference between these plots and the ones in Figures 2.4 and 2.8 is that here, as soon as the unresolvable part of the background dominates, all signals become unresolvable.

Signals of binaries evolve more rapidly at higher frequencies, and spend therefore less time in a frequency bin. Eventually, at frequencies and redshifts larger than certain f and z , the interval of time $\tau_e(f, \Delta f, z)$ can become smaller than the time resolution Δt . When this happens, all signals spend effectively an interval of time Δt in each frequency bin, and no less than that (since smaller intervals of time cannot be distinguished). Thus, if the signals are unresolvable at f and z , they stay unresolvable for any larger values of frequency and redshift. Equation (2.41) could be generalized to take into account this effect,

$$\mathcal{N}(f, \Delta f, \Delta t, z) = \int_{z_{\text{low}}(f)}^z \max(\tau_e(f, \Delta f, z'), \Delta t[1+z]^{-1}) \dot{n}(z') \frac{d\mathcal{V}_c}{dz'} dz'. \quad (2.121)$$

The factor $[1+z]^{-1}$ is necessary to compare our time resolution (which is an observed interval of time) with the interval of time at emission $\tau_e(f, \Delta f, z)$.

The effect of introducing Δt affects our calculations only if $\tau_e(f, \Delta f, z) \leq \Delta t[1+z]^{-1}$ when $\mathcal{N} \geq 1$, i.e., if there is more than one coalescence every $\Delta t[1+z]^{-1}$. Taking the highest rate of Table 2.1 (which is the maximum rate of WD-WD), we see that

$$\int_0^5 \Delta t[1+z']^{-1} R \frac{d\mathcal{V}_c}{dz'} dz'$$

is greater than one for Δt greater than $\sim 1/9$ s. A reasonable choice for the time resolution is the inverse of the sampling rate of a detector, which, in the case of current ground-based detectors, is much smaller than $1/9$ s. Therefore, the generalization (2.121) is not necessary; the overlap function is well defined by (2.41).

By artificially increasing the time resolution by several orders of magnitude, we see the effect that the overlap function of Equation (2.121) produces in $\bar{z}(f, \Delta f, \Delta t, \mathcal{N}_0)$ (which is obtained by inserting Equation (2.121) in (2.43)) and in $\Omega(f, \Delta f, \Delta t, \mathcal{N}_0)$ (inserting (2.121) in (2.44)).

2 Gravitational wave background from binary systems

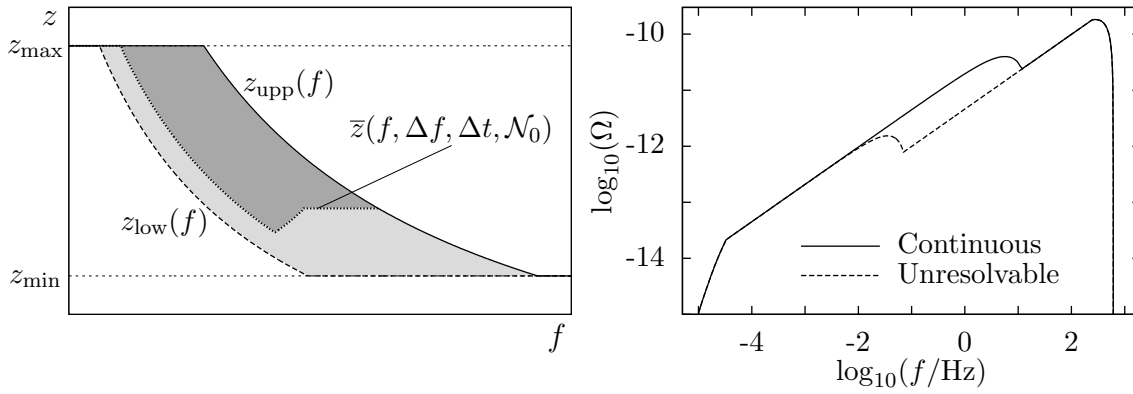


Figure 2.13: Redshift versus observed frequency (left plot, analogous to that in Figure 2.4) and spectral function versus observed frequency (right plot, analogous to that in Figure 2.8), corresponding to NS-NS with the most likely values of masses and coalescence rates). These plots (unlike those in Figures 2.4 and 2.8) are calculated assuming an unrealistic time resolution of $\Delta t = 600$ s. With such a large time resolution, an unresolvable background would be present in the frequency band of ground-based detectors.

This effect is plotted in Figure 2.13. There we see that, above a certain redshift and a certain frequency, all signals contribute to the unresolvable background. With this example we see that a large time resolution would lead to the existence of an unresolvable background in the frequency band of ground-based detectors.

2.5.6 Comparison with previous work

Unresolvable backgrounds

In Figure 2.14 we show the unresolvable background produced by the superensemble of MBH-MBH, and the sum of the unresolvable backgrounds of all stellar binaries (which is almost equal to the background made by only WD-WD). These curves are compared with other predictions from the literature. The curve (a) is obtained from [223], using its Equation (14) with the mean values of the parameters in (45), (46) and (47). That formula is given in terms of the characteristic amplitude, h_c , which is related to the spectral function by

$$\Omega(f) = \frac{\pi f^2}{4\rho_c G} h_c^2(f). \quad (2.122)$$

In terms of the strain amplitude $S_h(f)$, the characteristic amplitude is

$$h_c(f) = \sqrt{f S_h(f)}. \quad (2.123)$$

The curve (b) is taken from Figure 4 of [222], where h_{rms} also represents a characteristic amplitude. Finally, the curve (c) is taken from Figure 16 of [63]. In all cases we find a good agreement of our predictions with those from the mentioned papers.

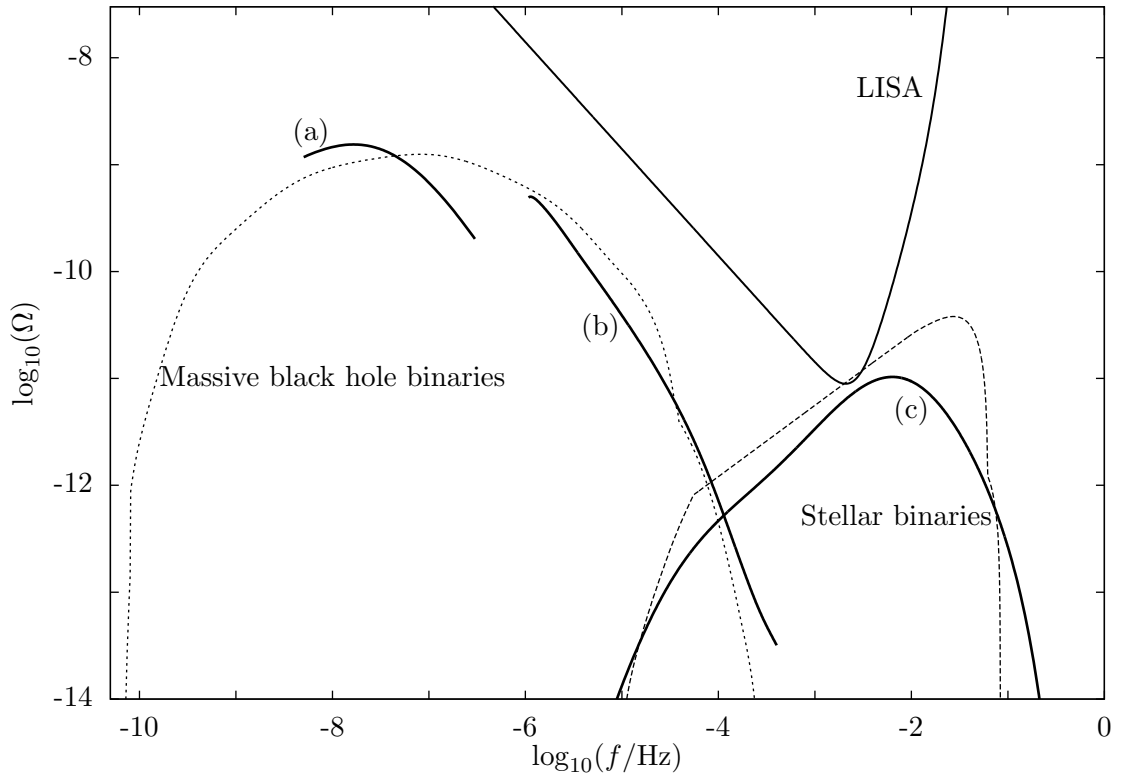


Figure 2.14: Spectral function of the unresolvable background of MBH-MBH (dotted line) and of all stellar binaries (dashed line), versus observed frequency. These curves are compared with previous predictions from the literature, which correspond to the unresolvable backgrounds of: (a) MBH-MBH from [223], (b) MBH-MBH from [222] and (c) extragalactic stellar binaries from [63].

In Figure 2.15 the unresolvable background of MBH-MBH is shown, calculated with the four different models (see Section 2.3). The unresolvable backgrounds calculated in [222] and [223] are also plotted for comparison.

Background of neutron star binaries

In Figure 2.16 we see that our estimate of the total background of NS-NS is in good agreement with the one in [201]. The curve (a) in Figure 2.16 represents what in [201] is called *shot noise* (see Figure 2 of that paper). In that work, the existence of a continuous (and Gaussian) background is also asserted; this corresponds to the curve (b) in Figure 2.16. If we compare (b) with either our continuous or our unresolvable curves, we find a big discrepancy.

We now explain the origin of this discrepancy. In Section 2.2.3 we pointed out that signals of equal observed frequency but different redshifts need different intervals of time to coalesce. However, in Section 3 of [201], all binaries are assumed to spend the same amount of time in a certain frequency interval, leading to the conclusion that the background is continuous at high frequencies. The same has been claimed in similar papers, for example [43, 195].

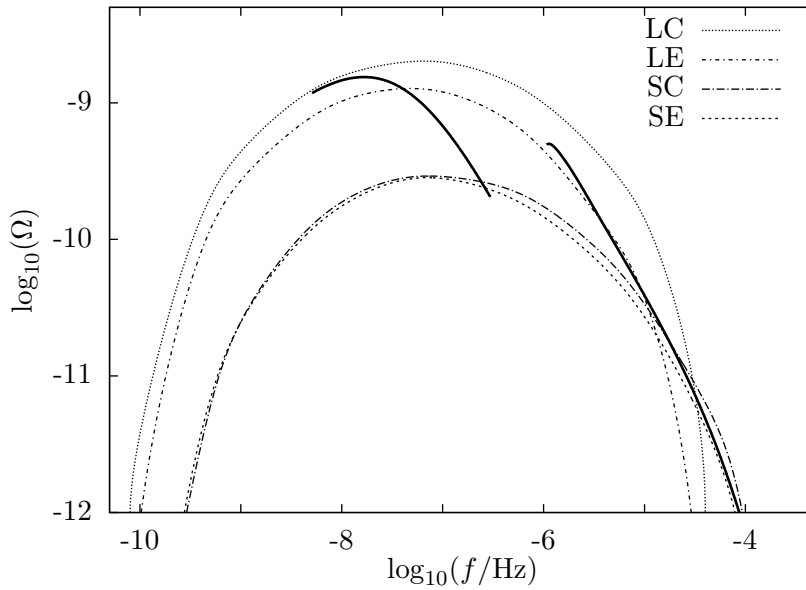


Figure 2.15: Spectral function of the unresolvable background of MBH-MBH, calculated with the four different models (LE, LC, SE and SC), versus observed frequency. For comparison we include the curves of the unresolvable backgrounds of [222] and [223].

In a later work, [200], the continuity of the background is calculated in a similar manner as we do; the redshift of the signals is properly taken into account to measure the interval of time that they spend in the frequency window of the detector. But in this paper, the continuous background is treated as unresolvable, which is incorrect, as we justify now. Suppose there is a continuous background of NS-NS in the frequency band of ET, such that there is an average of a few signals present in the band. Even if these few signals are observed at the same time, they do not overlap in the frequency domain; the signals can still be distinguished in frequency, so they are resolvable.

Overlap function versus duty cycle

In the literature, the so-called *duty cycle* is often used. It is defined by

$$D(z) = \int_0^z \bar{\tau}_e \dot{n}(z') \frac{d\mathcal{V}_c}{dz'} dz', \quad (2.124)$$

where $\bar{\tau}_e$ is the duration of a signal in the detector window. If one assumes that $\bar{\tau}_e$ is constant, as for example in [43, 195, 201], $D(z)$ does not give any valuable information (this has just been commented on in the previous section). If $\bar{\tau}_e = \tau_e(f_1, f_2 - f_1, z)$, i.e., if $\bar{\tau}_e$ is the time that each signal of redshift z spends in the frequency window $[f_1, f_2]$ of a certain detector, $D(z)$ characterizes the continuity of the background. But the property of the background that is indeed relevant is the resolvability, which is measured by the overlap function, defined in Equation (2.41).

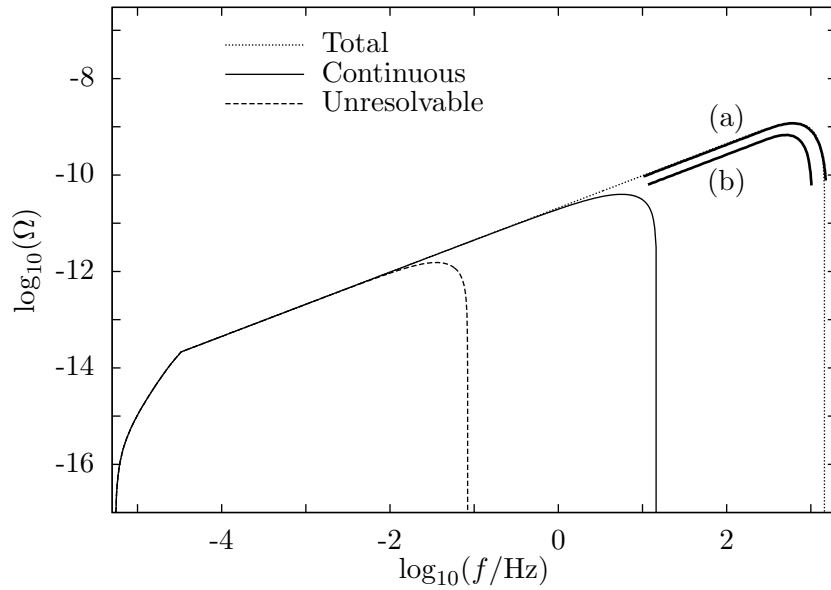


Figure 2.16: Spectral function of the total, continuous and unresolvable backgrounds of the ensemble of NS-NS (with the most likely values of masses and coalescence rates), versus observed frequency. We compare these curves with those given in [201]. Curves (a) and (b) correspond to what in that paper is called *shot noise* and *Gaussian background*, respectively. In the text we explain the origin of the discrepancy between (b) and our continuous or unresolvable backgrounds.

An overlap function like the one in Equation (2.41) is useful for quantifying the resolvability of long signals. Now suppose that there is an ensemble of systems that do not emit gravitational waves during a long period of time, but rather in a *burst*. For such systems one cannot obtain an accurate function $\tau_e(f, \Delta f, z)$. In this case, the resolvability can be quantified using the overlap function, by changing $\tau_e(f, \Delta f, z)$ to $\bar{\tau}_e$, the typical duration of a burst. This overlap function would then coincide with the duty cycle. In the case that $\bar{\tau}_e$ could be smaller than the time resolution Δt , one should rather use the generalized overlap function of (2.121).

The overlap function is therefore a generalization of the duty cycle, that can be used for short or long signals.

2.6 Summary and conclusions

We have reviewed basic aspects of the gravitational wave background. We have derived a formula (Equation (2.39)) for the spectral function, $\Omega(f)$, for an ensemble of many similar systems emitting gravitational radiation at different times and locations. This formula has been generalized to account for the duration of the signals and the observation time. With the generalized spectral function, $\Omega(f, \Delta f, \mathcal{N}_0)$ (in Equation (2.44)), one can distinguish between unresolvable and resolvable backgrounds (Equations (2.45) and (2.46), respectively), and between continuous and discontinuous backgrounds (Equations (2.50) and (2.51), respectively).

The resolvability is a fundamental property of the background. An unresolvable background

2 Gravitational wave background from binary systems

(often called confusion noise or stochastic background) is fully characterized by $\Omega(f, \Delta f, \mathcal{N}_0)$. A resolvable background is composed of signals whose waveforms can be distinguished and in some circumstances subtracted out of the data. Precise definitions of resolvable and unresolvable backgrounds can be found in Section 2.2.6. Figure 2.4 illustrates the different regimes of the background.

The resolvability is characterized by the overlap function, $\mathcal{N}(f, \Delta f, z)$, which gives the average number of signals, with frequency f and redshifts smaller than z , per frequency bin Δf (the frequency resolution). A formula for the overlap function is given in Equation (2.41). In Section 2.5.6 we have shown that the overlap function is a generalization of the duty cycle. The latter has been often used in the literature to quantify the continuity and even the resolvability of the background, leading in some cases to incorrect results.

The continuity is a secondary property of the background, which just gives an idea of how often the signals are present in the frequency window of a detector. The overlap function can also be used to characterize the continuity of the background, as explained in Section 2.2.7.

We have calculated the spectral functions of the backgrounds of stellar binaries (those containing white dwarfs, neutron stars or stellar-mass black holes) and of massive black hole binaries. In Table 2.1 we have summarized the values, taken from the literature, of the coalescence rates of each ensemble. The ranges of masses assumed for neutron stars, white dwarfs and stellar-mass black holes are in Equations (2.106), (2.107) and (2.108), respectively. A semi-analytical solution of the generalized spectral function has been derived for stellar binaries (Equation (2.105)). The calculations involving massive black hole binaries have been performed numerically, using the coalescence rates obtained with the four models of [15].

The spectral functions of the backgrounds produced by the different ensembles are plotted in Section 2.4, over the frequencies of all present and planned detectors. The total, continuous and unresolvable backgrounds are plotted in Figures 2.5, 2.6 and 2.7, respectively, with the most likely values of masses and coalescence rates. In Figure 2.8 the same curves are plotted separately for each ensemble, with their uncertainties. The total, continuous and unresolvable backgrounds, using the rate of BH-BH recently predicted in [31], are plotted in Figures 2.9 and 2.10.

The unresolvable background is dominated by white dwarf binaries, below $\sim 10^{-1}$ Hz, and by massive black hole binaries, below $\sim 10^{-4}$ Hz. These backgrounds could enter the frequency window of LISA, PPTA and BBO. The continuous background of BH-BH, using the recent coalescence rate predicted in [31], becomes more important than the one made by NS-NS, especially in the band of BBO. The confusion noise produced by galactic binaries has not been shown in the figures, since it cannot be calculated using the spectral function. Some papers in the literature which cover this issue are [116, 165, 209].

Finally, with Figures 2.6 and 2.7, we conclude that present and planned ground-based detectors are in a frequency range where no continuous or unresolvable backgrounds from binary systems are present. Therefore, without considering other possible sources of confusion noise, this band could be suitable for searching for primordial backgrounds.

3 Gravitational wave background from rotating neutron stars

Originally published as:
P. A. Rosado, *Phys. Rev. D* 86:104007, 2012.
Copyright 2012 by the American Physical Society.

The background of gravitational waves produced by the ensemble of rotating neutron stars (which includes pulsars, magnetars, and gravitars) is investigated. A formula for $\Omega(f)$ (a function that is commonly used to quantify the background, and is directly related to its energy density) is derived, without making the usual assumption that each radiating system evolves on a short time scale compared to the Hubble time; the time evolution of the systems since their formation until the present day is properly taken into account. Moreover, the formula allows one to distinguish the different parts of the background: the unresolvable (which forms a stochastic background or confusion noise, since the waveforms composing it cannot be either individually observed or subtracted out of the data of a detector) and the resolvable. Several estimations of the background are obtained, for different assumptions on the parameters that characterize neutron stars and their population. In particular, different initial spin period distributions lead to very different results. For one of the models, with slow initial spins, the detection of the background by present or planned detectors can be rejected. However, other models do predict the detection of the background, that would be unresolvable, by the future ground-based gravitational wave detector ET. A robust upper limit for the background of rotating neutron stars is obtained; it does not exceed the detection threshold of two cross-correlated Advanced LIGO interferometers. If gravitars exist and constitute more than a few percent of the neutron star population, then they produce an unresolvable background that could be detected by ET. Under the most reasonable assumptions on the parameters characterizing a neutron star, the background is too faint to be detected. Previous work has suggested neutron star models in which large magnetic fields (like the ones that characterize magnetars) induce big deformations in the star, which produce a stronger emission of gravitational radiation. Considering the most optimistic (in terms of the detection of gravitational waves) of these models, an upper limit for the background produced by magnetars is obtained; it could be detected by ET, but not by BBO or DECIGO. Simple approximate formulas to characterize both the total and the unresolvable backgrounds are given for the ensemble of rotating neutron stars, and, for completion, also for the ensemble of binary star systems.

3.1 Introduction

The topic of this chapter is the gravitational wave background [11, 145] produced by the ensemble of rotating neutron stars in the universe. These systems are modeled as isolated neutron stars [124] that are formed with an initial spin frequency, and lose energy via electromagnetic dipole emission [54, 169] and via quadrupolar gravitational radiation (see Section 9.4.2 (b) of [90, 189]). The ensemble of rotating neutron stars contains the populations of pulsars, magnetars, and gravitars.

Pulsars [138] are neutron stars that emit electromagnetic radiation in a beam which, if pointing

3 Gravitational wave background from rotating neutron stars

towards Earth, is observed as a “lighthouse” of great regularity. We neglect the contribution of recycled pulsars [137].

Magnetars [238, 239, 240, 87] are neutron stars with a magnetic field a few orders of magnitude stronger than usual pulsars. That magnetic field may support large ellipticities [47] leading to an enhanced production of gravitational radiation. We obtain an upper limit for the background produced by the magnetars.

Gravitars [170, 111] are hypothetical neutron stars that have a magnetic field weaker than usual pulsars, and lose rotational energy primarily via gravitational radiation. There may exist a population of gravitars that cannot yet be detected because they emit very little or no electromagnetic radiation. A simulation performed in [184] shows that the conditions for neutron stars to be gravitars described in [170] are possible. In this chapter we investigate the detection prospects for the background produced by such a population. The ensemble of gravitars provides an upper limit for the background of rotating neutron stars.

This work is a follow-on study to [207], where the background produced by binary systems is studied (including binaries formed by white dwarfs, neutron stars, and black holes). With both works, two of the most promising sources of contemporary background are covered.

Other potential sources of contemporary background, not discussed in this chapter or in the previous one, are newborn neutron stars undergoing r-mode instabilities [168, 261], compact objects captured by massive black holes [20], inspiralling black hole binaries with intermediate or extreme mass-ratio [12], supernovae [34], and population II and III stars [153, 118].

Besides the contemporary background, there may exist a primordial one [10, 145, 32], arising from processes in the early history of the universe.

We calculate what part of the total background of rotating neutron stars is unresolvable (commonly named *confusion noise* or *stochastic background*). The signals composing this part cannot be distinguished from each other or subtracted from the data of a gravitational wave detector (we do not study the problem of the subtraction of resolvable signals, treated, for example, in [46, 48, 258]). The resolvability of the background is quantified by the *overlap function*, $\mathcal{N}(f, \Delta f, z)$, introduced in [207]. This function gives the expected number of signals, with redshifts smaller than z , that are observed within a frequency bin $[f, f + \Delta f]$, where Δf is the frequency resolution allowed by the detector and the data analysis method. When a frequency bin is constantly occupied by one or more overlapping signals, i.e., $\mathcal{N}(f, \Delta f, \infty) \geq 1$, these signals cannot be disentangled, and form an unresolvable background.

The spectral gravitational wave density parameter, or, simply, *spectral function*, $\Omega(f)$, is often used to quantify the background [11]. It gives the average energy density of gravitational radiation (per logarithmic frequency interval) divided by the critical density. The generalized spectral function [207], $\Omega(f, \Delta f, \mathcal{N}_0)$, has the same meaning as $\Omega(f)$, but it quantifies only the part of the background with more than \mathcal{N}_0 overlapping signals per frequency bin. The total background and the unresolvable one are calculated by taking $\mathcal{N}_0 = 0$ and $\mathcal{N}_0 = 1$, respectively. In this chapter, the spectral function accounts for the time evolution of the systems, that is not assumed to be short compared to cosmic time scales.

Previous work has studied the gravitational wave background from pulsars [197] and magnetars [198, 201, 154]. These articles assume that all neutron stars are formed with the same initial spin frequency. We show that the results change dramatically if the initial spin frequency follows a probability distribution. In particular, for one of the distributions considered [64], the detection of the background by present and planned detectors is rather unrealistic.

For some of the models considered, the detection of the background of rotating neutron stars could be possible by cross-correlating two interferometers of the Einstein Gravitational Wave Telescope (ET), assuming two of the proposed configurations (called ETB and ETD) [190]. Furthermore, this background is unresolvable. The current generation of present ground-based detectors [80, 4, 130], and the advanced version of the Laser Interferometer Gravitational Wave Observatory (aLIGO) [88], are not sensitive enough to detect this background. For future space missions like the Big Bang Observer (BBO) [48] and the Decihertz Interferometer Gravitational Wave Observatory (DECIGO) [106], the detection is rather unlikely.

The outline of the chapter is as follows:

In Section 3.2, the notation and nomenclature of this chapter is explained, and the quantification of the gravitational wave background, its resolvability and detectability are briefly reviewed. A general formula for $\Omega(f, \Delta f, \mathcal{N}_0)$ is derived for a population of systems that emit at different times and locations, without assuming that the evolution of each system is short compared to cosmological time scales. We also give a formula for $\mathcal{N}_0(f, \Delta f, z)$ which is more general than the one presented in the previous work [207].

In Section 3.3 we expand upon the expressions of $\Omega(f, \Delta f, \mathcal{N}_0)$ and $\mathcal{N}_0(f, \Delta f, z)$, to account for the evolution of the population. We obtain formulas that depend on the energy and frequency evolution of a system, the initial frequency distribution and the formation rate of the ensemble, and certain cosmological parameters. Then, assuming that all systems start emitting at the same frequency and evolve in short time scales, we obtain the formula of the spectral function that is commonly used in the literature.

In Section 3.4 we describe the models assumed for a neutron star and its population.

Section 3.5 contains the main results of this chapter. We present a robust upper limit for the background of rotating neutron stars, the *gravitar limit*. We then obtain the background produced by gravitars, and study the likelihood of planned detectors to observe it and to place limits on the abundance of gravitars. The most realistic expectation of the background of rotating neutron stars is calculated, using a magnetic field and an ellipticity distribution from the literature. An upper limit on the background produced by magnetars is obtained. We study the detection prospects of ETB, ETD, BBO and DECIGO, for different assumptions on the initial frequency, magnetic field, and ellipticity of neutron stars.

In Section 3.6 we compare our results with others from the literature. We also comment on the insensitivity of the spectral function on the choice of star formation rate.

The main results and conclusions are put together in Section 3.7. First, in Section 3.7.1, the technical achievements regarding the calculation of $\Omega(f, \Delta f, \mathcal{N}_0)$ are summarized. Then, in 3.7.2, we compress all results and predictions regarding the detection of the background of rotating neutron stars.

In Sections 3.8 and 3.9 we give simple approximate formulas for the spectral function of the background of rotating neutron stars, and also for the one of binary systems. Finally, in Section 3.10 we point out a feature in the gravitar limit that is analogous to Blandford's argument [111].

3.2 Characterization of the background: an overview

We follow the notation and terminology explained in Section 2.2. The index “*e*” (for *emitted*) is used for frequencies and energies of the gravitational waves, as well as intervals of time, measured close to the system (for example, a single rotating neutron star) at the time of emission

3 Gravitational wave background from rotating neutron stars

of the radiation. Observed frequencies, energies and intervals of time (measured here and now) have no index. Emitted quantities f_e , E_e , and Δt_e (and infinitesimal emitted intervals df_e , dE_e , and dt_e) are affected by the expansion of the universe. They are related to the observed quantities f , E , and Δt (df , dE , and dt), by

$$f = [1 + z]^{-1} f_e, \quad df = [1 + z]^{-1} df_e, \quad (3.1)$$

$$E = [1 + z]^{-1} E_e, \quad dE = [1 + z]^{-1} dE_e, \quad (3.2)$$

and

$$\Delta t = [1 + z] \Delta t_e, \quad dt = [1 + z] dt_e, \quad (3.3)$$

where z is the cosmological redshift. Any given function x that depends on f_e can be written in terms of observed frequencies. The notation $x|_f$ means that the function $x(f_e)$ must be written in terms of observed frequencies, i.e. $x|_f = x(f[1 + z])$.

For convenience, a *look-back time* interval is sometimes used, and denoted by an index L . The relation between a look-back time interval Δt^L and an ordinary look-forward time interval Δt is $\Delta t^L = -\Delta t$.

3.2.1 Quantification of the background

The gravitational wave background is usually characterized by the spectral energy density parameter [11] (or, simply, *spectral function*),

$$\Omega(f) = \frac{\rho_{\ln}(f)}{\rho_c} = \frac{\varepsilon_{\ln}(f)}{c^2 \rho_c}, \quad (3.4)$$

where c is the speed of light. The present critical density of the universe is

$$\rho_c = \frac{3H_0^2}{8\pi G}, \quad (3.5)$$

where G is the gravitational constant, and H_0 is the present Hubble expansion rate¹, of $74.2 \text{ km s}^{-1} \text{ Mpc}^{-1}$ [205, 206]. The function $\varepsilon_{\ln}(f)$ is defined in such a way that $\varepsilon_{\ln}(f) d \ln f$ is the energy per unit volume of gravitational waves between $\ln f$ and $\ln f + d \ln f$. Thus, $\Omega(f)$ is related to the total density of gravitational radiation in the universe, that is

$$\rho_{\text{gw}} = \int_{-\infty}^{+\infty} \rho_{\ln}(f) d \ln f = \rho_c \int_{-\infty}^{+\infty} \Omega(f) d \ln f. \quad (3.6)$$

Here, $\Omega(f)$ is the spectral function of all sources of gravitational radiation in our past light cone. For simplicity, we use the same symbol to characterize the background produced only by the systems we are interested in (rotating neutron stars).

The spectral function fully characterizes a Gaussian, stationary, isotropic and unpolarized background [11]. As claimed in [207], the spectral function is also the right tool to characterize an unresolvable background. On the other hand, one loses information when using the spectral function for a resolvable background.

¹Again, these cosmological parameters were the most recent by the time when this work was written. We do not expect the main results to change significantly by using the parameters obtained with more modern measurements.

3.2 Characterization of the background: an overview

We now derive $\Omega(f)$ for an ensemble of many sources, emitting at different times and locations, that can experience a time evolution. The radiation we observe today has been produced by many individual systems in the past. The energy emitted by one system during an infinitesimal interval of time is

$$dE_e = \frac{dE_e}{dt_e} dt_e = \frac{dE_e}{dt_e} \frac{dt_e}{dt_e^L} dt_e^L = -\frac{dE_e}{dt_e} dt_e^L. \quad (3.7)$$

Two waves that reach us now and were emitted at different look-back times t_e^L and $t_e^L + dt_e^L$, have different redshifts z and $z + dz$. Look-back time intervals can thus be written as redshift intervals,

$$dt_e^L = \frac{dt_e^L}{dz} dz. \quad (3.8)$$

The number of systems, per unit comoving volume, contributing to the background with observed frequencies between $\ln f$ and $\ln f + d \ln f$ is

$$dn = \frac{dn}{d \ln f} d \ln f. \quad (3.9)$$

The present energy density of gravitational waves, per unit logarithmic frequency interval, produced by the collection of all systems is

$$\varepsilon_{\ln(f)} = \int_0^{t_0} \frac{dE}{dt} \frac{dn}{d \ln f} dt = \int_0^\infty \frac{dE}{dt} \frac{dn}{d \ln f} \frac{dt^L}{dz} dz, \quad (3.10)$$

where t_0 is the current age of the universe. Using Equations (3.1), (3.2), and (3.3), we can write

$$\varepsilon_{\ln(f)} = \int_0^\infty [1+z]^{-1} \left. \frac{dE_e}{dt_e} \right|_f \left. \frac{dn}{d \ln f_e} \right|_f \frac{dt_e^L}{dz} dz. \quad (3.11)$$

Replacing (3.11) in (3.4), we finally reach the formula for the spectral function of the total background,

$$\Omega(f) = \frac{1}{\rho_c c^2} \int_0^\infty [1+z]^{-1} \left. \frac{dE_e}{dt_e} \right|_f \left. \frac{dn}{d \ln f_e} \right|_f \frac{dt_e^L}{dz} dz. \quad (3.12)$$

The functions dE_e/dt_e and $dn/d \ln f_e$ are obtained in Sections 3.4.3 and 3.3.2, respectively, for the ensemble of rotating neutron stars. The function dt_e^L/dz depends on the choice of the cosmological model; we assume a Lambda-Cold Dark Matter universe, so

$$dt_e^L = \frac{1}{[1+z]H_0\mathcal{E}(z)} dz, \quad (3.13)$$

where

$$\mathcal{E}(z) = \sqrt{\Omega_m[1+z]^3 + \Omega_\Lambda}. \quad (3.14)$$

Here, Ω_m and Ω_Λ are the density parameters of matter and dark energy, respectively, whose values [96] are assumed to be $\Omega_m = 0.27$ and $\Omega_\Lambda = 0.73$. In Section 3.2.2 we explain how to modify the integration limits of Equation (3.12) to measure only the unresolvable part of the background.

In the literature, one usually finds the spectral function written as

$$\Omega(f) = \frac{1}{\rho_c c^2} \int_0^\infty [1+z]^{-1} \left. \frac{dE_e}{d \ln f_e} \right|_f \dot{n}(z) \frac{dt_e^L}{dz} dz \quad (3.15)$$

3 Gravitational wave background from rotating neutron stars

(see, for example, Equation (35) of [207] or Equation (5) of [180]). In Section 3.3.3, we show that (3.15) can be derived from (3.12) if one assumes that systems are short-lived and start emitting with the same initial frequency.

3.2.2 Resolvability of the background

The overlap function, $\mathcal{N}(f, \Delta f, z)$, allows us to define and quantify the resolvability of the background. We now define the overlap function more generally than in [207], as

$$\mathcal{N}(f, \Delta f, z) = \int_0^z \int_f^{f+\Delta f} \frac{dn}{df'} \frac{dV_c}{dz'} df' dz' = \int_0^z \int_f^{f+\Delta f} [1+z'] \left. \frac{dn}{df_e} \right|_{f'} \frac{dV_c}{dz'} df' dz'. \quad (3.16)$$

Here, dV_c is the element of comoving volume, given by

$$dV_c = 4\pi \left[\int_0^z \frac{c}{H_0 \mathcal{E}(z')} dz' \right]^2 \frac{c}{H_0 \mathcal{E}(z)} dz. \quad (3.17)$$

The frequency resolution Δf can be chosen as the inverse of the observation time (typically of order one year). The condition of unresolvability is fulfilled from a certain redshift z , i.e. $\mathcal{N}(f, \Delta f, z) \geq 1$, when each bin is always filled by one or more signals. These signals cannot be distinguished, because for that we would need to improve our frequency resolution; we therefore say that they are considered unresolvable. One can invert $\mathcal{N}(f, \Delta f, z) = \mathcal{N}_0$ with respect to z , obtaining a function $\bar{z} = \bar{z}(f, \Delta f, \mathcal{N}_0)$. Signals with redshifts greater than this produce an overlap greater than \mathcal{N}_0 . Using this redshift function as lower limit of the integral in Equation (3.12), one considers only the contribution to the background of those signals that produce an overlap greater than \mathcal{N}_0 .

Therefore, the spectral function of a background with more than \mathcal{N}_0 signals per frequency bin $[f, f + \Delta f]$ is

$$\Omega(f, \Delta f, \mathcal{N}_0) = \frac{1}{\rho_c c^2} \int_{\bar{z}(f, \Delta f, \mathcal{N}_0)}^{\infty} [1+z]^{-1} \left. \frac{dE_e}{dt_e} \right|_f \left. \frac{dn}{d \ln f_e} \right|_f \frac{dt_e^L}{dz} dz. \quad (3.18)$$

For simplicity, we assume that the background is unresolvable if the number of overlapping signals in a frequency bin is ≥ 1 (other criteria are discussed in Section V.D of [207]). Then, the spectral function of the unresolvable part of the background is given by

$$\Omega_{\text{unresolvable}}(f) = \Omega(f, \Delta f, 1). \quad (3.19)$$

On the other hand, the spectral function of the resolvable part is

$$\Omega_{\text{resolvable}}(f) = \Omega_{\text{total}}(f) - \Omega_{\text{unresolvable}}(f). \quad (3.20)$$

Here, the spectral function of the total background (which coincides with Equation (3.12)), is

$$\Omega_{\text{total}}(f) = \Omega(f, \Delta f, 0), \quad (3.21)$$

where the value of Δf becomes irrelevant.

In Section 3.3.3 we prove that Equation (3.16) leads to the definition of the overlap function given in Equation (41) of [207], if one assumes all systems start emitting with the same initial frequency and the evolution of each system is short compared to cosmic time scales.

The definition of resolvability given in this section is the one that was introduced in [207] and that will be used throughout the entire chapter. More thorough definitions can be a topic for future work, for example taking into account the ability of the data analysis method to distinguish individual signals from the instrumental noise, or to even distinguish unresolvable signals with different amplitudes or directions of arrival. The advantage of our definition is that the resolvability becomes an intrinsic property of the background, i.e., independent of the characteristics of the detector (such as its sensitivity) and of the data analysis method. The only parameter related to the observation that affects the resolvability is the frequency resolution. However, the observation time T_{obs} of any realistic experiment is of the order of a year or a few years; the best frequency resolution achievable (calculated as $\Delta f = T_{\text{obs}}^{-1}$), can thus be considered equal for all possible detectors.

3.2.3 Detectability of the background

In practice, the instrumental noise of a detector cannot be modeled with perfect accuracy; if an unresolvable background is present in the data of a detector, it is therefore indistinguishable from instrumental noise (unless one can construct a *null stream*, which is a very advantageous feature of ET [202]). The usual technique to cope with this issue is the cross-correlation of the data of two detectors (see, for example, Section 7.8.3 of [147]).

If a background (characterized by a spectral function $\Omega(f)$) is present in the data of two interferometers, one can cross-correlate the outputs of both, that span an interval of time T_{obs} . Doing this, the resulting *signal-to-noise ratio* (Equation (7.241) of [147]), or SNR, is given by

$$\text{SNR} = \frac{3H_0^2}{4\pi^2} \left[2T_{\text{obs}} \int_0^\infty df \frac{\Gamma^2(f)\Omega^2(f)}{f^6 S_{n,1}(f)S_{n,2}(f)} \right]^{1/2}. \quad (3.22)$$

Here, $S_{n,1}(f)$ and $S_{n,2}(f)$ are the noise spectral densities of the detectors 1 and 2, respectively, and $\Gamma(f)$ is the non-normalized overlap reduction function (Equation (7.226) of [147]), defined by

$$\begin{aligned} \Gamma(f) = & \frac{1}{8\pi^2} \int_0^{2\pi} d\phi \int_0^\pi \sin(\theta) d\theta \cos\left(\frac{2\pi f \vec{u}(\theta, \phi) \cdot \vec{\Delta x}}{c}\right) \\ & \times \int_0^{2\pi} d\psi \sum_{p=+, \times} F_1^p(\theta, \phi, \psi) F_2^p(\theta, \phi, \psi). \end{aligned} \quad (3.23)$$

In this definition, $\vec{\Delta x} = \vec{x}_2 - \vec{x}_1$, where \vec{x}_d is the position of the detector d (for $d = 1$ or 2), and $\vec{u}(\theta, \phi)$ is a unit vector pointing to the direction defined by the angles θ and ϕ . The function $F_d^p(\theta, \phi, \psi)$ (for the polarization $p = +$ or \times) is the antenna pattern function, evaluated at the direction (θ, ϕ) , for a wave with a polarization angle ψ . The antenna pattern functions can be found in Section II.B of [202] for ET, and in Section 2.1 of [219] for aLIGO. Notice that Equation (3.22) is equivalent to Equation (3.75) of [11]; however, the normalized overlap reduction function $\gamma(f)$ defined in [147] and in [11] are only equivalent for the case of an L-shaped detector. A detailed study on the overlap reduction function can be found in [69].

Following [147], the non-normalized overlap reduction function can be written as

$$\Gamma(f) = F_{1,2}\gamma(f). \quad (3.24)$$

3 Gravitational wave background from rotating neutron stars

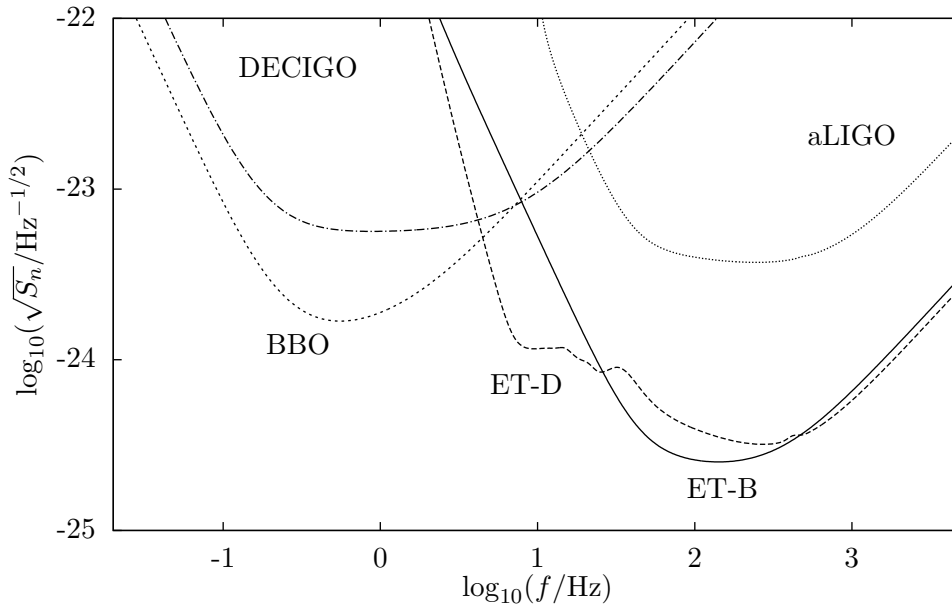


Figure 3.1: Spectral strain sensitivity of aLIGO, two possible configurations of ET (named ETB and ETD), DECIGO and BBO. The sources of the curves are given in the text.

For two colocated and coaligned detectors, $\gamma(f) = 1$ for all frequencies. For the correlation between two interferometric V-shaped detectors like ET, one obtains $F_{1,2} = 3/10$, whereas for L-shaped detectors like aLIGO, $F_{1,2} = 2/5$. In Section 3.5 the SNR is calculated for two interferometers of ET, and for two aLIGO interferometers (one at Livingston and one at Hanford), using the full overlap reduction function (Equation (3.23)) and assuming an observation time of one year. For simplicity, the SNR for two interferometers of BBO or DECIGO will be calculated by using $F_{1,2} = 3/10$ and $\gamma(f) = 1$, and an observation time of one year.

Figure 3.1 shows the spectral strain sensitivity $\sqrt{S_n(f)}$ of aLIGO (taken from [131]), two possible configurations of ET², DECIGO (from the fitting formula in Equation (1) of [166]) and BBO (Equation (2) of [166]). We consider two pairs of detectors: the two aLIGO detectors, at Hanford and Livingston, and two V-shaped ET detectors sharing one arm of the triangle.

A background is said to be *detectable* if it produces SNR larger than a certain threshold value. Be aware that a background can be resolvable without being detectable; it would consist of signals that are separated in a frequency-time plot but would be buried in noise (for example, instrumental noise, or confusion noise produced by another background).

²The spectral strain sensitivities of ETB and ETD were kindly provided by Tania Regimbau in a private communication.

3.3 Characterization of the background: a detailed derivation of $\Omega(f, \Delta f, \mathcal{N}_0)$ for an evolving population of systems

3.3.1 Formation rate of systems

The comoving density rate of systems formed $\dot{n}(z)$ (or, simply, *rate*), is defined such that $\dot{n}(z)dz$ is the number of systems formed per unit emitted interval of time, dt_e , per unit comoving volume, dV_c , between redshifts z and $z + dz$.

Sometimes it is convenient to write the rate as a function of time, instead of redshift. We define a function, $\mathcal{T}(z)$, that gives the interval of time elapsed between the formation of the first systems (at redshift z_{\max}), and the formation of the systems at redshift z . This function can be derived, for our cosmological model, using the formulas given in Section II.13 of [172],

$$\mathcal{T}(z) = \frac{2}{3H_0\sqrt{\Omega_\Lambda}} \left[\operatorname{asinh} \left(\sqrt{\frac{\Omega_\Lambda}{\Omega_m}} [1+z]^{-3/2} \right) - \xi \right]. \quad (3.25)$$

Here, we have introduced the constant

$$\xi = \operatorname{asinh} \left(\sqrt{\frac{\Omega_\Lambda}{\Omega_m}} [1+z_{\max}]^{-3/2} \right), \quad (3.26)$$

that imposes a time offset between the Big Bang and the formation of the first systems³. One can invert $\mathcal{T}(z) = \Delta t$ with respect to the redshift and obtain another useful formula,

$$\mathcal{Z}(\Delta t) = \left[\sqrt{\frac{\Omega_m}{\Omega_\Lambda}} \sinh \left(\frac{3H_0\sqrt{\Omega_\Lambda}\Delta t}{2} + \xi \right) \right]^{-2/3} - 1. \quad (3.27)$$

This gives the redshift observed in a signal that was emitted an interval of time Δt after the formation of the first systems. Using Equation (3.27), one can write the rate as a function of time, $\dot{n}(\mathcal{Z}(t))$.

3.3.2 Time evolution of the ensemble

We now explain how to calculate the term $[dn/d \ln f_e]_f$ in Equation (3.12), that is the number of systems per unit comoving volume per unit logarithmic frequency interval emitting around an observed frequency f .

Suppose a gravitational wave of redshift z was emitted by a system an interval of time $\mathcal{T}(z)$ after the formation of the first systems. At the instant of emission, the system had already evolved during a certain interval of time t_e (smaller than $\mathcal{T}(z)$). The system was thus formed an interval of time $\mathcal{T}(z) - t_e$ after the formation of the first systems. At the instant of formation, the system was emitting waves that have now a redshift $\mathcal{Z}(\mathcal{T}(z) - t_e)$. The formation rate at that instant was $\dot{n}(\mathcal{Z}(\mathcal{T}(z) - t_e))$. Then, during an infinitesimal interval of time dt_e , the number of systems formed per unit comoving volume that emit waves of redshift z is $\dot{n}(\mathcal{Z}(\mathcal{T}(z) - t_e))dt_e$.

³By imposing $\xi = 0$, the function $\mathcal{T}(z)$ gives the age of the universe at the instant when the waves of redshift z were emitted, as in Equation (13.20) of [172].

3 Gravitational wave background from rotating neutron stars

Assume a probability density function $p_e(f_e, t_e)$, such that $p_e(f_e, t_e)df_e$ is the probability of a system to emit between f_e and $f_e + df_e$ after a time evolution t_e . Then, the number of systems formed during dt_e per unit comoving volume that emit waves of redshift z in the frequency interval $[f_e, f_e + df_e]$ is $p_e(f_e, t_e)\dot{n}(\mathcal{Z}(\mathcal{T}(z) - t_e))dt_e df_e$. The total number of systems per unit comoving volume per unit frequency interval emitting with redshift z and frequency f_e is

$$\frac{dn}{df_e} = \int_0^{\mathcal{T}(z)} p_e(f_e, t_e)\dot{n}(\mathcal{Z}(\mathcal{T}(z) - t_e))dt_e. \quad (3.28)$$

We now show how to calculate the probability density function $p_e(f_e, t_e)$. For this purpose, we follow a similar approach as [111, 110], although we do not use any distribution of systems in the galaxy, but rather assume that systems are homogeneously distributed in the universe.

Additionally, suppose we know the initial probability density function $p_{\text{ini}}(f_{\text{ini}})$, such that $p_{\text{ini}}(f_{\text{ini}})df_{\text{ini}}$ is the probability of a system to emit between f_{ini} and $f_{\text{ini}} + df_{\text{ini}}$ at the instant of formation. Now we make the following assumption: a formed system never stops emitting gravitational waves. This means that all systems that were initially emitting in the frequency range $[f_{\text{ini}}, f_{\text{ini}} + df_{\text{ini}}]$ are now emitting in $[f_e, f_e + df_e]$. Then, in order to conserve the number of systems,

$$p_e(f_e, t_e)df_e = p_{\text{ini}}(f_{\text{ini}})df_{\text{ini}} \quad (3.29)$$

must be fulfilled.

The radiation we observe now from a system, at frequency f , was emitted in the past at frequency f_e ; that system was formed an interval of time t_e before emitting at f_e . The frequency at which the system was emitting at its formation is given by $f_{\text{ini}} = f_{\text{ini}}(f_e, t_e)$. Using this function we can rewrite Equation (3.29),

$$p_e(f_e, t_e) = p_{\text{ini}}(f_{\text{ini}}(f_e, t_e)) \frac{\partial f_{\text{ini}}}{\partial f_e}(f_e, t_e). \quad (3.30)$$

Equations (3.28) and (3.30) can be combined into

$$\frac{dn}{df_e} = \int_0^{\mathcal{T}(z)} dt_e p_{\text{ini}}(f_{\text{ini}}(f_e, t_e)) \frac{\partial f_{\text{ini}}}{\partial f_e}(f_e, t_e) \dot{n}(\mathcal{Z}(\mathcal{T}(z) - t_e)). \quad (3.31)$$

Finally, we can rewrite Equation (3.31) in terms of observed frequencies per logarithmic frequency interval to obtain

$$\begin{aligned} \left. \frac{dn}{d \ln f_e} \right|_f &= \left[f_e \frac{dn}{df_e} \right] \Big|_f = f[1+z] \int_0^{\mathcal{T}(z)} dt_e p_{\text{ini}}(f_{\text{ini}}(f[1+z], t_e)) \\ &\quad \times \frac{\partial f_{\text{ini}}}{\partial f_e}(f[1+z], t_e) \dot{n}(\mathcal{Z}(\mathcal{T}(z) - t_e)). \end{aligned} \quad (3.32)$$

In Section 3.3.3, we derive general formulas for the spectral function and for the overlap function, that depend on the shape of the function $p_{\text{ini}}(f_{\text{ini}})$; then, we highlight a special case where all systems emit at the same frequency at the instant of formation.

3.3.3 Spectral function and overlap function

General case

The spectral function of a background, with more than \mathcal{N}_0 signals per frequency bin Δf , produced by an ensemble that follows an initial frequency distribution $p_{\text{ini}}(f_{\text{ini}})$, is given by

$$\Omega(f, \Delta f, \mathcal{N}_0) = \frac{f}{\rho_c c^2} \int_{\bar{z}(f, \Delta f, \mathcal{N}_0)}^{z_{\text{max}}} dz \frac{dE_e}{dt_e} \Big|_f \frac{dt_e^L}{dz} \int_0^{\mathcal{T}(z)} dt_e p_{\text{ini}}(f_{\text{ini}}(f[1+z], t_e)) \times \frac{\partial f_{\text{ini}}}{\partial f_e}(f[1+z], t_e) \dot{n}(\mathcal{Z}(\mathcal{T}(z) - t_e)). \quad (3.33)$$

This is obtained by replacing Equation (3.32) in (3.18); the upper limit of the integral has been replaced by z_{max} , since we assume that no systems were formed at larger redshifts.

The overlap function of a background produced by an ensemble that follows an initial frequency distribution $p_{\text{ini}}(f_{\text{ini}})$ is given by

$$\mathcal{N}(f, \Delta f, z) = \int_0^z dz' \int_f^{f+\Delta f} df' [1+z'] \frac{dV_c}{dz'} \int_0^{\mathcal{T}(z')} dt_e p_{\text{ini}}(f_{\text{ini}}(f'[1+z'], t_e)) \times \frac{\partial f_{\text{ini}}}{\partial f_e}(f'[1+z'], t_e) \dot{n}(\mathcal{Z}(\mathcal{T}(z') - t_e)). \quad (3.34)$$

This is obtained by replacing $[dn/df_e]_f$ (from Equation (3.32)) in (3.16). The frequency resolution is typically much smaller than the range of frequencies of interest for rotating neutron stars. Equation (3.34) can thus be simplified with the approximation

$$\mathcal{N}(f, \Delta f, z) \approx \int_0^z dz' \Delta f [1+z'] \frac{dV_c}{dz'} \int_0^{\mathcal{T}(z')} dt_e p_{\text{ini}}(f_{\text{ini}}(f[1+z'], t_e)) \times \frac{\partial f_{\text{ini}}}{\partial f_e}(f[1+z'], t_e) \dot{n}(\mathcal{Z}(\mathcal{T}(z') - t_e)), \quad (3.35)$$

which is accurate as long as $\Delta f \ll f$.

For a fixed initial frequency

From all possible initial frequency distributions $p_{\text{ini}}(f_{\text{ini}})$, we now study a particular case with the form

$$p_{\text{ini}}(f_{\text{ini}}) = \delta(f_{\text{ini}} - f_{\text{fix}}). \quad (3.36)$$

Using this distribution, one assumes that all systems start emitting at a fixed initial frequency f_{fix} . Suppose we have a function $f_{\text{ini}}(f_e, t_e)$ (that was introduced in Section 3.3.2, and will be derived in Section 3.4.4 for the case of a rotating neutron star). Using one of the properties of the Dirac delta function, one can rewrite Equation (3.36) as

$$p_{\text{ini}}(f_{\text{ini}}(f_e, t_e)) = \frac{\partial t_e}{\partial f_{\text{ini}}}(f_e, \tau_e(f_{\text{fix}}, f_e)) \delta(t_e - \tau_e(f_{\text{fix}}, f_e)). \quad (3.37)$$

Here, $\tau_e(f_{\text{fix}}, f_e)$ is the interval of time that a system spends emitting between f_{fix} and f_e such that

$$f_{\text{ini}}(f_e, \tau_e(f_{\text{fix}}, f_e)) = f_{\text{fix}} \quad (3.38)$$

3 Gravitational wave background from rotating neutron stars

is fulfilled. The transformation of the Dirac delta function performed is valid as long as $\partial f_{\text{ini}}/\partial t_e$ is non-zero for all values of f_e and t_e . This condition holds for rotating neutron stars⁴. By replacing Equation (3.37) in (3.31), one obtains

$$\frac{dn}{df_e} = \frac{\partial t_e}{\partial f_{\text{ini}}}(f_e, \tau_e(f_{\text{fix}}, f_e)) \frac{\partial f_{\text{ini}}}{\partial f_e}(f_e, \tau_e(f_{\text{fix}}, f_e)) \dot{n}(\mathcal{Z}(\mathcal{T}(z) - \tau_e(f_{\text{fix}}, f_e))) \Theta(z, f_e), \quad (3.39)$$

where we have introduced the function

$$\Theta(z, f_e) = \theta(\mathcal{T}(z) - \tau_e(f_{\text{fix}}, f_e)) \theta(\tau_e(f_{\text{fix}}, f_e) - 0). \quad (3.40)$$

Here, $\theta(x - y)$ is the Heaviside step function; it is equal to one for $x > y$, and equal to zero for $x < y$. For rotating neutron stars, $\partial t_e/\partial f_e$ is not a function of t_e . Therefore, without loss of generality, we write $\partial t_e/\partial f_e(f_e)$. Then,

$$\frac{dn}{df_e} = \frac{\partial t_e}{\partial f_e}(f_e) \dot{n}(\mathcal{Z}(\mathcal{T}(z) - \tau_e(f_{\text{fix}}, f_e))) \Theta(z, f_e). \quad (3.41)$$

We now substitute this result in the formulas of the overlap function and the spectral function.

Inserting Equation (3.41) in (3.16), we obtain

$$\begin{aligned} \mathcal{N}(f, \Delta f, z) &= \int_0^z dz' \int_f^{f+\Delta f} df' [1+z'] \frac{dt_e}{df_e}(f'[1+z']) \\ &\quad \times \frac{dV_c}{dz'} \dot{n}(\mathcal{Z}(\mathcal{T}(z') - \tau_e(f_{\text{fix}}, f'[1+z']))) \Theta(z', f'[1+z']), \end{aligned} \quad (3.42)$$

which is the overlap function of a population of systems that start emitting at the same initial frequency f_{fix} . Similarly, inserting Equation (3.41) in (3.18), we obtain the spectral function

$$\begin{aligned} \Omega(f, \Delta f, \mathcal{N}_0) &= \frac{1}{\rho_c c^2} \int_{\bar{z}(f, \Delta f, \mathcal{N}_0)}^{z_{\text{max}}} [1+z]^{-1} \left. \frac{dE_e}{d \ln f_e} \right|_f \\ &\quad \times \dot{n}(\mathcal{Z}(\mathcal{T}(z) - \tau_e(f_{\text{fix}}, f[1+z]))) \Theta(z, f[1+z]) \frac{dt_e^L}{dz} dz. \end{aligned} \quad (3.43)$$

Performing the same approximation as in Equation (3.35), the overlap function can be simplified as

$$\begin{aligned} \mathcal{N}(f, \Delta f, z) &\approx \Delta f \int_0^z dz' [1+z'] \frac{dV_c}{dz'} \frac{dt_e}{df_e}(f[1+z']) \\ &\quad \times \dot{n}(\mathcal{Z}(\mathcal{T}(z') - \tau_e(f_{\text{fix}}, f[1+z']))) \Theta(z', f[1+z']), \end{aligned} \quad (3.44)$$

which is accurate for $\Delta f \ll f$.

For short-lived systems with fixed initial frequency

We now prove that if systems are assumed to evolve rapidly compared to cosmic time scales, then one obtains the definition of $\mathcal{N}(f, \Delta f, z)$ and $\Omega(f, \Delta f, \mathcal{N}_0)$ given in Equations (41) and

⁴One can prove it by partially differentiating Equation (3.81) with respect to t_e .

(44) of [207], respectively. Under this assumption, $\tau_e(f_{\text{fix}}, f_e)$, which is the time a system has evolved since formation, is much smaller than $\mathcal{T}(z)$, and therefore,

$$\dot{n}(\mathcal{Z}(\mathcal{T}(z) - \tau_e(f_{\text{fix}}, f_e))) \approx \dot{n}(\mathcal{Z}(\mathcal{T}(z))) = \dot{n}(z). \quad (3.45)$$

Using this, we can rewrite Equation (3.42) to obtain

$$\begin{aligned} \mathcal{N}(f, \Delta f, z) &\approx \int_0^z dz' \dot{n}(z') \frac{dV_c}{dz'} \times \int_{f[1+z']}^{[f+\Delta f][1+z']} \frac{dt_e}{df_e}(f_e) \Theta(z', f_e) df_e \\ &= \int_{z_{\text{low}}(f)}^z \tau_e(f, \Delta f, z') \dot{n}(z') \frac{dV_c}{dz'} dz'. \end{aligned} \quad (3.46)$$

Here, the function $\tau_e(f, \Delta f, z)$ gives the interval of time that a system, whose radiation is now observed with redshift z , spends emitting between observed frequencies f and $f + \Delta f$. Alternatively, inserting Equation (3.45) in (3.43), the spectral function becomes

$$\Omega(f) \approx \frac{1}{\rho_c c^2} \int_{\bar{z}(f, \Delta f, \mathcal{N}_0)}^{z_{\text{upp}}(f)} [1+z]^{-1} \left. \frac{dE_e}{d \ln f_e} \right|_f \dot{n}(z) \frac{dt_e^L}{dz} dz. \quad (3.47)$$

In Equations (3.46) and (3.47), the functions $z_{\text{low}}(f)$ and $z_{\text{upp}}(f)$ ensure that the integration is performed only where $\Theta(z, f[1+z])$ is non-zero.

Let us examine the spectral function of the total background, i.e., the one obtained by imposing no restriction ($\mathcal{N}_0 = 0$) in the number of signals per frequency bin. By inverting $\mathcal{N}(f, \Delta f, z) = 0$ (Equation (3.46)) with respect to the redshift, one obtains $\bar{z}(f, \Delta f, 0) = z_{\text{low}}(f)$. Replacing this in Equation (3.47), the canonical formula for the spectral function (used for example in [180, 207], and in the corrected version⁵ of [194]) is recovered,

$$\Omega(f) \approx \frac{1}{\rho_c c^2} \int_{z_{\text{low}}(f)}^{z_{\text{upp}}(f)} [1+z]^{-1} \left. \frac{dE_e}{d \ln f_e} \right|_f \dot{n}(z) \frac{dt_e^L}{dz} dz. \quad (3.48)$$

By carefully studying the limits of this integral, one realizes that the redshift functions $z_{\text{low}}(f)$ and $z_{\text{upp}}(f)$ are not exactly the same as the ones defined in Equations (37) and (38) of [207], or in Equations (10) and (9) of the corrected version of [194]. The difference, however, occurs only at the low-frequency part of the spectrum, at which the time scales needed for the systems to evolve are comparable to cosmic ones⁶.

3.4 Model for the ensemble of rotating neutron stars

3.4.1 Neutron star model

A neutron star is modeled as a rigid rotating ellipsoid of mass m . Its semiaxes with respect to the coordinate axes x , y , and z have lengths a , b , and c , respectively. The rotation occurs around the

⁵<http://arxiv.org/abs/1101.2762v3>

⁶In this regard, one should read Section 3.4.7; the plots in this section, for instance the ones in Figure (3.3), can be qualitatively compared with Figures (2) and (4) of [207].

3 Gravitational wave background from rotating neutron stars

z -axis at an angular velocity ω , which slowly decreases in time. Assuming a uniform density, the moment of inertia about the z -axis is

$$I_3 = I = \frac{m}{5}[a^2 + b^2]. \quad (3.49)$$

The *ellipticity* is defined by

$$\epsilon = [I_1 - I_2]/I_3, \quad (3.50)$$

where I_1 and I_2 are the moments of inertia about the x and y axes, respectively. The average ellipticity of the ensemble of neutron stars is very uncertain; reasonable values for ϵ can range from 10^{-8} to 10^{-4} . For such values, $\epsilon \approx [b - a]/a$, and, replacing it in (3.49), we can very accurately approximate

$$I \approx \frac{2ma^2}{5}. \quad (3.51)$$

We assume $m = 1.4 M_\odot$ (where M_\odot is the solar mass) and $a = 12$ km [123, 244], obtaining a moment of inertia of $I \approx 1.6 \times 10^{38}$ kg m² (see Sections 3.1.1 and 3.1.2 of [138] and references therein for a discussion about these values). Other mechanisms of gravitational wave emission, like dynamical bar-mode [29] or r-mode [168] instabilities, are not taken into account in this work.

A neutron star behaves like a rotating dipole magnet. The value of the magnetic field at the magnetic pole is B , where it forms an angle α (assumed, for simplicity, of $\alpha = \pi/2$) with the direction of the rotation. We do not consider any magnetic field decay (see Section 3.5 of [139] and references therein); B is the same during the entire life of the star.

With this toy model, one can infer the average value of B by looking at the rotating period and its time derivative (the so-called $P - \dot{P}$ diagram) of a pulsar catalogue (like the ATNF catalogue [150]). Without taking into account recycled pulsars, a reasonable average value for pulsars is $B = 10^8$ T. For magnetars, larger values (of $B \approx 10^{10}$ T) can be reached.

The maximum gravitational wave frequency at which a rotating neutron star can emit is estimated by

$$f_{\max}^{\text{escape}} = \frac{1}{\pi} \sqrt{\frac{Gm}{a^3}} \approx 3.3 \text{ kHz}. \quad (3.52)$$

Above this frequency, the material at the equator would have enough velocity to escape the gravitational potential, since the latter becomes lower than the centrifugal potential [123]. A gravitational wave frequency of 3.3 kHz corresponds to a rotation period of 0.6 ms, which is roughly the half of the fastest rotation period known in a pulsar [19]. A more realistic estimate of the maximum frequency (see Section 7.4 of [227]) is

$$f_{\max}^{\text{Roche}} = \left[\frac{2}{3} \right]^{3/2} f_{\max}^{\text{escape}} \approx 1.8 \text{ kHz}. \quad (3.53)$$

This frequency takes into account the deformation of the equatorial radius because of the rotation. From now on, we make the choice

$$f_{\max} = f_{\max}^{\text{escape}}, \quad (3.54)$$

which leads to the most optimistic results, regarding the detection of the background. The conclusions of this chapter would be unaffected, however, by choosing the alternative maximum frequency in Equation (3.53).

3.4.2 Formation rate of neutron stars

The amount of mass converted into stars per unit emitted interval of time per unit comoving volume between redshifts z and $z + dz$ is given by $\dot{\rho}(z)dz$, where $\dot{\rho}(z)$ is the *star formation rate*. The models for the star formation rate [144, 186, 1, 236, 93, 162, 62, 254] usually present a similar shape: $\dot{\rho}(z)$ increases from its local value (at $z = 0$) until $z \approx 1$ or 2, and then decays, reaching negligible values for redshifts larger than 5 or 6. For this reason, the range of redshifts considered in the calculations is $[0, z_{\max}]$, with

$$z_{\max} = 5. \quad (3.55)$$

All calculations shown in the plots of Section 3.5 are obtained by assuming the star formation rate given in Section 5.4 of [1],

$$\dot{\rho}(z) = h_0 \frac{a + bz}{1 + \left[\frac{z}{c}\right]^d} M_{\odot} \text{yr}^{-1} \text{Mpc}^{-3}, \quad (3.56)$$

with the parameters found in Table I of [93], namely $(a, b, c, d) = (0.0170, 0.13, 3.3, 5.3)$, and $h_0 = H_0/[100 \text{ km s}^{-1} \text{Mpc}^{-1}] = 0.742$. In Section 3.6.2 we comment on the fact that the specific choice of star formation rate does not affect the spectral function significantly. Furthermore, the results would not be affected by the use of a constant rate.

Only a fraction λ of all stars formed become neutron stars, so the rate is

$$\dot{n}(z) = \lambda \dot{\rho}(z). \quad (3.57)$$

The fraction of stars formed with masses between m and $m + dm$ is $\Phi(m)dm$, where $\Phi(m)$ is the *initial mass function*. We assume a Salpeter initial mass function [211],

$$\Phi(m) = Am^{-2.35}, \quad (3.58)$$

where the value of the normalization constant A turns out to be unnecessary, as we now see. The fraction of stellar mass converted into neutron stars is

$$\lambda = \frac{\int_{8 M_{\odot}}^{20 M_{\odot}} \Phi(m) dm}{\int_{0.1 M_{\odot}}^{100 M_{\odot}} m \Phi(m) dm} = 5 \times 10^{-3} M_{\odot}^{-1}. \quad (3.59)$$

The denominator is the average mass of a star (considering all stars with masses between $0.1 M_{\odot}$ and $100 M_{\odot}$), and the numerator is the fraction of stars that can be progenitors of neutron stars (namely stars with masses between $8 M_{\odot}$ and $20 M_{\odot}$). The value of λ tells us that, for each $10^3 M_{\odot}$ of gas converted into stellar mass, 5 neutron stars are produced. We assume that this fraction is the same at all redshifts.

3.4.3 Energy evolution

The rotational energy of a system is given by

$$E_{e,\text{rot}} = \frac{1}{2} I \omega_e^2. \quad (3.60)$$

3 Gravitational wave background from rotating neutron stars

For convenience, we write the angular velocity ω_e in terms of the frequency of the emitted gravitational waves, f_e , which fulfills

$$\omega_e = \pi f_e. \quad (3.61)$$

Differentiating (3.60) with respect to the time, and using (3.61), one obtains

$$\frac{dE_{e,\text{rot}}}{dt_e} = \pi^2 I f_e \frac{df_e}{dt_e}. \quad (3.62)$$

In the following we show that df_e/dt_e is negative, thus, $dE_{e,\text{rot}}/dt_e$ is also negative; the system loses rotational energy with the time. This energy loss is due to the emission of both electromagnetic and gravitational radiation.

Suppose that the system lost energy only via the magnetic dipole emission. Such a system is studied in [54]. Rewriting Equation (15) of that paper with our notation,

$$\frac{dE_{e,\text{md}}}{dt_e} = -\frac{2\pi^5 a^6 B^2 \sin^2(\alpha)}{3c^3 \mu_0} f_e^4 = -\frac{\pi^2 I}{2\delta_{\text{md}}} f_e^4, \quad (3.63)$$

where the index ‘md’ stands for *magnetic dipole* and

$$\delta_{\text{md}} = \frac{3\mu_0 c^3 I}{4\pi^3 B^2 a^6 \sin^2(\alpha)}. \quad (3.64)$$

Here, μ_0 is the magnetic permeability of the vacuum. We have used that $B = \mu_0 H$, where H is called R_1 in [54]. The magnetic field is often expressed in Gaussian units [201, 154]. For clarity, recall that $B_{\text{Gauss}} = \sqrt{\frac{4\pi}{\mu_0}} B$. Equation (3.63) gives the rate at which the system loses energy by emitting electromagnetic waves.

Suppose now that the system emitted only gravitational radiation. This system is studied, for example, in Section 4.2.1 of [147]. Rewriting Equation (4.227) of [147] with our notation,

$$\frac{dE_{e,\text{gr}}}{dt_e} = -\frac{32\pi^6 G \epsilon^2 I^2}{5c^5} f_e^6 = -\frac{\pi^2 I}{4\delta_{\text{gr}}} f_e^6, \quad (3.65)$$

where the index ‘gr’ stands for *gravitational radiation*, and

$$\delta_{\text{gr}} = \frac{5c^5}{128\pi^4 G \epsilon^2 I}. \quad (3.66)$$

Equation (3.65) gives the rate at which the system loses energy by emitting gravitational waves.

The system we study loses energy via both magnetic dipole emission and gravitational radiation. Thus, the total loss of energy (which is a loss in rotational energy) fulfills

$$\frac{dE_{e,\text{rot}}}{dt_e} = \frac{dE_{e,\text{md}}}{dt_e} + \frac{dE_{e,\text{gr}}}{dt_e}. \quad (3.67)$$

Rewriting Equation (3.67) in terms of Equations (3.62), (3.63), and (3.65), we obtain

$$\frac{df_e}{dt_e} = -\frac{1}{2\delta_{\text{md}}} f_e^3 - \frac{1}{4\delta_{\text{gr}}} f_e^5, \quad (3.68)$$

3.4 Model for the ensemble of rotating neutron stars

where we see that the frequency of the rotation (written in terms of gravitational wave frequencies) decreases with time. The energy lost by the rotating star is the energy gained by the gravitational waves, so

$$\frac{dE_e}{dt_e} = -\frac{dE_{e,\text{gr}}}{dt_e} = \frac{\pi^2 I}{4\delta_{\text{gr}}} f_e^6 \quad (3.69)$$

is the amount of gravitational wave energy produced by a system per unit time. The amount of gravitational wave energy produced by one system contained in an infinitesimal logarithmic interval of frequency $d \ln f_e$ is

$$\frac{dE_e}{d \ln f_e} = f_e \frac{dE_e}{df_e} = f_e \left| \frac{dE_e}{dt_e} \left[\frac{df_e}{dt_e} \right]^{-1} \right|, \quad (3.70)$$

where we have used the chain rule. Using Equations (3.68) and (3.69),

$$\frac{dE_e}{d \ln f_e} = \frac{\pi^2 I f_e^4}{f_C^2 + f_e^2}, \quad (3.71)$$

where we have introduced the *cut frequency*,

$$f_C = \sqrt{\frac{2\delta_{\text{gr}}}{\delta_{\text{md}}}}. \quad (3.72)$$

At this frequency, both terms on the right side of Equation (3.68) become equal; this is the frequency at which both mechanisms of energy loss “cut” each other. The absolute value in Equation (3.70) is used because dE_e must be a positive quantity; it represents the amount of gravitational wave energy within a logarithmic frequency interval, regardless of whether the energy of the system increases or decreases with the frequency.

The three main expressions of this section are in Equations (3.68), (3.69), and (3.71). They can be rewritten, using (3.1), in terms of observed frequencies. The resulting formulas are:

$$\left. \frac{df_e}{dt_e} \right|_f = -\frac{1}{2\delta_{\text{md}}} f^3 [1+z]^3 - \frac{1}{4\delta_{\text{gr}}} f^5 [1+z]^5, \quad (3.73)$$

$$\left. \frac{dE_e}{dt_e} \right|_f = \frac{\pi^2 I}{4\delta_{\text{gr}}} f^6 [1+z]^6, \quad (3.74)$$

and

$$\left. \frac{dE_e}{d \ln f_e} \right|_f = \frac{\pi^2 I f^4 [1+z]^4}{f_C^2 + f^2 [1+z]^2}, \quad (3.75)$$

respectively.

We can distinguish two frequency intervals: one where the magnetic dipole emission dominates (let us call it the *md-range*) and one where the gravitational radiation dominates (the *gr-range*). The frequency at which both mechanisms are equally dominant is f_C . For simplicity, some of the next calculations are performed in the two frequency intervals separately. The energy spectrum can be approximated by

$$\left. \frac{dE_e}{d \ln f_e} \right|_f \approx \frac{\pi^2 I}{f_C^2} f^4 [1+z]^4 \quad (3.76)$$

3 Gravitational wave background from rotating neutron stars

in the md-range, and by

$$\left. \frac{dE_e}{d \ln f_e} \right|_f \approx \pi^2 I f^2 [1 + z]^2 \quad (3.77)$$

in the gr-range.

The *braking index* n_b is defined by [138]

$$\frac{df_e}{dt_e} = -K(f_e)^{n_b}, \quad (3.78)$$

where K is a constant. Equation (3.68) shows that the braking index is equal to 3 in the md-range and equal to 5 in the gr-range for all neutron stars. Observational measurements of the braking index, however, obtain very different values. For example, in Table 4 of [64] n_b is smaller than 3 for some known pulsars. Alternatively, the braking index measured in other pulsars can be orders of magnitude larger than 3, or even negative [99]. The results of this chapter would differ considerably if one used models with different braking indices. The consideration of such other models is out of the purposes of this work.

3.4.4 Frequency evolution

We now calculate the lapse of time $\tau_e(f_{e,1}, f_{e,2})$ that a system spends emitting within a certain frequency interval $[f_{e,1}, f_{e,2}]$. This is achieved by integrating Equation (3.68), which leads to the analytical formula

$$\tau_e(f_{e,1}, f_{e,2}) = \delta_{\text{md}} \left[f_{e,2}^{-2} - f_{e,1}^{-2} + f_C^{-2} \ln \left(\frac{f_{e,2}^2 [f_C^2 + f_{e,1}^2]}{f_{e,1}^2 [f_C^2 + f_{e,2}^2]} \right) \right]. \quad (3.79)$$

A system that starts emitting at an initial frequency f_{ini} , needs an interval of time $\tau_e(f_{\text{ini}}, f_e)$ to reach the frequency f_e .

It is useful to obtain a function $f_{\text{ini}} = f_{\text{ini}}(f_e, \Delta t_e)$, that gives the frequency at which a system, that now emits at f_e , was emitting an interval of time Δt_e before. One cannot invert Equation (3.79) with respect to f_{ini} analytically. For this reason, it is more convenient to approximate $\tau_e(f_{\text{ini}}, f_e)$ by

$$\tau_e(f_{\text{ini}}, f_e) = \begin{cases} \delta_{\text{gr}} [f_e^{-4} - f_{\text{ini}}^{-4}] & f_C \leq f_e < f_{\text{ini}} \\ \delta_{\text{gr}} [f_C^{-4} - f_{\text{ini}}^{-4}] + \delta_{\text{md}} [f_e^{-2} - f_C^{-2}] & f_e < f_C < f_{\text{ini}} \\ \delta_{\text{md}} [f_e^{-2} - f_{\text{ini}}^{-2}] & f_e < f_{\text{ini}} \leq f_C \end{cases}. \quad (3.80)$$

With this approximation, one can analytically invert $\tau(f_{\text{ini}}, f_e) = \Delta t_e$ with respect to f_{ini} , obtaining

$$f_{\text{ini}}(f_e, \Delta t_e) = \begin{cases} \left[f_e^{-4} - \frac{\Delta t_e}{\delta_{\text{gr}}} \right]^{-1/4} & f_C \leq f_e \text{ \& } f_e < \left[\frac{\Delta t_e}{\delta_{\text{gr}}} \right]^{-1/4} \\ \left[f_C^{-2} [2f_e^{-2} - f_C^{-2}] - \frac{\Delta t_e}{\delta_{\text{gr}}} \right]^{-1/4} & \left[f_C^{-2} + \frac{\Delta t_e}{\delta_{\text{md}}} \right]^{-1/2} < f_e < f_C \text{ \& } f_e < \left[\frac{1}{2} f_C^{-2} + \frac{\Delta t_e}{\delta_{\text{md}}} \right]^{-1/2} \\ \left[f_e^{-2} - \frac{\Delta t_e}{\delta_{\text{md}}} \right]^{-1/2} & f_e \leq \left[f_C^{-2} + \frac{\Delta t_e}{\delta_{\text{md}}} \right]^{-1/2} \end{cases}. \quad (3.81)$$

In this equation, the conditions $f_e < \left[\frac{1}{2} f_C^{-2} + \frac{\Delta t_e}{\delta_{\text{md}}} \right]^{-1/2}$ and $f_e < \left[\frac{\Delta t_e}{\delta_{\text{gr}}} \right]^{-1/4}$ are introduced to avoid unphysical values for f_{ini} .

3.4.5 Initial frequency distribution

We consider three simple initial frequency distributions $p_{\text{ini}}(f_{\text{ini}})$ in the calculations.

The first one was already introduced in Equation (3.36). Let us call it *Distribution 0*.

Distribution 1 is obtained from the log-normal initial period distribution given in [16],

$$p_P(P_{\text{ini}}) = \frac{1}{\sqrt{2\pi}\sigma P_{\text{ini}}} \exp\left(-\frac{[\ln(P_{\text{ini}}/s) - \mu]^2}{2\sigma^2}\right), \quad (3.82)$$

where $\mu = \ln(0.005)$, $\sigma = 0.3/\log_{10}(e) \approx 0.69$. This distribution hence assumes that the average initial spin period is of 5 ms. The initial period, P_{ini} , is related to the initial spin frequency f_{ini} (in terms of gravitational wave frequencies) by

$$P_{\text{ini}} = \frac{2}{f_{\text{ini}}}. \quad (3.83)$$

Therefore,

$$p_{\text{ini}}(f_{\text{ini}}) = \frac{2}{f_{\text{ini}}^2} p_P\left(\frac{2}{f_{\text{ini}}}\right) \quad (3.84)$$

is the corresponding probability density function of the initial frequency.

Lastly, *Distribution 2* is obtained from the normal initial period distribution given in [64],

$$p_P(P_0) = \frac{1}{\sqrt{2\pi}\sigma} \exp\left(-\frac{[P_0 - \mu]^2}{2\sigma^2}\right), \quad (3.85)$$

with $\mu = 300$ ms and $\sigma = 150$ ms. Similar distributions to this one are used in [196] and in [185]. To obtain the corresponding probability density function of the initial frequency, one can again use Equation (3.84).

Initial frequency distributions like Distributions 0 and 1 are more favorable for the detection of the background than Distribution 2. Some studies do predict large initial frequencies for the population of magnetars [238]; on the other hand, an initial period of 5 ms (like the average of Distribution 1) or shorter may be considered too small to properly describe the ensemble of known pulsars [196, 175]. Another possible distribution, used in [77], could be a Gaussian distribution like that of Equation (3.85) with $\mu = 50$ ms and $\sigma = 50$ ms. This distribution leads to intermediate results between those of Distributions 1 and 2. Regarding gravitars, our current knowledge about their population statistics is so poor that any of the previous distributions is equally plausible.

3.4.6 Magnetic field and ellipticity distributions

Some of the calculations in Section 3.5 are performed using a magnetic field distribution and an ellipticity distribution. The formulas for the overlap function (Equation (3.35)) and the spectral

3 Gravitational wave background from rotating neutron stars

function (Equation (3.33)) can be modified to take into account these distributions. The overlap function becomes

$$\hat{\mathcal{N}}(f, \Delta f, z) = \int_{\epsilon_{\min}}^{\epsilon_{\max}} d\epsilon p_{\epsilon}(\epsilon) \int_{B_{\min}}^{B_{\max}} dB p_B(B) \mathcal{N}(f, \Delta f, z). \quad (3.86)$$

Inverting $\hat{\mathcal{N}}(f, \Delta f, z) = \mathcal{N}_0$ with respect to the redshift, one obtains a function $\hat{z}(f, \Delta f, \mathcal{N}_0)$. This function can be used as a lower limit of the redshift integral in (3.33), to obtain $\hat{\Omega}'(f, \Delta f, \mathcal{N}_0)$. The spectral function is obtained by solving

$$\hat{\Omega}(f, \Delta f, \mathcal{N}_0) = \int_{\epsilon_{\min}}^{\epsilon_{\max}} d\epsilon p_{\epsilon}(\epsilon) \int_{B_{\min}}^{B_{\max}} dB p_B(B) \Omega'(f, \Delta f, \mathcal{N}_0). \quad (3.87)$$

In these two formulas, the magnetic field and ellipticity distributions are assumed to be independent. We point out that these distributions could in fact be correlated; as an example, in Section 3.5.3 we mention that a high magnetic field can increase the ellipticity. We now specify the magnetic field and ellipticity distributions used.

The probability density function of the magnetic field is taken from [16] (also used in [170, 111]),

$$p_B(B) = \frac{1}{\sqrt{2\pi}\sigma B} \exp\left(-\frac{[\ln(B/\text{T}) - \mu]^2}{2\sigma^2}\right), \quad (3.88)$$

with $\mu = \ln(10^{8.35})$ and $\sigma = 0.4/\log_{10}(e) \approx 0.9$. This means that the average magnetic field is of $10^{8.35}$ T. The distribution is normalized to unity between a minimum value of $B_{\min} = 10^{7.2}$ T and a maximum value of $B_{\max} = 10^{9.8}$ T.

The probability density function of the ellipticity is taken from [170],

$$p_{\epsilon}(\epsilon) = A \frac{\exp\left(-\frac{\epsilon}{\tau}\right)}{\tau \left[1 - \exp\left(-\frac{\epsilon_{\max}}{\tau}\right)\right]}, \quad (3.89)$$

where τ is the solution of

$$\bar{\epsilon} = \tau - \frac{\epsilon_{\max}}{\exp\left(\frac{\epsilon_{\max}}{\tau}\right) - 1}. \quad (3.90)$$

The values for $\bar{\epsilon}$ and ϵ_{\max} are 10^{-7} and 2.5×10^{-6} , respectively. The normalization constant A is obtained by imposing

$$\int_{\epsilon_{\min}}^{\epsilon_{\max}} p_{\epsilon}(\epsilon) d\epsilon = 1, \quad (3.91)$$

where the minimum ellipticity is $\epsilon_{\min} \approx 0$.

3.4.7 Minimum and maximum frequencies

In Section 3.3.3, a formula for the spectral function is obtained (in Equation (3.43)), assuming a fixed initial frequency; $\Omega(f, \Delta f, \mathcal{N}_0)$ contains the function $\Theta(z, f[1+z])$, defined in Equation (3.40), that determines the redshifts and observed frequencies of the systems that can contribute to the background. Introducing (3.1) in (3.40), one gets

$$\Theta(z, f[1+z]) = \theta(\mathcal{T}(z) - \tau(f_{\text{fix}}, f[1+z]))\theta(\tau(f_{\text{fix}}, f[1+z]) - 0). \quad (3.92)$$

We now study the limits that this function sets on the possible observed frequencies and redshifts of the gravitational waves, for the ensemble of rotating neutron stars. For that, the fixed initial frequency can be replaced by the maximum frequency (in Equation (3.54)), i.e. $f_{\text{fix}} = f_{\text{max}}$.

The first Heaviside step function in (3.92) becomes zero for a certain observed frequency $f = f_{\text{low}}(z)$. This function gives the minimum observed frequency that a gravitational wave with redshift z can have. Using Equations (3.25) and (3.80), the condition $\mathcal{T}(z) = \tau(f_{\text{max}}, f_{\text{low}}(z)[1+z])$ leads to

$$f_{\text{low}}(z) = \begin{cases} f_1(z) & f_C \leq f_1(z) \\ f_2(z) & f_1(z) < f_C < f_{\text{max}} \\ f_3(z) & f_{\text{max}} \leq f_C \end{cases}, \quad (3.93)$$

where

$$f_1(z) = \left[\frac{\mathcal{T}(z)}{\delta_{\text{gr}}} + f_{\text{max}}^{-4} \right]^{-1/4} [1+z]^{-1}, \quad (3.94)$$

$$f_2(z) = \left[\frac{\mathcal{T}(z) - \delta_{\text{gr}}[f_C^{-4} - f_{\text{max}}^{-4}]}{\delta_{\text{md}}} + f_C^{-2} \right]^{-1/2} [1+z]^{-1}, \quad (3.95)$$

and

$$f_3(z) = \left[\frac{\mathcal{T}(z)}{\delta_{\text{md}}} + f_{\text{max}}^{-2} \right]^{-1/2} [1+z]^{-1}. \quad (3.96)$$

One should notice that $f_{\text{low}}(z)$ is an observed frequency, unlike f_C and f_{max} , that are emitted frequencies; the e -index in the two latter quantities has been omitted to ease the notation.

The second Heaviside step function in Equation (3.92) becomes zero when evaluated at the observed frequency $f = f_{\text{upp}}(z)$. This function gives the maximum observed frequency that a gravitational wave with redshift z can have. Using Equation (3.80), the condition $\tau(f_{\text{max}}, f_{\text{upp}}(z)[1+z]) = 0$ leads to

$$f_{\text{upp}}(z) = f_{\text{max}}[1+z]^{-1}. \quad (3.97)$$

Again, notice that f_{upp} is an observed frequency, whereas f_{max} is an emitted frequency.

With the previous results, we can calculate the maximum and minimum observed frequencies possible. The maximum observed frequency, as Equation (3.97) clearly shows, is achieved at redshift 0, and is precisely f_{max} . On the other hand, to find the minimum observed frequency, one has to minimize Equation (3.93). The redshift at which $f_{\text{low}}(z)$ is minimum is the solution of

$$\left[\mathcal{T}(z) + \frac{\delta_{\text{md}}}{f_{\text{max}}^2} \right]^{-1} \frac{d\mathcal{T}}{dz}(z) + 2[1+z]^{-1} = 0, \quad (3.98)$$

if $f_C \leq f_1(z)$, of

$$\left[\mathcal{T}(z) + \frac{\delta_{\text{md}}^2}{4\delta_{\text{gr}}} + \frac{\delta_{\text{gr}}}{f_{\text{max}}^4} \right]^{-1} \frac{d\mathcal{T}}{dz}(z) + 2[1+z]^{-1} = 0, \quad (3.99)$$

if $f_1(z) < f_C < f_{\text{max}}$, and of

$$\left[\mathcal{T}(z) + \frac{\delta_{\text{gr}}}{f_{\text{max}}^4} \right]^{-1} \frac{d\mathcal{T}}{dz}(z) + 4[1+z]^{-1} = 0, \quad (3.100)$$

3 Gravitational wave background from rotating neutron stars

if $f_{\max} \leq f_C$. As a good approximation, one can assume that $\mathcal{T}(z) \gg \delta_{\text{md}} f_{\max}^{-2}$ and $\mathcal{T}(z) \gg \delta_{\text{gr}} f_{\max}^{-4}$. Doing this, Equations (3.98) and (3.100) depend only on cosmological parameters, and their numerical solutions are

$$z_{\text{gr}} \approx 3.39, \quad (3.101)$$

and

$$z_{\text{md}} \approx 1.54, \quad (3.102)$$

respectively. The solution of Equation (3.99) will depend on the values of the astrophysical parameters (B , ϵ , et cetera), but must lie between z_{md} and z_{gr} . As an example, for a rotating neutron star with $B = 10^8$ T and $\epsilon = 10^{-7}$, the cut frequency is $f_C > f_{\max}$, so the minimum observed frequency is given by $f_3(z_{\text{md}}) \approx 86$ mHz.

The upper plot in Figure 3.2 shows the redshifts and observed frequencies that the gravitational waves from the ensemble of gravitars with ellipticity $\epsilon = 10^{-7}$ can have. The lower plot is the same, but only for the unresolvable waves (those that produce an overlap larger than $\mathcal{N}_0 = 1$ in a frequency bin $\Delta f = 1 \text{ yr}^{-1}$). A point in the graph tells the present redshift observed in a gravitational wave emitted by a gravitar, and the gray scale tells the redshift of the waves emitted by that same gravitar at the instant of its formation. Figure 3.3 is analogous to 3.2, but for the ensemble of rotating neutron stars with $B = 10^8$ T and $\epsilon = 10^{-7}$.

3.5 Results

3.5.1 Gravitars

Let us first give a definition of gravitar: it is a rotating neutron star that emits gravitational waves at a frequency $f_e > f_C$, i.e., the dominating mechanism for the loss of rotational energy is the emission of gravitational waves (see the definition of the cut frequency in Section 3.4.3).

The gravitar limit is an upper limit on the gravitational wave background produced by rotating neutron stars. For simplicity, and in order to obtain a robust upper limit, we obtain the gravitar limit under the following assumptions: all neutron stars are gravitars; all gravitars start emitting with the same initial frequency; this frequency is infinite; and the spectrum can be extended to arbitrarily low frequencies, as if signals had an infinite amount of time to evolve. Under these unrealistic assumptions, the energy spectrum can be approximated by Equation (3.77), and the spectral function of the gravitar limit (using Equation (3.47)) becomes

$$\Omega_{\text{GL}}(f) = \frac{\pi^2 I}{\rho_c c^2 H_0} f^2 \int_0^{z_{\max}} \dot{n}(z) \mathcal{E}^{-1}(z) dz. \quad (3.103)$$

Using the star formation rate of Equation (3.56), the background yielded by such an ensemble would produce a SNR (Equation (3.22)) of ~ 1.3 for aLIGO, after one year of observation. We use the gravitar limit as a reference in the following plots.

We now justify that the background of rotating neutron stars cannot be larger than the gravitar limit. The spectral function in Equation (3.103) depends only on the rate $\dot{n}(z)$ and on the average moment of inertia I . The latter is well constrained by present neutron star equations of state. The abundance and even the existence of gravitars is unknown, but certainly not all neutron stars are gravitars, so the rate of gravitars must certainly be smaller than $\dot{n}(z)$. Equation (3.103) is obtained by assuming that $f_C = 0$. If the cut frequency were not zero, at frequencies lower

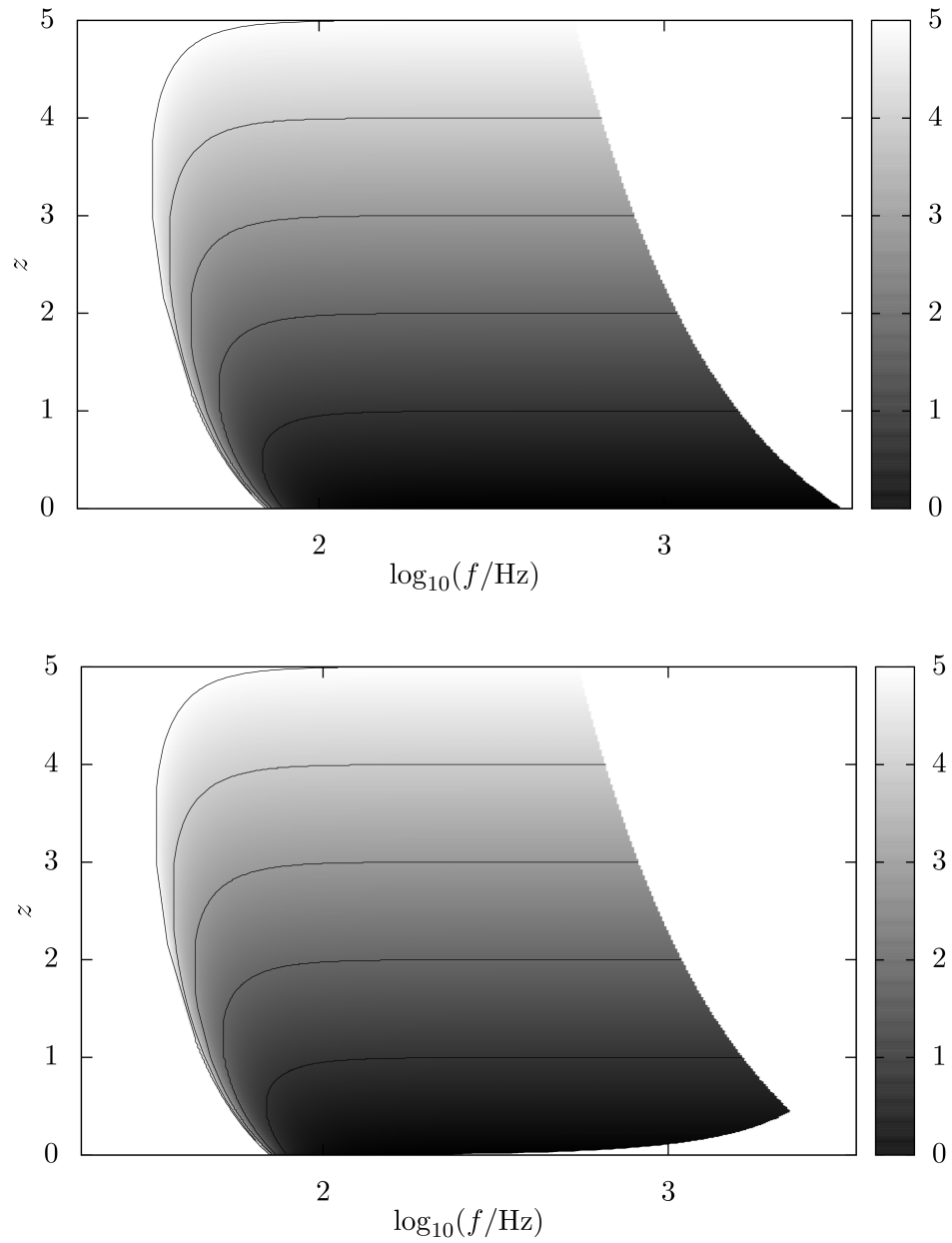


Figure 3.2: Redshift versus observed frequency of the gravitational waves produced by the ensemble of gravitars, assuming an ellipticity of $\epsilon = 10^{-7}$. The vertical axis gives the redshift of the gravitational waves observed today (redshift at present). Those waves were emitted by gravitars that started radiating at the redshifts given by the gray scale (redshift of formation). The solid lines follow points of equal redshifts of formation (corresponding, from bottom to top, to redshifts 1, 2, 3, 4, and 5). The upper plot accounts for all signals in the universe, whereas the lower plot accounts only for unresolvable signals.

3 Gravitational wave background from rotating neutron stars

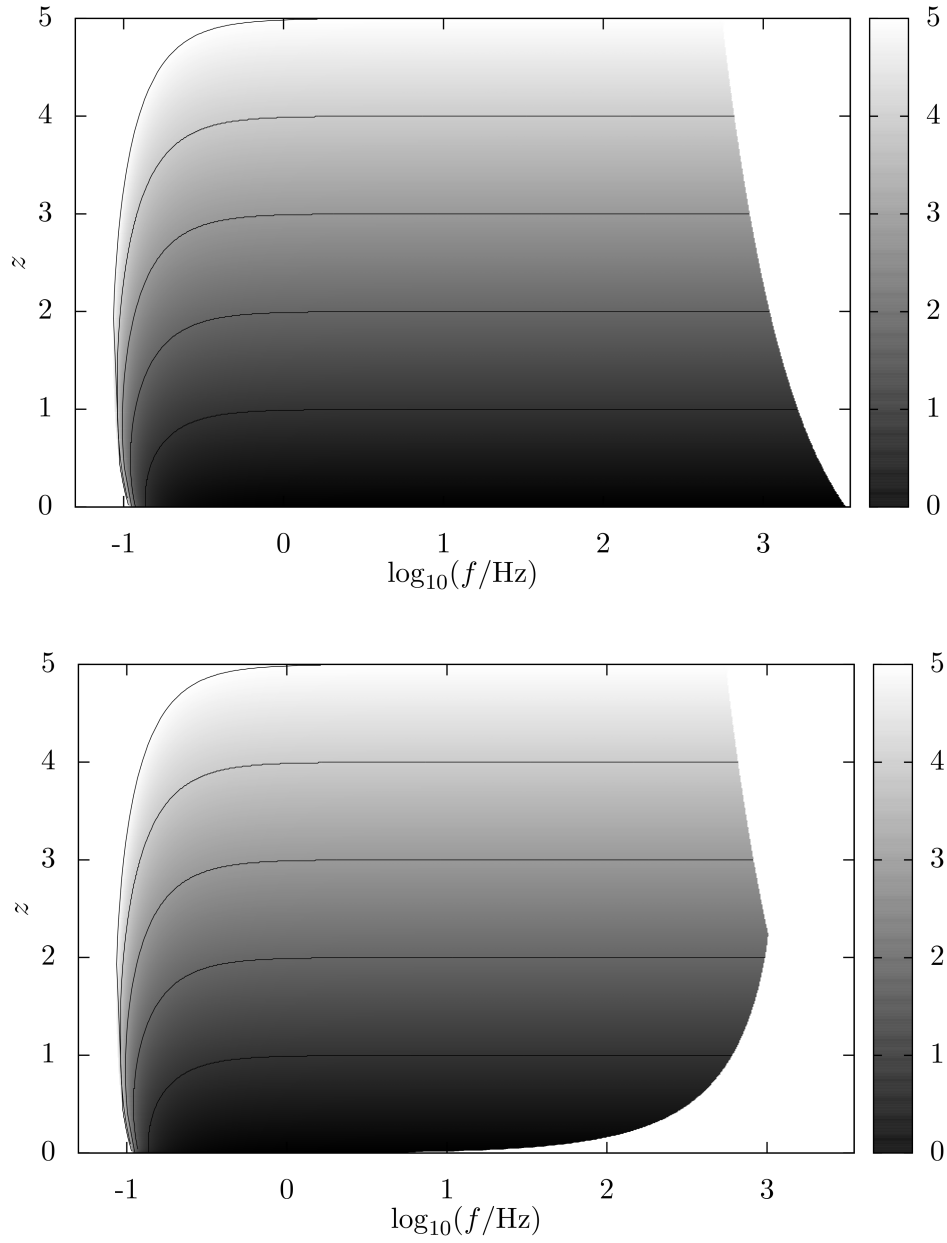


Figure 3.3: Same as Figure 3.2, but for the ensemble of rotating neutron stars with magnetic field $B = 10^8$ T and ellipticity $\epsilon = 10^{-7}$.

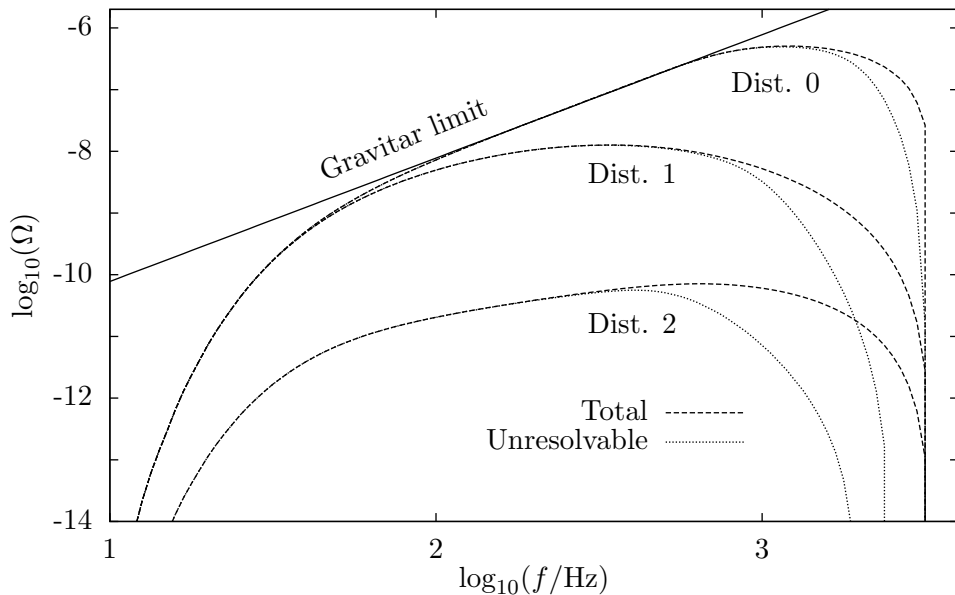


Figure 3.4: Spectral function, versus observed frequency, of the total and unresolvable backgrounds produced under the assumption that all rotating neutron stars are gravitars, i.e. neutron stars which spin down primarily by emitting gravitational waves. The gravitar limit is also shown, as a robust upper limit of the background from rotating neutron stars. The background is calculated by using three different initial frequency distributions (see Section 3.4.5). The unresolvable background is calculated with $\mathcal{N}_0 = 1$ and $\Delta f = 1 \text{ yr}^{-1}$.

than f_C the spectral function would be proportional to f^4 , reaching its maximum around the cut frequency. There is hence no choice of the parameters B , ϵ , and α , and there is no frequency at which the spectral function can be larger than (3.103), as long as the rate and the momentum of inertia (as well as the cosmological parameters) remain unchanged.

If all rotating neutron stars were gravitars, the background they would produce would be different than the gravitar limit. First, their initial frequency is finite, and second, they had a finite amount of time to evolve, so they cannot emit at arbitrarily low frequencies. In Figure 3.4, besides the gravitar limit, we show the background that would be produced if all rotating neutron stars were gravitars, assuming the three initial frequency distributions considered in Section 3.4.5. The curves for Distribution 0 are obtained by using Equation (3.43), whereas those for Distributions 1 and 2 are obtained by evaluating Equation (3.33). In all cases, the star formation rate is the one in Equation (3.56), the magnetic field is approximately zero, and the ellipticity follows the distribution given in Equation (3.89). The obtained background turns out to be almost entirely unresolvable.

The SNR produced by the total background, assuming Distribution 0, is of 0.64, 6.6×10^2 , and 3.5×10^2 , for aLIGO, ETB, and ETD, respectively (assuming one year of observation). With Distribution 1, these numbers are 0.56, 4.1×10^2 , and 1.8×10^2 . Finally, with Distribution 2, the values of SNR are 4.0×10^{-3} , 2.0, and 0.81. We can thus claim that aLIGO is not sensitive enough to either detect the background of rotating neutron stars, or to set upper limits on the

3 Gravitational wave background from rotating neutron stars

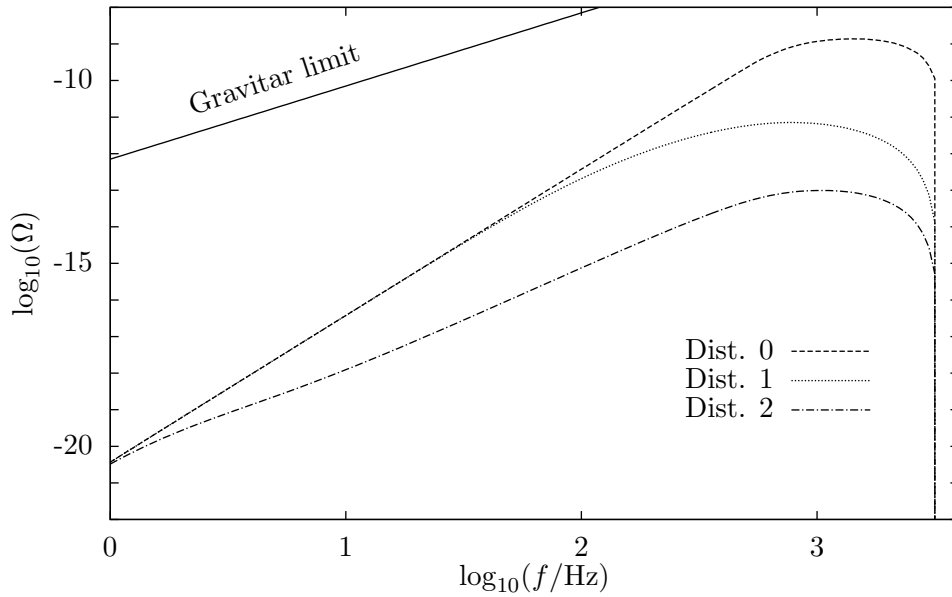


Figure 3.5: Spectral function, versus observed frequency, of the total background produced by rotating neutron stars, assuming the magnetic field distribution of Equation (3.88) (which is taken from [16]) and the ellipticity distribution of Equation (3.89) (from [170]). Three initial frequency distributions are used (see Section 3.4.5). None of the present or planned gravitational wave detectors is sensitive enough to observe such a background.

fraction of neutron stars that are gravitars. The SNR for BBO and DECIGO is in all cases much smaller than 1. Obviously, not all neutron stars are gravitars; if only a certain fraction of the population of neutron stars were gravitars, the values of the spectral function in Figure 3.4, as well as the values of SNR, would be multiplied by that fraction. Hence, if only 1% of neutron stars were gravitars, they would produce a background that could be detected by ETB with SNR 6.6, assuming Distribution 0, and 4.1, assuming Distribution 1. On the other hand, with Distribution 2, even if all neutron stars were gravitars the detection statistics of all detectors are below the detection threshold.

3.5.2 A more realistic expectation

In Figure 3.5, we show the spectral function of the total background of rotating neutron stars, calculated by assuming the magnetic field distribution of Equation (3.88), and the ellipticity distribution of (3.89). The star formation rate used is the one of Equation (3.56). The obtained SNR for such a background is much smaller than 1, for all detectors considered.

3.5.3 Upper limit for magnetars

There are two facts that make the detection of the magnetars background difficult: First, since they have a larger magnetic field, the electromagnetic emission dominates over the gravitational wave emission. Second, the fraction of magnetars is believed to be of order 10% of the total

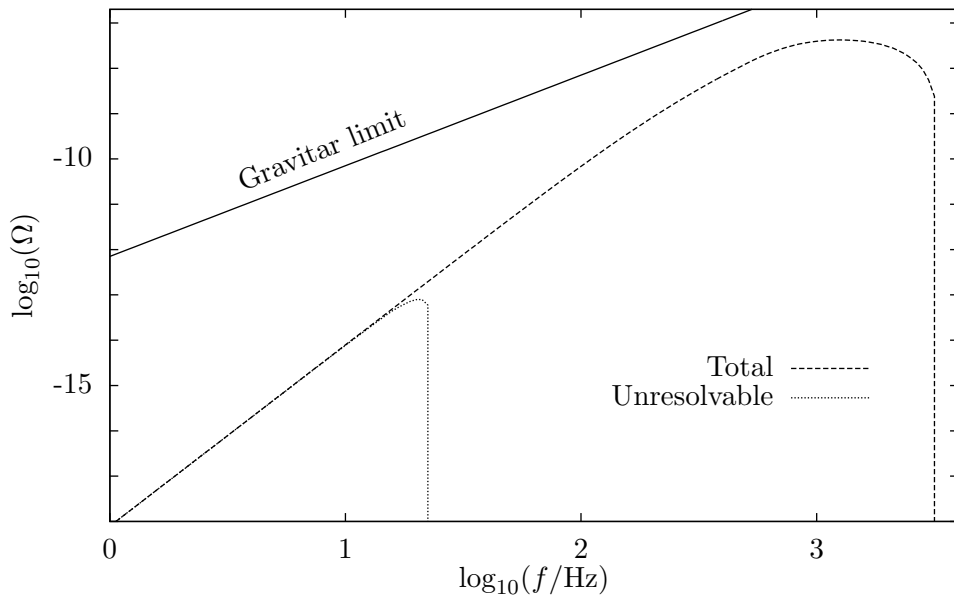


Figure 3.6: Spectral function, versus observed frequency, of the total and unresolvable backgrounds produced by magnetars. The rate of magnetars is assumed to be 10% of the one of neutron stars, the average magnetic field is $B = 10^{10}$ T, and the average ellipticity, $\epsilon = -6.4 \times 10^{-4}$. This corresponds to the TD model described in [154], which is the most optimistic model (regarding the detection) considered in that paper. Other models predict levels of background several orders of magnitude lower. The total background plotted here can thus be considered an upper limit for the background of magnetars.

population of neutron stars [198, 185]. On the other hand, large magnetic fields can deform a neutron star [47], increasing its ellipticity. If the ellipticity is large enough, the contribution of gravitational waves can be important. Furthermore, the larger the magnetic field, the faster systems evolve towards lower frequencies, entering the band of highly sensitive detectors like BBO and DECIGO. We now investigate if the background of magnetars has a good chance to be detected.

In [154], different models for the population of magnetars are compared. One of the models, with a dominating toroidal magnetic field, produces a gravitational wave background that can be detected by ET. This model predicts a poloidal magnetic field of $B = 10^{10}$ T and an ellipticity $\epsilon = -6.4 \times 10^{-4}$. In Figure 3.6 we show the background produced with this model, assuming that all magnetars start emitting gravitational waves of the same frequency, f_{\max} ⁷. Other models in [154] predict levels of background orders of magnitude lower than the one in Figure 3.6. The total background shown in this figure can thus be considered an optimistic upper limit for the background of magnetars.

The SNR with which the total background of Figure 3.6 would be detected by ETB and ETD is of 14 and 11, respectively (for one year of observation time). For aLIGO, as well as for BBO

⁷Some studies predict that magnetars are formed with fast initial spins [238]. Since we are interested in obtaining an upper limit, we assume that all magnetars start emitting at f_{\max} .

and DECIGO, the values of SNR are negligible. On the other hand, the SNR of the unresolvable background is lower than 10^{-2} for all detectors. This means that the magnetars background is resolvable in the band of ET.

3.5.4 Detection prospects

In Section 3.5.1, we have claimed that the background produced by gravitars could be detected even if they constituted only a 1% of the neutron star population. Nevertheless, the existence of gravitars is questionable. We now show that similar detection claims can be achieved for certain (plausible) choices of B and ϵ .

In Figures 3.7 and 3.8, the total and unresolvable backgrounds are plotted, respectively, assuming that all rotating neutron stars have the same magnetic field and ellipticity. These plots show that the spectral function is larger for smaller magnetic fields and larger ellipticities, as it was expected. Furthermore, with larger magnetic fields, lower frequencies are achieved, and a bigger part of the background becomes resolvable.

In Figures 3.9, 3.10, 3.11, and 3.12, we plot the SNR obtained by cross-correlating two interferometers of ETB, ETD, BBO or DECIGO, respectively, assuming one year of observation. To obtain the corresponding SNR for an interval of observation time T_{obs} , one can just multiply those values by $\sqrt{T_{\text{obs}}/[1 \text{ yr}]}$. Each point on each curve corresponds to one realization of the background, in which all neutron stars have the same magnetic field and the same ellipticity. We know, of course, that not all neutron stars are equal. However, these plots are interesting for the following reason: the SNR (as well as the spectral function) is proportional to the rate. So, all neutron stars may not have the same certain values of B and ϵ , but if only a given fraction does, the SNR produced would be the one of the plots, multiplied by that fraction. This allows us to draw a few interesting conclusions.

If Distribution 2 accurately describes the initial distribution of frequencies, the detection of the background of rotating neutron stars seems unlikely; instead, if Distributions 0 or 1 are accurate, the chances of detection (by ET) are high. For example, we see in Figure 3.9 (assuming Distribution 1) that, if all neutron stars have an ellipticity of $\epsilon = 10^{-6}$ and a magnetic field of $B = 10^7$ T, the obtained SNR is 1.0×10^2 for ETB; then, if at least a few percent of neutron stars have ellipticities larger than 10^{-6} and magnetic fields smaller than 10^7 T, ETB would detect the produced background with SNR of at least a few. Suppose now that neutron stars cannot have ellipticities larger than 10^{-7} . Even in this case, SNR of a few would be obtained for ETB if only a few percent of the rotating neutron stars have magnetic fields lower than 10^6 T.

As Figures 3.11 and 3.12 show, the SNR calculated for BBO and DECIGO reach relevant values for magnetic fields smaller than $\sim 10^7$ T, and, in Figure 3.7, we see that the spectral function, for such a magnetic field, has support only at frequencies larger than ≈ 1 Hz. The main contribution to the SNR of BBO and DECIGO thus comes from frequencies between 1 Hz and 10 Hz. In [167], the overlap reduction function is calculated for different configurations of the spacecraft constellations of BBO and DECIGO. Almost all configurations produce an overlap reduction function close to zero between 1 Hz and 10 Hz. The assumption made in Section 3.2.3 of an overlap reduction function equal to one is therefore very crude. The SNR obtained with a more realistic overlap reduction function would reasonably be much lower.

In Figures 3.13 and 3.14 we show the same SNR calculations as in Figures 3.9 and 3.10, but for the unresolvable part of the background. By comparison, one can conclude that, for

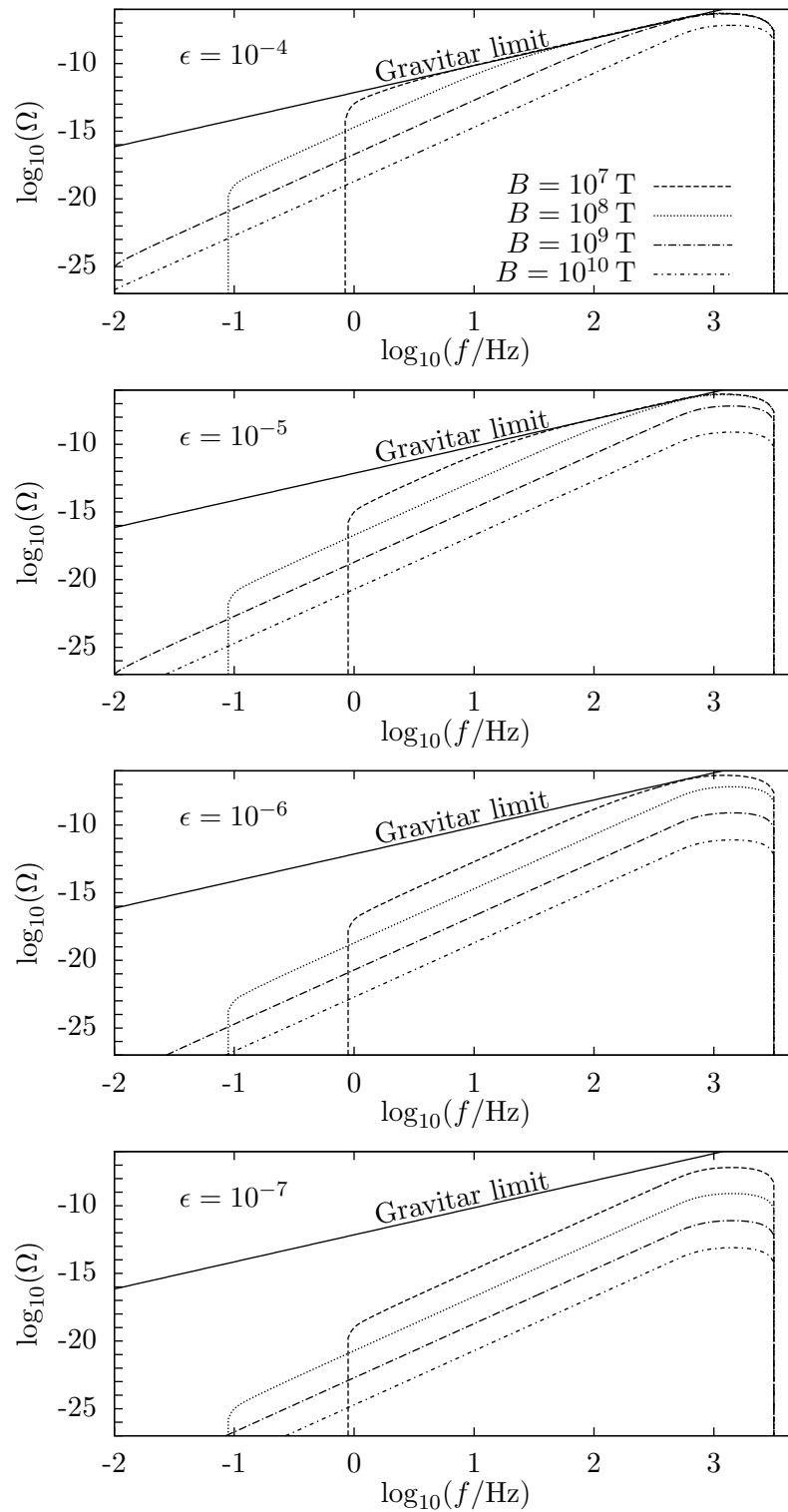


Figure 3.7: Spectral function, versus observed frequency, of the total background produced if all rotating neutron stars had the same magnetic field and ellipticity. Different line types correspond to different magnetic fields (as the legend of the upper plot describes). Each plot corresponds to a certain ellipticity.

3 Gravitational wave background from rotating neutron stars

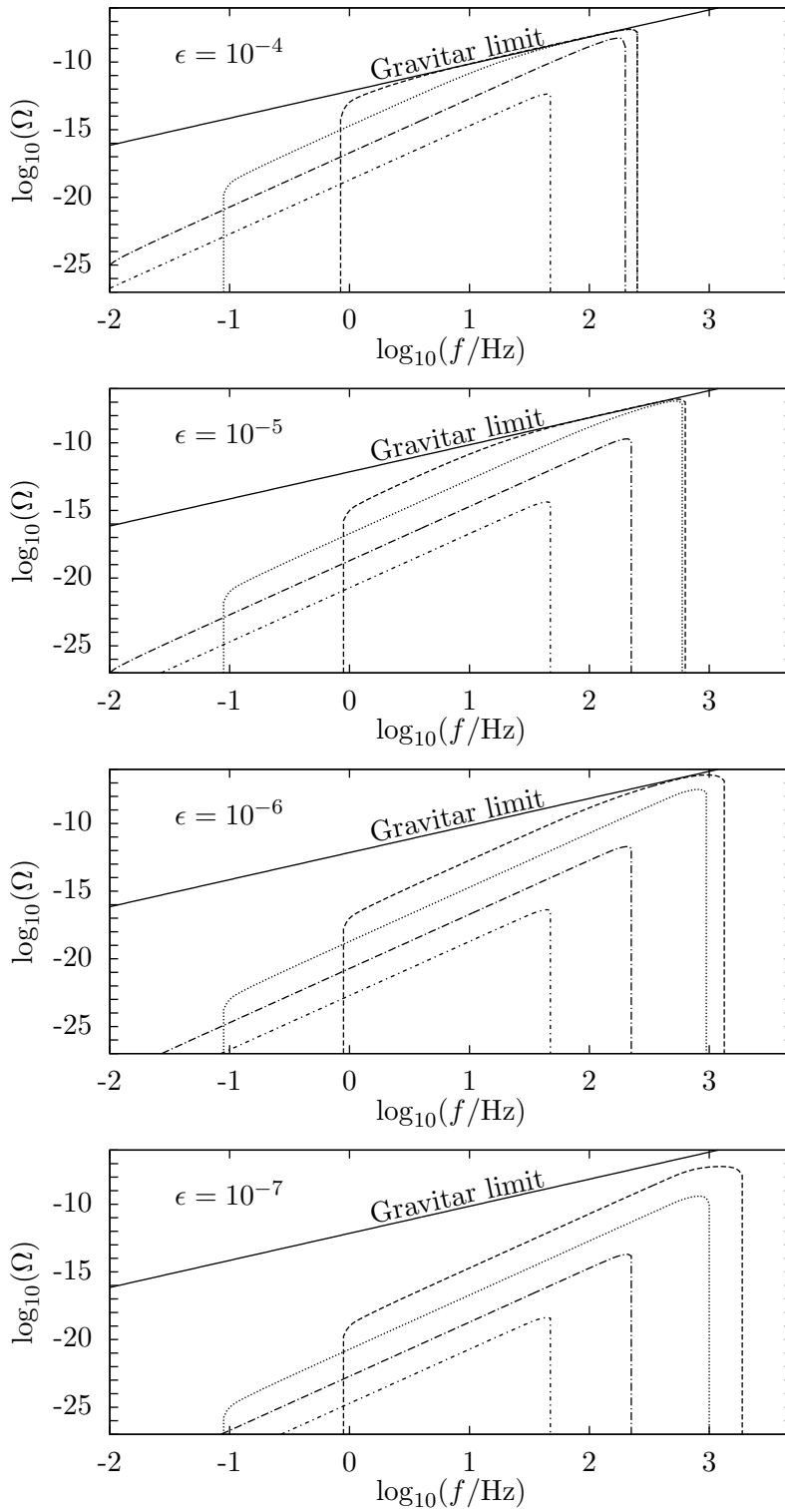


Figure 3.8: Same as Figure 3.7, but for the unresolvable part of the background.

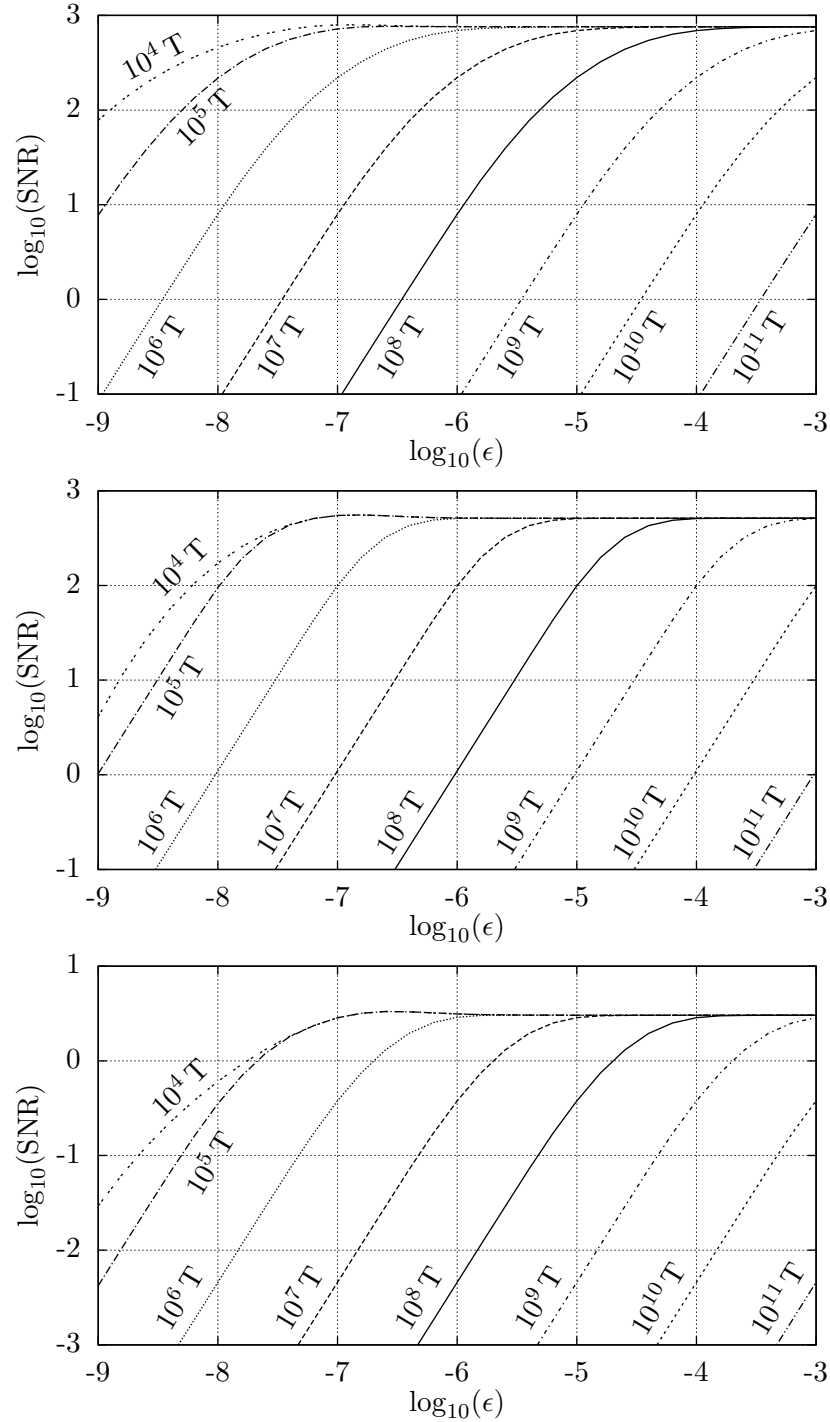


Figure 3.9: Signal-to-noise ratio produced by the total background of rotating neutron stars, assuming that all of them have the same magnetic field and ellipticity. Each curve corresponds to a certain magnetic field (specified on top of each curve), and each point on a curve corresponds to a certain ellipticity (specified on the horizontal axis). These values of SNR are obtained by cross-correlating 1 year of data of two interferometers of ETB. Upper, middle, and lower plots are obtained using the initial frequency distribution called Distribution 0, 1, and 2, respectively, in Section 3.4.5.

3 Gravitational wave background from rotating neutron stars

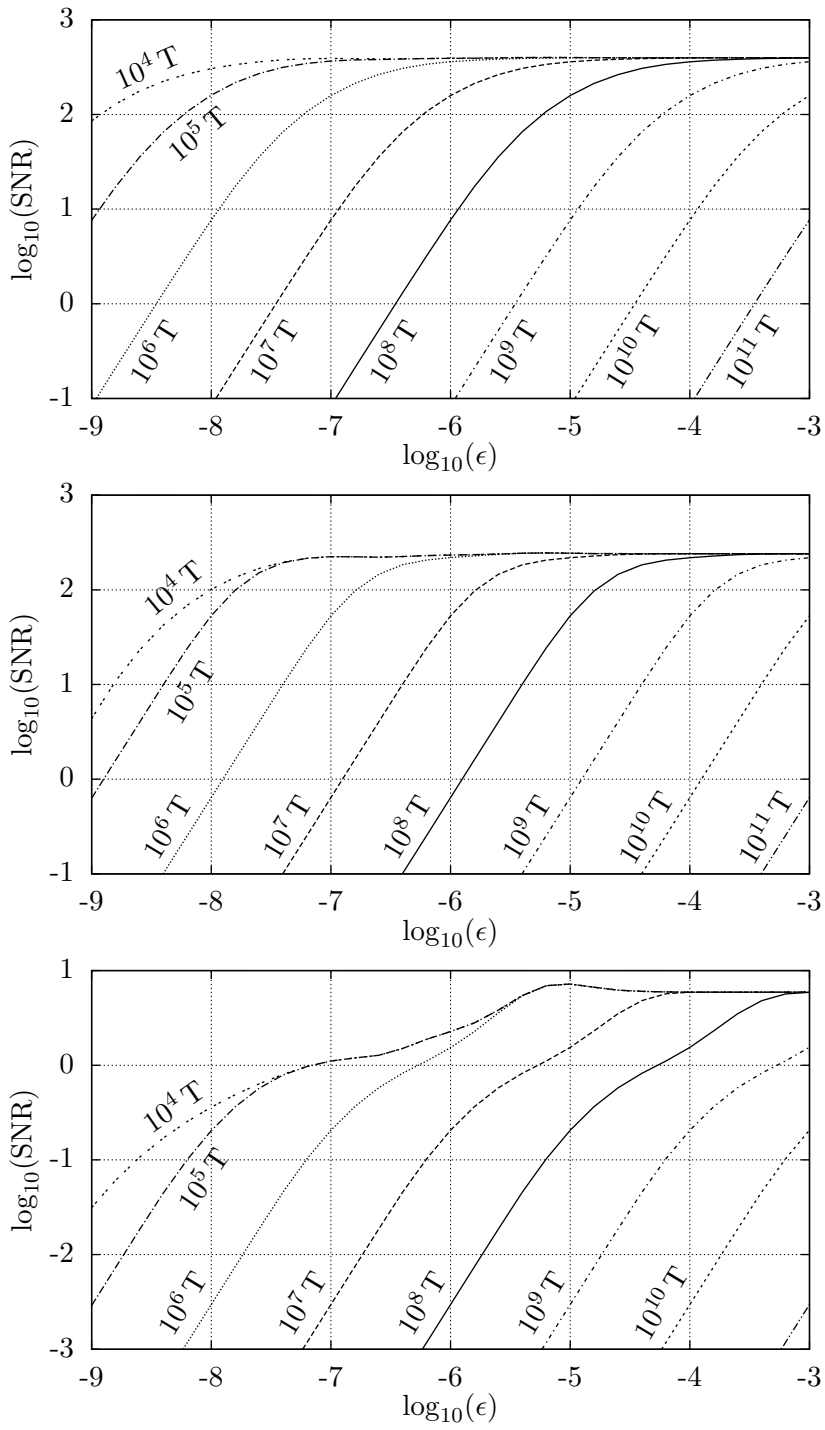


Figure 3.10: Same as Figure 3.9, calculated in this case for ETD.

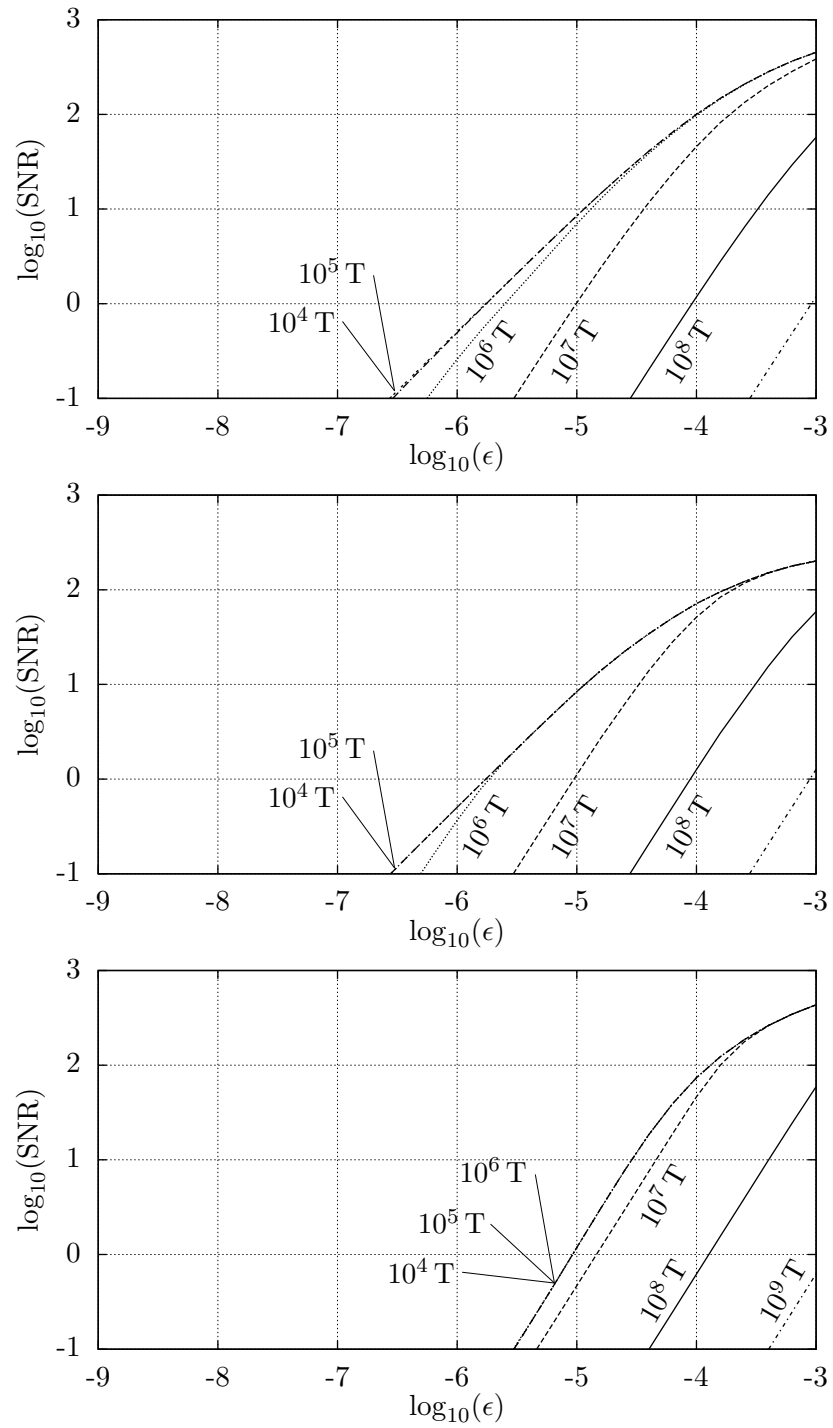


Figure 3.11: Same as Figure 3.9, but calculated for two interferometers of BBO. The observation time assumed is also of 1 year.

3 Gravitational wave background from rotating neutron stars

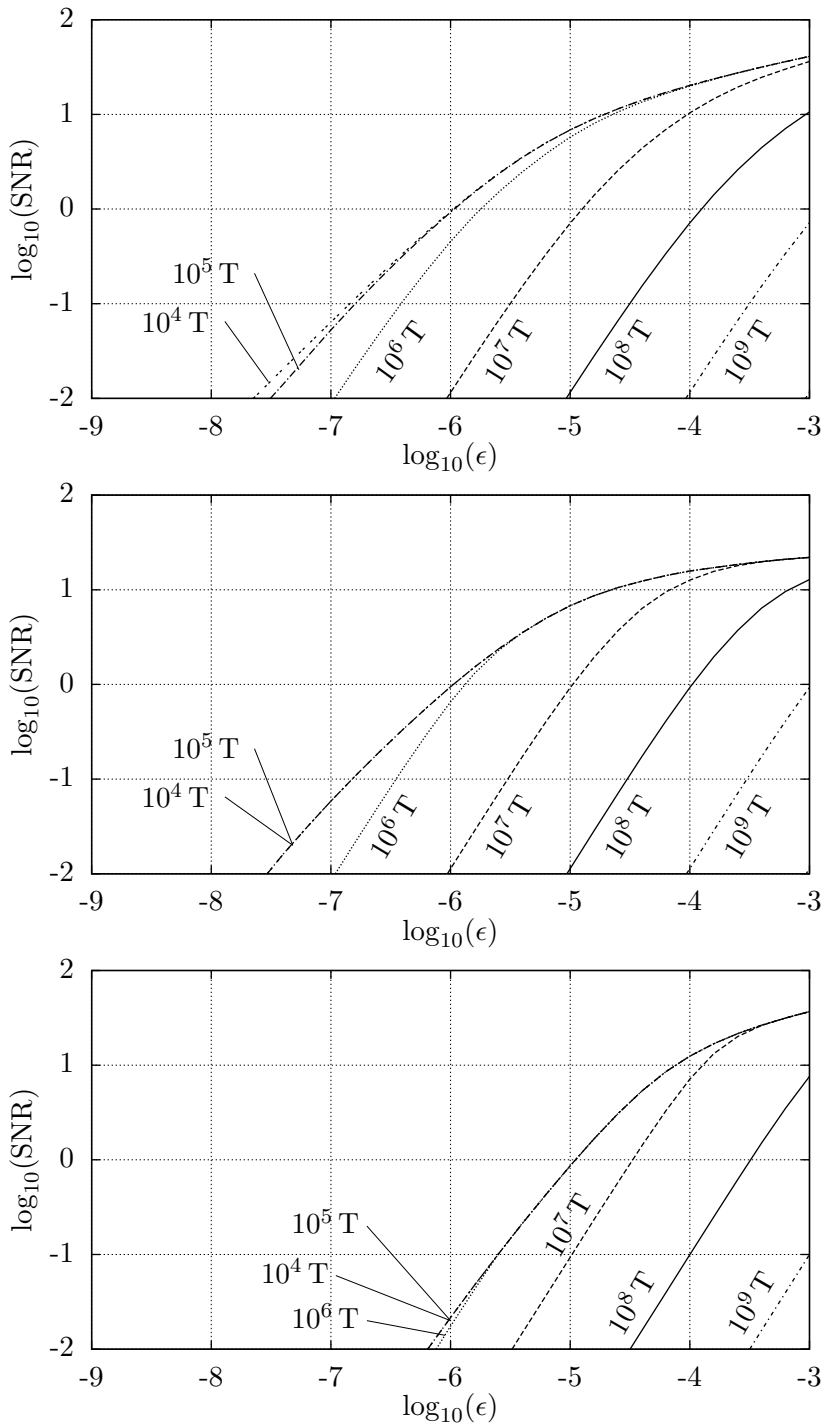


Figure 3.12: Same as Figure 3.9, but for two interferometers of DECIGO. The observation time assumed is also of 1 year.

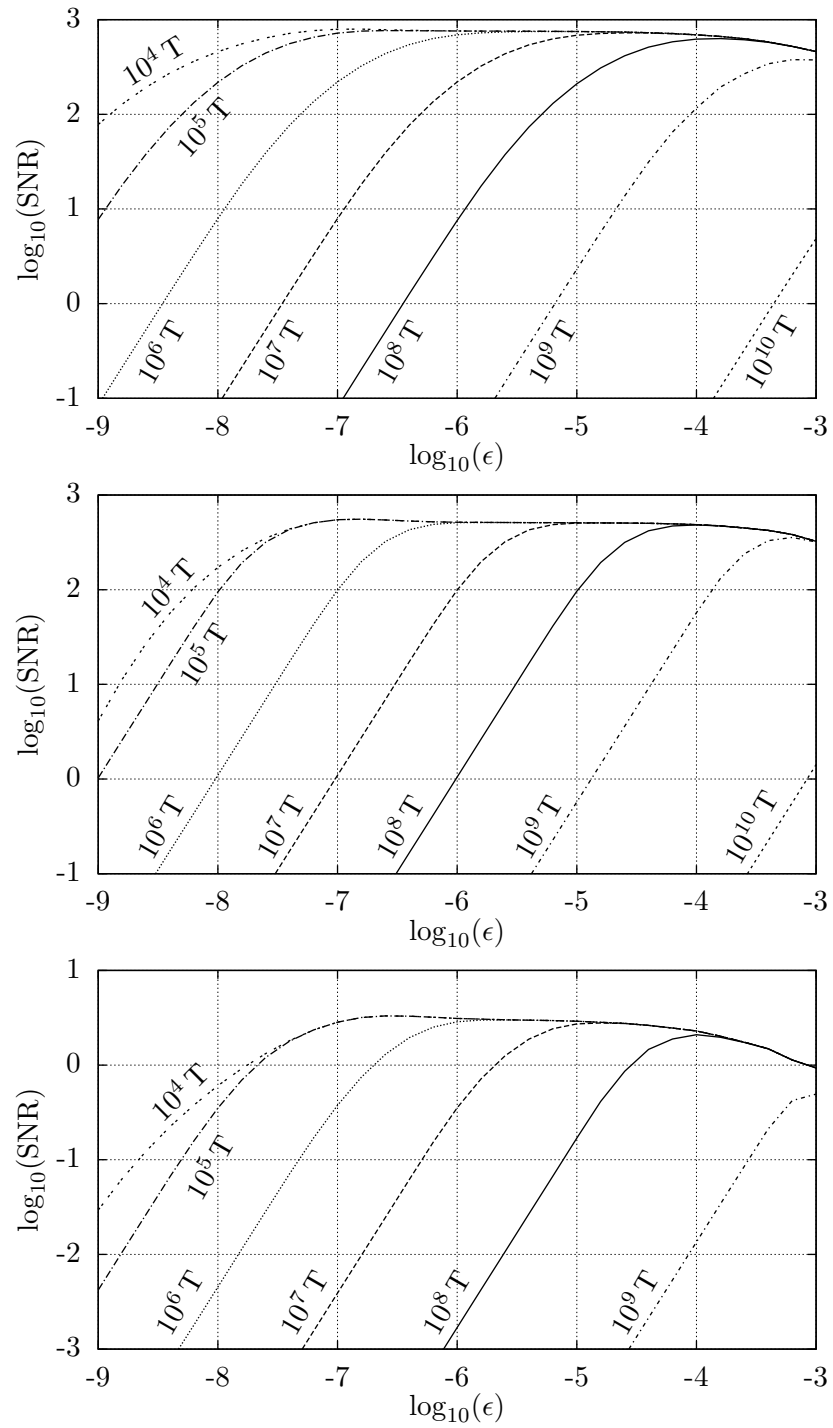


Figure 3.13: Same as Figure 3.9, but for the unresolvable part of the background (using $\mathcal{N}_0 = 1$ and $\Delta f = 1 \text{ yr}^{-1}$). These values of SNR are obtained by cross-correlating 1 year of data of two interferometers of ETB.

3 Gravitational wave background from rotating neutron stars

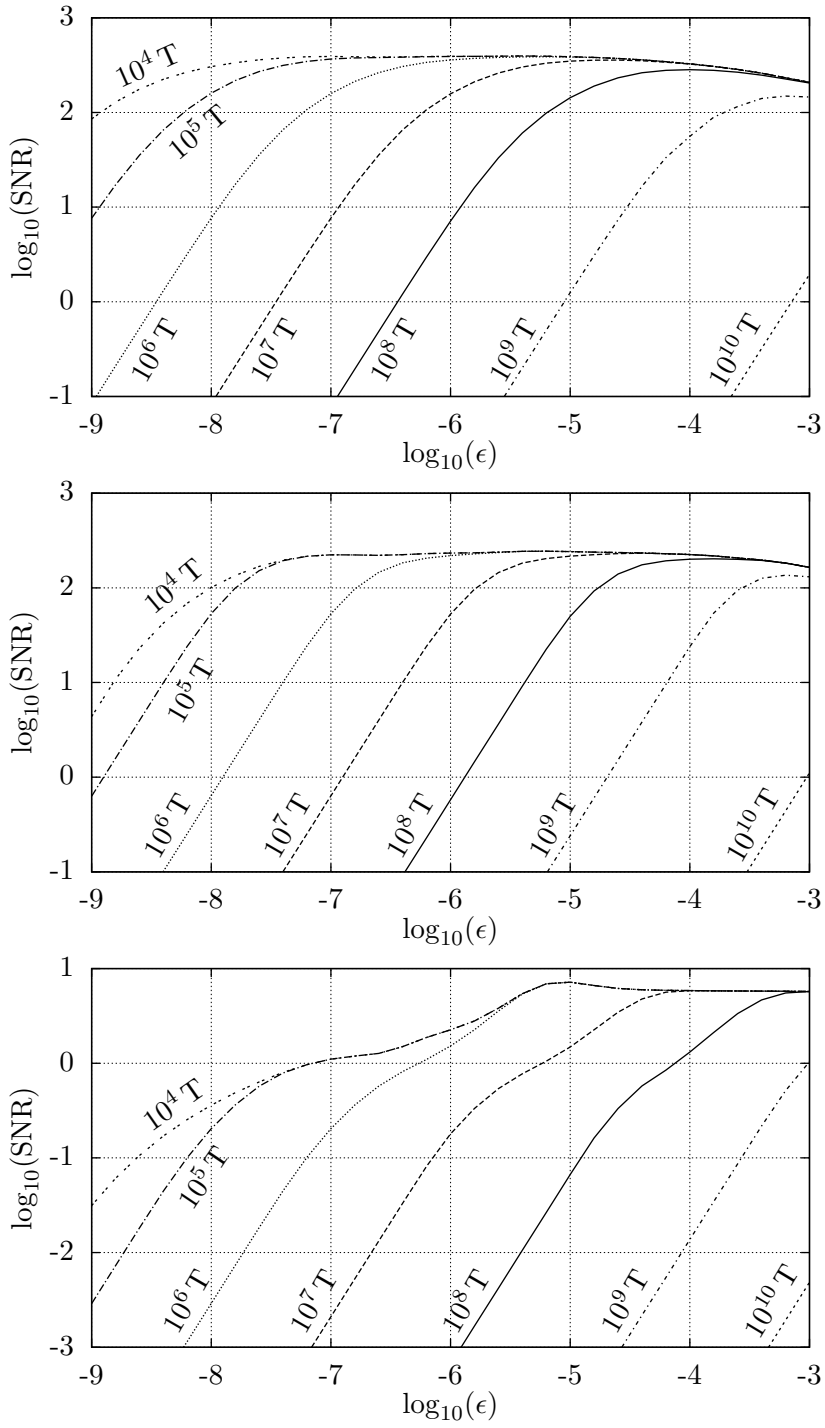


Figure 3.14: Same as Figure 3.13, but for ETD.

ellipticities smaller than $\epsilon \sim 10^{-4}$ and magnetic fields smaller than $B \sim 10^8$ T, the background is almost entirely unresolvable.

3.6 Discussion

3.6.1 Comparison with previous work

The background produced by magnetars has recently been calculated in [154], assuming different models. Our upper limit is obtained by assuming the magnetic field and ellipticity of one of the models given in that paper: the one that predicts the largest spectral function. All other models in that work, as well as the models used in previous papers [198, 201] produce smaller levels of background.

In [117], the gravitational wave background is calculated, assuming a population of magnetars that could fit the ultrahigh energy cosmic ray spectrum. The most optimistic of the expectations for the spectral function in that paper is, in a certain range of frequencies, a factor of ≈ 8 larger than the upper limit calculated by us in Section 3.5.3. That expectation of the background is said to possibly reach the sensitivities of BBO and DECIGO, but not that of ET; however, no calculation of SNR is performed in that paper. We now assert that, performing the SNR calculations, the claim is the opposite. The SNR that our magnetar upper limit would produce on BBO and DECIGO (assuming an overlap reduction function equal to one, which is already too optimistic), after one year of observation time, is of the order of 10^{-3} ; these values are too low to claim a possible detection, even if multiplied by that factor of ≈ 8 . However, the upper limit of [117] would produce an SNR of ≈ 5 and ≈ 2 on ETB and ETD, respectively. Therefore, one can conclude that the upper limit of magnetars (either with the estimate of [117] or with ours) is out of the reach of BBO and DECIGO, but could be detected by ET.

All the papers mentioned in this section use the so-called *duty cycle* to account for the statistical properties of the background. As commented in Section V.F.3 of [207], the overlap function (which is a generalization of the duty cycle) is the right tool to quantify the resolvability of the background. Moreover, the duty cycle can only be used for short (burst-like) signals, not for long signals, like the ones produced by rotating neutron stars. In Figures 3.6, 3.13, and 3.14, one sees that, even if having a duty cycle much larger than 1 (as reported in [154]), the background produced by magnetars is resolvable in the band of ET.

3.6.2 On the formation rate

The spectral function turns out to be rather insensitive to the shape of the rate. In this section we compare the spectral function obtained using the different star formation rates $\dot{\rho}(z)$ of [144, 186, 1, 236, 93, 162, 62, 254], and a star formation rate that has the same value over all cosmological epochs.

Let us first obtain a reasonable value for the constant rate $\dot{n}(z) = R$. Given one star formation rate $\dot{\rho}_i(z)$, one can calculate its average value over all redshifts,

$$\langle \dot{\rho}_i \rangle = \frac{\int_0^{z_{\max}} \dot{\rho}_i(z) dz}{\int_0^{z_{\max}} dz}. \quad (3.104)$$

Considering the $N = 11$ star formation rates from [144, 186, 1, 236, 93, 162, 62, 254], the mean

3 Gravitational wave background from rotating neutron stars

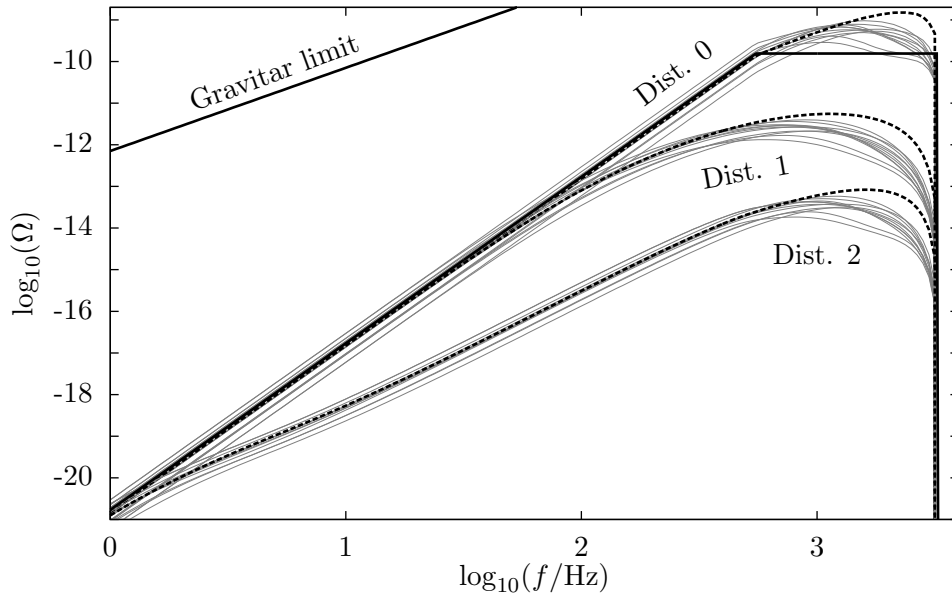


Figure 3.15: Spectral function, versus observed frequency, of the total background produced by the ensemble of rotating neutron stars, using the three initial frequency distributions (Distribution 0, 1, and 2, of Section 3.4.5). All systems are assumed to have $B = 10^8$ T, and $\epsilon = 10^{-7}$. The light-gray curves are obtained with different star formation rates [144, 186, 1, 236, 93, 162, 62, 254], whereas the black dashed lines use the constant star formation rate of Equation (3.106). The black solid line is obtained with the approximate formula of Equation (3.113).

value of $\langle \dot{\rho}_i \rangle$ is

$$\overline{\langle \dot{\rho} \rangle} = \frac{1}{N} \sum_{i=1}^N \langle \dot{\rho}_i \rangle = 0.10 M_{\odot} \text{ yr}^{-1} \text{ Mpc}^{-3}. \quad (3.105)$$

Finally, replacing this star formation rate in Equation (3.57), one obtains the value of the constant rate R ,

$$R = \lambda \overline{\langle \dot{\rho} \rangle} = 5 \times 10^{-4} \text{ yr}^{-1} \text{ Mpc}^{-3}. \quad (3.106)$$

This is the approximate number of neutron stars formed per unit emitted interval of time per unit comoving volume, at any cosmological epoch.

In Figure 3.15, we show the spectral function, with the three initial frequency distributions of Section 3.4.5, obtained with constant and non-constant rates. One sees that the spectral function using different rates differs just by a constant factor at almost all frequencies; only at frequencies close to the maximum one, the spectral function presents different shapes depending on the specific rate assumed. Given the lack of information on the population statistics (which is evident when comparing the results of different initial frequency distributions), the choice of one or another rate is irrelevant. A similar conclusion is drawn for binary systems in Section V.A of [207].

3.7 Summary and conclusions

3.7.1 Regarding the calculation of the spectral function

We have derived a formula for the spectral function $\Omega(f, \Delta f, \mathcal{N}_0)$, i.e., the density per logarithmic frequency interval (in units of critical density), around the observed frequency f , of a background made of signals that produce an overlap of \mathcal{N}_0 signals per frequency bin Δf . This formula (in Equation (3.18)) can be used for a population that evolves over long time scales. We also present an expression for the overlap function $\mathcal{N}(f, \Delta f, z)$, that gives the number of signals with observed frequency f per frequency bin Δf , with redshifts smaller than z . This overlap function (in Equation (3.16)) is more general than the one introduced in [207].

A more detailed expression of the spectral function is given in Equation (3.33), where the dependence on the initial frequency distribution of the ensemble is explicitly shown. Similarly, a more explicit formula for the overlap function is presented in Equation (3.34) (or, in a more convenient form, in Equation (3.35)). Assuming that all systems start emitting at the same frequency, the overlap function and the spectral function become the ones of Equations (3.42) (or, more conveniently, (3.44)), and (3.43), respectively. Equation (3.46) gives the overlap function calculated with the additional assumption that the evolution of the systems is short compared to cosmological time scales. This formula coincides with the definition given in [207]. The spectral function is then obtained under the same assumptions (Equation (3.47)). If one applies the latter formula to calculate the total background (with $\mathcal{N}_0 = 0$), one obtains Equation (3.48), which is the expression that usually appears in the literature.

In Section 3.4 we have described a simple but useful model for the energy and frequency evolution of rotating neutron stars. Figures 3.2 and 3.3 show the collection of possible redshifts and observed frequencies of gravitars and of normal pulsars, respectively, assuming in both cases that all systems have the same ellipticity, $\epsilon = 10^{-7}$. In these plots one can see the frequency range in which the usual assumption of short-lived systems (which has not been adopted for our results) is inaccurate.

In Sections 3.8 and 3.9, we propose simple approximate formulas for the spectral function of rotating neutron stars and, for completion, for binary systems too. Given the uncertainties in some astrophysical parameters, like the rate and the initial frequency distribution, these approximate formulas can be used as a reasonably good estimation for the levels of contemporary backgrounds.

3.7.2 Regarding the detection of the background of rotating neutron stars

The three initial spin period distributions considered in the calculations (see Section 3.4.5), lead to very disparate results. The first one (called Distribution 0), assumes that all systems are formed with the same initial frequency. The other distributions (called Distributions 1 and 2) are taken from the literature [16, 64]. If Distribution 2 is accurate, the detection of the background by present and planned detectors can be discarded.

In Section 3.5.1 we have justified that there is a robust upper limit (the gravitar limit, in Equation (3.103), or, more simply in (3.111)) on the level of background produced by rotating neutron stars. In Section 3.10, we point out an interesting characteristic of the background obtained under the unrealistic assumptions of the gravitar limit: its characteristic amplitude h_c is independent of the ellipticity of the systems and of their spin frequency. A similar feature was

3 Gravitational wave background from rotating neutron stars

predicted by Blandford, for the expected gravitational wave amplitude of the nearest system of a uniform galactic population of gravitars. This feature disappears with more realistic models, as it occurs with Blandford's argument.

In Figure 3.4, the spectral functions of the total and the unresolvable background are calculated, under the unrealistic assumption that all neutron stars are gravitars. One sees that the background is almost entirely unresolvable. Such a background, assuming Distributions 0 and 1, can be detected with ETB and ETD, but not with aLIGO, by using the typical cross-correlation method. If at least 1% of neutron stars behave like gravitars, they will produce an unresolvable background that can be detected by ET.

Using a magnetic field and an ellipticity distribution (from [16, 170]), a reasonable level of background of rotating neutron stars is obtained (see Figure 3.5); it is below the detection capabilities of any existing or planned instrument.

We have obtained an upper limit on the total background of magnetars (Figure 3.6), using one of the models presented in [154]. This background can only be detected by ET. However, other models predict levels of background several orders of magnitude lower. Hence, we claim that magnetars are not the most promising rotating neutron stars, regarding the detection of the background.

With Figures 3.7 and 3.8 one can get an idea of how the amplitude and the resolvability of the background depend on the values of the magnetic field and ellipticity (assuming that these values are equal for all neutron stars).

Figures 3.9, 3.10, 3.11, and 3.12 summarize the prospects of ETB, ETD, BBO, and DECIGO, respectively, to detect the total background of rotating neutron stars. The values of SNR in these plots are calculated for the cross-correlation of the data of two interferometers during 1 year (to obtain the values after 3 or 5 years, it is enough to multiply the vertical axis by $\sqrt{3}$ or $\sqrt{5}$). These graphs are useful because the SNR is proportional to the fraction of stars that are neutron stars. Suppose that some given values of magnetic field B and ellipticity ϵ are associated with SNR equal to S in the plots; then, if only a fraction x of all neutron stars have B and ϵ , they will produce a background observed with SNR equal to $x \times S$. For example, one can conclude from Figure 3.9 that, if at least a few percent of neutron stars have $\epsilon \geq 10^{-6}$ and $B \leq 10^7$ T, the background would be observed by ETB with SNR of a few. Another conclusion from Figure 3.9 is that, if the maximum ellipticity of neutron stars is of $\epsilon = 10^{-7}$, ETB will still observe a background of SNR of a few, if just a few percent of neutron stars have $B \leq 10^6$ T.

We point out that the SNR values of BBO and DECIGO are obtained by assuming an overlap reduction function (see Section 3.2.3) identically equal to 1. This is quite inaccurate between 1 Hz and 10 Hz (see [167], where the overlap reduction function is calculated for different configurations of the spacecrafts), which is the frequency interval where the background contributes the most to the SNR of BBO and DECIGO. The detection prospects of BBO and DECIGO should therefore be smaller than what Figures 3.11 and 3.12 suggest.

Figures 3.13 and 3.14 are analogous to 3.9 and 3.10, respectively, but for the unresolvable part of the background. They are included to show that the total and the unresolvable backgrounds are identical for all configurations with $\epsilon \leq 10^{-4}$ and $B \leq 10^8$ T; on the other hand, the background produced by magnetars (with larger magnetic fields) is mostly resolvable.

This work, together with [207], covers two of the most promising sources of contemporary gravitational wave background. If the most reasonable estimate of the background (in Section 3.5.2) is accurate, or if rotating neutron stars form with initial spin frequencies well described by

3.8 Appendix I: Simple formulas for the background of rotating neutron stars

Distribution 2 (in Equation (3.85)), then we can conclude that ground-based detectors operate in a frequency window that is free of contemporary unresolvable background from binaries and rotating neutron stars. However, if at least a few percent of neutron stars behave as gravitars, or if any of the configurations proposed in Section 3.5.4 that produce high SNR values is in good agreement with the real neutron star population, an unresolvable background of rotating neutron stars can obscure the searches of ET for other sources of background.

3.8 Appendix I: Simple formulas for the background of rotating neutron stars

In this section we present some approximate formulas for the spectral function of the total and the unresolvable background of rotating neutron stars. They are useful to obtain a simple estimate of the background; nevertheless, these formulas were not used to obtain the results of Section 3.5.

We first need to define the constants

$$C_{\text{gr}} = \int_0^{z_{\text{max}}} \mathcal{E}^{-1}(z) dz \approx 1.9, \quad (3.107)$$

$$C_{\text{md}} = \int_0^{z_{\text{max}}} [1+z]^2 \mathcal{E}^{-1}(z) dz = \frac{2\mathcal{E}(z_{\text{max}})}{3\Omega_m} \approx 19.0, \quad (3.108)$$

$$\bar{C}_{\text{md}} = \int_0^{z_{\text{max}}} [1+z]^{-2} \left[\int_0^z \mathcal{E}^{-1}(z') dz' \right]^2 \mathcal{E}^{-1}(z) dz \approx 0.23, \quad (3.109)$$

and

$$\bar{C}_{\text{gr}} = \int_0^{z_{\text{max}}} [1+z]^{-4} \left[\int_0^z \mathcal{E}^{-1}(z') dz' \right]^2 \mathcal{E}^{-1}(z) dz \approx 0.042, \quad (3.110)$$

which depend only on cosmological parameters.

A formula for the spectral function of the gravitar limit can be very easily obtained. Using a constant rate $\dot{n}(z) = R$, Equation (3.103) becomes

$$\Omega_{\text{GL}}(f) = \frac{8\pi^3 G I R C_{\text{gr}}}{3H_0^3 c^2} f^2. \quad (3.111)$$

A value for R can be found in Section 3.6.2.

In the following, we assume a fixed initial frequency f_{max} , and obtain the spectral function by solving Equation (3.47) for rotating neutron stars. Moreover, we assume a constant rate $\dot{n}(z) = R$, and perform the approximation introduced in Section 3.4.3 of distinguishing md- and gr-ranges. The spectral function of the background of rotating neutron stars, under these assumptions, has an analytical form. To account for the gr- and the md- regimes, we define the function

$$\bar{\Omega}(f) = \frac{\pi^2 I R}{\rho_c H_0 c^2} \begin{cases} C_{\text{gr}} f^2 & \sqrt{\frac{C_{\text{gr}}}{C_{\text{md}}}} f_C < f \\ C_{\text{md}} f^4 & f \leq \sqrt{\frac{C_{\text{gr}}}{C_{\text{md}}}} f_C \end{cases}, \quad (3.112)$$

where the cut frequency f_C is the one in Equation (3.72).

3 Gravitational wave background from rotating neutron stars

The total background can then be estimated using

$$\Omega_{\text{total}}(f) = \begin{cases} 0 & f < f_{\min} \\ \bar{\Omega}(f) & f_{\min} \leq f \leq \frac{f_{\max}}{1+z_{\max}} \\ \bar{\Omega}\left(\frac{f_{\max}}{1+z_{\max}}\right) & \frac{f_{\max}}{1+z_{\max}} < f \leq f_{\max} \\ 0 & f_{\max} < f \end{cases} . \quad (3.113)$$

The maximum frequency is the one defined in Equation (3.54), and the minimum frequency is

$$f_{\min} = \begin{cases} f_1(z_{\text{gr}}) & f_C \leq f_1(z_{\text{gr}}) \\ f_2\left(\frac{z_{\text{gr}}+z_{\text{md}}}{2}\right) & f_1(z_{\text{gr}}) < f_C < f_{\max} \\ f_3(z_{\text{md}}) & f_{\max} \leq f_C \end{cases} , \quad (3.114)$$

where $f_1(z)$, $f_2(z)$, $f_3(z)$, z_{gr} , and z_{md} are given in Equations (3.94), (3.95), (3.96), (3.101), and (3.102), respectively. Equation (3.114) is an approximation to the minimum value of $f_{\text{low}}(z)$, given by Equation (3.93); f_{\min} is, therefore, defined as an observed frequency (unlike f_{\max} , that is an emitted frequency).

The spectral function of the unresolvable background can be approximated by

$$\Omega_{\text{unresolvable}}(f) = \begin{cases} 0 & f < f_{\text{p,min}} \\ \Omega_{\text{total}}(f) & f_{\text{p,min}} \leq f \leq f_{\text{p,max}} \\ 0 & f_{\text{p,max}} < f \end{cases} . \quad (3.115)$$

In this equation we have introduced the *limiting frequencies* (see Section III.E.4 of [207]); $f_{\text{p,min}}$ ($f_{\text{p,max}}$) is the minimum (maximum) frequency above (below) which the unresolvable background is present. The limiting frequencies can be obtained from

$$f_{\text{p,min}} = f_{\min} , \quad (3.116)$$

and

$$f_{\text{p,max}} = \begin{cases} \min(\chi, f_{\max}) & \chi \leq f_C \\ \min\left(\chi^{3/5} \left[\sqrt{\frac{\bar{C}_{\text{gr}}}{\bar{C}_{\text{md}}}} f_C \right]^{2/5}, f_{\max}\right) & f_C < \chi \end{cases} , \quad (3.117)$$

where

$$\chi = \left[\frac{8\pi c^3 R \Delta f \delta_{\text{md}} \bar{C}_{\text{md}}}{H_0^3 \mathcal{N}_0} \right]^{1/3} . \quad (3.118)$$

The upper case in (3.117) occurs when the unresolvable background is restricted solely to the md-range, and the lower case occurs when the unresolvable background is either restricted to the gr-range or partially in both ranges. Instead of $f_{\text{p,min}}$ and $f_{\text{p,max}}$, one can use $f_{\text{d,min}}$ and $f_{\text{d,max}}$ in Equation (3.115); $f_{\text{d,min}}$ ($f_{\text{d,max}}$) is the minimum (maximum) frequency above (below) which the unresolvable background dominates over the resolvable. The unresolvable background is said to dominate over the resolvable when the spectral function of the former is larger than the spectral function of the latter. One can prove that $f_{\text{d,min}} \approx f_{\text{p,min}}$, whereas $f_{\text{d,max}}$ is constrained to the interval

$$F f_{\text{p,max}} \leq f_{\text{d,max}} < f_{\text{p,max}} . \quad (3.119)$$

The factor F depends only on cosmological parameters, and is $F \approx 0.9$ (both in the md and in the gr ranges). With Equation (3.119) we can conclude that, as soon as an unresolvable background appears at a certain frequency $f_{\text{p,max}}$, that background dominates over the resolvable background below $\approx 0.9 f_{\text{p,max}}$.

3.9 Appendix II: Simple formulas for the background of binary systems

To have a complete estimate of some of the most promising sources of contemporary backgrounds, we also give some simple approximate formulas regarding the background of stellar binary systems (those systems composed of neutron stars, white dwarfs, or stellar-mass black holes). These formulas are based on the calculations of [207].

The spectral function of the total background can be calculated again using Equation (3.113), but with different definitions of $\bar{\Omega}(f)$, f_{\max} , and f_{\min} . For binary systems, we have

$$\bar{\Omega}(f) = \frac{R_{\text{bin}}[G\pi]^{2/3}m_1m_2C_{\text{bin}}f^{2/3}}{3\rho_c c^2 H_0 [m_1 + m_2]^{1/3}}. \quad (3.120)$$

Here, m_1 and m_2 are the masses of the two components of the binary, R_{bin} is the binary rate (summarized in Table I of [207]), and

$$C_{\text{bin}} = \int_0^{z_{\max}} [1+z]^{-4/3} \mathcal{E}^{-1}(z) dz \approx 0.75. \quad (3.121)$$

The maximum frequency can be the frequency of the last stable orbit, which is given by

$$f_{\max} = \frac{c^3}{6\sqrt{6}\pi G [m_1 + m_2]}. \quad (3.122)$$

For systems containing a white dwarf, a better choice of the maximum frequency is

$$f_{\max}^{\text{WD}} = \sqrt{\frac{G[m_1 + m_2]}{\pi^2 [r_1 + r_2]^3}}, \quad (3.123)$$

where r_1 and r_2 are the radii of the components; this frequency corresponds to a separation of the two components equal the sum of their radii. On the other hand, the minimum frequency is approximately given by

$$f_{\min} = \left[\frac{256\mathcal{T}(z_{\max})\pi^{8/3}G^{5/3}m_1m_2}{5c^5 [m_1 + m_2]^{1/3}} \right]^{-3/8} [1 + z_{\max}]^{-1}, \quad (3.124)$$

where the function $\mathcal{T}(z)$ is the same function that has been used in the previous sections, defined in Equation (3.25). The minimum frequency for binary systems has been defined as an observed frequency (unlike in [207]) in analogy to the minimum frequency defined for rotating neutron stars, in Equation (3.114).

To obtain the spectral function of the unresolvable background, one can once more use Equation (3.115), with the definition of $\bar{\Omega}(f)$ given in Equation (3.120), and with the limiting frequencies given below. First, $f_{\text{p},\min} \approx f_{\min}$, which is given in Equation (3.124). Second, the limiting frequency $f_{\text{p},\max}$ is approximately

$$f_{\text{p},\max} \approx \min \left(\left[\frac{5\Delta f \bar{C}_{\text{bin}} c^8 R_{\text{bin}} [m_1 + m_2]^{1/3}}{24\pi^{5/3} G^{5/3} m_1 m_2 H_0^3 \mathcal{N}_0} \right]^{3/11}, f_{\max} \right), \quad (3.125)$$

3 Gravitational wave background from rotating neutron stars

where

$$\bar{C}_{\text{bin}} = \int_0^{z_{\text{max}}} [1+z]^{-8/3} \left[\int_0^z \mathcal{E}^{-1}(z') dz' \right]^2 \mathcal{E}^{-1}(z) dz \approx 0.12. \quad (3.126)$$

In Equation (3.115), instead of $f_{\text{p,min}}$ and $f_{\text{p,max}}$, one can use $f_{\text{d,min}}$ (which is approximately $f_{\text{p,min}}$) and $f_{\text{d,max}}$; the latter also fulfills Equation (3.119), but, in the case of binaries, the value of the F -factor is approximately 0.6.

3.10 Appendix III: On the connexion between the gravitar limit and Blandford's argument

Let us consider again the gravitar limit, described by the spectral function in Equation (3.111). If a stochastic background was characterized by such a spectral function, the characteristic amplitude of the gravitational wave spectrum [180] would be

$$h_c = \sqrt{f S_h(f)}, \quad (3.127)$$

where

$$S_h(f) = \frac{3H_0^2}{4\pi^2} f^{-3} \Omega_{\text{GL}}(f). \quad (3.128)$$

Using Equation (3.111), we obtain a characteristic amplitude of the form

$$h_c = \sqrt{\frac{2\pi G I R C_{\text{gr}}}{H_0 c^2}}, \quad (3.129)$$

which does not depend either on the frequency or on the ellipticity of the systems. This fact reminds us Blandford's argument (first cited in Section 9.4.2 (b) of [90], revisited in [129] and [111]). According to this argument, the expected gravitational wave amplitude of the nearest system of a uniform galactic population of gravitars, is independent of the ellipticity and the spin frequency of the systems. Some of the assumptions required to obtain Equation (3.129) are different from those of Blandford's argument. However, the result is similar: the expected gravitational wave characteristic amplitude of the background produced by a population of gravitars, uniformly distributed in the universe, is independent of the ellipticity and the spin frequency of the systems.

The assumptions needed for Blandford's argument to hold, as well as those needed for h_c not to be a function of ϵ and f , are quite unrealistic. Once one adopts more realistic assumptions on the galactic population (for example, that gravitars are not distributed on a two-dimensional disk), Blandford's argument vanishes [111]. Analogously, under more realistic assumptions on the ensemble of gravitars in the universe (for example, that they have a finite time to evolve, and a finite initial spin frequency), the characteristic amplitude in Equation (3.129) depends on the ellipticity and on the frequency.

4 A new method to search for supermassive black hole binaries

This chapter presents a technique to search for supermassive black hole binaries (MBHBs) in the Sloan Digital Sky Survey (SDSS). The search is based on the peculiar properties of merging galaxies that are found in a mock galaxy catalog from the Millennium Simulation. MBHBs are expected to be the main gravitational wave (GW) sources for pulsar timing arrays (PTAs); however, it is still unclear if the observed GW signal will be produced by a few single MBHBs, or if it will have the properties of a stochastic background. The goal of this work is to produce a map of the sky in which each galaxy is assigned a probability of having suffered a recent merger, and of hosting a MBHB that could be detected by PTAs. This constitutes a step forward in the understanding of the expected PTA signal: the skymap can be used to investigate the clustering properties of PTA sources and the spatial distribution of the observable GW signal power; moreover, galaxies with the highest probabilities could be used as inputs in targeted searches for individual GW sources. We also investigate the distribution of neighboring galaxies around galaxies hosting MBHBs, finding that the most likely detectable PTA sources are placed at dense galaxy environments. Different techniques are tried out in the search, including Bayesian and Machine Learning algorithms, with consistent outputs. The spectral coverage of the SDSS reaches less than a fifth of the sky, and the catalog becomes severely incomplete at large redshifts; however, this technique can be applied in the future to larger catalogs, to obtain a complete, observationally-based information of the expected GW signal detectable by PTAs.

4.1 Introduction

Studies of the dynamics of nearby galaxies [115, 204] suggest that a supermassive black hole (MBH) must reside at their centers, and there now exists plenty of observational evidence that almost all massive galaxies contain a MBH in their centers, our Milky Way being the most striking example [74, 75]. There is also a variety of investigations that confirm that the mass of the MBH is highly correlated to the mass and velocity dispersion of the bulge of the hosting galaxy [148, 66, 73, 155, 85, 78, 157]. In the context of the Λ cold dark matter (Λ CDM) cosmology, large dark matter structures in the Universe build up hierarchically [253]. Galaxies form as gas cools at the centers of dark matter halos; small dark matter halos fall onto greater ones, and the galaxies of the former become satellites of the new host. At some later time, the smaller galaxies can merge onto the more massive ones, that lie at the bottom of the potential well. Within this framework, following galaxy mergers, a large number of MBH binaries (MBHBs) must form along the cosmic history [21, 249].

Depending on the mass ratio (i.e., mass of the satellite over mass of the primary) of the two systems, it is customary to divide galaxy interactions in *minor mergers* and *major mergers*. In a *minor merger*, the satellite is much lighter than the primary and its material can be disrupted

before the two centers merge [83]. Furthermore, dynamical friction [39], which is the main mechanism that brings the two MBHs towards each other, can become inefficient (causing the merger to take longer than the age of the Universe) if the masses of the two galaxies differ too much. Alternatively, in a *major merger*, the two galaxies have similar masses and their merger can be completed within a Gyr [109]. Once the separation between the two galaxies is smaller than a few tens of kpc, the two MBHs can efficiently transfer energy and angular momentum to the surrounding stars and gas [191, 61, 56, 108, 188], spiraling towards each other. At pc separations, they form a bound Keplerian binary; when the binary is tight enough (order of 0.01 pc) gravitational wave (GW) emission takes over, leading to coalescence.

Gravitational radiation emission from binary systems [161, 147] is predicted by Einstein's theory of General Relativity, however, only indirect proofs of this phenomenon have been achieved so far [252]¹. When GW emission becomes the main mechanism of energy loss of a binary, the inspiral process is well described by General Relativity in its lower order, quadrupolar approximation [176]. The period of the orbit decreases with time, while the amplitude of the emitted GWs increases. At the end of the inspiral phase, when the binary approaches the last stable orbit (see for example Box 25.6 of [161]), the coalescence occurs, in which the amplitude of the GWs reaches its maximum [7]; after this, the binary enters the ring-down phase, and the GW emission rapidly decays. Merging MBHBs are the most powerful GW emitters in the Universe [225].

The direct detection of GWs, which is the main goal of several state of the art experiments around the world, including GEO600, LIGO, Virgo and KAGRA [182, 133, 130, 3, 230], will mark the beginning of the era of GW astronomy [218, 213]. Many other experiments have been proposed, like eLISA [226, 58] and the Einstein Telescope [190] to fully exploit this new window to the universe, which will unveil valuable information not only about astrophysics, but also about cosmology and fundamental physics [17].

One of the most fascinating means of detecting GWs directly involve the timing of an ensemble of millisecond pulsars (MSPs, pulsars with spinning periods of ~ 1 ms, [137]), forming a pulsar timing array (PTA). MSPs are the most regular astronomical objects known, and they play a double role in GW astronomy. On the one hand, they are potential sources of GWs [189, 13, 208]; on the other hand, they can also be used as parts of a galactic-scale GW detector. GWs perturb the space-time metric between the pulsars and Earth, and these small perturbations affect the times of arrival (TOAs) of the pulses [71, 98]. The differences between the expected and measured TOAs are the timing residuals. By studying the timing residuals, PTAs aim to detect GWs of frequencies between $\sim 10^{-6}$ Hz and $\sim 10^{-9}$ Hz. There are three independent PTA collaborations around the globe: the EPTA [65], NANOGrav [97], and the PPTA [151], which work jointly in the IPTA [92].

Two main sources are expected to contribute to the GW spectrum in the frequency band of the PTA: MBHBs [192, 95, 257] and cosmic strings [203, 212]. In particular, the incoherent superposition of the radiation of the numerous MBHBs in the universe may produce a background of GWs [223, 207]. Combining our current theoretical models with observational constraints, the present PTA sensitivity limit lies within the $\sim 95\%$ confidence level of the amplitude of the GW background from MBHBs [221]; this means that a detection may occur before the end of the decade.

To date, it is still unknown what kind of signal will be detected by the PTA; it can be dominated by the radiation of a handful of individually resolvable MBHBs [224, 159], or it can be an

¹A similar result based on the double pulsar PSR J0737-3039 [35, 143] by Kramer et al. is in preparation [119].

incoherent superposition of unresolvable sources, i.e. a stochastic background [146]. Very effective searching algorithms have been developed to detect a Gaussian isotropic GW background [246, 247], but the actual properties of the background (especially its isotropy) are currently under investigation [193, 160]. On the other hand, different data analysis techniques are under development to detect the signature of individually resolvable MBHBs [18, 59, 178]. Within this context, it is therefore meaningful to use available observations to better understand the distribution of MBHBs in the neighboring Universe.

The goal of this work is to assign to each galaxy of a catalog a probability of containing a MBHB. By doing that, we complement our theoretical models of galaxy mergers with information about their spatial distribution. This can be useful for on-going investigations regarding the anisotropy of the GW background [160, 237]. A skymap of potential nearby sources of GWs also provides candidates on which a targeted search for GWs can be applied [36], and on which algorithms for single MBHB searches can be tested. From a theoretical perspective, it is interesting to investigate the environments where MBHBs are formed, whether or not they are more likely to be found in galaxy clusters, and the relation of MBHBs with active galactic nuclei (AGN, [142, 104]).

In order to find a criterion to identify galaxies that may contain a MBHB, we rely on a simulated galaxy catalog. It is constructed from the Millennium Simulation (MS, [232]), using the galaxy formation models from [83] and the all-sky light-cone produced by [91], with the stellar population from [30]. In this fake universe we find that galaxies that suffered a major merger in the “recent” past (meaning in less than a few hundreds of Myr, which is the time lapse between snapshots of the simulation) have a distribution in redshifts and masses that does not follow that of non-merging galaxies. Moreover, they present a distinctive statistical distribution of neighbors in their surroundings (to distances up to a few Mpc). Therefore, we use the mass, the redshift, and the distribution of neighboring galaxies to characterize the signatures of major mergers.

A galaxy that recently experienced a major merger will be referred to as a *B-galaxy*, since it may contain a MBHB. Conversely, a galaxy that did *not* merge in less than a few hundred Myr, will be called an *N-galaxy*. Only a fraction of B-galaxies can contain a MBHB, because the binary lifetime is generally shorter than the time lapse between the MS snapshots, which is used to define B-galaxies. B-galaxies containing a MBHB that could be observed by the PTA (when emitting in some frequency interval accessible to the PTA) will be called *PTA-galaxies*. Once we are able to identify B-galaxies in the fake catalog, we adapt this catalog to the observational limitations of a real catalog (including, for example, the fact that redshifts are affected by peculiar velocities, and the incompleteness of observations at the low mass/luminosity end). We then perform a similar search on the adapted catalog, and study how the efficiency of the search is affected by these limitations. Finally, we perform the same search on a real catalog, namely the SDSS’ seventh data release (SDSS DR7, [259, 2]), and obtain probabilities for real candidates of B-galaxies and PTA-galaxies.

The search for B-galaxies is performed using several algorithms. The simplest of them (based on Bayesian statistics) takes into account only redshifts and masses to characterize galaxies. When considering the spatial distribution of neighbors around B-galaxies, the search is performed via a machine learning algorithm (MLA). The method presented here to search for MBHBs in galaxy catalogues provides an alternative to other recent proposals [245, 60, 229, 100]: its advantage is that it is applicable to all galaxies, independent of their emission properties; its

disadvantage is that it is a statistical, indirect method, that can be only used to pick candidates which are *more likely* to host a binary. The outcomes of this exploratory study could be improved in several ways (as discussed in Section 4.5); among other things, the way we adapt our fake catalog to the SDSS’ observational limitations is not optimal, which affects the selection of MBHB candidates.

The outline of this chapter is as follows. In Section 4.2 we describe the galaxy catalogs (both fake and real) employed in this work; here we also explain the process used to adapt the fake catalog to the observational limitations of the real one. Section 4.3 presents the methods applied to assign galaxies a probability of having suffered a major merger in the recent past, and the probability of containing an observable source of GW in the PTA frequency band. Section 4.4 contains the main results of this chapter. We depict our study of the clustering of B- and PTA-galaxies, show the efficiency of the different searches, and present skymaps of the SDSS galaxies with the largest probabilities of being B- or PTA-galaxies. We also investigate how the search could be improved by extending the search to deeper redshifts or by using a more complete catalog. In Section 4.5, the main drawbacks and issues of the searches and possible improvements are discussed. The main achievements, conclusions and caveats of this chapter are summarized in Section 4.6. In Section 4.7 one can find additional material on how the data used in this chapter have been obtained (from the MS and SDSS databases).

4.2 Description of the catalogs

4.2.1 Real catalog

The real galaxy catalog is the MPA/JHU value-added galaxy catalog² [105, 28, 243], which is based on the SDSS DR7³ [259, 234, 2]. In fact, we use the stellar masses in the MPA/JHU updated to DR8 photometry⁴ [5, 6]. The SDSS is the largest and most complete redshift survey to date, covering roughly a quarter of the sky. It contains photometry and imaging of galactic and extragalactic objects, and spectroscopy for a fraction of them. The MPA/JHU complements the spectroscopy with the stellar masses of galaxies, which are calculated following the prospects of [104] and [210]. The maximum redshift measured in this catalog is $z_{\max} = 0.7$, which is the maximum redshift considered in our search. More precisely, the search will be described and performed (in Section 4.3.1) with a maximum redshift of 0.1. Then, in Section 4.3.4, the search will be extended to $z \leq 0.7$. On the other hand, we set a minimum redshift of $z_{\min} = 0.01$ in the search. Below this redshift, the SDSS imaging is frequently broken up [25]; moreover, distances cannot be calculated from the redshift (since the assumption that galaxies drift with the Hubble flow does not hold), instead, one needs to complement the SDSS with other catalogs of nearby galaxies. The maximum and minimum stellar masses of galaxies found in the real catalog are $m_{\max} = 10^{13} M_{\odot}$ and $m_{\min} = 10^6 M_{\odot}$, respectively.

The SDSS spectroscopic redshift catalog has the advantage of permitting very precise calculations of the positions of galaxies (unlike photometric redshift catalogs, in which redshifts have much larger uncertainties); on the other hand, the surveyed area covers only 19.5% of the sky, and its completeness is affected by several effects [25, 82]. Spectroscopic targets of the SDSS

²Maintained by Jarle Brinchmann at <http://www.mpa-garching.mpg.de/SDSS/>.

³<http://www.sdss.org/dr7/>

⁴We thank Jarle Brinchmann for providing us with the updated stellar mass catalog.

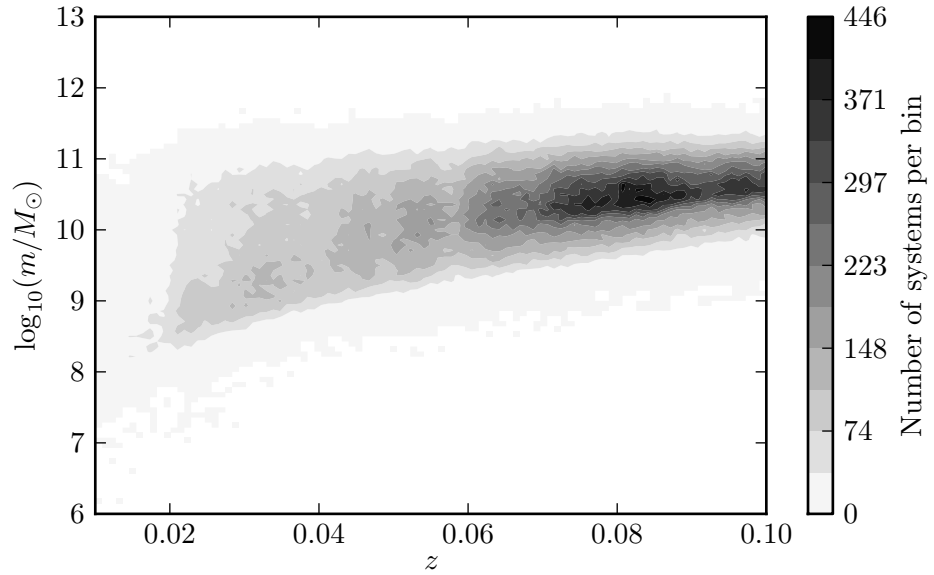


Figure 4.1: Contour plot of stellar mass versus apparent redshift of the real catalog. The horizontal axis is divided into 100 z -bins, and the vertical one into 100 m -bins. The gray scale gives the number of systems contained in each redshift-mass pixel (or z - m -bin).

are assigned fibers using a tiling algorithm that optimizes completeness [24]. But fibers have a finite size, so they cannot be placed close enough to each other in order to aim at targets that have too small angular separations. Thus, in areas of the sky with high galaxy density, the completeness of the spectroscopic catalog decreases considerably. This issue, called *fiber collision*, affects the measurements on galaxy clustering [82], specially at scales $\lesssim 1$ Mpc. Besides the fiber collision, the completeness of the spectroscopic catalog changes from one region of the sky to another. All these effects should be taken into account when adapting the simulated catalog to the limitations of the SDSS spectroscopic catalog (see Section 4.5). However, we apply a simple method (described in Section 4.2.3) that does not take them into account. In Figure 4.1 we show how galaxies in the real catalog are distributed in stellar mass and redshift. This distribution will be used to adapt our fake catalog to the observational limitations of the SDSS (see Section 4.2.3).

4.2.2 Fake catalog

The MS [232] is an N-body simulation in which 10^{10} particles of dark matter evolve in time, in a cubic region of comoving side $\sim 500h_{100}^{-1}$ Mpc, where $h_{100} = H_0/[100 \text{ km s}^{-1}\text{Mpc}^{-1}]$ and H_0 is the present-day Hubble expansion rate. These particles interact and form structures in a Λ CDM universe. Halos and subhalos are identified using the methods described in [233], and baryonic matter is then assigned to the halos, following the semi-analytical models of [83]. The distribution of halos and galaxies is recorded in 64 different snapshots, from redshift $z = 127$ to $z = 0$. Since galaxies at $z \gtrsim 0.1$ are distributed in a comoving volume larger than the simulation

cube, the latter is repeated periodically. The mock catalogs (in which equatorial coordinates and apparent redshifts are assigned to galaxies as if we were observers in the fake universe) are constructed as explained in [91].

The outcomes of the MS have been contrasted with many observations, confirming that the properties of the fake universe match well the current population of galaxies and MBHs (see for example [156, 27]). The cosmological parameters assumed in the MS are a combination of the 2dFGRS [40] with the first year of data from WMAP [231]. To be consistent with the cosmological model of the simulation, when dealing with MS data we assume that the density parameters of matter and dark energy are $\Omega_m = 0.25$ and $\Omega_\Lambda = 0.75$, respectively, and $h_{100} = 0.73$. On the other hand, SDSS derived data are treated with the cosmological parameters $\Omega_m = 0.3$, $\Omega_\Lambda = 0.7$, and $h_{100} = 0.7$, which are the values assumed in the MPA/JHU. Neither of these sets of cosmological parameters agree with the most recent measurements; the possible effect of the “outdated” cosmological parameters in the results is commented on in Section 4.5. A new release of the mock galaxy catalogs has been made public during the writing of this chapter; the simulation has been rescaled [84] to adapt the results to a cosmology based on the data of WMAP 7 [113]. Redoing this investigation using the “updated” fake universe may be considered for a future work.

Our fake galaxy catalog can be downloaded from the MS Internet site⁵ [126], using the SQL query given in Section 4.7. Each galaxy in the fake catalog has a unique identification number (called `galID`). However, as already pointed out, the simulated universe has a cubic finite size; this cube is repeated periodically, to permit galaxies at larger distances. A galaxy in one of the cubes has the same mass (as well as other intrinsic properties) and `galID` of its analogous ones in other cubes, but a different sky position and redshift.

B-galaxies are *descendants* of two (or rarely three) merging *progenitors*. A descendant suffered a *major merger* if the mass of at least two of the progenitors is ≥ 0.2 times the mass of the descendant. Moreover, the merger had to occur between the snapshot corresponding to the redshift of the descendant and the immediately previous snapshot. In Section 4.7 one can find more details on the selection of B-galaxies, and the query used to download their `galID`. Once we know which systems are B-galaxies, we can perform searches for B-galaxies in the fake catalog to check how well the methods work. These searches (described in Section 4.3) are first applied to the local universe (with a maximum redshift of 0.1); then in Section 4.3.4 we extend the algorithms to a maximum redshift of 0.7. For $z < 0.1$ we find (using the second query of Section 4.7) 8400 B-galaxies, of which $\sim 91\%$ are unique (and the rest are repetitions).

In Figure 4.2, redshift-mass histograms are plotted for all galaxies and for only B-galaxies. There we see that B-galaxies are biased towards larger masses. The histograms in Figure 4.2 provide a prescription to distinguish B-galaxies from N-galaxies. With only this information, one can already assign probabilities of galaxies in the real catalog (assuming we know their redshifts and masses well enough). The description of such a search is given in Section 4.3.1.

4.2.3 Adapted catalog

We now turn to the procedure we have used to adapt our fake catalog to the observational constraints of the SDSS spectroscopic catalog. As already mentioned in Section 4.2.1, this may not be optimal; more sophisticated methods (like the one described in [127]) should be used to

⁵<http://www.mpa-garching.mpg.de/millennium/>

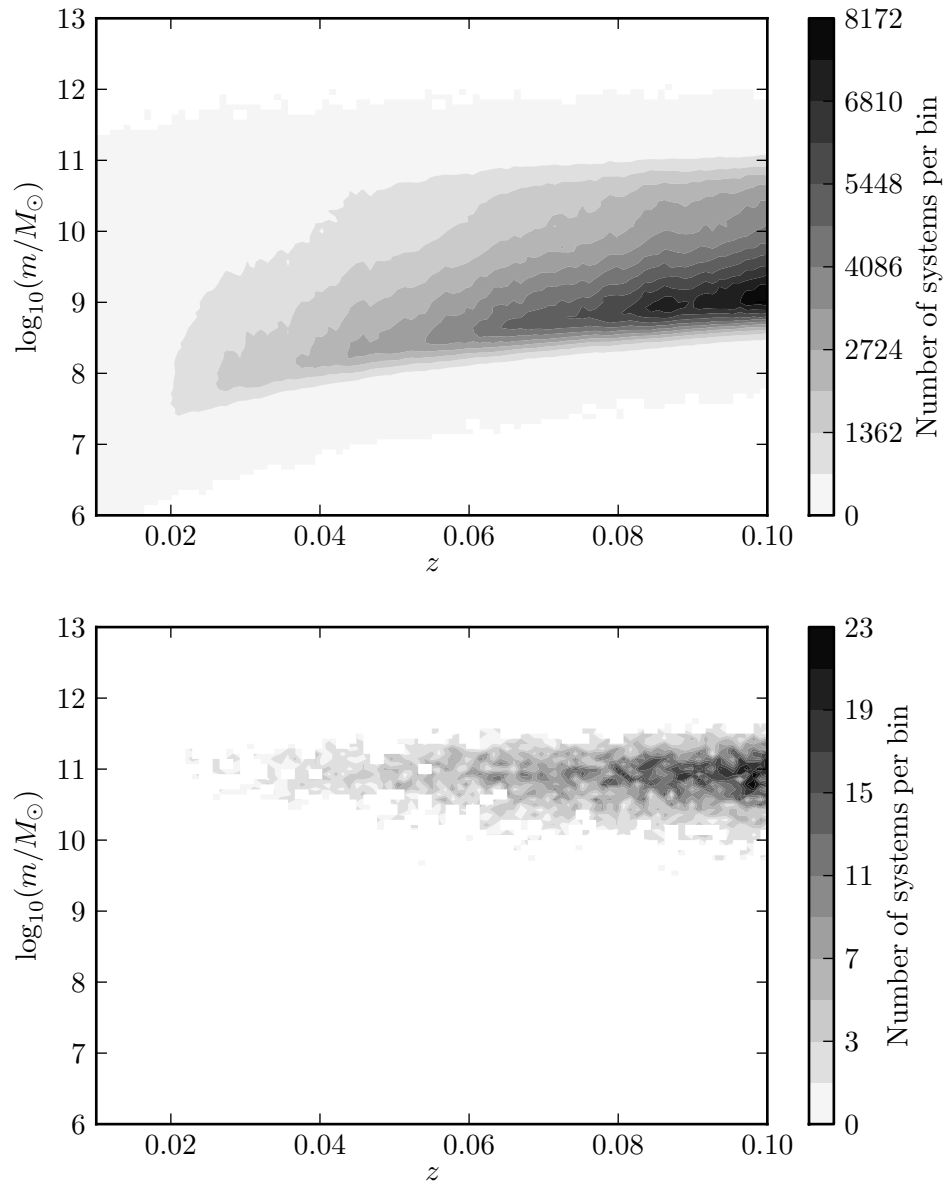


Figure 4.2: Contour plot of stellar mass versus redshift of the fake galaxy catalog (for systems with $z < 0.1$). Both axes are divided into 100 equal bins; the gray scale gives the number of systems contained in each z - m -bin. The upper plot considers all galaxies in the fake catalog, while the lower plot contains only B-galaxies.

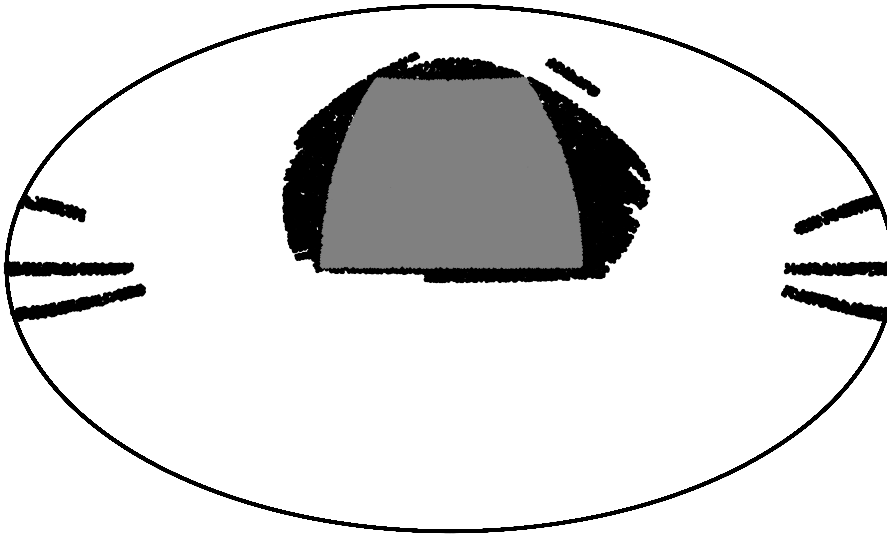


Figure 4.3: Two dimensional (Hammer) projection of the part of the sky covered by our real catalog (black area). The gray area is the border-free central region we have chosen as model for the redshift and mass distributions of real galaxies, in order to construct the adapted catalog.

properly account for the SDSS incompleteness.

Redshifts in the adapted catalog are *apparent redshifts*; these are the redshifts that would be measured if we were observers in the simulated universe, taking into account that galaxies have peculiar velocities. These apparent redshifts are included in the MS database (labeled z_{app} in the queries of Section 4.7).

We first select a region of the sky that is "almost completely included" in the SDSS spectroscopic catalog, i.e. far from the borders of the SDSS footprint. In Figure 4.3, a projected skymap of galaxies with spectroscopy is plotted. The selected border-free region is highlighted in gray; this area is limited by two fixed values of right ascension (RA) and declination (DEC), selected in such a way that the area is exactly 1/9th of the entire sky. The fake catalog is then divided into 9 regions of equal area. A z - m -histogram is calculated for the SDSS central region and for the 9 different patches of the simulated sky. In all histograms, the axes are divided into 100 bins; where redshifts and masses fulfill $z \in [0.01, 0.11]$, and $\log_{10}(m/M_{\odot}) \in [6, 13]$, respectively. Each histogram is thus a 100×100 matrix in which each element gives the number of systems with redshifts and masses in a particular z - m -bin. We compare each of the 9 histograms of the fake catalog with the SDSS histogram. If one z - m -bin from the fake catalog contains n more galaxies than the same pixel in the SDSS, n galaxies in that bin are randomly chosen and deleted from the fake catalog. On the other hand, if one pixel in the fake catalog contains less galaxies than the analogous SDSS pixel, nothing is done. This implies that the number of systems in the adapted catalog is slightly smaller than in the SDSS for some regions of the z - m -histogram; in fact, at the high-mass end, the fake catalog presents a small shortage of systems with respect to the real one (we will comment on this in Section 4.5). Finally, the adapted catalog is the result

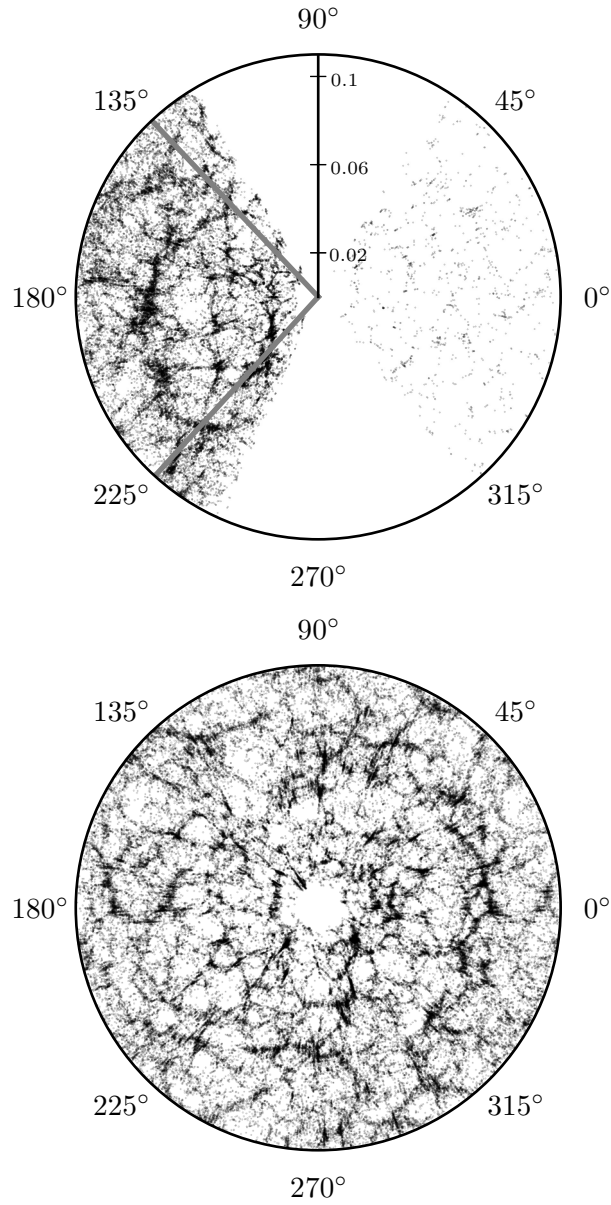


Figure 4.4: Sky distribution of galaxies (projected over the equatorial plane) with right ascension, declination, and redshift in the ranges $RA \in [0^\circ, 360^\circ)$, $DEC \in [1^\circ, 8^\circ]$, and $z \in [0.01, 0.11]$, respectively. The upper plot corresponds to the real catalog, and the lower one to the adapted catalog. The gray lines in the first plot delimit the region that has been chosen as reference to construct the adapted catalog (the gray region in Figure 4.3).

4 A new method to search for supermassive black hole binaries

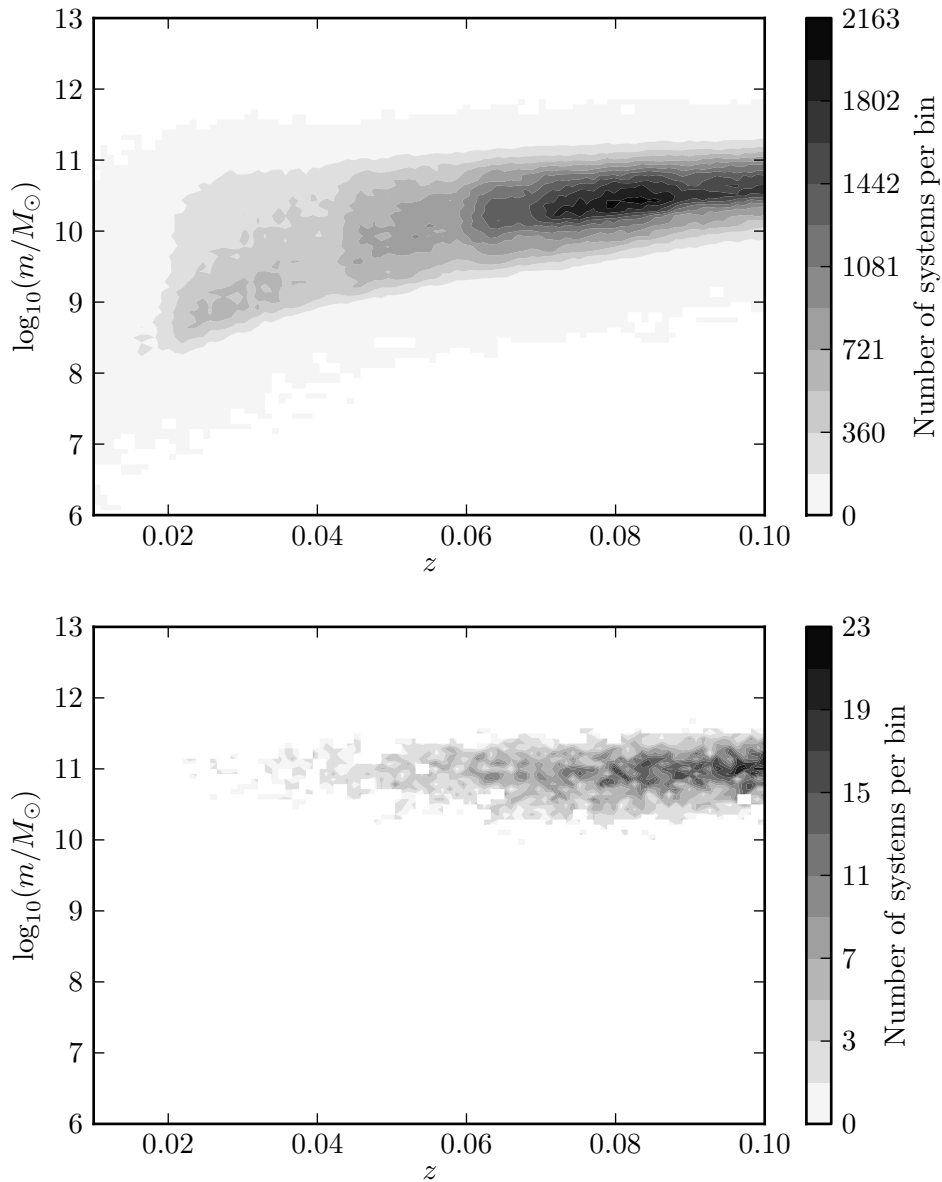


Figure 4.5: Contour plots of stellar mass versus apparent redshift of the adapted catalog. Both axes are divided into 100 bins; the gray scale gives the number of systems contained in each pixel. The upper plot considers all galaxies in the adapted catalog. This plot is to be compared with that of Figure 4.1 (but notice that the numbers of systems per z - m bin are larger here than on Figure 4.1, because the area of the sky covered by the real catalog is smaller than that of the adapted catalog). The lower plot is obtained for the subset of B-galaxies in the adapted catalog.

of combining the 9 sky regions of the fake catalog from which systems have been subtracted.

In Figure 4.4, a map of the real local universe (from the real catalog) is compared to a map of the simulated local universe (from the adapted catalog). The z - m -histogram of the adapted catalog is shown in the upper plot of Figure 4.5. This is, as expected, very similar to that of Figure 4.1, except for the fact that the real catalog contains less systems at each pixel, due to the smaller sky region that it covers. The lower plot of Figure 4.5 shows the z - m -histogram of B-galaxies in the adapted catalog.

4.3 Description of the searches

4.3.1 Probabilities of B-galaxies

In our searches, each system is characterized by a vector of parameters $\vec{\theta}$. We start here with the identification of B-galaxies through their peculiar mass and redshift distribution, therefore, for the time being, $\vec{\theta} = \{z, m\}$. For practical purposes, we divide each parameter range in 100 bins, so that the $z - m$ parameter space forms a matrix of 10^4 elements. We name a generic element of this matrix θ_i , where $i = 1, \dots, 10^4$. We now define two functions: $n_f^G(\theta_i)$ is the number of galaxies (B- or N-galaxies) in the fake catalog with parameters within θ_i ; $n_f^B(\theta_i)$ is the number of B-galaxies in the fake catalog with parameters within θ_i . The total number of galaxies in the fake catalog is thus

$$\mathcal{N}_f^G = \sum_i n_f^G(\theta_i). \quad (4.1)$$

Similarly,

$$\mathcal{N}_f^B = \sum_i n_f^B(\theta_i) \quad (4.2)$$

is the total number of B-galaxies in the fake catalog.

The probability of a system in the fake catalog being a B-galaxy, in the case of total ignorance about the parameters $\vec{\theta}$, is

$$p_f(\text{B}|I) = \frac{\mathcal{N}_f^B}{\mathcal{N}_f^G}, \quad (4.3)$$

which is our prior, using the typical notation and nomenclature of Bayesian statistics. The probability of a system in the fake catalog having z and m within θ_i , given that it is a B-galaxy, is

$$p_f(\theta_i|\text{B}) = \frac{n_f^B(\theta_i)}{\mathcal{N}_f^B}, \quad (4.4)$$

which is the likelihood. Equations (4.3) and (4.4) can be adapted to the case of N-galaxies; then,

$$p_f(\text{N}|I) = \frac{\mathcal{N}_f^G - \mathcal{N}_f^B}{\mathcal{N}_f^G} \quad (4.5)$$

is the probability of a system being an N-galaxy, in the absence of other information, and

$$p_f(\theta_i|\text{N}) = \frac{n_f^G(\theta_i) - n_f^B(\theta_i)}{\mathcal{N}_f^G - \mathcal{N}_f^B} \quad (4.6)$$

4 A new method to search for supermassive black hole binaries

is the probability of an N-galaxy having parameters within θ_i . Using Bayes' theorem, the probability of a system in the fake catalog being a B-galaxy, given that it has z and m within θ_i , is

$$p_f(\mathbf{B}|\theta_i) = p_f(\theta_i|\mathbf{B}) \frac{p_f(\mathbf{B}|I)}{p_f(\theta_i|I)}. \quad (4.7)$$

Here, the term in the denominator is the normalization, given by

$$p_f(\theta_i|I) = p_f(\theta_i|\mathbf{B}) p_f(\mathbf{B}|I) + p_f(\theta_i|\mathbf{N}) p_f(\mathbf{N}|I) = \frac{n_f^{\mathbf{G}}(\theta_i)}{\mathcal{N}_f^{\mathbf{G}}}. \quad (4.8)$$

Introducing Equations (4.3), (4.4), and (4.8) in (4.7), we get

$$p_f(\mathbf{B}|\theta_i) = \frac{n_f^{\mathbf{B}}(\theta_i)}{n_f^{\mathbf{G}}(\theta_i)}, \quad (4.9)$$

which is an expected result: the probability of a system within a z - m bin being a B-galaxy is just the ratio of the number of B-galaxies over the total number of galaxies in that pixel.

The same statistics can be applied to systems in the adapted catalog. The probability of a system in the adapted catalog to be a B-galaxy, given that it has z and m within θ_i , is

$$p_a(\mathbf{B}|\theta_i) = \frac{n_a^{\mathbf{B}}(\theta_i)}{n_a^{\mathbf{G}}(\theta_i)}, \quad (4.10)$$

where we have introduced $n_a^{\mathbf{G}}(\theta_i)$, the number of galaxies in the adapted catalog with parameters within θ_i , and $n_a^{\mathbf{B}}(\theta_i)$, the number of B-galaxies in the adapted catalog with parameters within θ_i . From now on, we will call $p_x(\mathbf{B}|\theta_i)$ the *B-galaxy probability* of a system of catalog x (where x can be 'f', 'a', or 'r', corresponding to the fake, adapted, or real catalog, respectively).

The number of B-galaxies in the real catalog, $n_r^{\mathbf{B}}(\theta_i)$, is (of course) unknown, but we do know $n_r^{\mathbf{G}}(\theta_i)$, the number of galaxies in the real catalog with parameters within θ_i . The function $n_r^{\mathbf{G}}(\theta_i)$ should be almost identical to $n_a^{\mathbf{G}}(\theta_i)$ (by construction of the adapted catalog), except for an overall normalization factor (given that the real catalog does not cover the entire sky). Then,

$$p_r(\mathbf{B}|\theta_i) = p_a(\mathbf{B}|\theta_i) \quad (4.11)$$

is assumed to be the probability of a system in the real catalog being a B-galaxy, given that it has z and m within θ_i .

Since we want to test the efficiency of the searches, the probability matrices $p_x(\mathbf{B}|\theta_i)$ (for $x = f$ or a) are calculated using systems of only one half of the sky (with $0^\circ \leq \text{RA} < 180^\circ$). These systems form the *training set*. Afterwards, the efficiency of the searches are tested (as will be explained in Section 4.4.2) using systems from the other half (with $180^\circ \leq \text{RA} < 360^\circ$), that form the *testing set*. Furthermore, the probability matrices $p_x(\mathbf{B}|\theta_i)$ are calculated as the average over 1000 realizations; in each realization, B- and N-galaxies are randomly chosen until covering 19.5% of the sky (the area of the SDSS spectroscopic footprint). In the case of $p_a(\mathbf{B}|\theta_i)$, in each realization we use a different adapted catalog (from a list of 100 different adapted catalogs, each one built as described in Section 4.2.3). This process reduces the amount of systems that are contained both in the training and in the testing sets (because of the repetitions of the simulated cube, mentioned in Section 4.2.2).

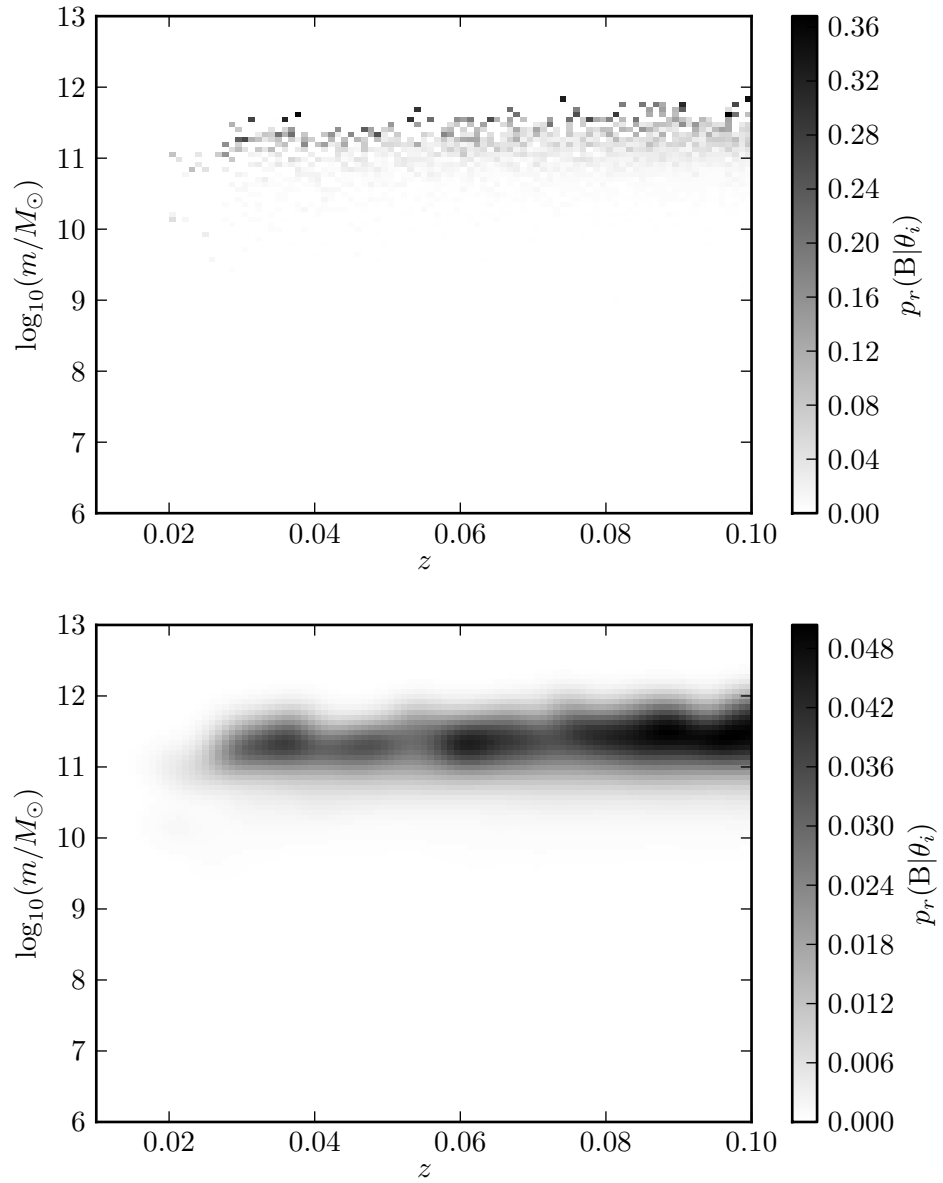


Figure 4.6: B-galaxy probability map as a function of redshift and mass, for systems in the adapted and real catalogs, i.e. $p_r(\mathbf{B}|\theta_i)$. The upper plot is the (unfiltered) average probability matrix obtained with the galaxies of the training set, as explained in the text. The lower plot shows the same matrix smoothed with a Gaussian filter; this is the probability matrix that will be used to assign B-galaxy probabilities to systems in the adapted and real catalogs.

An additional remark about the probabilities $p_x(\mathbf{B}|\theta_i)$ needs to be made. A certain galaxy may have z and m within a bin θ_i that contains zero B-galaxies, even when all bins around that particular one do contain B-galaxies. The B-galaxy probability would thus be zero for that system. But this would not be fair: the probabilities would strongly depend on the sizes of the z - and m -bins (since, for a different choice of the sizes, that bin θ_i would not be empty of B-galaxies). Moreover, our results would also depend too much on the particular realization of the universe that the MS provides. To avoid these biases, $p_x(\mathbf{B}|\theta_i)$ is smoothed with a two-dimensional Gaussian filter. The results nevertheless do not change significantly when using different types of filter or using no filter at all.

Finally, each system (from the fake, adapted, and real catalogs) is assigned a value of B-galaxy probability from the smoothed probability matrix $p_x(\mathbf{B}|\theta_i)$, depending on the z - m -bin θ_i it falls into. The unfiltered and filtered probability matrices are plotted in Figure 4.6.

4.3.2 Probabilities of PTA-galaxies

A galaxy is said to be a B-galaxy if, among other conditions mentioned in Section 4.2.2 or in Section 4.7, it is the descendant of two (or more, in the case of a multimerger) progenitors that existed only until the previous snapshot in the simulation. In other words, between a snapshot and the following one, two (or more) different galaxies became one. The resulting galaxy may or may not have a MBHB, depending on when the merger actually started and on the lifetime of the binary. We define the function $T^{\text{snap}}(z)$ as the interval of time elapsed between the current snapshot of a galaxy with redshift z and the previous one (in the fake catalog or in the adapted catalog).

During a galaxy merger several physical mechanisms contribute to shrink the distance between the two MBHs, the final one being the emission of GWs. At this stage, the time a MBHB spends emitting between two observed GW frequencies f_1 and f_2 can be calculated using the quadrupolar approximation, and gives

$$\tau(f_1, f_2) = \frac{5c^5[1+z]^{-8/3}}{256\pi^{8/3}[GM]^{5/3}} \left[f_1^{-8/3} - f_2^{-8/3} \right]. \quad (4.12)$$

Here, c and G are the speed of light and the gravitational constant, respectively, and

$$\mathcal{M} = \frac{[m_{\text{BH}}^1 m_{\text{BH}}^2]^{3/5}}{[m_{\text{BH}}^1 + m_{\text{BH}}^2]^{1/5}} \quad (4.13)$$

is the chirp mass of a binary composed of two MBHs of masses m_{BH}^1 and m_{BH}^2 . The lighter the mass of the binary, the longer the time interval it spends emitting in a certain frequency interval. We disregard the other mechanisms of energy loss that may play an important role when the binary orbits at distances larger than ~ 0.1 parsec. These mechanisms would enhance the loss of angular momentum at low frequencies, reducing the amount of time the MBHB is emitting GWs [112, 220]. The inclusion of these effects in the calculations could be subject of future work.

The GWs produced by a MBHB in a quasicircular orbit, at observed GW frequency f , would produce a strain amplitude of

$$h_0 = \frac{2[GM]^{5/3} [\pi f [1+z]]^{2/3}}{c^4 r(z)}. \quad (4.14)$$

Here, the function $r(z)$ is the comoving distance between Earth and a galaxy of redshift z , given in a Λ CDM universe by

$$r(z) = \frac{c}{H_0} \int_0^z [\Omega_m[1+z']^3 + \Omega_\Lambda]^{-1/2} dz'. \quad (4.15)$$

The values assumed for the cosmological parameters H_0 , Ω_m , and Ω_Λ are the ones given in Section 4.2.2 (we use different parameters for systems from the MS and from the MPA/JHU). The maximum frequency at which a system can be observed is

$$f_{\text{iso}} = \frac{c^3}{6\sqrt{6}\pi G[m_{\text{BH}}^1 + m_{\text{BH}}^2][1+z]}, \quad (4.16)$$

which is the frequency of the last stable orbit. On the other hand, the minimum frequency that can be observed is chosen in such a way that the interval of time until the coalescence is not longer than 0.1 Gyr; we assume that, at lower frequencies, other mechanisms of energy loss would dominate over the GW emission.

The PTA is sensitive to GWs within a certain interval of observed frequencies $[f_{\text{min}}, f_{\text{max}}]$. We choose this *frequency window* to be

$$[f_{\text{min}}, f_{\text{max}}] = [[10 \text{ yr}]^{-1}, [1 \text{ week}]^{-1}]. \quad (4.17)$$

The lower limit is given by the duration of the PTA campaign; we take 10 years as a default value. The upper limit is set by the cadence of individual pulsar observations, typically of one per week. The exact choice of this upper limit does not make any difference in the results, since we do not expect observable sources at such high frequencies anyway. The PTA frequency window $[f_{\text{min}}, f_{\text{max}}]$ is divided into 100 frequency bins, equally separated in logarithmic scale. Galaxies are assigned a probability of being PTA-galaxies at each frequency bin, i.e. they are assigned the probability of producing a strain amplitude larger than a certain threshold within a certain observed interval of frequencies.

Let us first calculate the probability of a system to be a PTA-galaxy at a certain frequency bin, assuming that it is a B-galaxy that contains a binary. To calculate this probability, $p_x(\text{P}|\text{B}; \mathcal{M}, f)$, we follow an iterative process. In each realization (of a total of 100), a total black hole mass m_{BH} is drawn from a log-normal distribution, with mean given by the fitting formula from [157],

$$\log_{10} \left(\frac{m_{\text{BH}}}{M_\odot} \right) = 8.46 + 1.05 \log_{10} \left(\frac{m_{\text{bulge}}}{10^{11} M_\odot} \right), \quad (4.18)$$

and standard deviation $\sigma = 0.34$. In Equation (4.18), m_{bulge} is the mass of the galactic bulge. Bulge masses are obtained directly from the MS database for systems in the fake and adapted catalogs (called `bulgemass` in the first query of Section 4.7); in Section 4.4.6 we explain how to calculate m_{bulge} for galaxies in the real catalog. To avoid considering very light MBH masses⁶, we discard all MBHs with masses smaller than $10^6 M_\odot$. The mass ratio of the binary, $q = m_{\text{BH}}^1/m_{\text{BH}}^2$ (with $m_{\text{BH}}^1 \leq m_{\text{BH}}^2$), is drawn at each realization from the distribution of the mass ratios of progenitors' black hole masses in the fake catalog. Hence, at each realization we

⁶We point out that the minimum black hole mass found among B-galaxies in the fake catalog is of $10^{6.2} M_\odot$.

4 A new method to search for supermassive black hole binaries

have $m_{\text{BH}}^1 = q m_{\text{BH}}$, and $m_{\text{BH}}^2 = m_{\text{BH}} - m_{\text{BH}}^1$. Then, the probability that a galaxy, assuming it contains a MBHB, of catalog x with redshift z is detectable by the PTA for a given minimum strain amplitude h_0^{thres} (the strain amplitude threshold) at a certain observed frequency bin $[f_1, f_2]$, is

$$p_x(\text{P}|\text{B}; \mathcal{M}, f) = \frac{1}{100} \sum_j^{100} p_x^j(\text{P}|\text{B}; \mathcal{M}, f). \quad (4.19)$$

Here, $f = (f_1 + f_2)/2$ is the central frequency of the bin, j denotes the number of the realization, and

$$p_x^j(\text{P}|\text{B}; \mathcal{M}, f) = \begin{cases} \min\left(1, \frac{\tau(f_1, f_2)}{T^{\text{snap}}(z)}\right) & \text{if } h_0 \geq h_0^{\text{thres}} \\ 0 & \text{if } h_0 < h_0^{\text{thres}} \end{cases}. \quad (4.20)$$

In the previous equation we have introduced the function $\min(\)$, to avoid probabilities larger than unity⁷.

Now, applying the product rule, the probability that a galaxy with z and m within θ_i , and MBHB chirp mass \mathcal{M} (if the galaxy hosts a MBHB), is a B-galaxy and a PTA-galaxy in a frequency bin centered at f is

$$p_x(\text{B}, \text{P}|\theta_i, \mathcal{M}, f) = p_x(\text{B}|\theta_i) p_x(\text{P}|\text{B}; \mathcal{M}, f). \quad (4.21)$$

Finally, the *PTA-galaxy probability* is

$$p_x(\text{B}, \text{P}|\theta_i, \mathcal{M}) = \sum_k p_x(\text{B}|\theta_i) p_x(\text{P}|\text{B}; \mathcal{M}, f_k), \quad (4.22)$$

where f_k is the center of a frequency bin; the summation sweeps all frequency bins within the PTA window (as long as the frequency of the last stable orbit, f_{iso} , is not exceeded, and the interval of time until the coalescence is not longer than 0.1 Gyr). The PTA-galaxy probability of a system (with m and z within θ_i) in catalog x is, therefore, its probability to be a B-galaxy that contains a MBHB (of chirp mass \mathcal{M}) producing a strain amplitude larger than h_0^{thres} within the PTA frequency band.

Note that later on we want to apply this machinery to galaxies in the real catalog, where we do not know with certainty which systems are B-galaxies. For this reason we calculate $p_x(\text{B}, \text{P}|\theta_i, \mathcal{M})$ for all galaxies in the different catalogs, even if we know that they are N-galaxies. Also note that it is meaningless to talk about snapshots of the real catalog (we observe only one snapshot of the universe); however, we expect the probabilities $p_x^j(\text{P}|\text{B}; \mathcal{M}, f)$ to have a similar behaviour in the simulated universe and in the real one. Hence we keep the definition of Equation (4.20) to calculate $p_x^j(\text{P}|\text{B}; \mathcal{M}, f)$, where $T^{\text{snap}}(z)$ is the time between snapshots in the simulation.

⁷This, in practice, does not affect the results, since massive binaries never spend a time exceeding $T^{\text{snap}}(z)$ at an observable PTA frequency interval.

4.3.3 Including clustering in the search

We find that B-galaxies tend to cluster differently than N-galaxies (as will be shown in Section 4.4.1); this fact motivates us to refine the search by adding information about the clustering of galaxies. Characterizing galaxies by means of their clustering properties is a common technique in observational astrophysics (see for example [128, 251]). These investigations are usually carried out by using the two-point correlation function (TPCF, [173, 86]), which is defined by the joint probability of finding an object simultaneously in two volume elements separated by a certain distance. The comoving distance between two galaxies is simply calculated as

$$D_{1,2} = \sqrt{[X_2 - X_1]^2 + [Y_2 - Y_1]^2 + [Z_2 - Z_1]^2}, \quad (4.23)$$

where (X_j, Y_j, Z_j) are the Cartesian coordinates of galaxy j (for $j \in \{1, 2\}$), related to the equatorial coordinates by

$$\begin{cases} X_j = r(z) \cos(\text{DEC}) \cos(\text{RA}) \\ Y_j = r(z) \cos(\text{DEC}) \sin(\text{RA}) \\ Z_j = r(z) \sin(\text{DEC}) \end{cases} . \quad (4.24)$$

These same equations are applied to obtain the positions of galaxies in the fake, the adapted, and the real catalog. In the adapted and real catalogs z is affected by the peculiar movement of galaxies, but we neglect this effect when calculating distances. The comoving distance $r(z)$ is defined in Equation (4.15), and the cosmological parameters are given in Section 4.2.2. One can find several definitions for the TPCF in the literature [50, 122, 86], which account for possible biases and selection effects of the catalog. The TPCF is thus a statistical tool that can be used to characterize the clustering of an ensemble of point particles; it is meaningless to talk about the TPCF of an individual galaxy.

Instead, we introduce the *number of neighbors at different shells* (NNDS): this is a set of numbers that measures how many galaxies are contained in spherical comoving shells around a selected object. For simplicity, we will use the term NNDS both for an ensemble of systems (in which case it denotes the average NNDS over all systems of the ensemble) and for individual systems. The systems for which the NNDS is calculated (i.e. systems that are at the centers of the shells when counting neighbors) are called *foreground galaxies*. The rest of the systems (that may be counted as neighbors of some other foreground galaxies) are *background galaxies*. For the calculation of the NNDS, systems in the *adapted* catalog will always be the foreground galaxies; we then investigate two different cases:

1. All galaxies of the fake catalog are considered as background galaxies. Redshifts are not affected by peculiar velocities (they are cosmological redshifts).
2. The set of background galaxies is the same as that of foreground galaxies (i.e. galaxies of the adapted catalog). Redshifts are affected by peculiar velocities (they are apparent redshifts).

The first case corresponds to an idealized case in which we have perfect knowledge of the positions of all galaxies in the universe. The second is a more realistic approach: the positions of galaxies cannot be precisely calculated (because we do not know the velocity and direction of the peculiar movement of the galaxies), and not all galaxies can be observed. For both cases,

the NNDS is calculated for different *shell sets*, corresponding to different choices of the shells' sizes. The borders of the shells of some of the sets are separated linearly, and some other logarithmically. The number of shells in all sets equals 50.

Let us consider case (ii) and a shell set made of 50 shells with borders linearly separated by 400 kpc. For each galaxy, we count the number of neighboring galaxies at a distance of less than 400 kpc; then we count the neighbors that are between 400 kpc and 800 kpc away, then between 800 kpc and 1200 kpc, etc. We keep counting neighbors at different shells until reaching a maximum distance of 20 Mpc (which corresponds to the 50th shell) from the initial galaxy. Then we average (over all galaxies) the number of neighbors at each shell. This is shown in the upper plot of Figure 4.7. The dotted curve shows the NNDS of systems inside the selected central region of the SDSS sky (the gray area in Figure 4.3). The solid line is the NNDS of all systems in the adapted catalog (the filled area contains the NNDS of each of the 9 patches of the sky in which the fake catalog is divided). The NNDS is also calculated for systems (in the redshift range $[0.01, 0.1]$) from the entire real catalog, including the region outside the selected central one (dotted-dashed curve). The latter NNDS is affected by border effects: galaxies close to the border of the observed area of the sky (those galaxies on the black area of Figure 4.3) have fewer neighbors. This effect is increasingly important (and the dotted-dashed line differs more from the other two) as more distant shells are considered. The dotted and solid lines agree quite well, even if there are other sources of incompleteness in the SDSS catalog (besides the effect of the border of the observed sky area) that are not taken into account.

As we mentioned in Section 4.2.2, the MPA/JHU uses different cosmological parameters than the MS. In the upper plot of Figure 4.7, distances of systems from the real catalog are calculated with the cosmological parameters used by the MPA/JHU; in the lower plot, these distances are calculated with the same parameters used by the MS, and the agreement is much better. The difference between these plots is the effect of the different sets of cosmological parameters. In order to properly compare the NNDS of the adapted and real catalogs, it would be convenient to use the updated simulated galaxy catalog of the MS [84] (this issue is commented on in Section 4.5).

In Section 4.3.1 we described a search in which each system is characterized by two parameters, z and m ; we now describe a search, carried out with a MLA, in which galaxies are characterized by a vector of 52 parameters, $\vec{\theta} = \{z, m, \text{NNDS}^1, \dots, \text{NNDS}^{50}\}$, where NNDS^k gives the number of neighbors at the shell k (which goes from 1 to 50). Machine learning is a growing subject of Artificial Intelligence, and include a vast variety of techniques, in which a program is trained on a number of samples of data (which are characterized by one or more parameters $\vec{\theta}$ called *features*), and tries to predict the characteristics of different sets of data. We use supervised learning methods of the Scikit-learn⁸ [171] library of Python⁹ [57]; in particular, a method that seems to be particularly fast and effective is the Stochastic Gradient Descent. The algorithm uses a training set as a playground to set up the engine that afterwards assigns a probability of being a B-galaxy, $p_x(\text{B}|\vec{\theta})$, to each of the elements in a testing set¹⁰.

The sky of the simulated universe is divided in 9 patches; the systems in one of them make up our testing set. We subtract from the rest of the sky all systems which `galID` is contained in

⁸scikit-learn.org

⁹<http://www.python.org/>

¹⁰The mathematical machinery that is used by the algorithm to obtain these probabilities can be consulted at <http://scikit-learn.org/stable/modules/sgd.html>.

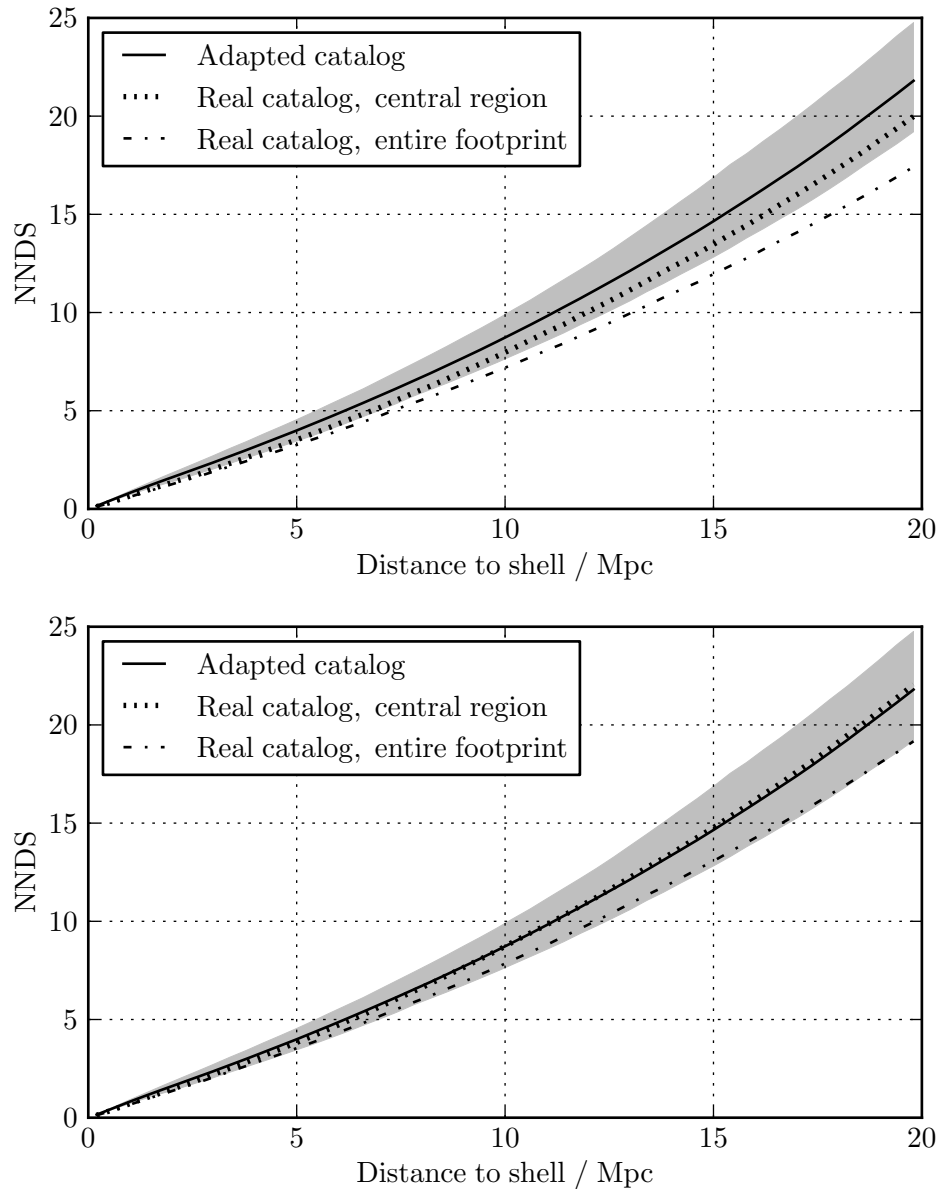


Figure 4.7: Average number of neighbors at different shells (NNDS) of systems in the adapted catalog (solid line), in the real catalog (dotted-dashed line), and in a volume of the real catalog that is not affected by the borders of the observed area of the sky (dotted line). The filled area contains the NNDS of each of the 9 patches into which the adapted catalog is divided. The number of neighbors is counted for each galaxy at 50 shells with borders equally separated by 400 kpc. For the upper plot, distances between systems of the real catalog are calculated assuming the cosmological parameters used by the MPA/JHU, whereas for the lower plot the parameters are those of the MS.

the testing set. This subtraction is performed to avoid systems in the training and in the testing set to be equal (these repetitions would artificially enhance the efficiency of the search). Then, from the part of the sky outside the testing set, we randomly pick 50% of B-galaxies and 5% of N-galaxies, to construct the training set¹¹. The training set is used as input for the MLA. Then, the MLA calculates the probabilities $p_x(\mathbf{B}|\vec{\theta})$ of systems in the testing set. In Section 4.4.4 we show the efficiency of this search.

4.3.4 Extending the search to larger redshifts

The search in which the clustering is taken into account (described in Section 4.3.3) is performed at redshifts below 0.1. We do not attempt to extend this search to larger redshifts for several reasons. Firstly, the completeness of a spectroscopic catalog decreases with distance; the distinct features that are found in the NNDS of B-galaxies will vanish as more neighbors become unobservable. Secondly, we expect that the method we use to build the adapted catalog will be less trustworthy (regarding the clustering) at larger redshifts. Finally, as will be shown in Section 4.4.4, the inclusion of the NNDS in the search for B-galaxies is already quite ineffective in the local universe; there is no reason why it should improve for $z > 0.1$. Therefore, we spare ourselves the computationally intricate task of calculating the NNDS at larger redshifts.

On the other hand, the simple Bayesian search described in Section 4.3.1 can be easily extended to z_{\max} . As Equations (4.9), (4.10), and (4.11) reveal, the only information we need to assign probabilities is the number of galaxies and B-galaxies within different z - m -bins. We do not need to download all systems with $z < 0.7$ from the MS database, but just a z - m -histogram of components $n_f^G(\theta_i)$, which means 10^4 integer numbers (for the choice of a 100×100 z - m -grid) with the numbers of galaxies within each pixel, and a histogram of components $n_f^B(\theta_i)$, with the number of B-galaxies. In Figure 4.8, z - m -histograms of galaxies and B-galaxies from the fake catalog up to z_{\max} are displayed as contour plots. For this extended fake catalog, apparent redshifts are used.

There is a simple way to construct an adapted catalog using only the functions $n_f^G(\theta_i)$ and $n_f^B(\theta_i)$, and the function $n_r^G(\theta_i)$. The histogram components $n_a^G(\theta_i)$ and $n_a^B(\theta_i)$ can be calculated as

$$n_a^G(\theta_i) = \min \left(1, \frac{n_r^G(\theta_i)}{n_f^G(\theta_i)} \right) n_f^G(\theta_i), \quad (4.25)$$

and

$$n_a^B(\theta_i) = \min \left(1, \frac{n_r^G(\theta_i)}{n_f^G(\theta_i)} \right) n_f^B(\theta_i). \quad (4.26)$$

What we are imposing here is that the number of systems in a certain z - m -bin of the adapted catalog cannot be larger than the same bin of the real catalog. Figure 4.9 is analogous to 4.8, but for galaxies and B-galaxies of the adapted catalog.

Once we have the functions $n_f^B(\theta_i)$ and $n_f^G(\theta_i)$ we can construct the B-galaxy probabilities in the extended fake catalog, $p_f(\mathbf{B}|\theta_i)$, using Equation (4.9). Analogously, with the functions $n_a^B(\theta_i)$ and $n_a^G(\theta_i)$, the probabilities for the extended adapted and real catalogs can be calculated

¹¹Notice that the exact amount of B- and N-galaxies in the training set is not relevant for the results; one just needs to be sure that one has a large enough number of systems of each class to train the MLA properly.

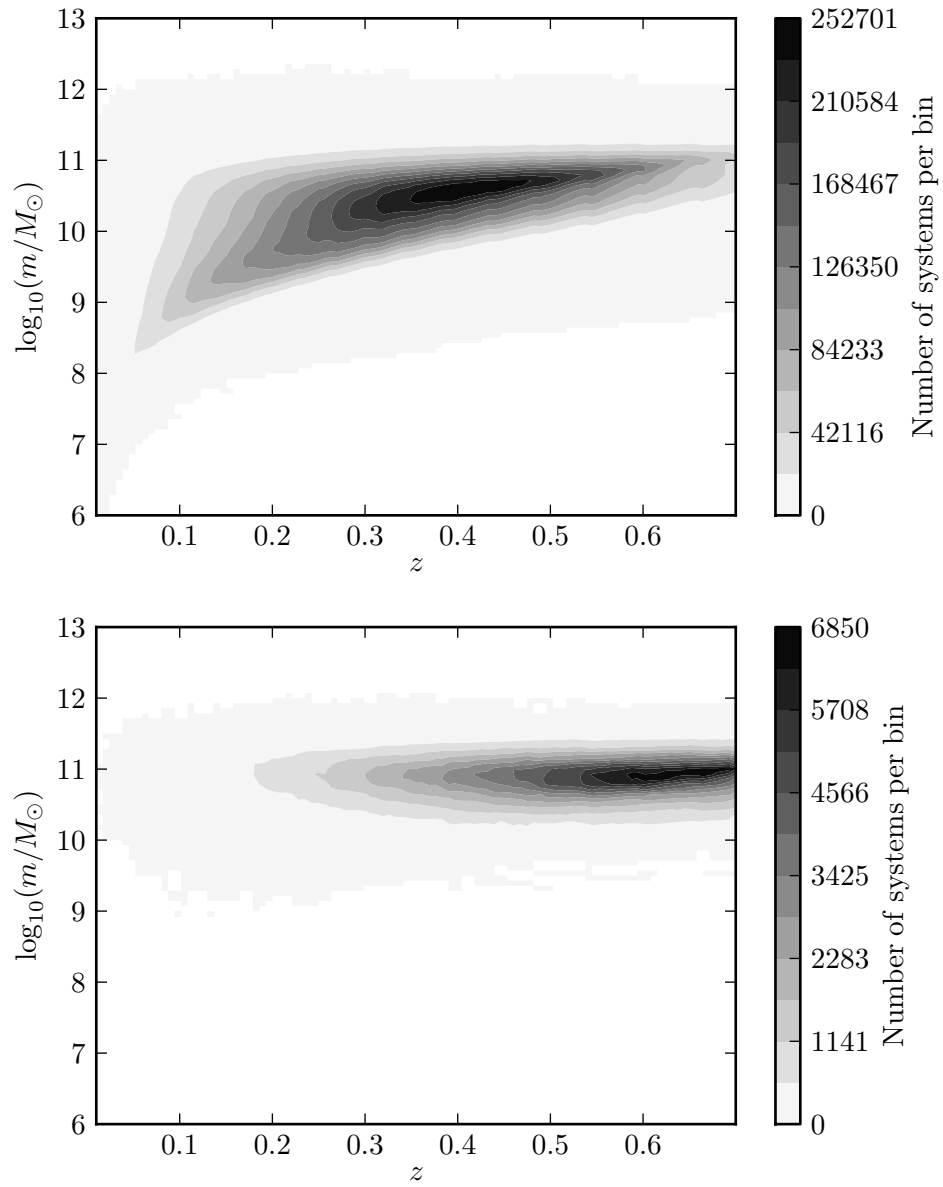


Figure 4.8: Contour plots of stellar mass versus apparent redshift of the entire fake catalog (with $z < 0.7$). Both axes are divided into 100 bins; the gray scale gives the number of systems contained in each pixel. Upper and lower plots consider all galaxies and B-galaxies, respectively.

4 A new method to search for supermassive black hole binaries

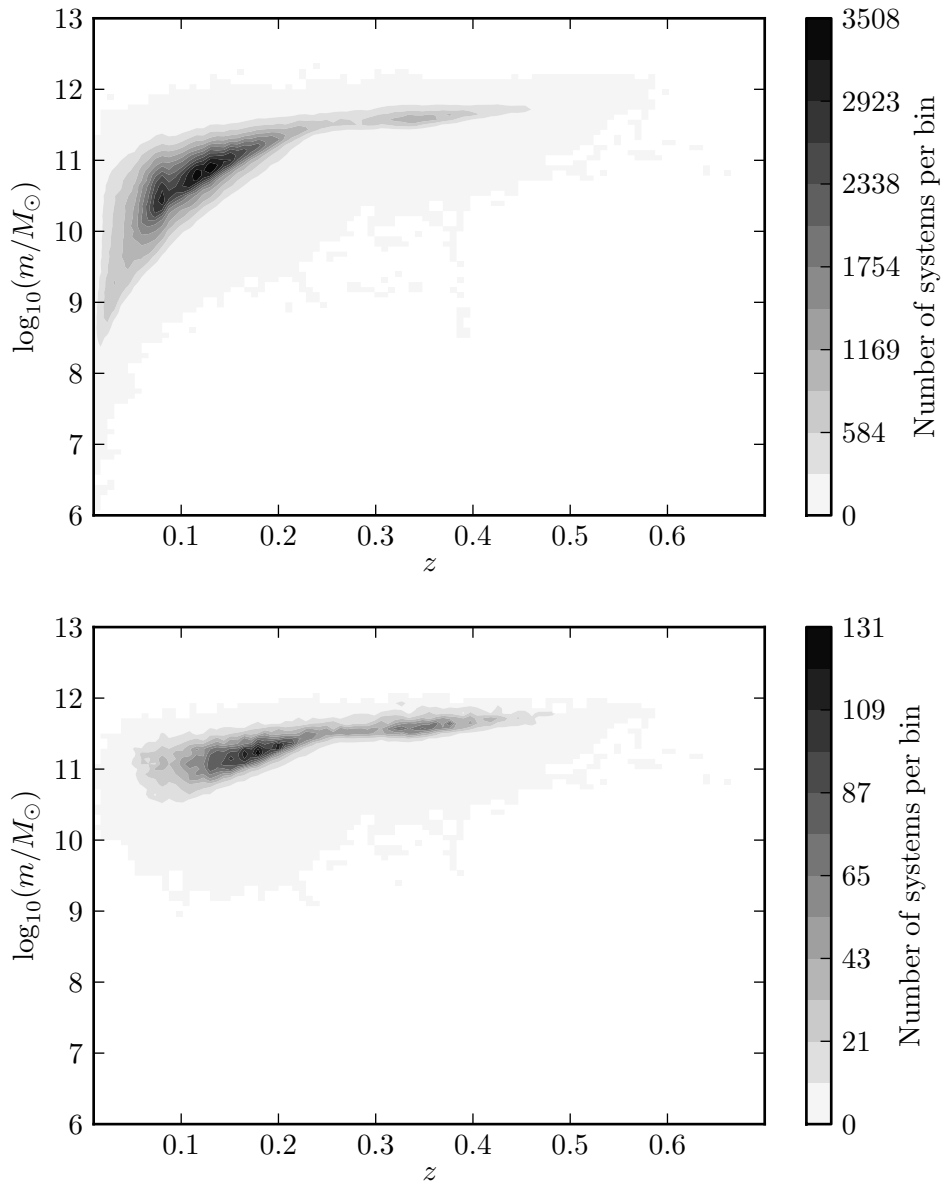


Figure 4.9: Contour plots of stellar mass versus apparent redshift of the extended adapted catalog (that includes systems with $z < 0.7$). Both axes are divided into 100 bins; the gray scale gives the number of systems contained in each pixel. Upper and lower plots consider all galaxies and B-galaxies, respectively.

using Equations (4.10) and (4.11), respectively. Finally, the probabilities $p_x(\mathbf{B}|\theta_i)$ are smoothed with a Gaussian filter, as performed at $z < 0.1$.

4.4 Results

4.4.1 Clustering of B-galaxies

In Section 4.3.3 we mentioned that B-galaxies present a characteristic clustering that could be used to distinguish them from N-galaxies; we now present this distinct shape of the NNDS of B-galaxies, and check how significantly it differs from the NNDS of N-galaxies, when using the fake and the adapted catalogs. First, the NNDS of B-galaxies, NNDS_B , needs to be calculated. Then, for each B-galaxy, we find an N-galaxy that has similar mass and redshift of that B-galaxy (the matching tolerances are $\Delta \log_{10}(m/M_\odot) = 0.1$ and $\Delta z = 0.001$). The NNDS of these selected N-galaxies is calculated, NNDS_N . The mean NNDS at each shell is obtained both for B- and for N-galaxies. In Figure 4.10 the ratio $\text{NNDS}_B/\text{NNDS}_N$ is plotted; the upper plots correspond to case (i) (as described in Section 4.3.3), in which all systems from the fake catalog can be counted as neighbors; the lower plots correspond to case (ii), and only systems from the adapted catalog can be background galaxies. The plots on the left are obtained for a set of shells with borders linearly separated by 400 kpc. The borders of the shells used for the right plots are logarithmically separated from 1 kpc to 10 Mpc. The error of NNDS_B and NNDS_N is assumed to be the square root of the variance of the mean; the error bars in Figure 4.10 are the propagated error of the ratio of both quantities. We point out that the error bars in the lower right plot are not meaningful at small distances; within those small shells, galaxies in the adapted catalog usually count zero or at most a few neighbors.

There are two reasons why the ratio $\text{NNDS}_B/\text{NNDS}_N$ is closer to one for systems in the adapted catalog. Firstly, distances in the adapted catalog are calculated using apparent redshifts (affected by peculiar velocities), which introduce some level of randomness in the positions of the neighbors. Secondly, many of the neighbors have been deleted in the process of building the adapted catalog, so the amount of information contained in the NNDS is smaller than when observing all galaxies.

Figure 4.10 shows the interesting fact that B-galaxies present an underdensity of galaxies at ~ 1 Mpc scale, when compared to N-galaxies of same redshift and mass. A similar pattern has already been found in the TPCF of narrow-line AGN in SDSS data (see for example Figure 3 of [127] but notice that, in that paper, projected proper distances are used, instead of spatial comoving distances). They find that this pattern is also typical of galaxies placed at the center of their dark matter halos, where AGN preferentially reside. It is thus interesting to check whether or not the underdensity of neighbors is due to the relative position of B-galaxies within their halos. This information can also be extracted from the MS database, by means of the parameter `type` (see Section 3.6 of [83]). Galaxies of `type` 0 are the principal galaxies of their halos, whereas `type` 1 and 2 are satellite galaxies. In the fake catalog we find that 80% of B-galaxies are of `type` 0, and 20% of `type` 1. No B-galaxy has `type` 2 (which corresponds to the so-called *orphan galaxies*). We construct a sample of N-galaxies that match mass, redshift, and `type` of the B-galaxies (this is the reason why the parameter `type` is included in the query of Section 4.7), and recalculate NNDS_B , NNDS_N , and the ratio of both. In the upper plot of Figure 4.11 we show the NNDS of B- and N-galaxies of `type` 0 and 1; the ratio $\text{NNDS}_B/\text{NNDS}_N$ is

4 A new method to search for supermassive black hole binaries

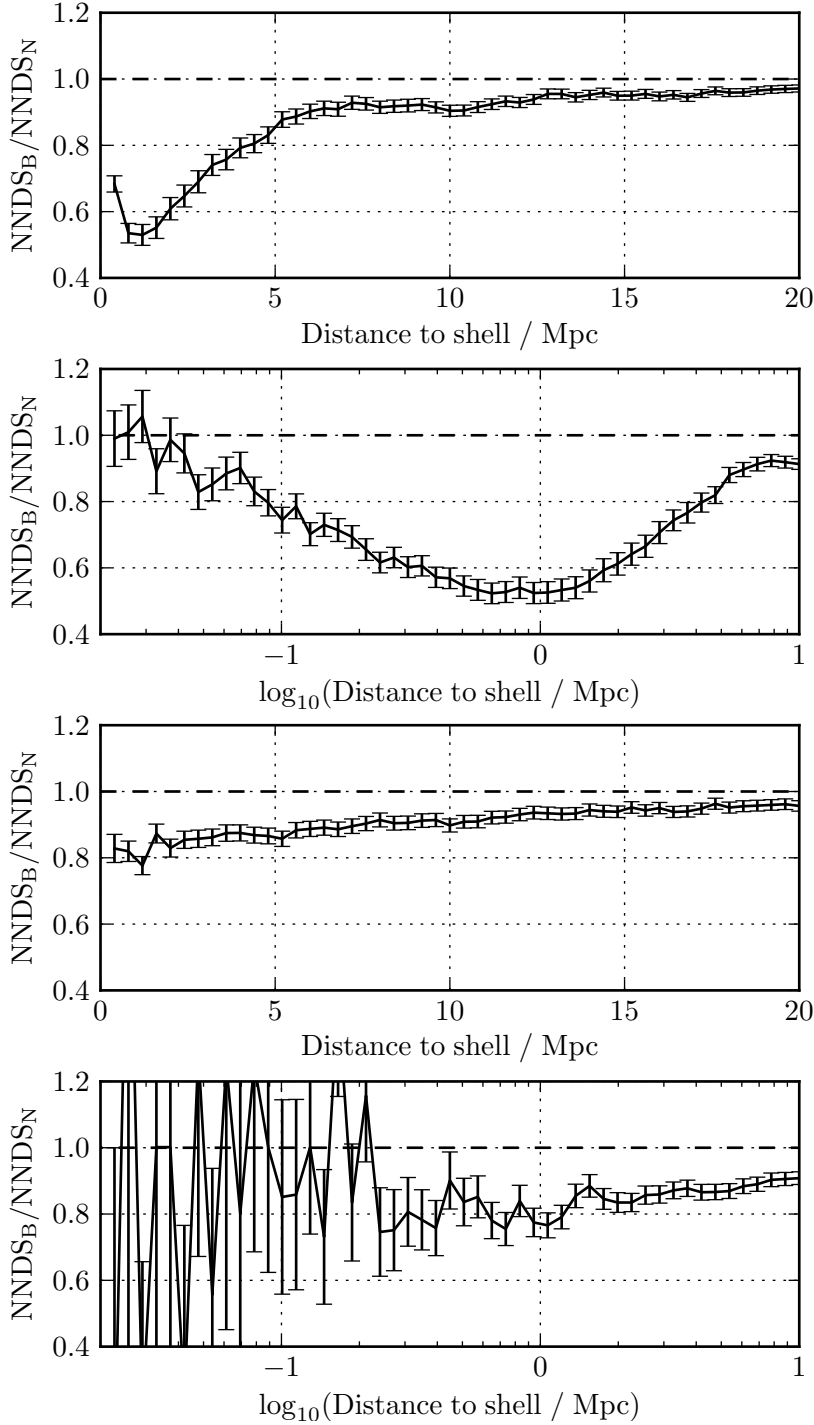


Figure 4.10: Ratio of the NNDS of B-galaxies over the one of N-galaxies, i.e. $\text{NNDS}_B / \text{NNDS}_N$, for systems in the fake catalog (upper plots) and in the adapted catalog (lower plots). N-galaxies are chosen to have the same masses and redshifts as B-galaxies (with matching tolerances of $\Delta \log_{10}(m/M_\odot) = 0.1$ and $\Delta z = 0.001$). Left and right plots correspond to different shell sets: shells with borders linearly separated from 0 to 20 Mpc (left) and logarithmically separated from 1 kpc to 10 Mpc (right). Similar patterns are found when using other shell sets and for other choices of matching N-galaxies. See the text for an explanation on the sizes of the error bars.

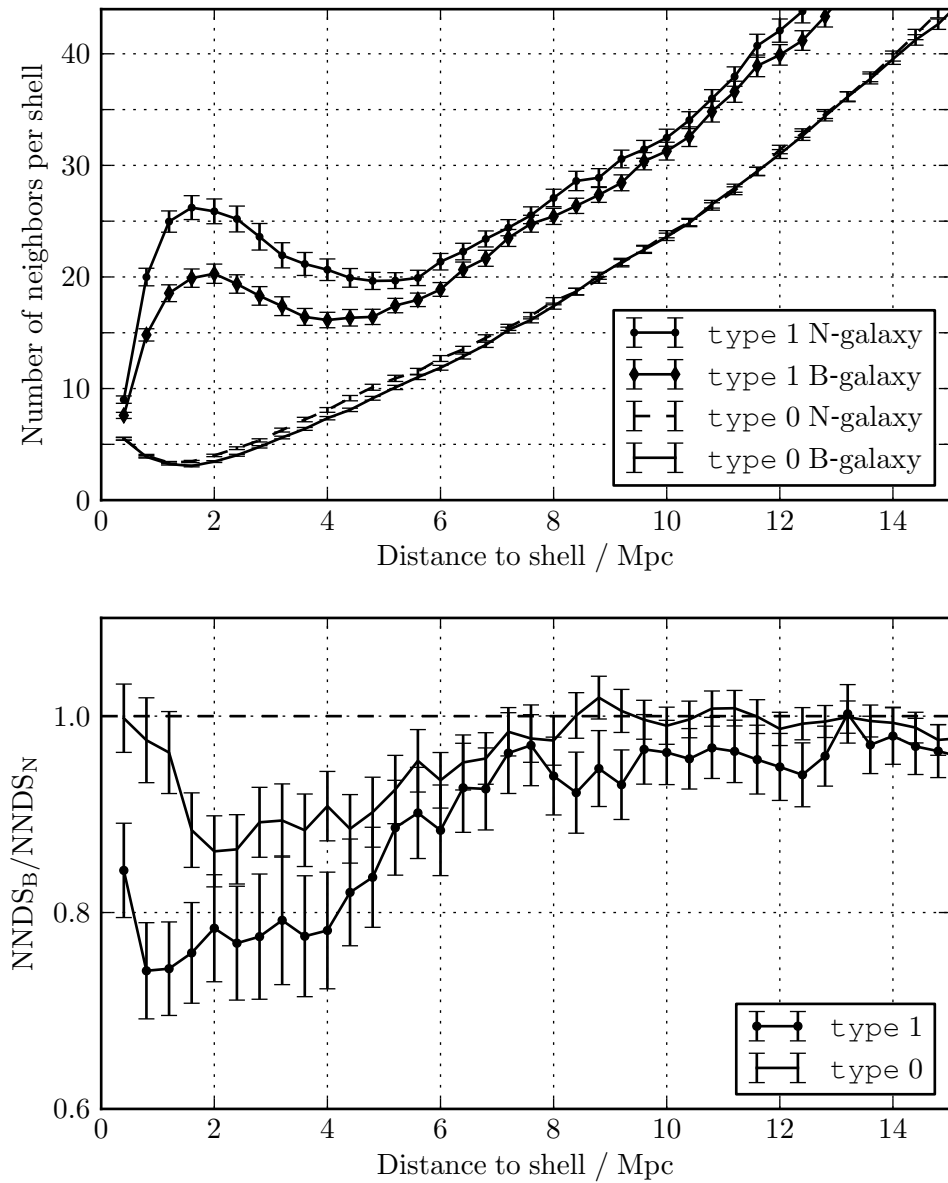


Figure 4.11: The upper plot shows the NNDS of N- and B-galaxies from the fake catalog, of *type* 0 and 1 (which determines the relative position of the galaxies in their dark matter halos). Galaxies of *type* 0 are central galaxies of their halo, whereas galaxies *type* 1 are associated to a non-dominant subhalo. The ratios $\text{NNDS}_B/\text{NNDS}_N$ of galaxies of same *type* are plotted below. N-galaxies are chosen in such a way that they match redshift, mass, and *type* of B-galaxies.

4 A new method to search for supermassive black hole binaries

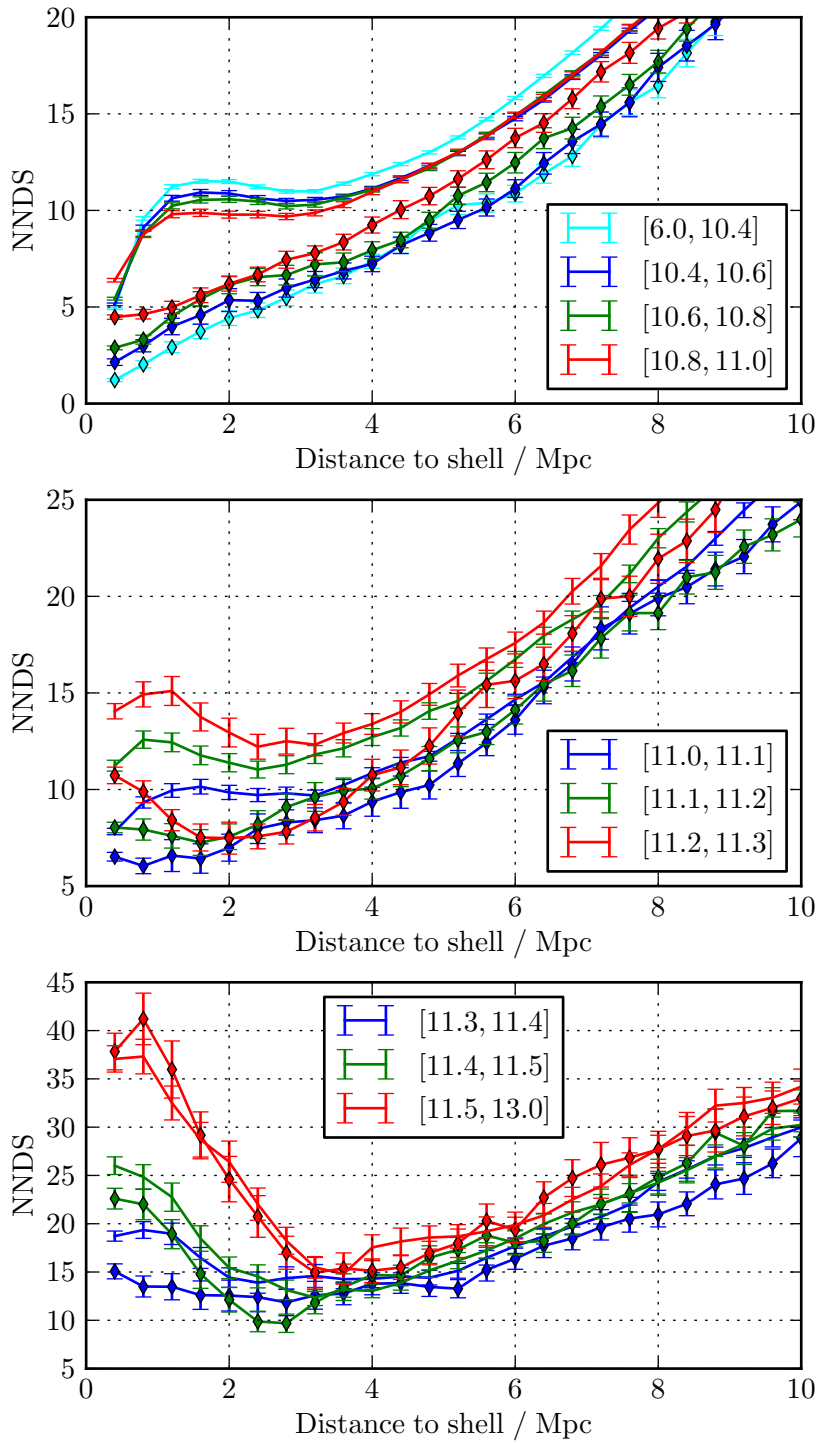


Figure 4.12: NNDS of B- and N-galaxies within different ranges of masses. Different intervals of masses m (depicted in the legends in units of $\log_{10}(m/M_{\odot})$) correspond to different colors. The NNDS of N- and B-galaxies are plotted using points and diamonds, respectively.

shown in the lower plot. There we see that, in the case of `type 0` galaxies, the underdensity is due to ~ 1 neighbor at distances of a few Mpc, hence the clustering of `type 0` B- and N-galaxies of similar masses and redshifts are almost indistinguishable. B-galaxies of `type 1`, however, still present a significant underdensity of neighbors with respect to matching N-galaxies at around 1 Mpc.

In Figure 4.12 we show the NNDS of B- and N- galaxies at different mass intervals. Galaxies within the same mass interval have NNDS displayed with the same color; the NNDS of B-galaxies is marked with diamonds. Here one can clearly see that B-galaxies have on average fewer neighbors (especially at distances of a few Mpc) than N-galaxies of similar masses. An important feature to note is that the larger the mass is, the larger the number of neighbors becomes, both for B- and for N-galaxies.

An interesting question is whether or not PTA-galaxies are more likely to be found in galaxy clusters. In a previous section we defined PTA-galaxies as B-galaxies that can contain a MBHB emitting GWs (of frequencies within the PTA window) that produces strain amplitudes larger than a certain threshold h_0^{thres} . According to Equation (4.14), the strain amplitude is proportional to $\mathcal{M}^{5/3}$, so MBHBs need to be very massive to produce large strains. On the other hand, the time a binary spends in the PTA frequency band is proportional to $\mathcal{M}^{-5/3}$, meaning that more massive binaries are less likely to be found in the GW emission phase. There exists a trade-off between the two arguments, that happens to favor larger masses. In Section 4.4.6, we will make a list of real PTA-galaxy candidates; their masses lie between $\sim 10^{11.1} M_\odot$ and $10^{12.1} M_\odot$, with a mean of $10^{11.7} M_\odot$. As Figure 4.12 shows, galaxies with such masses tend to have significantly more neighbors than average (lower-mass) galaxies. This argument is not enough to conclude that PTA-galaxies are usually in big galaxy clusters, but we can nonetheless claim that they are more likely placed in dense neighborhoods. A more precise answer to the question of PTA-galaxies being or not preferentially in clusters could be achieved by performing an exhaustive study of the list of PTA-galaxy candidates of Section 4.4.6.

4.4.2 Efficiency of the search for B-galaxies

In Section 4.3.1 we described how a training set of galaxies (chosen from one half of the simulated sky) is used to create a matrix of probabilities $p_x(\text{B}|\theta_i)$; we now address the question of how well we can identify B-galaxies from the testing set (constructed with systems of the other half of the sky). Galaxies are randomly chosen from the testing set, until covering 19.5% of the sky. We define a vector of threshold probabilities p_T , with components in the range $[0, 1]$. For each value of p_T , we count the number of N-galaxies classified as B-galaxies (i.e. with $p_f(\text{N}|\theta_i) > p_T$) and the number of B-galaxies classified as B-galaxies (with $p_f(\text{B}|\theta_i) > p_T$). This process is repeated 1000 times.

In Figure 4.13 we plot *receiver operating characteristic* (ROC) curves of the search in the fake catalog. A ROC graph represents the false alarm rate (number of N-galaxies classified as B-galaxies divided by the number of N-galaxies in the testing set) on the horizontal axis and the detection rate (number of B-galaxies classified as B-galaxies divided by the number of B-galaxies in the testing set) on the vertical one. The thin black line that crosses the plot diagonally would be the result of a totally random search (for each probability value, one gets the same fraction of good and bad classifications). The red area contains 1000 ROC curves (each one corresponding to a different testing set) for which galaxies are characterized by the parameters $\vec{\theta} = \{z, m\}$. The green area contains also 1000 ROC curves; in this case galaxies

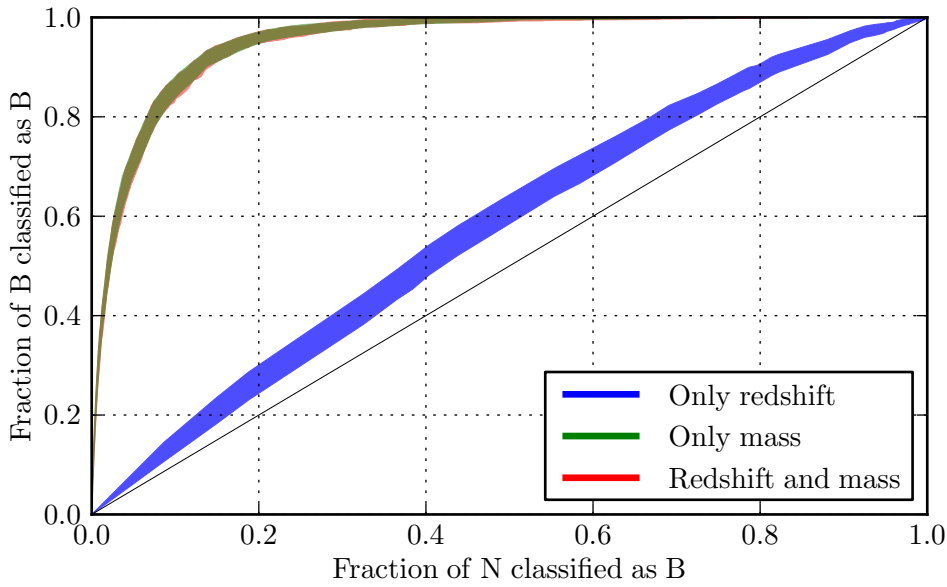


Figure 4.13: Results of 1000 realizations of the search for B-galaxies in the fake catalog using the simple Bayesian approach described in Section 4.3.1. The colored areas contain the ROC curves produced in each of the 1000 realizations. The red area contains the curves obtained when both mass and redshift are considered as parameters in the search. The green (or blue) areas contain the ROC curves obtained when characterizing galaxies only by their mass (or redshift).

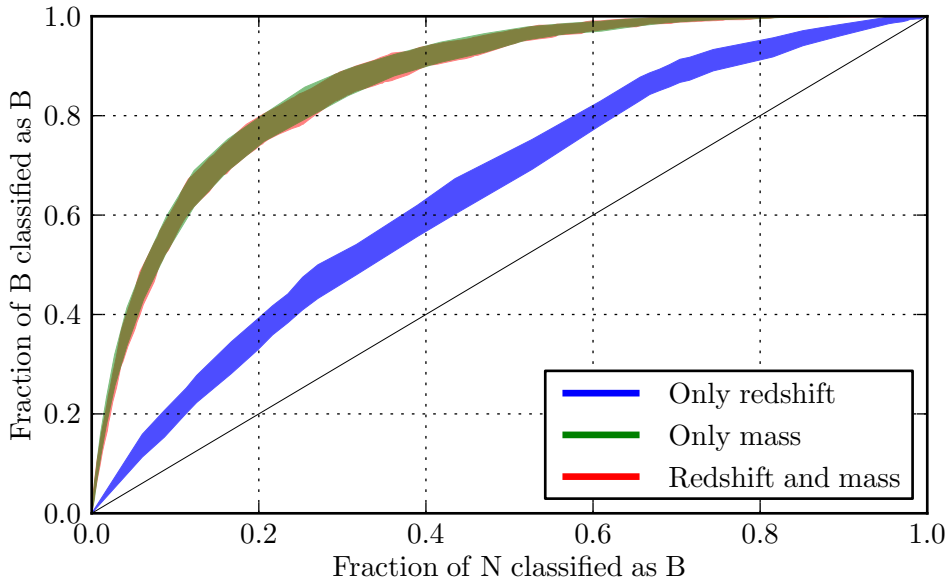


Figure 4.14: Analogous to Figure 4.13; now only systems from the adapted catalog are considered.

are characterized only by their mass, so $\vec{\theta} = \{m\}$. Finally, the blue area is filled with 1000 ROC curves for which galaxies have been characterized by their redshift, $\vec{\theta} = \{z\}$. This plot makes clear that the most useful piece of information to distinguish B-galaxies is their mass. The same procedure to test the efficiency of the search is applied to systems in the adapted catalog. Figure 4.14 is analogous to Figure 4.13, but now the training and testing sets are constructed with systems from the adapted catalog.

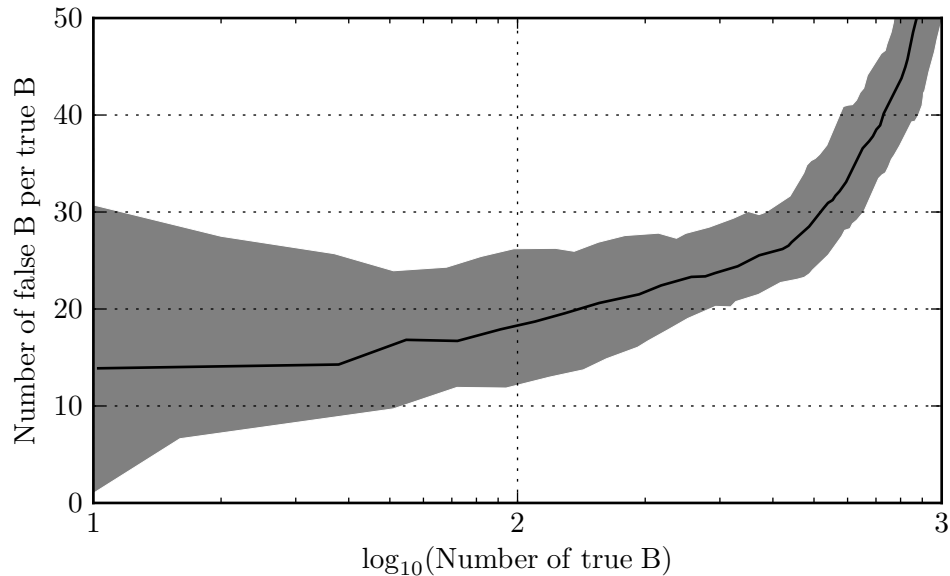


Figure 4.15: Number of wrong classifications per good one versus well-classified B-galaxies from the adapted catalog, after using the search described in Section 4.3.1. This figure is a different representation of the data contained in Figure 4.14. The gray area contains the curves corresponding to the 1000 realizations of the search (each one for a different choice of the galaxies in the testing set). The black curve is the average over the 1000 curves; each point corresponds to a value of B-galaxy probability.

ROC curves are commonly used to test the efficiency of classification algorithms, however, for our purposes, we find more convenient to present the data in a slightly different manner. In Figure 4.15 we present the number of well classified B-galaxies from the adapted catalog (on the horizontal axis) and the number of incorrectly classified N-galaxies per well-classified B-galaxy (on the vertical axis). The gray area contains the curves obtained for the 1000 realizations; the black line is the average over all of them. Each point of a curve corresponds to a certain value of probability $p_a(\text{B}|\theta_i)$. The points on the right part of the plot (where more B-galaxies are well classified) correspond to lower probabilities.

A probability threshold value p_T^{B} needs to be chosen, so that all galaxies with $p_a(\text{B}|\theta_i) \geq p_T^{\text{B}}$ are considered *candidates* for B-galaxies. We choose a threshold such that an average of ~ 100 B-galaxies are counted as candidates. More precisely, for $p_T^{\text{B}} = 4.16 \times 10^{-2}$, in the worst realizations we find 82 B-galaxies among 2166 candidates, whereas in the best ones, 143 B-galaxies out of 2106 galaxies are found. The average result produces 110 B-galaxies among

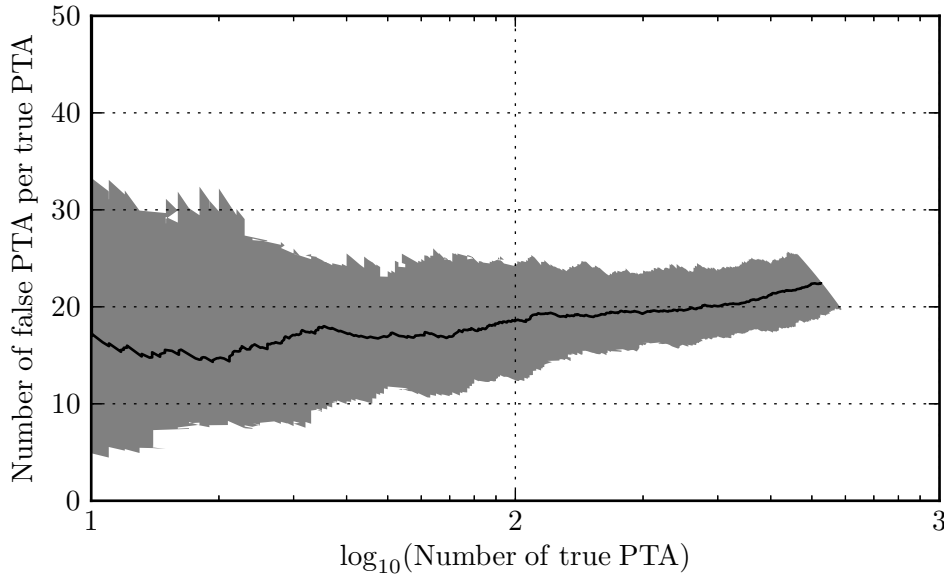


Figure 4.16: Efficiency of the search for PTA-galaxies in the adapted catalog. This plot is analogous to that in Figure 4.15, but now using the probabilities $p_a(\text{B}, \text{P}|\theta_i, \mathcal{M})$. Hence, galaxies in this plot are selected such that their hosted MBH produces (if it is a binary) a strain amplitude larger than the threshold $h_0^{\text{thres}} = 10^{-15}$.

2168 candidates. Further on we apply this same search to galaxies in the real catalog. B-galaxy candidates are chosen using the same probability threshold p_T^{B} , so we expect to have a similar number of galaxies with $p_r(\text{B}|\theta_i) \geq p_T^{\text{B}}$, and thus a similar number of real B-galaxies among them too. We point out that our choice of p_T^{B} is arbitrary. One could have chosen a smaller one, and more B-galaxies would be counted among the candidates; nonetheless, as Figure 4.15 shows, for a smaller threshold the ratio of N-galaxies per B-galaxy considered as candidates would also be larger.

4.4.3 Efficiency of the search for PTA-galaxies

We now test the efficiency of the search for PTA-galaxies in the adapted catalog, following a similar procedure to the one explained in Section 4.4.2. The strain amplitude threshold is set to $h_0^{\text{thres}} = 10^{-15}$; with this we calculate, for each system, its PTA-galaxy probability, $p_x(\text{B}, \text{P}|\theta_i, \mathcal{M})$. Because of the iterative nature of the procedure used to assign PTA-galaxy probabilities, systems cannot be repeated: even if two galaxies have the same `galID` and m , the masses of their MBHs will be different, leading to different probabilities. For this reason the adapted catalog is not divided into a training and a testing set. Galaxies (that could contain a MBHB producing a strain amplitude larger than h_0^{thres}) are chosen randomly from the whole simulated sky until covering an area of the sky of 19.5%; we then count the number of B- and N-galaxies passing each value of the probability threshold. This procedure is repeated 1000 times.

Figure 4.16 is analogous to 4.15, but now the PTA-galaxy probabilities are used, instead of

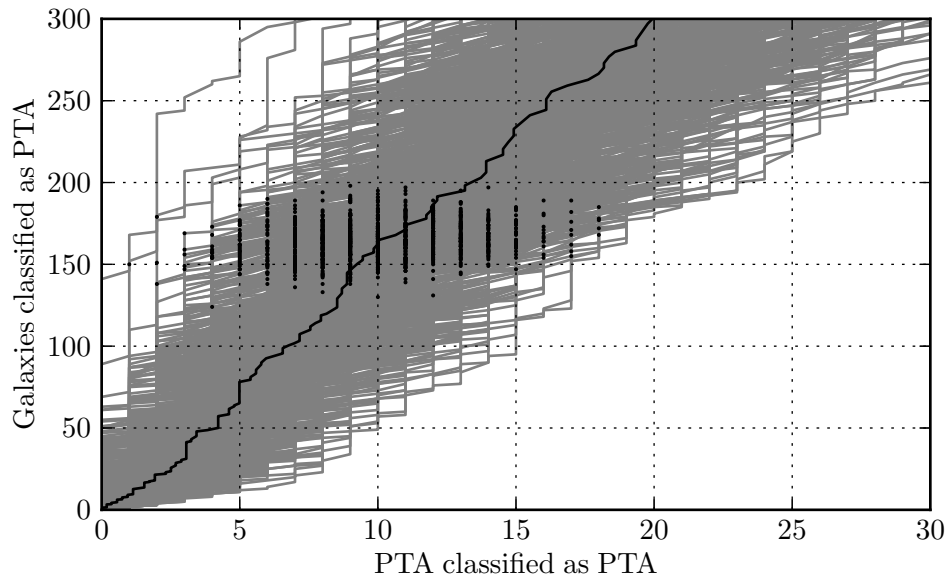


Figure 4.17: Total number of galaxies classified as PTA-galaxies versus the number of good classifications. Each gray curve corresponds to a different realization (a different choice of galaxies from the adapted catalog covering 19.5% of the sky). The black line is the average over all 1000 realizations. For each realization, we plot a black point corresponding to the PTA-galaxy probability threshold p_T^{PTA} . Galaxies considered here are such that their hosted MBH produces (if it is a binary) a strain amplitude larger than the threshold $h_0^{\text{thres}} = 10^{-15}$.

the B-galaxy probabilities, to test the efficiency of the search in the adapted catalog. This plot is used to decide upon a probability threshold p_T^{PTA} to select our real PTA-galaxy candidates later on. Let us first consider the case in which the chosen probability threshold corresponds to the rightmost point on the plot. The worst results for such a threshold find 462 PTA-galaxies among 11764 candidates, whereas the best results have 588 PTA-galaxies of 11610 candidates. The average is a number of 525 PTA-galaxies of a total of 11770 candidates. An important remark is that these ~ 500 PTA-galaxies are all B-galaxies with $z < 0.1$ that produce a strain amplitude larger than 10^{-15} in the adapted catalog. In other words, *all* possible PTA-galaxies contained in the adapted catalog are counted as candidates, by choosing such a probability threshold.

A detection rate of 100% is a great feature, however, the false alarm rate is large. The list of candidates can be reduced, by choosing a larger probability threshold, so that the number of bad candidates per good one decreases (by the cost of losing PTA-galaxies). We now want to select a threshold such that only the ~ 10 most likely PTA-galaxies are counted as candidates. For that, we choose a probability threshold corresponding to the leftmost point in Figure 4.16. This threshold is $p_T^{\text{PTA}} = 8.01 \times 10^{-06}$. Now, in the worst realizations, 1 PTA-galaxy is found among 190 candidates; whereas in the best realizations 18 PTA-galaxies are counted among 137 candidates. On average, we count 10 PTA-galaxies in a list of 164 candidates.

In Figure 4.17 we have plotted the same data as in Figure 4.16 in a different manner (and at a different range of probabilities). Each gray line corresponds to one realization; the black line

contains the average values over all (1000) realizations. Each one of the 1000 black points gives the number of galaxies (on the vertical axis) and PTA-galaxies (on the horizontal axis), for a particular realization, that have PTA-galaxy probabilities larger than p_T^{PTA} . Here we see that, for such a threshold, ~ 10 galaxies among the ~ 150 selected as candidates are well classified. We expect similar numbers when applying the search to the real catalog.

4.4.4 Efficiency of the search when including clustering information

We now turn to the results of the search including clustering information, as described in Section 4.3.3. We applied the MLA 1000 times; for each realization, the systems of the training set were different, but the testing set was always composed of the galaxies of one particular patch of the sky (of the 9 in which the adapted catalog is divided). After each realization we construct a ROC curve with the probabilities assigned to the B- and N-galaxies of the testing set. In order to determine the amount of information provided by the parameters (z , m and NNDS), the MLA is used in three different circumstances. First, we characterize galaxies only using the NNDS (blue curves in the plots of Figure 4.18). Second, only z and m are used as features (green curves). Third, all pieces of information (z , m , and NNDS) are considered (red curves). The NNDS is always calculated for 50 shells with borders separated from 0 to 4 Mpc in linear steps.

Figure 4.18 shows the ROC curves resulting from this search. Upper and lower plots correspond to cases (i) and (ii) (as described in Section 4.3.3), respectively. The colored areas contain all ROC curves after the 1000 realizations. In the lower plot, the NNDS is affected by the inclusion of peculiar velocities and by the subtraction of neighbors; the efficiency of the search using only the NNDS is not significantly different from a totally random search. A discouraging result is that the inclusion of the NNDS introduces some level of randomness in the search. On the upper plot of Figure 4.18, we see that the red and green areas are approximately equal; but on the lower plot, the red area is shifted to the right (to higher values of false alarm rate) with respect to the green one.

Summarizing, the inclusion of the clustering does not ameliorate (in case (i)) or even deteriorates (in case (ii)) the efficiency of the search. However, the fact that the blue curve differs from the black thin line, on the upper plot, means that the clustering of B-galaxies presents in fact features that distinguish them from N-galaxies. The plots in Figure 4.18 change, although not drastically, by using other choices of the shells, reducing the number of shells (from 50 to 10 or 20), or assigning the testing set to another patch of the sky. Nevertheless, the conclusions already drawn about the efficiency of the searches using the NNDS remain unaffected. By comparing the ROC curves obtained in this and in Section 4.4.2, one can also conclude that the efficiency of our Bayesian search is consistent to that of the MLA (when characterizing galaxies only by their redshift and mass).

4.4.5 Efficiency of the search at larger redshifts

Here we show how well the search for B-galaxies performs at redshifts as large as 0.7. The probabilities $p_x(\text{B}|\theta_i)$ are calculated following the method described in Section 4.3.4. We build a z - m -histogram of 100×100 pixels; redshifts and masses are in the ranges $[z_{\min}, z_{\max}]$ and $[m_{\min}, m_{\max}]$, respectively. Each pixel is assigned a value of $p_x(\text{B}|\theta_i)$. We then count the number of B- and N-galaxies contained in pixels with probabilities larger than a certain value that goes from 0 to 1. We do this for different maximum redshifts: 0.1, 0.2, ..., 0.7. The results are

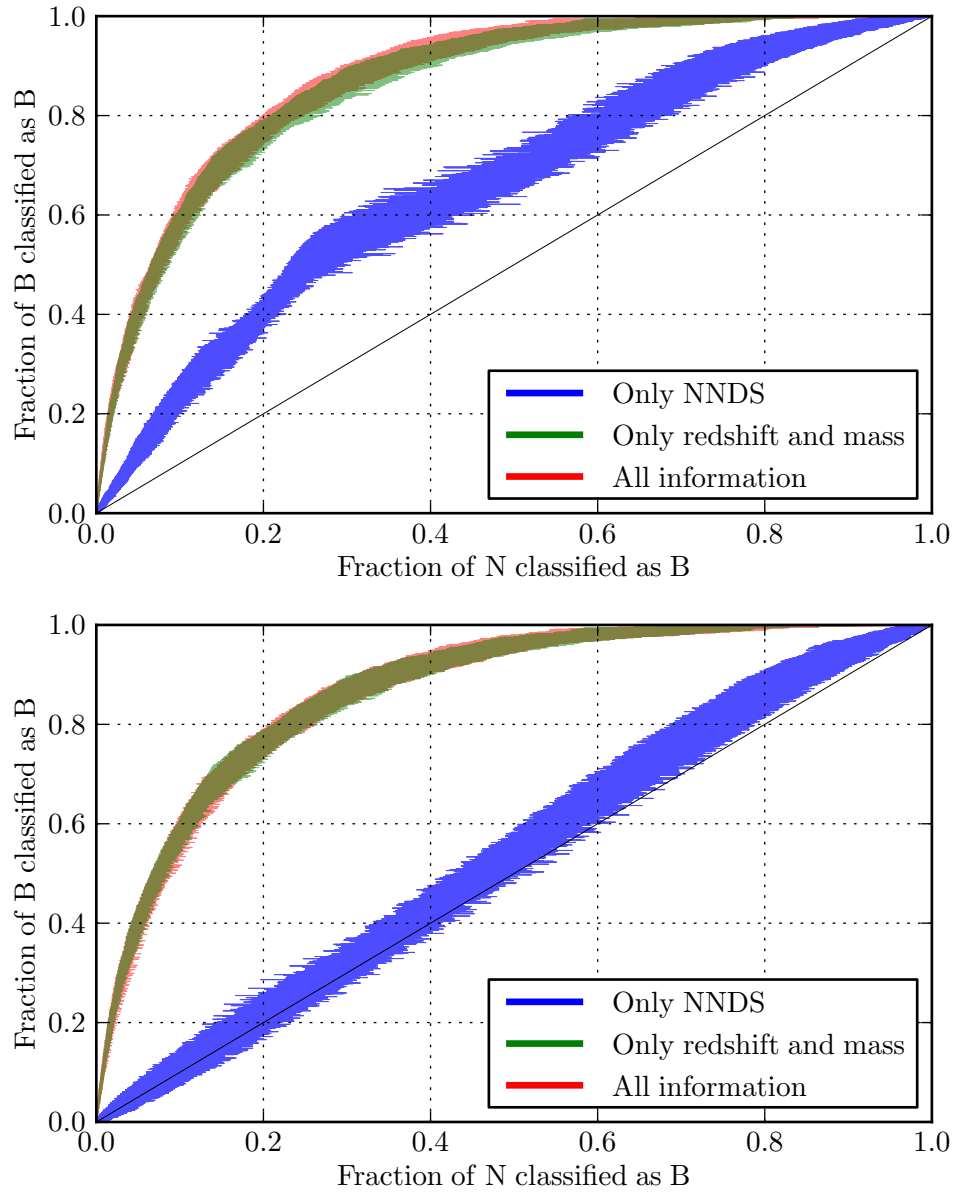


Figure 4.18: ROC curves obtained for the search for B-galaxies using a MLA. The upper and lower plots correspond to case (i) and (ii) (described in Section 4.3.3), respectively. Filled areas contain all the curves produced after the 1000 realizations. Blue and green curves correspond to searches in which only the NNDS, and only z - m , respectively, are taken as features. Red curves are the results of searches in which all parameters (z , m , and NNDS) are considered.

depicted in Figure 4.19, that contains two plots similar to those in Figures 4.15 and 4.16. Upper and lower plots correspond to the probabilities $p_f(\text{B}|\theta_i)$ (using the fake catalog) and $p_a(\text{B}|\theta_i)$ (using the adapted catalog), respectively.

One notices with Figure 4.19 that the number of bad classifications per good one does not grow (and even decreases) when considering galaxies at larger redshifts. For example, considering systems in the adapted catalog all the way up to z_{max} , there exists a certain probability threshold such that ~ 1000 B-galaxies (and a factor of ~ 11 more N-galaxies) have larger probabilities than that threshold. Applying this search to the real catalog we could then make a list with ~ 11000 candidates containing ~ 1000 true B-galaxies. If the trend found on the search for PTA-galaxies at $z < 0.1$ (in Section 4.4.3) also holds at larger redshifts, we could then presumably make a list with the, say, ~ 1000 most likely single PTA sources contained in the SDSS footprint (for $z < 0.7$).

Although extending the searches to larger redshifts looks potentially very interesting, such a task is not performed for the moment. We believe that, to create a trustworthy list of real PTA-galaxy candidates at such large redshifts, the method used to adapt our fake catalog to the limitations of the real one should be more accurate than that described in Section 4.3.4. A proper extension of the search towards larger redshift is thus left for a possible follow-up work.

4.4.6 Assigning probabilities to real galaxies

A B-galaxy probability is now assigned to each system in the real catalog. This probability, determined by the matrix $p_r(\text{B}|\theta_i)$ (whose construction is explained in Section 4.3.1), depends only on the bin θ_i in which the values of z and m of the galaxy are contained. In Figure 4.20 we plot a projected skymap of the systems from the real catalog that have probabilities larger than the threshold p_T^{B} introduced in Section 4.4.2. All galaxies that are not candidates are gray points; B-galaxy candidates have colors corresponding to different values of probabilities $p_r(\text{B}|\theta_i)$. Redder points are candidates with larger B-galaxy probabilities. In this skymap there are 3870 candidates, a factor ~ 1.79 more systems than in the adapted catalog for the same probability threshold p_T^{B} . The reason for this is the overabundance of high-mass galaxies in the SDSS with respect to the MS, discussed in Section 4.5. We thus expect that, among these candidates, $\sim 1.79 \times 110 \approx 196$ are true B-galaxies (since 110 was the number of B-galaxies found in the adapted catalog for the same probability threshold).

In order to assign to each real galaxy its probability of hosting a MBHB observable by the PTA, $p_r(\text{B}, \text{P}|\theta_i, \mathcal{M})$, we follow the prescriptions described in Section 4.3.2; for that we first need the bulge mass m_{bulge} of each galaxy,

$$m_{\text{bulge}} = f_b m, \quad (4.27)$$

where f_b is the bulge mass fraction. Elliptical galaxies are expected to have f_b close to 1, while for spiral galaxies, reasonable values of f_b lie between ~ 0.1 and ~ 0.3 . We now explain how these bulge mass fractions have been obtained. The Galaxy Zoo [136, 135] is a project in which volunteers assign SDSS galaxies a morphological classification by visual criterion. The data is public¹² and contains a final morphological type classification, constructed after processing the votes of the volunteers and reducing possible visual biases. The three possible types are “elliptical”, “spiral”, and “unknown” (in those cases when the voting for elliptical or

¹²<http://data.galaxyzoo.org>

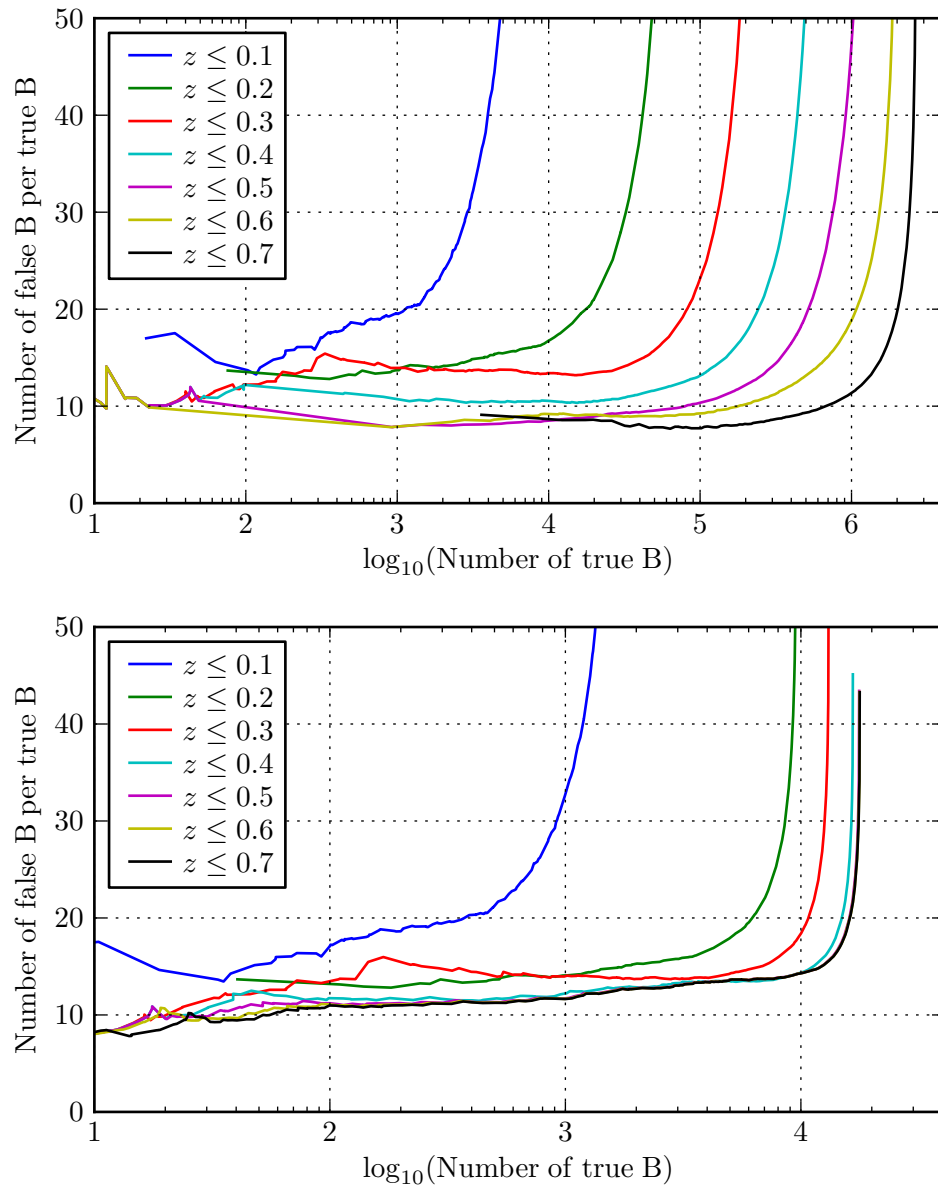


Figure 4.19: Estimate of the efficiency of a search for B-galaxies extended to larger redshifts (up to 0.7). The plot shows the ratio of bad classifications per good one versus good classifications of B-galaxies, within different redshift intervals. The upper (or lower) plot is obtained when applying the extended search to the fake (or adapted) catalog.

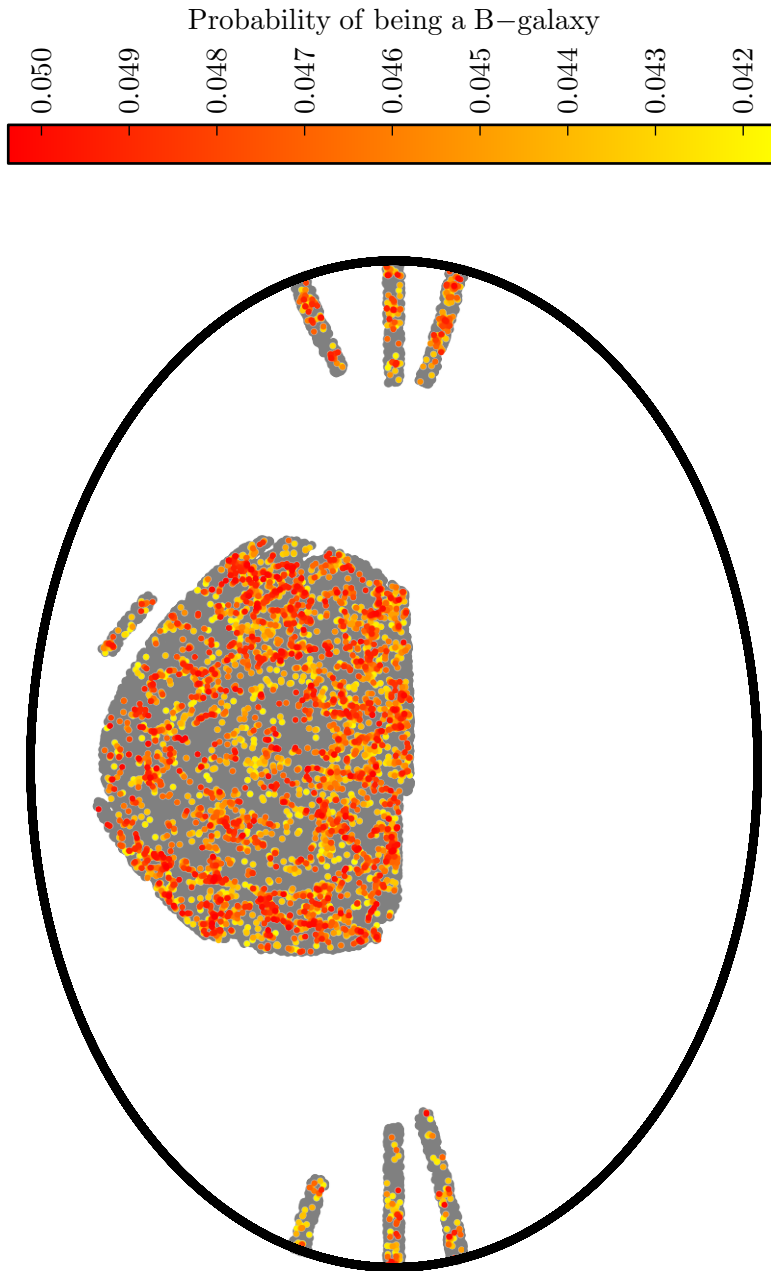


Figure 4.20: Projected skymap (using a Hammer projection) of galaxies from the real catalog. Colored points are B-galaxies candidates. The color bar gives the B-galaxy probability $p_r(\text{B}|\theta_i)$; redder points are galaxies with larger probabilities. Gray points are galaxies with probabilities below the chosen threshold p_T^B . From the 3870 candidates we expect ~ 196 of them to be real B-galaxies.

spiral was not significant enough). Unfortunately, not all galaxies in our real catalog have a final classification in the Galaxy Zoo. We use those galaxies with a type classification different than “unknown” that are contained in both catalogs, to adopt a criterion on the morphologies of all galaxies in our real catalog.

In Figure 4.21 we show contour plots of galaxies classified in the Galaxy Zoo as ellipticals (on top) and as spirals (bottom). The horizontal axis shows the *surface mass density* (SMD), defined as

$$\text{SMD} = \log_{10} \left(\frac{m}{2\pi R^2} \frac{\text{kpc}^2}{M_{\odot}} \right). \quad (4.28)$$

The radius R is the half-light proper radius in the z-band, calculated using

$$R = [1 + z]^{-1} r(z) \mathcal{R}_{50,z}, \quad (4.29)$$

where $r(z)$ is the comoving distance to the galaxy (Equation (4.15)), and $\mathcal{R}_{50,z}$ is the angular radius in which 50% of the Petrosian flux in the z-band is contained (called `petroR50_z` in the SDSS server). The vertical axis shows the concentration parameter C , for which we use the definition

$$C = \frac{\mathcal{R}_{50,r}}{\mathcal{R}_{90,r}}. \quad (4.30)$$

This means, C is the ratio of the 50% and 90% Petrosian radii in the r-band (called `petroR50_r` and `petroR90_r` in the SDSS server, respectively). The query used to obtain the parameters `petroR50_z`, `petroR50_r`, and `petroR90_r` is included in Section 4.7. From Figure 4.21 we see that elliptical and spiral galaxies cannot be clearly distinguished in a certain region of the SMD- C plane; there is an important overlap. The darkest regions in the upper and lower plots show the maximum accumulation of elliptical and spiral galaxies, respectively. The intermediate value of C between those two maxima is $\bar{C} = 0.335$ (which is plotted as a black horizontal line). The vertical line is at the value of SMD above which 90% of elliptical galaxies are contained, $\bar{\text{SMD}} = 8.70$. We take these two values and construct the functions

$$f_b^{\text{SMD}}(c_s, \bar{\text{SMD}}, \text{SMD}) = \min(1, \exp(c_s[\text{SMD} - \bar{\text{SMD}}])) \quad (4.31)$$

and

$$f_b^C(c_r, \bar{C}, C) = \min(1, \exp(c_r[C - \bar{C}])). \quad (4.32)$$

Then, the bulge mass fraction is calculated as the product of the two previous functions,

$$f_b(\text{SMD}, C) = f_b^{\text{SMD}}(7, 8.70, \text{SMD}) f_b^C(-13, 0.335, C), \quad (4.33)$$

where the parameters c_s and c_r have been chosen in such a way that the average f_b is ~ 0.9 for elliptical galaxies and ~ 0.3 for spiral galaxies. We point out that this particular choice of functions and parameters is arbitrary; the aim of this calculation is to construct a simple procedure to assign bulge mass fractions based on observational data. In Figure 4.22, a contour plot of $f_b(\text{SMD}, C)$ is shown, and on top we have superimposed the distributions of ellipticals (on green) and spirals (on red) previously shown (in Figure 4.21).

Once the bulge masses are known, the rest of the calculation of the PTA-galaxy probabilities is as described in Section 4.3.2. The list of real PTA-galaxy candidates is constructed as explained in Section 4.4.3: we select galaxies from the real catalog that have PTA-galaxy probabilities

4 A new method to search for supermassive black hole binaries

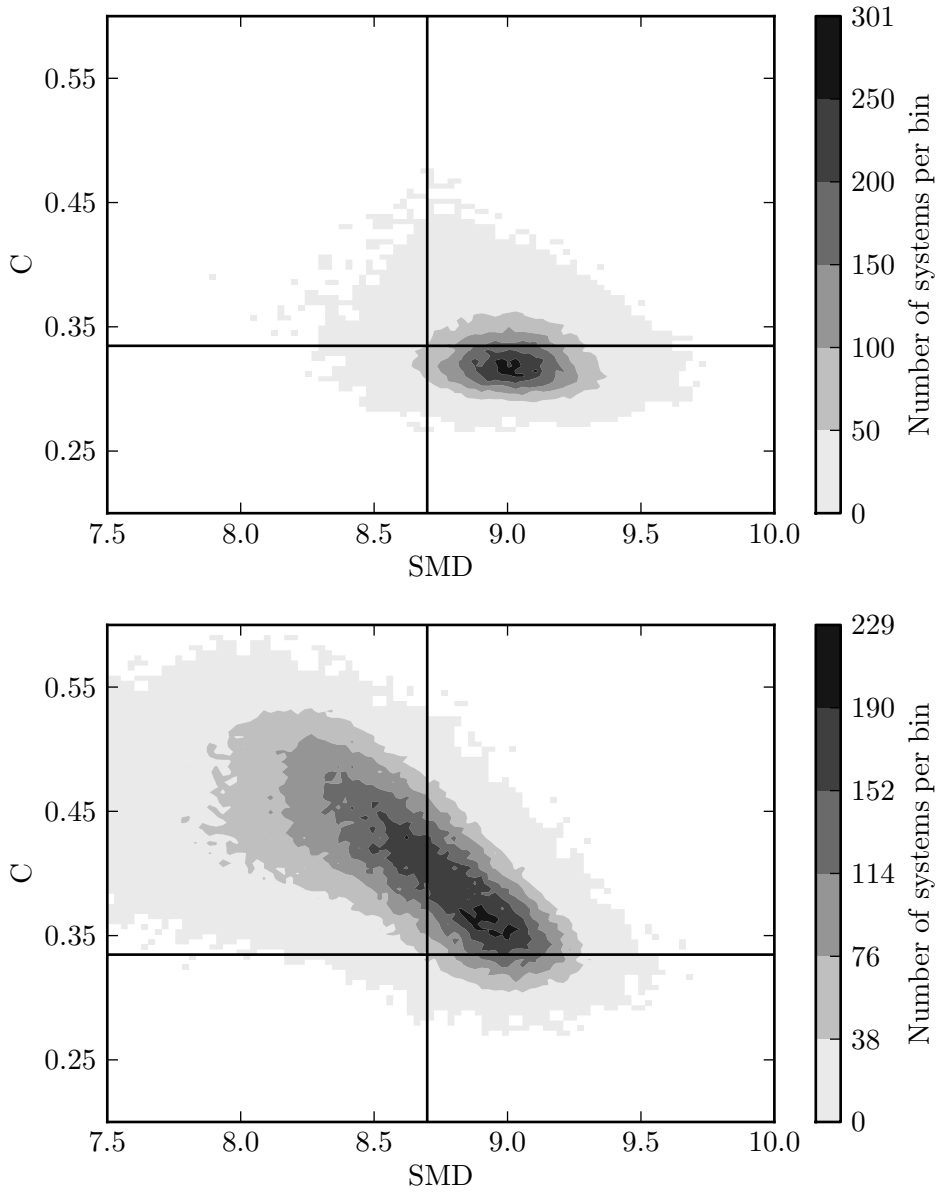


Figure 4.21: Contour plots of the distribution of galaxies classified as elliptical (above) and spiral (below) in the Galaxy Zoo. The horizontal axis shows the surface mass density, and the vertical one is the concentration parameter. Both axes are divided into 100 linearly spaced bins, and the color bar gives the number of systems per bin. We use these distributions to find a criterion to calculate the bulge mass fractions of systems in our real catalog.

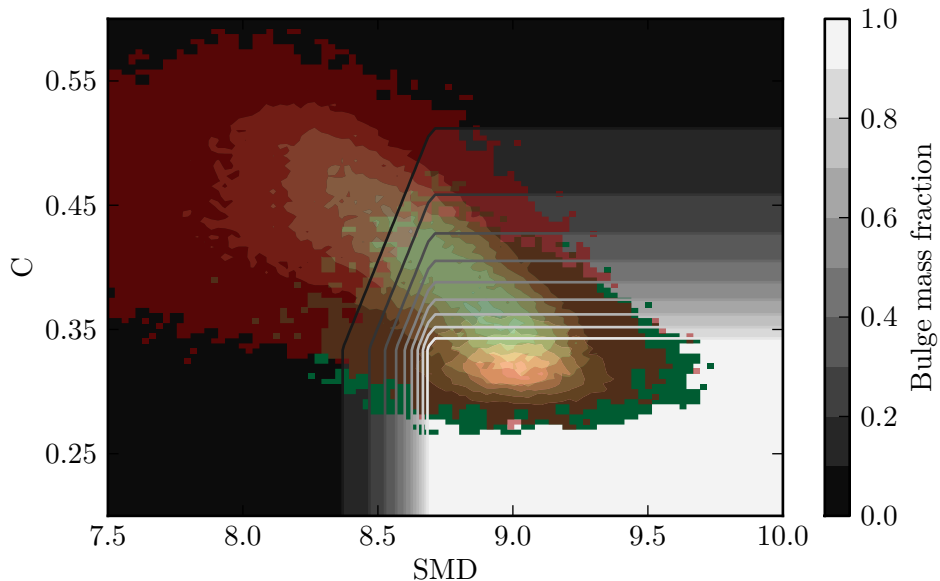


Figure 4.22: Contour plot of the function $f_b(\text{SMD}, C)$, that gives, at each point of the SMD- C plane, the bulge mass fraction that we assign to galaxies in our real catalog. Galaxies falling within the lower-right square (with a white background) will have a bulge mass fraction equal to 1, whereas the bulge mass fraction of galaxies far from these region will decay exponentially. On top of it, the contour plots of Figure 4.21 have been superimposed: elliptical galaxies from the Galaxy Zoo on green and spiral ones on red.

larger than p_T^{PTA} . In Figure 4.23 we show a projected skymap with these candidates. They are 232, which is a factor of ~ 1.41 larger than the average number of candidates produced in the adapted catalog. Therefore, we expect that $\sim 1.41 \times 10 \approx 14$ true PTA-galaxies are counted among them. These candidates are the most likely single PTA sources in the local universe (contained in the SDSS window at $z < 0.1$). Notice that we do not expect to observe ~ 14 MBHBs emitting at $h_0 \geq 10^{-15}$ in the SDSS window; in fact, the PTA-galaxy probability of each of the candidates is fairly small (see the numbers in the color bar of Figure 4.23), since they spend a relatively short interval of time emitting at frequencies at which they are observable. However, if we do observe a PTA source from this part of the sky with $z < 0.1$, it will most likely be one of these candidates. If one wanted to perform a targeted search, one could use this list of galaxies; the list could also be reduced by combining ours with other searching criteria, for example, by looking for signs of recent galaxy interaction in the SDSS images (that can be accessed from the SDSS server).

As we pointed out in Section 4.4.3, we could also construct a list of PTA-galaxy candidates such that *all* possible PTA-galaxies observed by the SDSS are counted. Taking into account this factor of ~ 1.41 difference with respect to the adapted catalog, the resulting list would contain $\sim 1.41 \times 11770 \approx 1.66 \times 10^4$ galaxies, of which $\sim 1.41 \times 525 \approx 740$ would be PTA-galaxies. They would be the only galaxies in the local universe that could possibly be observed emitting GWs of a strain amplitude $h_0 \geq 10^{-15}$ within the spectroscopic SDSS catalog.

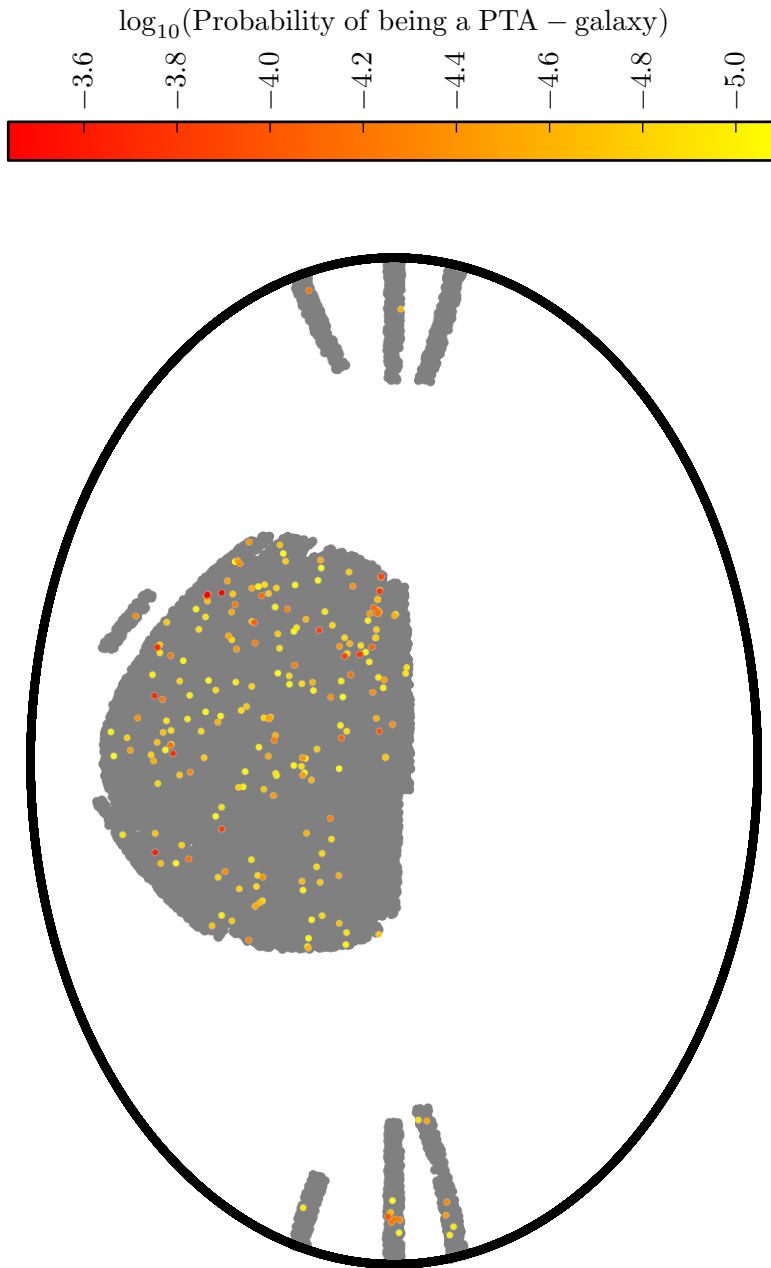


Figure 4.23: Projected skymap of galaxies from the real catalog (analogous to Figure 4.20). Now the color bar gives the PTA-galaxy probabilities. Colored points in this plot correspond to real PTA-galaxy candidates, i.e. galaxies that may host a MBHB emitting GWs that produce a maximum strain amplitude larger than $h_0^{\text{thres}} = 10^{-15}$. We expect ~ 14 of these 232 candidates to actually be B-galaxies (so they may contain an observable MBHB). The probability of observing one of them is small (as the numbers in the color bar reveal); however, if we do observe a single source from this region of the sky (at $z < 0.1$) with a sensitivity of h_0^{thres} , it will most likely be one of these candidates.

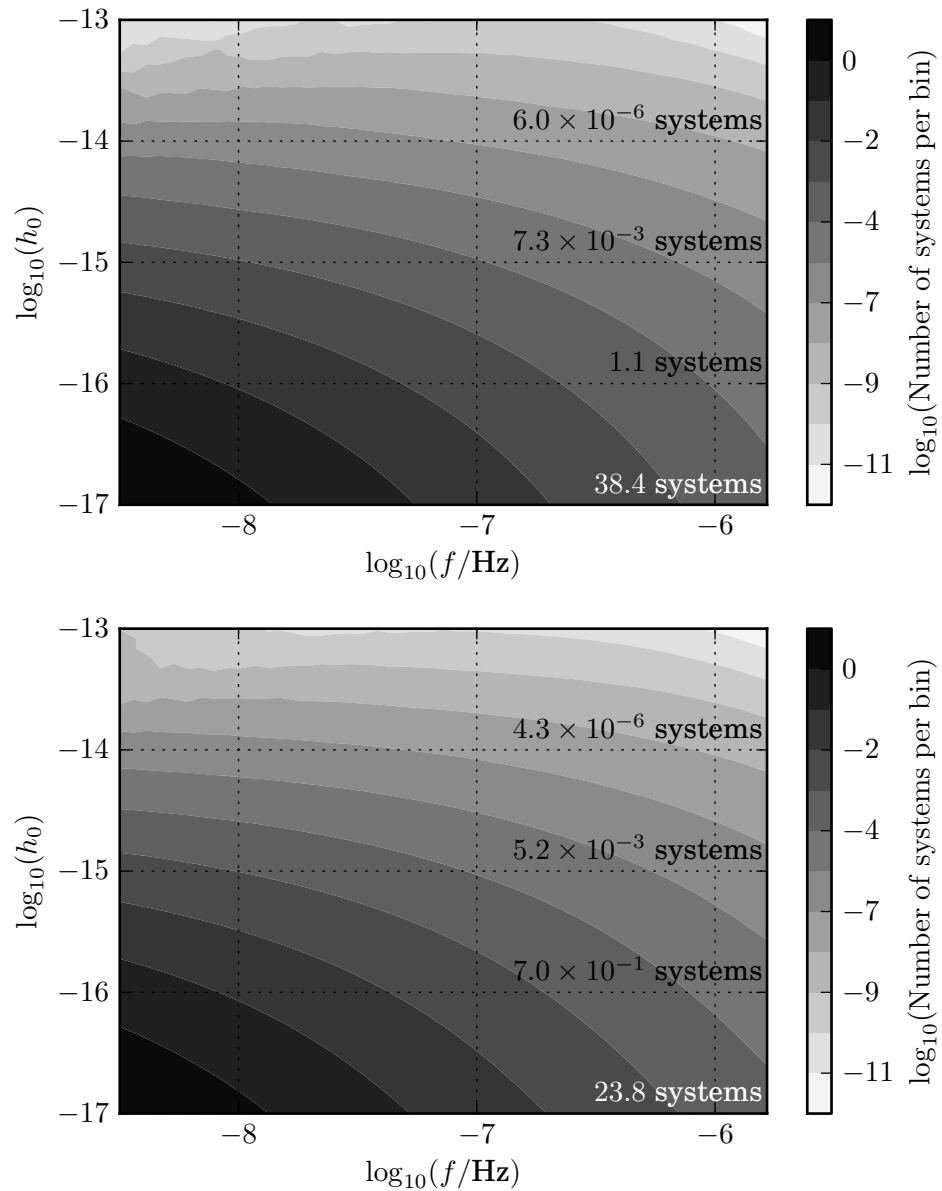


Figure 4.24: Strain amplitude versus observed GW frequency (averaged over 100 realizations). The horizontal axis is divided into 50 frequency bins, and the vertical axis into 50 strain amplitude bins. The color of each pixel in the upper plot gives the sum of probabilities of all galaxies from the real catalog (with $z < 0.1$) that produce a strain amplitude larger than a certain value (given in the vertical axis) within a certain frequency bin (given in the horizontal axis). The numbers written on top give the sum of probabilities over all frequency bins at a fixed strain amplitude, i.e. these are the average numbers of PTA-galaxies (for different strain amplitude thresholds) that are contained in the real catalog at $z < 0.1$. The lower plot is analogous to the upper one, but for systems in the adapted catalog.

4 A new method to search for supermassive black hole binaries

In Figure 4.24 the strain amplitude of systems in the real catalog is plotted as a function of the observed GW frequency. Each point of the upper plot gives the average number of galaxies from the real catalog with $z < 0.1$ that can be found within a certain frequency bin (whose central frequency is given by the horizontal axis), producing a strain amplitude larger than a certain value (given by the vertical axis). The numbers written on top of the graph are the sum over all frequency bins of the window, for a particular strain amplitude threshold (10^{-17} , 10^{-16} , 10^{-15} , and 10^{-14}). For example, we expect on average 1.1 systems in the real catalog producing a strain amplitude larger than 10^{-16} within the PTA frequency window. The number of systems is calculated as the sum of the probabilities $p_r(\mathbf{B}, \mathbf{P}|\theta_i, \mathcal{M})$ of all galaxies. The lower plot in Figure 4.24 represents the same as the upper one, but for systems in the adapted catalog. We see that the numbers in both plots agree well; although the numbers are slightly smaller in the adapted catalog case, again due to the shortage of systems at the high-mass end, with respect to the real catalog (see Section 4.5). In Figure 4.25 the total number of PTA-galaxies expected to be observed with $z < 0.1$ is plotted against the strain amplitude threshold. The gray area contains the curves obtained for each of the 100 realizations described in Section 4.3.2. The black line is the average over all realizations. Upper and lower plots count systems from the real and adapted catalogs, respectively.

The upper plot in Figure 4.26 is analogous to the upper plot in 4.24, but now considering systems with $z < 0.7$. Still, in order to count an average number of PTA-galaxies larger than 1 in the real catalog, a strain amplitude threshold smaller than $\sim 10^{-16}$ is necessary. The lower plot in Figure 4.26 shows the same as the upper one, but considering only B-galaxies from the whole fake catalog. In this case, the probabilities $p_f(\mathbf{B}, \mathbf{P}|\theta_i, \mathcal{M}, f)$ are also defined by Equation (4.21), but the B-galaxy probabilities $p_f(\mathbf{B}|\theta_i)$ are identically 1 for all galaxies (since we know they are B-galaxies). Hence, this graph reveals the average number of PTA-galaxies that would be contained in an ideal all-sky galaxy catalog (more complete than a spectroscopic catalog like the one we use). One could plot, on top of the graphs in Figure 4.26, the exact sensitivity of the PTA to single MBHBs for a given array of MSPs [59]; the sum of the pixels swept by the sensitivity curve would give the average number of systems that should be observable for such an array. The total number of PTA-galaxies with $z < 0.7$ as a function of the strain amplitude threshold is shown in Figure 4.27, for galaxies of the real catalog (upper plot) and for B-galaxies of the entire fake catalog (lower plot). The upper plot is analogous to the upper plot in Figure 4.25, but now considering all systems in the real catalog, and not only those with $z < 0.1$. The lower graph informs on the average number of PTA-galaxies that could be observed with an ideally complete all-sky galaxy catalog.

4.5 Discussion

The searches described in Section 4.3 can be improved in several ways. One of the main shortcomings is in the method used to construct the adapted catalog. We are assuming that all galaxies with the same redshift and mass are affected by the same observational limitations. Moreover, we assume that the same limitations hold for galaxies that recently suffered a major merger and galaxies that did not. If we consider that the latter assumption is not too crude, then our adaptation method should be good enough when calculating the efficiency of the simple Bayesian search explained in Section 4.3.1. This is so because the efficiency of the search depends only on the distribution of galaxies in z and m , which we know for our real catalog, regardless of

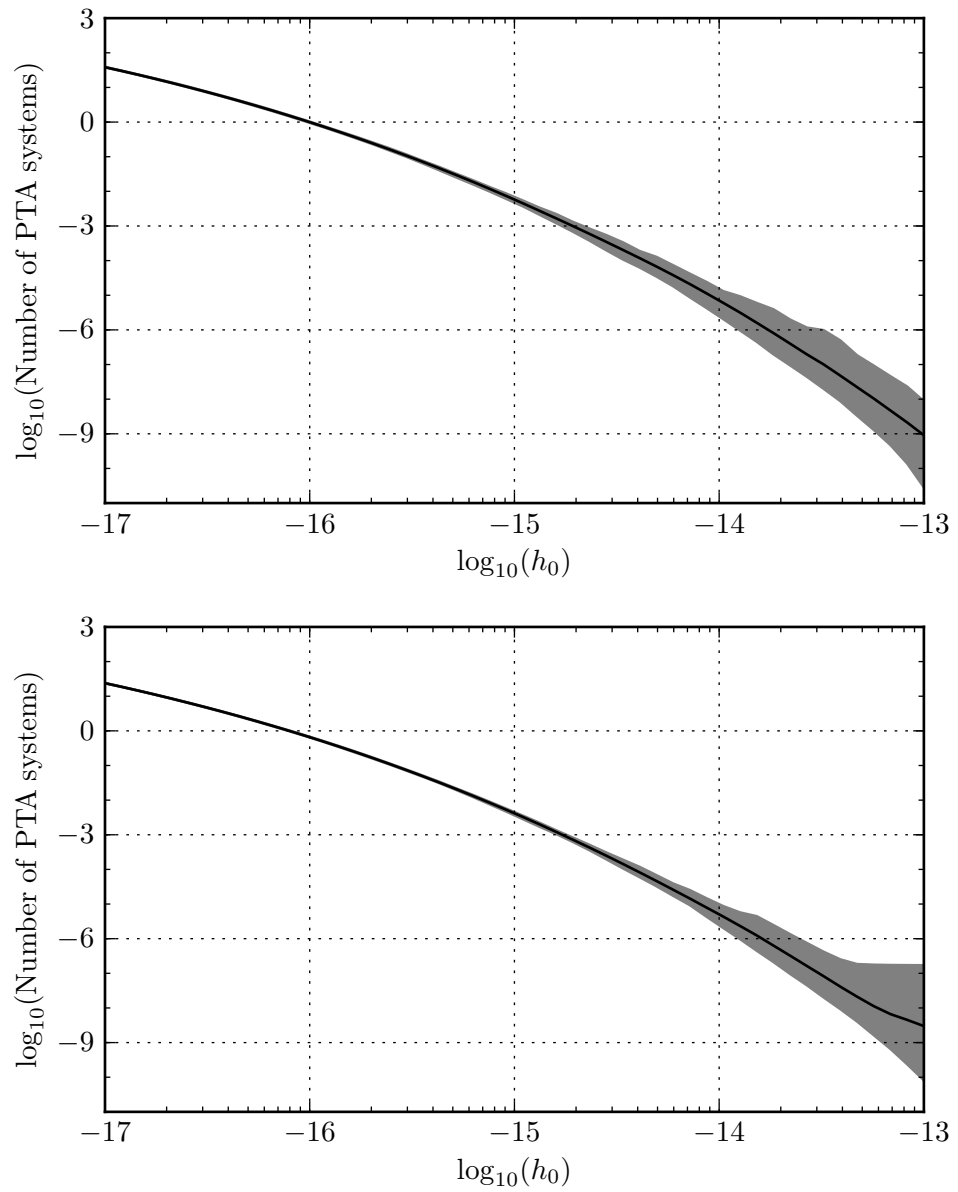


Figure 4.25: Average number of PTA-galaxies that are contained in the real (above) and adapted (below) catalog for $z < 0.1$, as a function of the strain amplitude threshold. For example, to have an average of 1 galaxy in the real catalog, the PTA needs to be able to detect strain amplitudes smaller than 10^{-16} . These plots are obtained by integrating the plots in Figure 4.24 over all frequencies in the PTA frequency window.

4 A new method to search for supermassive black hole binaries

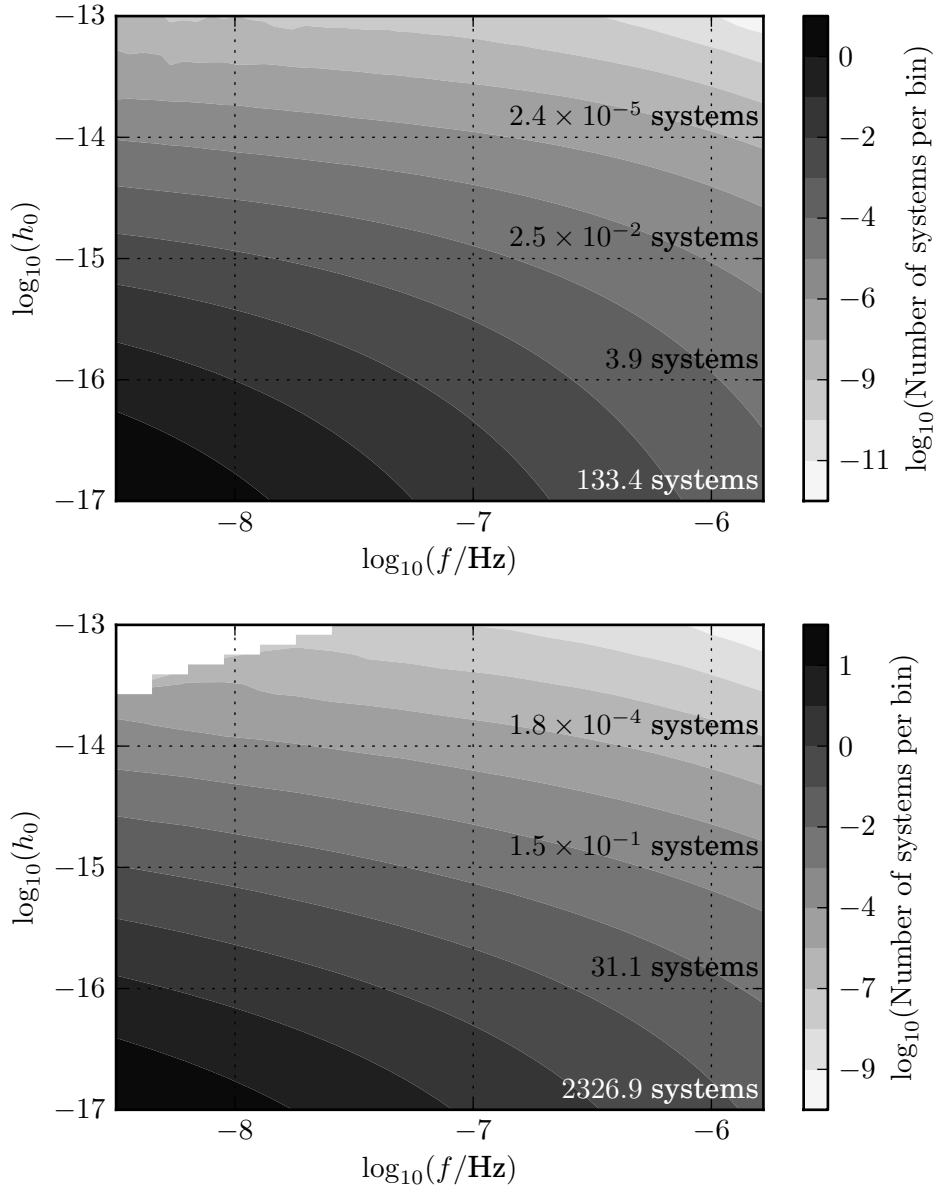


Figure 4.26: The upper plot is analogous to the upper plot in Figure 4.24; now, all systems in the real catalog (with $z < 0.7$) are considered. The lower plot is calculated considering all B-galaxies from the entire fake catalog; on top are written the average numbers of PTA-galaxies (for different strain amplitude thresholds) that could be observed in a very complete, all-sky galaxy catalog (with $z < 0.7$). The upper-left corner is empty simply because, among the 100 realizations, there were no B-galaxies observable at that region of frequencies producing such a large strain.

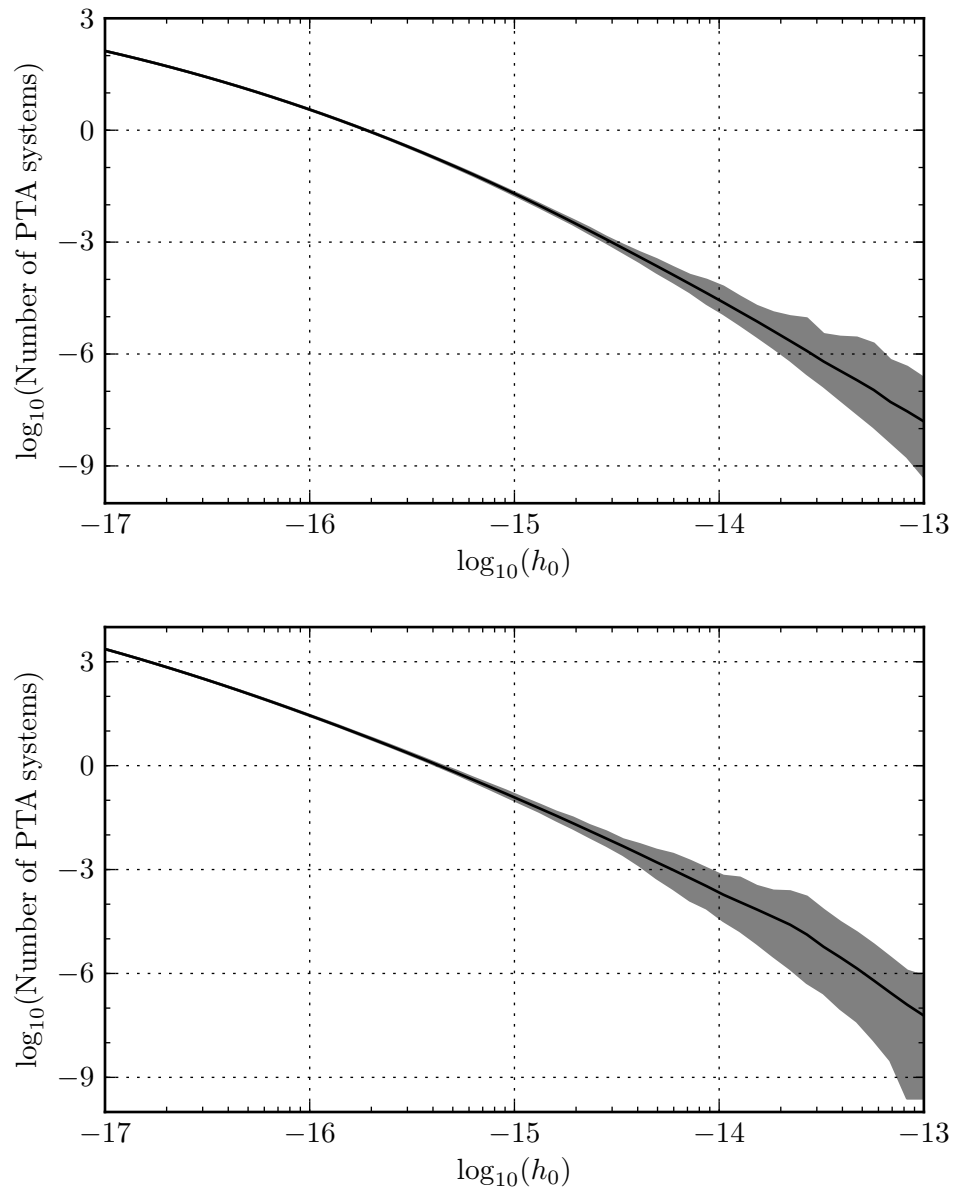


Figure 4.27: The upper plot is analogous to the upper plot in Figure 4.25, but now all systems in the real catalog are considered (with $z < 0.7$). The lower plot gives the average number of PTA-galaxies that would be contained in a very complete, all-sky galaxy catalog (the fake catalog) as a function of their maximum strain amplitude.

the observational processes that caused the distribution to be so. When considering the galaxy clustering as a piece of information for the search, the adaptation method becomes crucial. Nevertheless, the NNDS does not ameliorate the search performed using only z and m as parameters. Therefore, even if the clustering information is affected by our adaptation method, the inclusion of the NNDS in a search on a properly adapted catalog is not expected to be efficient. There may be yet other ways to improve the searches by including the clustering; as shown in Sections 4.3.3 and 4.4.4 there are indeed some features contained in the number of neighbors that distinguish B- from N-galaxies.

Another drawback of this work is the incompleteness of our real catalog. The spectroscopic SDSS catalog covers a small fraction of the sky. It would be interesting to apply the algorithms of this chapter to a full sky survey. With such a catalog we could do a more complete study of the distribution of PTA-galaxy candidates. Data from Pan-STARRS [242, 214] will soon be publicly released. Their coverage is of roughly three quarters of the sky, although the redshifts will be photometric (instead of spectroscopic), inferred from the four different wavebands measured, which would be a source of uncertainty in the calculations of redshifts and masses. On the other hand, the incompleteness of our real catalog at very low redshifts ($z_{\min} < 0.01$) could be easily solved by combining this with other complete catalogs of nearby galaxies. Nonetheless, at such low redshifts we do not expect to find more than ~ 1 PTA-galaxy candidates.

The cosmological parameters assumed by the MS are based on WMAP 1 data, which significantly differ from more modern measurements [113, 183]. According to [84], updating the simulation to the cosmological parameters of WMAP 7 does not affect galaxy clustering significantly, since the changes in the values of Ω_m and σ_8 (the amplitude of mass fluctuations at $8h_0^{-1}$ Mpc) effectively compensate each other, at least below $z \lesssim 3$. Overall, they report a small difference in the outcomes of the simulation for the two sets of cosmological parameters. Nevertheless, an update of this work to the most recent models would be a sensible follow up. Also, to avoid our method to be too dependent on the particular realization of the universe provided by the MS, we could redo our calculations using other simulations, like DEUS¹³ [8].

In different sections of this chapter, we have mentioned that the adapted catalog contains fewer high-mass systems than the real catalog. This difference in masses is the reason why the number of B- and PTA-galaxy candidates found in the real and adapted catalogs disagree (by less than a factor of 2). For the calculations of stellar masses of real galaxies, it is necessary to calculate the distance to the galaxy, which depends on the cosmological parameters; therefore, the reason for the discrepancy at the high-mass end could be related to the different parameters assumed by the two catalogs. In Figure 4.28 one can clearly see that discrepancy in masses. Again, using a simulated universe updated to the most recent cosmological parameters could be the solution for this issue.

In Figure 4.29 we show the distributions of B-galaxy and PTA-galaxy probabilities (upper and lower plots, respectively) from the adapted and real catalogs. Each point in a curve tells the number of galaxies (on the vertical axis) that have probabilities larger than a certain value (on the horizontal-axis). The vertical lines mark the probability thresholds p_T^B and p_T^{PTA} chosen to select B- and PTA-galaxy candidates. This plot demonstrates that probabilities are assigned in the real catalog in a similar way than in the adapted catalog, except for a factor of $\lesssim 2$ due to the mass discrepancy that we just mentioned.

¹³<http://www.deus-consortium.org/>

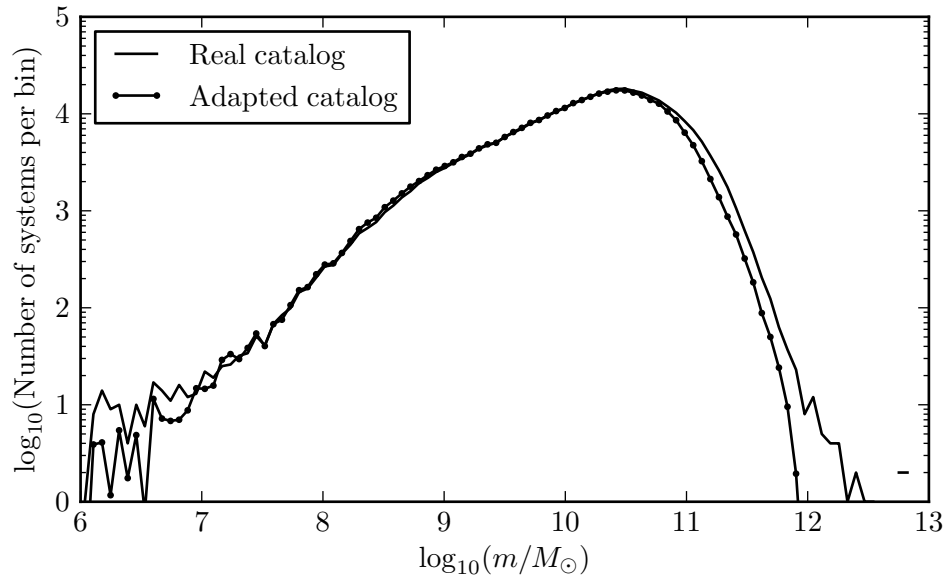


Figure 4.28: Mass histograms of systems in the real and adapted catalogs (taking a fraction of the sky in the adapted catalog that is equal to the area covered by the real one). Here we see that the MS has an underdensity of high-mass galaxies with respect to the SDSS.

4.6 Summary and conclusions

MBHBs are expected to form in the center of massive galaxies following merger events, and the detection of their emitted GWs is the main goal of ongoing PTAs. Whether or not MBHBs will be observed as an unresolvable background or as the sum of only a few bright signals is unknown, and also depends on the spatial distribution of very massive systems in the low redshift Universe. As such, an effective tool to predict the properties of the PTA signal is to study the distribution of putative MBHB hosts in large galaxy surveys.

In this chapter we have first investigated possible criteria to assign to each system a probability of hosting a MBHB (technically, of being a B-galaxy, i.e., a galaxy that has suffered a major merger in less than ~ 300 Myr with respect to the galaxy’s proper time). We have used a fake (simulated) galaxy catalog (result of the MS with the semi-analytical galaxy formation models of [83]) and used the peculiar two-dimensional mass-redshift distribution of merging galaxies as a selection criterion. The fake catalog was then adapted to the observational constraints of the real catalog, the SDSS spectroscopic catalog, and the same search for B-galaxies was performed. We caution that this method of adaptation may not be optimal (as commented on in Sections 4.2.3 and 4.5).

For each galaxy, we also calculated the probability of being a PTA-galaxy, i.e. a B-galaxy that contains a MBHB emitting GWs that produce a strain amplitude $h_0 \geq h_0^{\text{thres}} = 10^{-15}$ (in some frequency interval within the PTA frequency band). To do this, we populated galaxies with MBHBs, for which the knowledge of each galaxy’s bulge mass was required. To infer the latter, we have constructed a simple model based on the morphological classification of the Galaxy

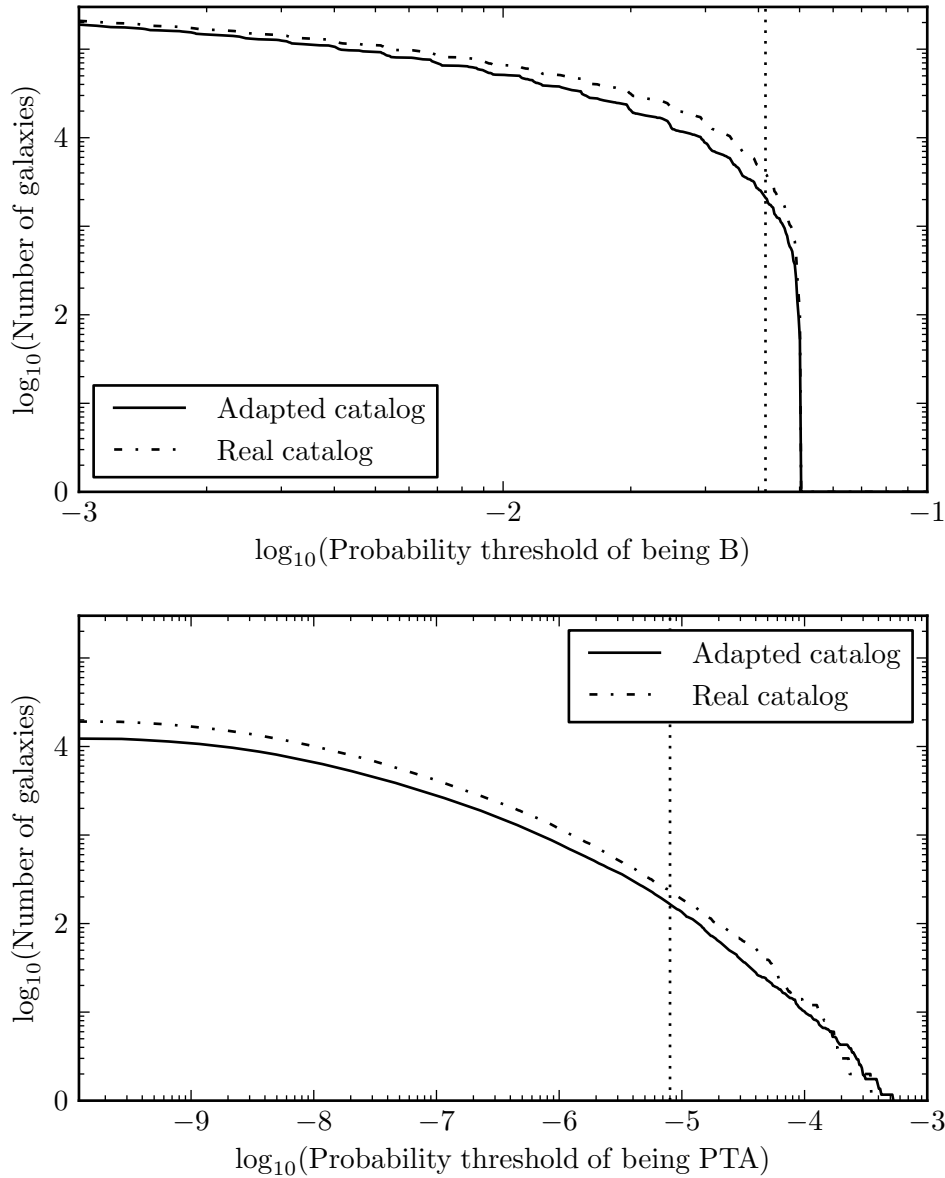


Figure 4.29: Distribution of B-galaxy probabilities (upper plot) and PTA-galaxy probabilities (below) for the real (dotted-dashed lines) and adapted (solid lines) catalogs with $z < 0.1$. The vertical axis gives the number of galaxies that have probabilities larger than a certain threshold, given on the horizontal axis. The numbers for the adapted catalog have been multiplied by the fraction of the sky covered by the real catalog (19.5%), so that solid and dotted-dashed lines are comparable. The probability thresholds p_T^B and p_T^{PTA} chosen to select B-galaxy candidates and PTA-galaxy candidates are marked with vertical dotted lines. Systems on the right of the vertical lines are B-galaxy (PTA-galaxy) candidates, in the upper (lower) plot.

Zoo (explained in Section 4.4.6).

Our fiducial search is based only on the mass-redshift distribution of galaxies, and extends in the redshift interval $0.01 < z < 0.1$. The search has been extended up to $z = 0.7$, even though the severe incompleteness of the SDSS spectroscopic catalog at those redshifts and our simple fake catalog adaptation technique make the results of this search less robust. We also included clustering information in our search (using a machine learning algorithm), which did not improve the efficiency of the searches for B- or PTA- galaxies.

The main results are summarized below:

- In the fake universe, B-galaxies show a distinct distribution in redshift and mass (as shown in Figure 4.2): they tend to have larger masses than average (N-) galaxies, which is a reasonable consequence of the conditions in which major mergers take place.
- By using only this information we were able to construct a list of 3870 candidates for B-galaxies with $z < 0.1$ in the SDSS footprint, of which ~ 196 are expected to be actual B-galaxies (a skymap with these real candidates is shown in Figure 4.20). All of them have stellar masses larger than $10^{11} M_{\odot}$.
- The search seems to keep (and even ameliorate) its efficiency when applied to redshifts larger than 0.1, as shown in Figure 4.19.
- Applying our PTA-galaxy search to the real catalog, we created a list of 232 real PTA-galaxy candidates; this list is expected to include the ~ 14 most likely first detectable individual sources in the local universe (assuming a PTA with a sensitivity to strain amplitudes $\geq h_0^{\text{thres}}$) that are observed by the SDSS. A skymap with these candidates is given in Figure 4.23. Also PTA-galaxy candidates have masses $\geq 10^{11} M_{\odot}$.
- According to Figure 4.12, galaxies with such large masses ($\geq 10^{11} M_{\odot}$) are expected to have more neighbors than average galaxies, which supports B- and PTA-galaxies being found more likely in large groups or clusters.
- The probability to actually observe these PTA-galaxy candidates is small (since they spend a relatively short interval of time producing a strain amplitude larger than h_0^{thres}), ranging from 10^{-3} to 10^{-5} ; nevertheless, if the PTA manages to detect single sources from the part of the sky covered by the SDSS with $z < 0.1$, those sources are expected to be among the list of candidates shown in Figure 4.23.
- Sensitivities to strain amplitudes smaller than $\sim 10^{-16}$ are required to have a sizable number of detectable sources. This result supports the idea that the first PTA detection will most likely involve a low frequency stochastic background type of signal, as opposed to a loud individual source.

As shown in Figure 4.25, the expected number of observable PTA-galaxies in the local universe contained in our real catalog is, for a threshold of $h_0^{\text{thres}} = 10^{-15}$, smaller than 0.01. This number does not contradict the expected number of PTA-galaxy candidates contained in the skymap of Figure 4.23, which is ~ 14 . Among the systems in the skymap, we do expect ~ 14 of them to be producing a strain amplitude $\geq h_0^{\text{thres}}$, but only during a relatively short interval of time; the PTA-galaxy probabilities of the candidates in the skymap sum thus less than 0.01.

4 A new method to search for supermassive black hole binaries

More encouraging numbers can be achieved by setting a smaller strain amplitude threshold (to which future PTA campaigns will be sensitive), or by considering a more complete (or deeper) set of galaxies. The upper plot in Figure 4.27 is analogous to the upper plot in Figure 4.25, but for redshifts up to 0.7. The lower plot on this figure gives insight on the average number of systems that could be observed simultaneously by the PTA and an ideal telescope, able to produce a complete all-sky galaxy catalog up to 0.7.

Our work has important practical implications for searches for MBHBs and PTA-sources. If our understanding of the galaxy formation process is correct, there *must* be hundreds of binaries at $z < 0.1$, and our method provides a useful way to narrow down the number of selected targets for deep imaging and spectroscopy to unveil MBHBs in the local Universe. Note, moreover, that these are massive, very low redshift systems, where the search for kinematic signatures of massive binaries at several parsec separations might be already possible with the Hubble Space Telescope¹⁴, and will be definitely in the capabilities of the European Extremely Large Telescope [76]. Several tens of such binaries are PTA sources, but unfortunately only a few of them will produce a strain amplitude $\geq 10^{-16}$ which might be achievable with the SKA [125]. However, even if very small, there is a chance that a nearby galaxy hosts a loud source of GWs detectable in the PTA band, and our method proved effective in selecting the most likely candidates. Our list of PTA-galaxy candidates can be used to perform targeted searches, also in combination with other searching criteria, for example, by looking for signs of recent galaxy interaction in the SDSS images. Finally, being able to assign a probability to each galaxy in the Universe is a powerful tool to construct PTA signals with the ‘right’ spatial properties.

The SDSS spectroscopic catalog covers $\sim 20\%$ of the sky, but surveys like Pan-STARRS and LSST [140] will cover almost the entire sky. Our technique applied to all-sky, deep galaxy catalogs will allow a complete study of the expected properties (in terms of number and location of putative resolvable sources and level of anisotropy) of the low frequency GW signal in the PTA band. This has a double value for the PTA community: on the one hand, it will provide useful guidance to the development of data analysis algorithms to search for GWs in PTA data; on the other hand, in the presence of a detection, it will provide a useful tool to interpret the results from an astrophysical standpoint.

4.7 Appendix: queries for the data

The SQL query sent to the MS site to download the fake catalog (for systems with redshifts $z < 0.11$) is the following:

```
select h.galID,  
       h.ra,  
       h.dec,  
       h.z_geo,  
       h.z_app,  
       g.stellarmass,  
       g.blackholemass,  
       g.bulgemass,  
       g.type
```

¹⁴www.hubblesite.org

```
from Henriques2012a.wmap1.bc03_AllSky_001 h,
    Guo2010a..MR g
```

```
where h.galID = g.galaxyid
      and g.stellarmass > 7e-5
      and h.z_geo <= 0.11
```

The stellar mass in the database is given in units of $10^{10} M_{\odot}/h_{100}$, where $h_{100} = 0.73$ (for the set of cosmological parameters assumed by the MS), so the minimum mass imposed in this query is of $\approx 9.6 \times 10^5 M_{\odot}$. Once the catalog is downloaded, we select only galaxies with masses $\geq 10^6 M_{\odot}$ (minimum mass of the real catalog).

This query is limited to redshifts smaller than 0.11, and outputs $\approx 1.0 \times 10^7$ galaxies. A query with a maximum redshift of 0.7 would produce $\approx 1.8 \times 10^8$ galaxies. As we explain in Section 4.3.4, we do not need to download all these data to extend the search to all redshifts considered in the real catalog. Instead, we just need a histogram with the number of galaxies contained in each z - m -bin.

The searches described in Sections 4.3.1 and 4.3.2 are restricted to $z < 0.1$. However, we download systems with $z < 0.11$ to avoid border effects: when calculating the NNDS of systems close to $z = 0.1$, one needs to consider background galaxies that have larger redshifts; for our choices of shells, all background galaxies are safely contained below $z = 0.11$.

The query used to construct the list of B-galaxies in the fake catalog is:

```
select h.galID,
       h.z_geo,
       h.z_app,
       p1.blackholemass,
       p2.blackholemass

from Henriques2012a.wmap1.bc03_AllSky_001 h,
     Guo2010a..MR p1,
     Guo2010a..MR p2,
     Guo2010a..MR d
```

```
where h.galID = d.galaxyid
      and h.z_geo <= 0.7
      and p1.descendantid = d.galaxyid
      and p2.descendantid = d.galaxyid
      and p1.galaxyid < p2.galaxyid
      and p1.snapnum = p2.snapnum
      and p1.stellarmass >= 0.2*d.stellarmass
      and p2.stellarmass >= 0.2*d.stellarmass
      and p1.blackholemass > 1e-6
      and p2.blackholemass > 1e-6
      and d.blackholemass > 1e-6
      and d.stellarmass > 7e-5
```

4 A new method to search for supermassive black hole binaries

```
and p1.disruptionon = 0
and p2.disruptionon = 0
and p1.snapnum = d.snapnum-1
```

This query outputs the `galID` of galaxies that suffered a major merger between their snapshot and the previous one. Since the `galID` can be repeated (as mentioned in Section 4.2.2), cosmological and apparent redshifts are also downloaded, to be able to identify systems without any ambiguity. The progenitors' black hole masses are downloaded to construct the black hole mass ratio, necessary for the calculations presented in Section 4.3.2.

The condition of major merger is that at least two progenitors of a galaxy must have mass ≥ 0.2 times the mass of the galaxy. Furthermore, we discard progenitors that were disrupted before the merger. We also impose that the progenitor must have a black hole mass larger than $\approx 1.4 \times 10^4 M_{\odot}$. The same condition is imposed to the descendant, although this condition turns out to be unnecessary, since the minimum black hole mass found among B-galaxies is of $\approx 10^{6.2} M_{\odot}$.

Several major multimergers are found with this query. These are mergers of three galaxies¹⁵ that have a mass larger than 0.2 times the mass of the descendant. When such a multimerger occurs, the query outputs the descendant galaxy three times, because three possible pairs of progenitors are considered (first and second, first and third, and second and third). If that descendant galaxy appears twice (or three times, or four times, etc.) in the galaxy catalog (due to a repetition of the cube of the simulation), the query will output 6 (or 9, or 12, etc.) times the same galaxy. One has to properly correct for these repetitions to avoid ambiguities when identifying galaxies.

The query used in the SDSS DR7 server to obtain the morphological parameters introduced in Section 4.4.6 is the following:

```
select g.objid,
       s.specobjid,
       g.petr50_r,
       g.petr90_r,
       g.petr50_z

from galaxy g,
     specobj s

where g.objid=s.bestobjid
     and s.z<=0.7
```

The two first items, `objid` and `specobjid` were used to identify the galaxies of this query with the ones of our real catalog.

¹⁵The unlikely cases of major multimergers involving more than three progenitors were not found with this query.

Bibliography

- [1] 2dFGRS Team. The 2dF galaxy redshift survey: near-infrared galaxy luminosity functions. *MNRAS*, 326:255–273, 2001.
- [2] K. Abazajian et al. The seventh data release of the Sloan Digital Sky Survey. *Astrophys. J. Suppl.*, 182:543–558, 2009.
- [3] T. Accadia et al. Virgo: a laser interferometer to detect gravitational waves. *Journal of Instrumentation*, 7(03):P03012, 2012.
- [4] T. Accadia and B. L. Swinkels. Commissioning status of the Virgo interferometer. *Clas. Quantum Grav.*, 27:084002, 2010.
- [5] H. Aihara et al. The eighth data release of the Sloan Digital Sky Survey: first data from SDSS-III. *Astrophys. J. Suppl.*, 193:29, 2011.
- [6] H. Aihara et al. Erratum: “The eighth data release of the Sloan Digital Sky Survey: first data from SDSS-III”. *Astrophys. J. Suppl.*, 195:26, 2011.
- [7] P. Ajith et al. Inspiral-merger-ringdown waveforms for black-hole binaries with non-precessing spins. *Phys. Rev. Lett.*, 106:241101, 2011.
- [8] J.-M. Alimi et al. DEUS full observable CDM universe simulation: the numerical challenge. *ArXiv:astro-ph.CO/1206.2838v1*, 2012.
- [9] B. Allen. Stochastic gravity-wave background in inflationary-universe models. *Phys. Rev. D*, 37:2078–2085, 1988.
- [10] B. Allen. The stochastic gravitational wave background: sources and detection. *ArXiv:gr-qc/9604033v3*, 1996.
- [11] B. Allen and J. D. Romano. Detecting a stochastic background of gravitational radiation: signal processing strategies and sensitivities. *Phys. Rev. D*, 59:102001, 1999.
- [12] P. Amaro-Seoane et al. Intermediate and extreme mass-ratio inspirals-astrophysics, science applications and detection using LISA. *Clas. Quantum Grav.*, 24:R113, 2007.
- [13] N. Andersson et al. Gravitational waves from neutron stars: promises and challenges. *Gen. Rel. Grav.*, 43:409–436, 2011.
- [14] M. Ando et al. Stable operation of a 300-m laser interferometer with sufficient sensitivity to detect gravitational-wave events within our galaxy. *Phys. Rev. Lett.*, 86:3950, 2001.
- [15] K. G. Arun et al. Massive black hole binary inspirals: results from the LISA parameter estimation taskforce. *Clas. Quantum Grav.*, 26:094027, 2009.

Bibliography

- [16] Z. Arzoumanian, D. F. Chernoff, and J. M. Cordes. The velocity distribution of isolated radio pulsars. *Astrophys. J.*, 568:289–301, 2002.
- [17] S. Babak et al. Fundamental physics and cosmology with LISA. *Clas. Quantum Grav.*, 28:114001, 2011.
- [18] S. Babak and A. Sesana. Resolving multiple supermassive black hole binaries with pulsar timing arrays. *Phys. Rev. D*, 85:044034, 2012.
- [19] D. C. Backer et al. A millisecond pulsar. *Nature*, 300:615, 1982.
- [20] L. Barack and C. Cutler. Confusion noise from LISA capture sources. *Phys. Rev. D*, 70:122002, 2004.
- [21] M. Begelman, R. Blandford, and M. Rees. Massive black hole binaries in active galactic nuclei. *Nature*, 287:307–309, 1980.
- [22] K. Belczynski et al. The effect of metallicity on the detection prospects for gravitational waves. *Astrophys. J. Letters*, 715:L138–L–141, 2010.
- [23] C. L. Bennett et al. The microwave anisotropy probe mission. *Astrophys. J.*, 583:1–23, 2003.
- [24] M. R. Blanton et al. An efficient targeting strategy for multiobject spectrograph surveys: the Sloan Digital Sky Survey “tiling” algorithm. *Astron. J.*, 125:2276–2286, 2003.
- [25] M. R. Blanton et al. NYU-VAGC: a galaxy catalog based on new public surveys. *Astron. J.*, 129:2562–2578, 2005.
- [26] N. W. Boggess et al. The COBE mission: its design and performance two years after the launch. *Astrophys. J.*, 397:420–429, 1992.
- [27] S. Bonoli et al. Modeling the cosmological co-evolution of supermassive black holes and galaxies: II. The clustering of quasars and their dark environment. *MNRAS*, 396:423, 2009.
- [28] J. Brinchmann et al. The physical properties of star forming galaxies in the low redshift universe. *MNRAS*, 351:1151, 2004.
- [29] J. D. Brown. Gravitational waves from the dynamical bar instability in a rapidly rotating star. *Phys. Rev. D*, 62:084024, 2000.
- [30] G. Bruzual and S. Charlot. Stellar population synthesis at the resolution of 2003. *MNRAS*, 344:1000, 2003.
- [31] T. Bulik, K. Belczynski, and A. Prestwich. IC10 X-1/NGC300 X-1: the very immediate progenitors of bh-bh binaries. *Astrophys. J.*, 730:140, 2011.
- [32] A. Buonanno. TASI lectures on gravitational waves from the early universe. *ArXiv:gr-qc/0303085v2*, 2004.
- [33] A. Buonanno. Gravitational waves. *ArXiv:gr-qc/0709.4682v1*, 2007.

- [34] A. Buonanno et al. Stochastic gravitational wave background from cosmological supernovae. *Phys. Rev. D*, 72:084001, 2005.
- [35] M. Burgay et al. An increased estimate of the merger rate of double neutron stars from observations of a highly relativistic system. *Nature*, 426:531–533, 2003.
- [36] S. Burke-Spolaor. Multi-messenger approaches to binary supermassive black holes in the “continuous-wave” regime. *ArXiv:1308.4408*, 2013.
- [37] B. Caron et al. The Virgo interferometer. *Clas. Quantum Grav.*, 14:1461–1469, 1997.
- [38] J. Casares. Observational evidence for stellar-mass black holes. *Proceedings IAU Symposium*, 238:3, 2007.
- [39] S. Chandrasekhar. Dynamical friction. I. General considerations: the coefficient of dynamical friction. *Astrophys. J.*, 97:255, 1943.
- [40] M. Colless et al. The 2dF galaxy redshift survey: spectra and redshifts. *MNRAS*, 328:1039, 2001.
- [41] A. J. Connolly et al. The evolution of the global star formation history as measured from the Hubble Deep Field. *Astrophys. J.*, 486:L11–L14, 1997.
- [42] N. J. Cornish. Gravitational wave confusion noise. *ArXiv:gr-qc/0304020v1*, 2003.
- [43] D. Coward and T. Regimbau. Detection regimes of the cosmological gravitational wave background from astrophysical sources. *New Astronomy Reviews*, 50:461–467, 2006.
- [44] D. M. Coward, R. R. Burman, and D. G. Blair. The stochastic background of gravitational waves from neutron stars formation at cosmological distances. *MNRAS*, 324:1015–1022, 2001.
- [45] D. M. Coward, R. R. Burman, and D. G. Blair. Simulating a stochastic background of gravitational waves from neutron star formation at cosmological distances. *MNRAS*, 329:411–416, 2002.
- [46] C. Cutler and J. Harms. Big Bang Observer and the NS binary subtraction problem. *Phys. Rev. D*, 73:042001, 2006.
- [47] C. Cutler. Gravitational waves from neutron stars with large toroidal B-fields. *Phys. Rev. D*, 66:084025, 2002.
- [48] C. Cutler and D. E. Holz. Ultra-high precision cosmology from gravitational waves. *Phys. Rev. D*, 80:104009, 2009.
- [49] K. Danzmann and LISA study team. LISA: laser interferometer space antenna for gravitational wave measurements. *Clas. Quantum Grav.*, 13:A247–A250, 1996.
- [50] M. Davis and P. J. E. Peebles. A survey of galaxy redshifts. V. The two-point position and velocity correlations. *Astrophys. J.*, 267:465, 1983.

Bibliography

- [51] J. C. N. de Araujo and O. D. Miranda. Star formation rate density and the stochastic background of gravitational waves. *Phys. Rev. D*, 71:127503, 2005.
- [52] J. C. N. de Araujo, O. D. Miranda, and O. D. Aguiar. Gravitational wave background from black holes of the Springel & Hernquist star formation epoch. *MNRAS*, 348:1373–1378, 2004.
- [53] J. A. de Freitas Pacheco. The NS-NS coalescence rate in galaxies and its significance to the Virgo gravitational antenna. *Astroparticle Physics*, 8:21–26, 1997.
- [54] A. J. Deutsch. The electromagnetic field of an idealized star in rigid rotation in vacuo. *Annales d’Astrophysique*, 18:1–10, 1955.
- [55] M. Dotti, M. Colpi, and F. Haardt. LISA double black holes: dynamics in gaseous nuclear discs. *MNRAS*, 367:103–112, 2006.
- [56] M. Dotti et al. Supermassive black hole binaries in gaseous and stellar circumnuclear discs: orbital dynamics and gas accretion. *MNRAS*, 379:956–962, 2007.
- [57] F. L. Drake and G. van Rossum. *The Python language reference manual : for Python version 3,2*. Network theory Ltd., 2011.
- [58] eLISA Consortium. The gravitational universe. *ArXiv:1305.5720*, 2013.
- [59] J. Ellis, X. Siemens, and J. Creighton. Optimal strategies for continuous gravitational wave detection in pulsar timing arrays. *Astrophys. J.*, 756:175, 2012.
- [60] M. Eracleous et al. A large systematic search for recoiling and close supermassive binary black holes. *Astrophys. J. Suppl.*, 201:23, 2012.
- [61] A. Escala et al. The role of gas in the merging of massive black holes in galactic nuclei. II. Black hole merging in a clumpy disk. *Astrophys. J.*, 630:152–166, 2005.
- [62] M. A. Fardal et al. On the evolutionary history of stars and their fossil mass and light. *MNRAS*, 379:985–1002, 2007.
- [63] A. J. Farmer and E. S. Phinney. The gravitational wave background from cosmological compact binaries. *MNRAS*, 346:1197–1214, 2003.
- [64] C.-A. Faucher-Giguere and V. M. Kaspi. Birth and evolution of isolated radio pulsars. *Astrophys. J.*, 643:332–355, 2006.
- [65] R. D. Ferdman. The European Pulsar Timing Array: current efforts and a leap toward the future. *Clas. Quantum Grav.*, 27:084014, 2010.
- [66] L. Ferrarese and D. Merritt. A fundamental relation between supermassive black holes and their host galaxies. *Astrophys. J.*, 539:L9–L12, 2000.
- [67] V. Ferrari, S. Matarrese, and R. Schneider. Gravitational wave background from a cosmological population of core-collapse supernovae. *MNRAS*, 303:247–257, 1999.

- [68] V. Ferrari, S. Matarrese, and R. Schneider. Stochastic background of gravitational waves generated by a cosmological population of young, rapidly rotating neutron stars. *MNRAS*, 303:258–264, 1999.
- [69] L. S. Finn, S. L. Larson, and J. D. Romano. Detecting a stochastic gravitational-wave background: the overlap reduction function. *Phys. Rev. D*, 79:062003, 2009.
- [70] R. Flaminio et al. Advanced Virgo white paper. *VIR-NOT-DIR-1390-304*, 2005.
- [71] R. Foster and D. Backer. Constructing a pulsar timing array. *Astrophys. J.*, 361:300, 1990.
- [72] J. M. Fregeau et al. The dynamical effects of white dwarf birth kicks in globular star clusters. *Astrophys. J.*, 695:L20–L24, 2009.
- [73] K. Gebhardt et al. A relationship between nuclear black hole mass and galaxy velocity dispersion. *Astrophys. J.*, 539:L13–L16, 2000.
- [74] A. Ghez et al. Measuring distance and properties of the Milky Way’s central supermassive black hole with stellar orbits. *Astrophys. J.*, 689:1044, 2008.
- [75] S. Gillessen et al. Monitoring stellar orbits around the massive black hole in the galactic center. *Astrophys. J.*, 692:1075–1109, 2009.
- [76] R. Gilmozzi and J. Spyromilio. The 42m European ELT: status. *Proc. of SPIE*, 7012:19, 2008.
- [77] P. L. Gonthier et al. Population synthesis of radio and gamma-ray pulsars in the fermi era. *AIP Conf. Proc.*, 1357:245–248, 2011.
- [78] A. W. Graham et al. An expanded $M_{bh} - \sigma$ diagram, and a new calibration of active galactic nuclei masses. *MNRAS*, 412:2211, 2011.
- [79] L. P. Grishchuk et al. Gravitational wave astronomy: in anticipation of first sources to be detected. *Physics-Uspokhi*, 44:1–51, 2001.
- [80] H. Grote. The GEO600 status. *Clas. Quantum Grav.*, 27:084003, 2010.
- [81] K. Gültekin et al. The M-sigma and M-L relations in galactic bulges, and determinations of their intrinsic scatter. *Astrophys. J.*, 698:198–221, 2009.
- [82] H. Guo, I. Zehavi, and Z. Zheng. A new method to correct for fiber collisions in galaxy two-point statistics. *Astrophys. J.*, 756:127, 2012.
- [83] Q. Guo et al. From dwarf spheroidals to cDs: simulating the galaxy population in a LCDM cosmology. *MNRAS*, 413:101, 2011.
- [84] Q. Guo et al. Galaxy formation in WMAP1 and WMAP7 cosmologies. *MNRAS*, 428:1351, 2013.
- [85] N. Haering and H.-W. Rix. On the black hole mass - bulge mass relation. *Astrophys. J.*, 604:L89, 2004.

Bibliography

- [86] A. Hamilton. Toward better ways to measure the galaxy correlation function. *Astrophys. J.*, 417:19, 1993.
- [87] A. K. Harding and D. Lai. Physics of strongly magnetized neutron stars. *Rept. Prog. Phys.*, 69:2631, 2006.
- [88] G. M. Harry. Advanced LIGO: the next generation of gravitational wave detectors. *Clas. Quantum Grav.*, 27:084006, 2010.
- [89] S. W. Hawking and G. F. R. Ellis. *The large scale structure of space-time*. Cambridge University Press, 1973.
- [90] S. W. Hawking and W. Israel. *300 years of gravitation*. Cambridge University Press, 1987.
- [91] B. Henriques et al. Confronting theoretical models with the observed evolution of the galaxy population out to $z=4$. *MNRAS*, 421:2904, 2012.
- [92] G. Hobbs et al. The International Pulsar Timing Array project: using pulsars as a gravitational wave detector. *Clas. Quantum Grav.*, 27:084013, 2010.
- [93] A. M. Hopkins and J. F. Beacom. On the normalization of the cosmic star formation history. *Astrophys. J.*, 651:142–154, 2006.
- [94] R. A. Hulse and J. H. Taylor. Discovery of a pulsar in a binary system. *Astrophys. J.*, 195:L51–L53, 1975.
- [95] A. H. Jaffe and D. C. Backer. Gravitational waves probe the coalescence rate of massive black hole binaries. *Astrophys. J.*, 583:16, 2003.
- [96] N. Jarosik et al. Seven-year Wilkinson microwave anisotropy probe (WMAP) observations: sky maps, systematic errors, and basic results. *Astrophys. J. Suppl.*, 192:14, 2011.
- [97] F. Jenet et al. The north American nanohertz observatory for gravitational waves. *ArXiv:0909.1058v1*, 2009.
- [98] F. A. Jenet et al. Detecting the stochastic gravitational wave background using pulsar timing. *Astrophys. J.*, 625:L123–L126, 2005.
- [99] S. Johnston and D. Galloway. Pulsar braking indices revisited. *MNRAS*, 306:L50–L54, 1999.
- [100] W. Ju et al. Search for supermassive black hole binaries in the Sloan Digital Sky Survey spectroscopic sample. 2013.
- [101] V. Kalogera et al. The coalescence rate of double neutron star systems. *Astrophys. J.*, 556:340–356, 2001.
- [102] V. Kalogera et al. The cosmic coalescence rates for neutron star binaries. Erratum. *Astrophys. J.*, 614:L137–L138, 2004.

- [103] V. Kalogera et al. Formation of double compact objects. *Phys. Reports*, 442:75–108, 2007.
- [104] G. Kauffmann et al. The host galaxies of AGN. *MNRAS*, 346:1055, 2003.
- [105] G. Kauffmann et al. Stellar masses and star formation histories for 10^5 galaxies from the Sloan Digital Sky Survey. *MNRAS*, 341:33, 2003.
- [106] S. Kawamura et al. The Japanese space gravitational wave antenna: DECIGO. *Clas. Quantum Grav.*, 28:094011, 2011.
- [107] S. O. Kepler et al. White dwarf mass distribution in the SDSS. *MNRAS*, 375:1315–1324, 2007.
- [108] F. M. Khan, A. Just, and D. Merritt. Efficient merger of binary supermassive black holes in merging galaxies. *Astrophys. J.*, 732:89, 2011.
- [109] M. G. Kitzbichler and S. D. M. White. A calibration of the relation between the abundance of close galaxy pairs and the rate of galaxy mergers. *MNRAS*, 391:1489, 2008.
- [110] B. Knispel. *Pulsar discoveries by volunteer distributed computing*. PhD thesis, Leibniz Universität Hannover, 2011.
- [111] B. Knispel and B. Allen. Blandford’s argument: the strongest continuous gravitational wave signal. *Phys. Rev. D*, 78:044031, 2008.
- [112] B. Kocsis and A. Sesana. Gas driven massive black hole binaries: signatures in the nHz gravitational wave background. *MNRAS*, 411:1467, 2011.
- [113] E. Komatsu et al. Seven-year Wilkinson microwave anisotropy probe (WMAP) observations: cosmological interpretation. *Astrophys. J. Suppl.*, 192:18, 2011.
- [114] R. K. Kopparapu et al. Host galaxies catalog used in LIGO searches for compact binary coalescence events. *Astrophys. J.*, 675:1459–1467, 2008.
- [115] J. Kormendy and D. Richstone. Inward bound - the search for supermassive black holes in galactic nuclei. *Annu. Rev. Astron. Astrophys.*, 33:581–624, 1995.
- [116] D. I. Kosenko and K. A. Postnov. On the gravitational wave noise from unresolved extragalactic binaries. *Astron. Astrophys.*, 336:786–790, 1998.
- [117] K. Kotera. Ultrahigh energy cosmic ray acceleration in newly born magnetars and their associated gravitational wave signatures. *Phys. Rev. D*, 84:023002, 2011.
- [118] I. Kowalska, T. Bulik, and K. Belczynski. Gravitational wave background from population III binaries. *Astron. Astrophys.*, 541:A120, 2012.
- [119] M. Kramer. Probing gravitation with pulsars. *Proceedings IAU Symposium*, 291:19, 2012.
- [120] K. Kuroda and LCGT Collaboration. The status of LCGT. *Clas. Quantum Grav.*, 23:S215–S221, 2006.

Bibliography

- [121] C. Lämmerzahl, C. W. F. Everitt, and F. W. Hehl. *Gyros, clocks, interferometers...: testing relativistic gravity in space*. Springer Verlag, 2001.
- [122] S. Landy and A. Szalay. Bias and variance of angular correlation functions. *Astrophys. J.*, 412:64, 1993.
- [123] J. M. Lattimer. Neutron star equation of state. *New Astronomy Reviews*, 54:101–109, 2010.
- [124] J. M. Lattimer and M. Prakash. The physics of neutron stars. *Science*, 304:536–542, 2004.
- [125] J. Lazio. The Square Kilometre Array. *ArXiv:0910.0632v1*, 2009.
- [126] G. Lemson and Virgo Consortium. Halo and galaxy formation histories from the Millennium Simulation: public release of a VO-oriented and SQL-queryable database for studying the evolution of galaxies in the LCDM cosmogony. *ArXiv:astro-ph/0608019*, 2006.
- [127] C. Li et al. The clustering of narrow-line AGN in the local universe. *MNRAS*, 373:457–468, 2006.
- [128] C. Li et al. The dependence of clustering on galaxy properties. *MNRAS*, 368:21–36, 2006.
- [129] LIGO Scientific Collaboration. Coherent searches for periodic gravitational waves from unknown isolated sources and Scorpius X-1: results from the second LIGO science run. *Phys. Rev. D*, 76:082001, 2007.
- [130] LIGO Scientific Collaboration. LIGO: the laser interferometer gravitational wave observatory. *Rep. Prog. Phys.*, 72:076901, 2009.
- [131] LIGO Scientific Collaboration. Advanced LIGO anticipated sensitivity curves. Technical Report LIGO-T1000414-v13, LIGO Scientific Collaboration, 2010.
- [132] LIGO Scientific Collaboration. Predictions for the rates of compact binary coalescences observable by ground-based gravitational wave detectors. *Clas. Quantum Grav.*, 27:173001, 2010.
- [133] LIGO Scientific Collaboration. A gravitational wave observatory operating beyond the quantum shot-noise limit: squeezed light in application. *Nature Physics Letters*, 7:962, 2011.
- [134] M. M. Limoges and P. Bergeron. A spectroscopic analysis of white dwarfs in the Kiso Survey. *Astrophys. J.*, 714:1037–1051, 2010.
- [135] C. Lintott et al. Galaxy Zoo 1 : data release of morphological classifications for nearly 900,000 galaxies. *MNRAS*, 410:166, 2011.
- [136] C. J. Lintott et al. Galaxy Zoo : morphologies derived from visual inspection of galaxies from the Sloan Digital Sky Survey. *MNRAS*, 389:1179–1189, 2008.

- [137] D. Lorimer. Binary and millisecond pulsars. *Living Rev. Relativity*, 11:8, 2008.
- [138] D. Lorimer and M. Kramer. *Handbook of pulsar astronomy*. Cambridge University Press, Cambridge, England, 2005.
- [139] D. R. Lorimer. Radio pulsar populations. *Astrophysics and Space Science Proceedings*, pages 21–36, 2011.
- [140] LSST Collaboration. LSST: from science drivers to reference design and anticipated data products. *ArXiv:0805.2366v2*, 2011.
- [141] H. Lück and GEO600 team. The GEO600 project. *Clas. Quantum Grav.*, 14:1471–1476, 1997.
- [142] D. Lynden-Bell. Galactic nuclei as collapsed old quasars. *Nature*, 223:690, 1969.
- [143] A. Lyne et al. A double-pulsar system - a rare laboratory for relativistic gravity and plasma physics. *Science*, 303:1153–1157, 2004.
- [144] P. Madau, M. D. Valle, and N. Panagia. On the evolution of the cosmic supernova rates. *MNRAS*, 297:L17–L22, 1998.
- [145] M. Maggiore. Gravitational wave experiments and early universe cosmology. *Phys. Reports*, 331:283–367, 2000.
- [146] M. Maggiore. Stochastic background of gravitational waves. *ArXiv:gr-qc/0008027v1*, 2000.
- [147] M. Maggiore. *Gravitational waves volume 1: theory and experiments*. Oxford University Press, 2008.
- [148] J. Magorrian et al. The demography of massive dark objects in galaxy centers. *Astron. J.*, 115:2285–2305, 1998.
- [149] R. N. Manchester. The Parkes Pulsar Timing Array project. *AIP Conf. Proc.*, 983:584, 2008.
- [150] R. N. Manchester et al. The ATNF pulsar catalogue. *Astron. J.*, 129:1993, 2005.
- [151] R. Manchester. The Parkes Pulsar Timing Array project. *Publ.Astron.Soc.Austral.*, 30:17, 2013.
- [152] I. Mandel and R. O’Shaughnessy. Compact binary coalescences in the band of ground-based gravitational-wave detectors. *Clas. Quantum Grav.*, 27:114007, 2010.
- [153] S. Marassi, R. Schneider, and V. Ferrari. Gravitational-wave backgrounds and the cosmic transition from pop. III to pop. II stars. *MNRAS*, 398:293–302, 2009.
- [154] S. Marassi et al. Stochastic background of gravitational waves emitted by magnetars. *MNRAS*, 411:2549–2557, 2011.

Bibliography

- [155] A. Marconi and L. K. Hunt. The relation between black hole mass, bulge mass, and near-infrared luminosity. *Astrophys. J.*, 589:L21–L24, 2003.
- [156] F. Marulli et al. Modeling the cosmological co-evolution of supermassive black holes and galaxies: I. BH scaling relations and the AGN luminosity function. *MNRAS*, 385:1846, 2008.
- [157] N. J. McConnell and C.-P. Ma. Revisiting the scaling relations of black hole masses and host galaxy properties. *Astrophys. J.*, 764:184, 2013.
- [158] M. Milosavljević and D. Merritt. The final parsec problem. *AIP Conf. Proc.*, 686:201–210, 2003.
- [159] C. M. F. Mingarelli et al. Observing the dynamics of super-massive black hole binaries with pulsar timing arrays. *Phys. Rev. Lett.*, 109:081104, 2012.
- [160] C. M. F. Mingarelli et al. Characterising gravitational wave stochastic background anisotropy with pulsar timing arrays. *ArXiv:1306.5394*, 2013.
- [161] C. W. Misner, K. S. Thorne, and J. A. Wheeler. *Gravitation*. W. H. Freeman and Co., San Francisco, USA, 1973.
- [162] K. Nagamine et al. The history of cosmological star formation: 3 independent approaches and a critical test using the extragalactic background light. *Astrophys. J.*, 653:881–893, 2006.
- [163] M. Nauenberg. Analytic approximations to the mass-radius relation and energy of zero-temperature stars. *Astrophys. J.*, 175:417–430, 1972.
- [164] G. Nelemans. Galactic binaries as sources of gravitational waves. *AIP Conf. Proc.*, 686:263–272, 2003.
- [165] G. Nelemans, L. R. Yungelson, and S. F. Portegies Zwart. The gravitational wave signal from the galactic disk population of binaries containing two compact objects. *Astron. Astrophys.*, 375:890–898, 2001.
- [166] A. Nishizawa et al. Cosmology with space-based gravitational-wave detectors — dark energy and primordial gravitational waves —. *Phys. Rev. D*, 85:044047, 2012.
- [167] A. Nishizawa, A. Taruya, and S. Kawamura. Cosmological test of gravity with polarizations of stochastic gravitational waves around 0.1-1 Hz. *Phys. Rev. D*, 81:104043, 2010.
- [168] B. J. Owen et al. Gravitational waves from hot young rapidly rotating neutron stars. *Phys. Rev. D*, 58:084020, 1998.
- [169] F. Pacini. Rotating neutron stars, pulsars and supernova remnants. *Nature*, 219:145–146, 1968.
- [170] C. Palomba. Simulation of a population of isolated neutron stars evolving through the emission of gravitational waves. *MNRAS*, 359:1150–1164, 2005.

- [171] F. Pedregosa et al. Scikit-learn: Machine Learning in Python. *Journal of Machine Learning Research*, 12:2825, 2011.
- [172] P. J. E. Peebles. *Principles of physical cosmology*. Princeton series in physics. Princeton University Press, 1993.
- [173] P. Peebles. *The large-scale structure of the universe*. Princeton University Press, Princeton, USA, 1980.
- [174] A. A. Penzias and R. W. Wilson. A measurement of excess antenna temperature at 4080 Mc/s. *Astrophys. J.*, 142:419–421, 1965.
- [175] R. Perna et al. How rapidly do neutron stars spin at birth? Constraints from archival X-ray observations of extragalactic supernovae. *MNRAS*, 384:1638–1648, 2008.
- [176] P. C. Peters. Gravitational radiation and the motion of two point masses. *Phys. Rev.*, 136:4B, 1964.
- [177] P. C. Peters and J. Mathews. Gravitational radiation from point masses in a Keplerian orbit. *Phys. Rev.*, 131:435, 1963.
- [178] A. Petiteau, S. Babak, A. Sesana, and M. de Araújo. Resolving multiple supermassive black hole binaries with pulsar timing arrays. II. Genetic algorithm implementation. *Phys. Rev. D*, 87:064036, 2013.
- [179] E. S. Phinney. The rate of neutron star binary mergers in the universe: minimal predictions for gravity wave detectors. *Astrophys. J.*, 380:L17–L21, 1991.
- [180] E. S. Phinney. A practical theorem on gravitational waves backgrounds. *ArXiv:astro-ph/0108028v1*, 2001.
- [181] E. S. Phinney et al. The Big Bang Observer: direct detection of gravitational waves from the birth of the universe to the present. *NASA OSS Vision Missions Program, Proposal VM03-0021-0021*, 2004.
- [182] M. Pitkin et al. Gravitational wave detection by interferometry (ground and space). *Living Rev. Relativity*, 14:5, 2011.
- [183] Planck Collaboration. Planck 2013 results. XVI. Cosmological parameters. *ArXiv:1303.5076*, 2013.
- [184] S. B. Popov et al. The neutron stars census. *Astrophys. J.*, 530:896, 2000.
- [185] S. B. Popov et al. Population synthesis studies of isolated neutron stars with magnetic field decay. *MNRAS*, 401:2675–2686, 2010.
- [186] C. Porciani and P. Madau. On the association of gamma ray bursts with massive stars: implications for number counts and lensing statistics. *Astrophys. J.*, 548:522–531, 2001.
- [187] K. A. Postnov and L. R. Yungelson. The evolution of compact binary star systems. *Living Rev. Relativity*, 9:6, 2006.

Bibliography

- [188] M. Preto et al. Fast coalescence of massive black hole binaries from mergers of galactic nuclei: implications for low-frequency gravitational-wave astrophysics. *Astrophys. J. Letters*, 732:L26, 2011.
- [189] R. Prix. Gravitational waves from spinning neutron stars. In *Neutron Stars and Pulsars*, volume 357 of *Astrophysics and Space Science Library*, pages 651–685. Springer Berlin Heidelberg, 2009.
- [190] M. Punturo et al. The Einstein Telescope: a third-generation gravitational wave observatory. *Clas. Quantum Grav.*, 27:194002, 2010.
- [191] G. D. Quinlan. The dynamical evolution of massive black hole binaries. I. Hardening in a fixed stellar background. *New Astronomy*, 1:35–36, 1996.
- [192] M. Rajagopal and R. W. Romani. Ultra-low-frequency gravitational radiation from massive black hole binaries. *Astrophys. J.*, 446:543, 1995.
- [193] V. Ravi et al. Does a ‘stochastic’ background of gravitational waves exist in the pulsar timing band? *Astrophys. J.*, 761:84, 2012.
- [194] T. Regimbau. The astrophysical gravitational wave stochastic background. *Research in Astron. Astrophys.*, 11:369–390, 2011.
- [195] T. Regimbau and B. Chauvineau. A stochastic background from extra-galactic double neutron stars. *Clas. Quantum Grav.*, 24:S627–S637, 2007.
- [196] T. Regimbau and J. A. de Freitas Pacheco. Gravitational wave emission from radio pulsars revisited. *Astron. Astrophys.*, 359:242, 2000.
- [197] T. Regimbau and J. A. de Freitas Pacheco. Cosmic background of gravitational waves from rotating neutron stars. *Astron. Astrophys.*, 376:381–385, 2001.
- [198] T. Regimbau and J. A. de Freitas Pacheco. Gravitational wave background from magnetars. *Astron. Astrophys.*, 447:1–7, 2006.
- [199] T. Regimbau and J. A. de Freitas Pacheco. Stochastic background from coalescences of ns-ns binaries. *Astrophys. J.*, 642:455–461, 2006.
- [200] T. Regimbau and S. A. Hughes. Gravitational wave confusion background from cosmological compact binaries: implications for future terrestrial detectors. *Phys. Rev. D*, 79:062002, 2009.
- [201] T. Regimbau and V. Mandic. Astrophysical sources of stochastic gravitational-wave background. *Clas. Quantum Grav.*, 25:184018, 2008.
- [202] T. Regimbau et al. A mock data challenge for the Einstein Gravitational-Wave Telescope. *Phys. Rev. D*, 86:122001, 2012.
- [203] T. Regimbau et al. The stochastic background from cosmic (super)strings: popcorn and (Gaussian) continuous regimes. *Phys. Rev. D*, 85:066001, 2012.

- [204] D. Richstone et al. Supermassive black holes and the evolution of galaxies. *Nature*, 395:A14, 1998.
- [205] A. G. Riess et al. A redetermination of the Hubble Constant with the Hubble Space Telescope from a differential distance ladder. *Astrophys. J.*, 699:539–563, 2009.
- [206] A. G. Riess et al. A 3% solution: determination of the Hubble Constant with the Hubble Space Telescope and Wide Field Camera 3. *Astrophys. J.*, 730:119, 2011.
- [207] P. A. Rosado. Gravitational wave background from binary systems. *Phys. Rev. D*, 84:084004, 2011.
- [208] P. A. Rosado. Gravitational wave background from rotating neutron stars. *Phys. Rev. D*, 86:104007, 2012.
- [209] A. J. Ruiter et al. The LISA gravitational wave foreground: a study of double white dwarfs. *Astrophys. J.*, 717:1006–1021, 2010.
- [210] S. Salim et al. UV star formation rates in the local universe. *Astrophys. J. Suppl.*, 173:267–292, 2007.
- [211] E. E. Salpeter. The luminosity function and stellar evolution. *Astrophys. J.*, 121:161, 1955.
- [212] S. A. Sanidas, R. A. Battye, and B. W. Stappers. Constraints on cosmic string tension imposed by the limit on the stochastic gravitational wave background from the European Pulsar Timing Array. 2012.
- [213] B. Sathyaprakash and B. F. Schutz. Physics, astrophysics and cosmology with gravitational waves. *Living Rev. Relativity*, 12:2, 2009.
- [214] E. F. Schlafly et al. Photometric calibration of the first 1.5 years of the Pan-STARRS1 survey. *Astrophys. J.*, 756:158, 2012.
- [215] R. Schneider et al. Low-frequency gravitational waves from cosmological compact binaries. *MNRAS*, 324:797–810, 2001.
- [216] R. Schneider, V. Ferrari, and S. Matarrese. Stochastic backgrounds of gravitational waves from cosmological populations of astrophysical sources. *ArXiv:astro-ph/9903470v1*, 1999.
- [217] R. Schneider, S. Marassi, and V. Ferrari. Stochastic backgrounds of gravitational waves from extragalactic sources. *Clas. Quantum Grav.*, 27:194007, 2010.
- [218] B. F. Schutz. Gravitational wave astronomy. *Clas. Quantum Grav.*, 16:A131, 1999.
- [219] B. F. Schutz. Networks of gravitational wave detectors and three figures of merit. *ArXiv:1102.5421*, 2011.
- [220] A. Sesana. Insights on the astrophysics of supermassive black hole binaries from pulsar timing observations. *ArXiv:1307.2600*, 2013.

Bibliography

- [221] A. Sesana. Systematic investigation of the expected gravitational wave signal from super-massive black hole binaries in the pulsar timing band. *MNRAS*, 433:L1–L5, 2013.
- [222] A. Sesana et al. The gravitational wave signal from massive black hole binaries and its contribution to the LISA data stream. *Astrophys. J.*, 623:23–30, 2005.
- [223] A. Sesana, A. Vecchio, and C. N. Colacino. The stochastic gravitational-wave background from massive black hole binary systems: implications for observations with pulsar timing array. *MNRAS*, 390:192–209, 2008.
- [224] A. Sesana, A. Vecchio, and M. Volonteri. Gravitational waves from resolvable massive black hole binary systems and observations with pulsar timing arrays. *MNRAS*, 394:11, 2009.
- [225] A. Sesana et al. Low-frequency gravitational radiation from coalescing massive black hole binaries in hierarchical cosmologies. *Astrophys. J.*, 611:623–632, 2004.
- [226] D. A. Shaddock. Space-based gravitational wave detection with LISA. *Clas. Quantum Grav.*, 25:114012, 2008.
- [227] S. L. Shapiro and S. A. Teukolsky. *Black holes, white dwarfs, and neutron stars: the physics of compact objects*. Physics textbook. Wiley, 1983.
- [228] R. O. Shaughnessy et al. Constraining population synthesis models via empirical binary compact object merger and supernova rates. *Astrophys. J.*, 672:479–488, 2008.
- [229] Y. Shen et al. Constraining sub-parsec binary supermassive black holes in quasars with multi-epoch spectroscopy. I. The general quasar population. *Astrophys. J.*, 775:49, 2013.
- [230] K. Somiya and KAGRA Collaboration. Detector configuration of KAGRA - the Japanese cryogenic gravitational-wave detector. *Clas. Quantum Grav.*, 29:124007, 2012.
- [231] D. N. Spergel et al. First year Wilkinson microwave anisotropy probe (WMAP) observations: determination of cosmological parameters. *Astrophys. J. Suppl.*, 148:175–194, 2003.
- [232] V. Springel et al. Simulations of the formation, evolution and clustering of galaxies and quasars. *Nature*, 435:629, 2005.
- [233] V. Springel et al. Populating a cluster of galaxies - I. Results at $z=0$. *MNRAS*, 328:726, 2001.
- [234] C. Stoughton et al. Sloan Digital Sky Survey: early data release. *Astron. J.*, 123:485–548, 2002.
- [235] K. Strobel and M. K. Weigel. On the minimum and maximum mass of neutron stars and the delayed collapse. *Astron. Astrophys.*, 367:582–587, 2001.
- [236] L. G. Strolger et al. The Hubble higher z supernovae search: supernovae to $z=1.6$ and constraints on type Ia progenitors models. *Astrophys. J.*, 613:200–223, 2004.

- [237] S. R. Taylor and J. R. Gair. Searching for anisotropic gravitational-wave backgrounds using pulsar timing arrays. *ArXiv:1306.5395*, 2013.
- [238] C. Thompson and R. C. Duncan. Neutron star dynamos and the origins of pulsar magnetism. *Astrophys. J.*, 408:194, 1993.
- [239] C. Thompson and R. C. Duncan. The soft gamma repeaters as very strongly magnetized neutron stars - I Radiative mechanism for outbursts. *MNRAS*, 275:255–300, 1995.
- [240] C. Thompson, M. Lyutikov, and S. R. Kulkarni. Electrodynamics of magnetars: implications for the persistent X-ray emission and spin-down of the soft-gamma repeaters and anomalous X-ray pulsars. *Astrophys. J.*, 574:332–355, 2002.
- [241] E. Thrane. Measuring the non-Gaussian stochastic gravitational-wave background: a method for realistic interferometer data. *Phys. Rev. D*, 87:043009, 2013.
- [242] J. Tonry et al. The Pan-STARRS1 photometric system. *Astrophys. J.*, 750:99, 2012.
- [243] C. A. Tremonti et al. The origin of the mass–metallicity relation: insights from 53,000 star-forming galaxies in the SDSS. *Astrophys. J.*, 613:898–913, 2004.
- [244] J. E. Trümper. Observations of neutron stars and the equation of state of matter at high densities. *Progress in Particle and Nuclear Physics*, 66:674–680, 2011.
- [245] P. Tsalmantza et al. A systematic search for massive black hole binaries in SDSS spectroscopic sample. *Astrophys. J.*, 738:20, 2011.
- [246] R. van Haasteren et al. Placing limits on the stochastic gravitational-wave background using European Pulsar Timing Array data. *MNRAS*, 414:3117–3128, 2011.
- [247] R. van Haasteren et al. Analysis of the first IPTA mock data challenge by the EPTA timing data analysis working group. *ArXiv:1301.6673*, 2013.
- [248] A. Vilenkin. Cosmic strings and domain walls. *Phys. Reports*, 121:263–315, 1985.
- [249] M. Volonteri, F. Haardt, and P. Madau. The assembly and merging history of supermassive black holes in hierarchical models of galaxy formation. *Astrophys. J.*, 582:15, 2003.
- [250] R. Wald. *General Relativity*. University of Chicago Press, 1983.
- [251] W. Wang and S. D. M. White. Satellite abundances around bright isolated galaxies. *MNRAS*, 424:2574, 2012.
- [252] J. M. Weisberg, D. J. Nice, and J. H. Taylor. Timing measurements of the relativistic binary pulsar PSR B1913+16. *Astrophys. J.*, 722:1030–1034, 2010.
- [253] S. White and M. Rees. Core condensation in heavy halos - a two-stage theory for galaxy formation and clustering. *MNRAS*, 183:341–358, 1978.
- [254] S. M. Wilkins, N. Trentham, and A. M. Hopkins. The evolution of stellar mass and the implied star formation history. *MNRAS*, 385:687–694, 2008.

Bibliography

- [255] B. Willems et al. Understanding compact object formation and natal kicks I. Calculation methods and the case of GRO J1655-40. *Astrophys. J.*, 625:324–346, 2005.
- [256] B. Willems et al. On the formation and progenitor of PSR J0737-3039: New constraints on the supernova explosion forming pulsar B. *Phys. Rev. D*, 74:043003, 2006.
- [257] J. S. B. Wyithe and A. Loeb. Low-frequency gravitational waves from massive black hole binaries: predictions for LISA and pulsar timing arrays. *Astrophys. J.*, 590:16, 2003.
- [258] K. Yagi and N. Seto. Detector configuration of DECIGO/BBO and identification of cosmological neutron-star binaries. *Phys. Rev. D*, 83:044011, 2011.
- [259] D. G. York et al. The Sloan Digital Sky Survey: technical summary. *Astron. J.*, 120:1579, 2000.
- [260] X.-J. Zhu et al. On the gravitational wave background from compact binary coalescences in the band of ground-based interferometers. *MNRAS*, 431:882, 2013.
- [261] X.-J. Zhu, X.-L. Fan, and Z.-H. Zhu. Stochastic gravitational wave background from neutron star r-mode instability revisited. *Astrophys. J.*, 729:59, 2011.
- [262] J. Ziółkowski. Masses of black holes in the universe. *Chin. J. Astron. Astrophys. Supplement*, 8:273–280, 2008.

Acknowledgements

The Millennium Simulation databases used in this thesis and the web application providing online access to them were constructed as part of the activities of the German Astrophysical Virtual Observatory (GAVO).

Funding for the SDSS and SDSS-II has been provided by the Alfred P. Sloan Foundation, the Participating Institutions, the National Science Foundation, the U.S. Department of Energy, the National Aeronautics and Space Administration, the Japanese Monbukagakusho, the Max Planck Society, and the Higher Education Funding Council for England. The SDSS Web Site is <http://www.sdss.org/>.

The SDSS is managed by the Astrophysical Research Consortium for the Participating Institutions. The Participating Institutions are the American Museum of Natural History, Astrophysical Institute Potsdam, University of Basel, University of Cambridge, Case Western Reserve University, University of Chicago, Drexel University, Fermilab, the Institute for Advanced Study, the Japan Participation Group, Johns Hopkins University, the Joint Institute for Nuclear Astrophysics, the Kavli Institute for Particle Astrophysics and Cosmology, the Korean Scientist Group, the Chinese Academy of Sciences (LAMOST), Los Alamos National Laboratory, the Max-Planck-Institute for Astronomy (MPIA), the Max-Planck-Institute for Astrophysics (MPA), New Mexico State University, Ohio State University, University of Pittsburgh, University of Portsmouth, Princeton University, the United States Naval Observatory, and the University of Washington.

This work was supported by the IMPRS on Gravitational Wave Astronomy.

I thank Marta Volonteri and Alberto Sesana for providing me with the numerical models of the coalescence rates of massive black hole binaries used in Chapter 2; also thanks to Tania Regimbau for the sensitivity curves of the Einstein Telescope, and Jarle Brinchmann, for the updated catalog of galaxy masses.

I thank Bruce Allen, Pau Amaro-Seoane, Berit Behnke, Jarle Brinchmann, Colin Clark, Tito Dal Canton, Roberto Decarli, Vladimir Dergachev, Evan Goetz, Rutger van Haasteren, Guinevere Kauffmann, David Keitel, Drew Keppel, Benjamin Knispel, Iraklis Konstantopoulos, Giulio Mazzolo, Holger Pletsch, Reinhard Prix, Tania Regimbau, Joe Romano, Francesco Salemi, Alberto Sesana, Miroslav Shaltev, and Karl Wette, for their help on the realisation of this work.

I especially thank Bruce Allen for several reasons. First, for giving me the opportunity to do my PhD at the AEI, surrounded by such great colleagues in an enjoyable working atmosphere. I thank him also for the fruitful and encouraging discussions at the blackboard and at the table during these years, not only for what I have learnt about Physics, but also about how to properly present my scientific work. Finally, I thank him for letting me attend amazing conferences around the world, where I learnt on state-of-the-art research, met the best experts in many different fields of Physics, and made new friends from disparate nationalities and cultures.

Other persons that have helped me by making my daily work at the AEI more enjoyable are my colleagues and ex-colleagues, Giulio Mazzolo, Tito Dal Canton, Miroslav Shaltev, Miriam

Cabero Müller, Letizia Sammut, Natalia Korsakova, Benjamin Knispel, Shaon Ghosh, Berit Behnke, David Keitel, and many others, with whom I shared great seminars, football matches, amazing trips, concerts...

I made great friends during the PhD, many of them in the city of Hanover, and many others in different places in the world. They all contributed in a different and special manner to this thesis, so I thank them for the great times we have spent together.

Finally, I must thank other people that are responsible for the existence of this thesis: my family and friends in Spain. They supported me from the distance, haciendo la distancia soportable.

Curriculum Vitae

Personal Information

- Date of birth: 28th November 1986.
- Place of birth: Seville (Spain).

Education & Research

- January 2010 - December 2013, Hannover (Germany).
Doctoral Studies at the Max Planck Institute for Gravitational Physics (Albert Einstein Institute in Hannover) and the Leibniz Universität Hannover, with an International Max Planck Research School (IMPRS) on Gravitational Wave Astronomy.
Observational Relativity and Cosmology group (supervisor: Prof. Dr. Bruce Allen).
- October 2008 - October 2009, Münster (Germany).
Master of Science at the Westfälische Wilhelms-Universität Münster.
Neutrino Physics group (supervisor: Prof. Dr. Dieter Frekers).
The last year of undergraduate studies was carried out at this university (completing a double degree at the universities of Sevilla and Münster). The achieved marks surpassed those awarded with the Spanish national prize for best academic qualifications (Premios Nacionales a la Excelencia en el Rendimiento Académico Universitario).
- July 2008 - September 2008, Barcelona (Spain).
Summer research fellowship at the Institute of Photonic Sciences (ICFO).
Quantum Information Theory group (supervisor: Prof. Dr. Antonio Acín).
- September 2004 - July 2008, Seville (Spain).
First four years of the higher university degree in Physics at the Universidad de Sevilla.
- Before September 2004, Jerez de la Frontera (Spain).
High school degree (with highest honors) at José Manuel Caballero Bonald.
Scholar studies at Manuel de Falla Public School.

List of publications

Refereed publications

- **Pablo A. Rosado**, *Gravitational wave background from binary systems*, Phys. Rev. D 84, 084004 (2011).
- **Pablo A. Rosado**, *Gravitational wave background from rotating neutron stars*, Phys. Rev. D 86, 104007 (2012).

Awaiting publication

- **Pablo A. Rosado & Alberto Sesana**, *Targeting supermassive black hole binaries and gravitational wave sources for the pulsar timing array*, to be submitted to Mon. Not. Roy. Astron. Soc.

Science outreach

- **Pablo A. Rosado, Benjamin Knispel, Thomas Adams, Natalia Korsakova, Gabriel Incertis, Jota Eslava & Rutger van Haasteren**, *The invisible colours of the universe*, published in YouTube in August 2013. Presented to the European science outreach video contest Fast Forward Science 2013. URL of the video:

<http://www.youtube.com/watch?v=SVHm3tAjnNQ>